UNIVERSITAT POLITÈCNICA DE CATALUNYA
BARCELONATECH

Advanced methods for Earth observation data synergy for geophysical parameter retrieval

Christoph Josef Herbert

ADVERTIMENT La consulta d'aquesta tesi queda condicionada a l'acceptació de les següents condicions d'ús: La difusió d'aquesta tesi per mitjà del repositori institucional UPCommons (http://upcommons.upc.edu/tesis) i el repositori cooperatiu TDX (http://www.tdx.cat/) ha estat autoritzada pels titulars dels drets de propietat intel·lectual **únicament per a usos privats** emmarcats en activitats d'investigació i docència. No s'autoritza la seva reproducció amb finalitats de lucre ni la seva difusió i posada a disposició des d'un lloc aliè al servei UPCommons o TDX. No s'autoritza la presentació del seu contingut en una finestra o marc aliè a UPCommons (*framing*). Aquesta reserva de drets afecta tant al resum de presentació de la tesi com als seus continguts. En la utilització o cita de parts de la tesi és obligat indicar el nom de la persona autora.

ADVERTENCIA La consulta de esta tesis queda condicionada a la aceptación de las siguientes condiciones de uso: La difusión de esta tesis por medio del repositorio institucional UPCommons (http://upcommons.upc.edu/tesis) y el repositorio cooperativo TDR (http://www.tdx.cat/?locale-attribute=es) ha sido autorizada por los titulares de los derechos de propiedad intelectual **únicamente para usos privados enmarcados** en actividades de investigación y docencia. No se autoriza su reproducción con finalidades de lucro ni su difusión y puesta a disposición desde un sitio ajeno al servicio UPCommons No se autoriza la presentación de su contenido en una ventana o marco ajeno a UPCommons (*framing)*. Esta reserva de derechos afecta tanto al resumen de presentación de la tesis como a sus contenidos. En la utilización o cita de partes de la tesis es obligado indicar el nombre de la persona autora.

WARNING On having consulted this thesis you're accepting the following use conditions: Spreading this thesis by the institutional repository UPCommons (http://upcommons.upc.edu/tesis) and the cooperative repository TDX (http://www.tdx.cat/?locale- attribute=en) has been authorized by the titular of the intellectual property rights **only for private uses** placed in investigation and teaching activities. Reproduction with lucrative aims is not authorized neither its spreading nor availability from a site foreign to the UPCommons service. Introducing its content in a window or frame foreign to the UPCommons service is not authorized (framing). These rights affect to the presentation summary of the thesis as well as to its contents. In the using or citation of parts of the thesis it's obliged to indicate the name of the author.

UNIVERSITAT POLITÈCNICA DE CATALUNYA
BARCELONATECH
Departament de Teoria del Senyal
i Comunicacions

Advanced Methods for Earth Observation Data Synergy for Geophysical Parameter Retrieval

Author

Christoph Herbert

Thesis Advisors

Prof. Mercè Vall-llossera Ferran
Prof. Adriano José Camps Carmona

A thesis submitted to attain the degree of
DOCTOR OF PHILOSOPHY
Universitat Politècnica de Catalunya - BarcelonaTech (UPC)

PhD program on Signal Theory and Communications
CommSensLab Group
Barcelona, May 29, 2022

The project that gave rise to these results received the support of a fellowship from ”la Caixa” Foundation (ID 100010434). The fellowship code is LCF/BQ/DI18/11660050.

This project has received funding from the European Union´s Horizon 2020 research and innovation programme under the Marie Skłodowska-Curie grant agreement No. 713673.

Christoph Herbert, *Advanced Methods for Earth Observation Data Synergy for Geophysical Parameter Retrieval*, © 2022

May 29, 2022

To my love Eva-Maria,
may the values that she lives by abide.

Abstract

Soil moisture (SM) and sea ice parameters are recognized as essential climate variables (ECV). A comprehensive understanding of the temporal variability of the root-zone SM (RZSM) is paramount in hydrological and agricultural applications, and droughts have become more frequent in the wake of climate change. Arctic sea ice volume has decreased significantly in recent decades, and this trend is particularly evident during the local summer months. Parameters such as sea ice thickness (SIT) and concentration (SIC) are crucial to continuously monitor the state of sea ice.

Since the launch of the Soil Moisture and Ocean Salinity (SMOS) mission in 2009, globally available satellite-based SM products have been used to investigate SM dynamics, based on the fact that useful information about subsurface SM can be extracted from their time series. Time series analysis techniques can be used to estimate the RZSM based on preceding information of satellite-based SM. Most notably in regions with extreme SM conditions the response time between surface-sensitive and subsurface SM depends on related processes occurring at different timescales, and it can be seasonally and spatially variable.

The first part of the thesis focuses on the analysis of the relevant factors to estimate the response time between satellite-based and in-situ SM at different depths using a Dynamic Time Warping (DTW) technique. DTW was applied to the high-resolution SMOS L4 SM product developed by the Barcelona Expert Center (BEC), and was compared to in-situ RZSM measurements of four representative stations in the REMEDHUS network in Western Spain. The method was customized to control the rate of accumulation and reduction of time lag during wetting and drying conditions and to consider the onset dates of pronounced precipitation events to increase sensitivity to prominent features of the input series. The temporal variability of climate factors in combination with crop growing seasons were used to indicate prevailing SM-related processes. The spatial heterogeneity of land use was analyzed using high-resolution images of Normalized Difference Vegetation Index (NDVI) from Sentinel-2 to provide information about the level of spatial representativity of SMOS data to each in-situ station. The comparison of long-term precipitation records and potential evapotranspiration (PET) allowed estimation of SM seasons describing different SM conditions depending on climate and soil properties. An exponential filter approach was used as an independent method to estimate subsurface

SM from the SMOS time series by finding the optimal characteristic time length for each SM season after validation with the corresponding profile series. Hereby, a seasonally representative time length was determined for each station and depth, and they resembled the average response time for each SM season obtained using DTW. Future work may comprise the application of the approach to different SM networks to understand the seasonal, climate, and site-specific characteristic behaviour of time lag.

Processed-based models for sea ice parameter retrieval rely largely on empirically determined small-scale sea ice properties that are assumed to be captured in space-based observations, while direct analyses of sea ice are limited to a characteristic length scale similar to the resolution of polar-orbiting satellites acquiring data in the microwave spectrum ($\sim$10–50 km). Operational sea ice products often depend on manual categorization by experienced analysts and reliable parameter estimation requires a model framework to effectively extract the sea ice composition information contained in various satellite observations.
The second part of the thesis focuses on data-driven methods for sea ice segmentation and parameter retrieval. A Bayesian inference framework is employed and adopted to segment different sets of multi-source satellite data. A regression neural network approach for estimating SIT based on brightness temperature data (T_B) from the first results of the Federated Satellite Systems CubeSat (FSSCat) mission, which introduced an innovative concept for a federated satellite system developed at the UPC NanoSat Lab in Barcelona, is investigated.

The Bayesian unsupervised learning algorithm is a probabilistic approach which allows to investigate the 'hidden link' between multiple satellite data. The statistical properties are accounted for by a Gaussian Mixture Model (GMM), and the spatial interactions are reflected using Hidden Markov Random Fields (HMRF). The algorithm segments spatial data into a number of classes, which are represented as a latent field in physical space and as clusters in feature space, which can be used for subsequent analysis and classification. In a first application, a two-step probabilistic approach based on Expectation-Maximization and the Bayesian segmentation algorithm was used to segment Sentinel-1 SAR images into a number of separable classes, which enables to discriminate surface water from the remaining sea ice types. Information on surface roughness conditions is contained in the distribution of radar backscattering images which can be - in principle - used to detect melt ponds and to estimate high-resolution sea ice concentration (SIC). In a second study, the algorithm was applied to multi-incidence angle T_B data at L-band (1.4 GHz) from the SMOS L1C product to capture their differences in sea ice sensitivity to thin ice up to $\sim$0.5 m. The resulting spatial patterns clearly discriminate well-determined areas of open water, old sea ice and a transition zone, which is sensitive to thin sea ice SIT and SIC. Classes are temporally analyzed in terms of stability and separability to investigate the geophysical meaning of the segmentation result. Preliminary validation comprised a

comparison of the spatial patterns with existing maps of sea ice stages of development and sea ice concentration. Model uncertainty is quantified using an entropy-based statistical criterion. This enables to distinguish well-determined zones from ambiguous zones, where additional information for validation and classification is needed, and from critical areas, where the inference of SIT and SIC with L-band radiometry is particularly problematic.

Given the dynamic nature and complexity of sea ice, geostatistical analysis is required to integrate both the temporal and the spatial interactions into the model. The Bayesian inference algorithm was extended to 3D to enable segmentation of sea ice in a complete spatio-temporal context. In a third application, measurements of SMOS and the Advanced Microwave Scanning Radiometer-2 (AMSR2) T_B data are used as input features to examine the joint effect of CIMR-like observations at 1.4, 6.9, 10.6, 18.7, and 36.5 GHz. The goal was to segment the Arctic region into a set of relevant classes based on the synergy effects of the multiple observations. Comparison of the resulting class patterns with images of common operational sea ice products SIT and SIC revealed that class shapes are largely consistent with those of developmental stages and thickness ranges. The information contained in the low-frequency channels allows the algorithm to reveal ranges of thin sea ice, and thicker ice can be determined from the relationship between the high-frequency channels and the changing surface conditions as the sea ice ages and thickens during freeze-up. Evaluation of class formation over several years indicated the temporal stability of obtained classes, recognizing annually recurring patterns that can be considered consistent. Based on the statistical model parameters, clusters are analyzed to understand the individual and combined sensitivity of input features to the obtained classes and associated sea ice properties. Preliminary results have shown that – subsequent to classification – class probabilities can also be related to the distribution of SIT. The proposed approach is suitable for combining large data sets and provides appropriate metrics for class analysis and interpretation, allowing informed decisions to be made about integrating data from future missions into sea ice products.

Neural networks can be trained to find hidden links among large data sets and often perform better on convoluted problems for which traditional approaches miss out important relationships between the observations. A predictive regression neural network approach is investigated with the goal to infer SIT using T_B data from the Flexible Microwave Payload 2 (FMPL-2) of the FSSCat mission, and ancillary data (SIT, surface temperature, and sea ice freeboard). Two models – covering thin ice up to 0.6 m and the full-range of SIT – were separately trained on Arctic data in a two-month period from mid-October to the beginning of December 2020, while using ground truth data derived from the SMOS and Cryosat-2 missions. The thin ice and the full-range models resulted in a mean absolute error of 6.5 cm and 23 cm, respectively. Both models allowed to produce weekly composites of Arctic maps and monthly composites of Antarctic SIT based on the Arctic full-range model.

This work presents the first results of the FSSCat mission over the polar regions.

It reveals the benefits of neural networks for sea ice retrievals and demonstrates that moderate-cost CubeSat missions can provide valuable data for applications in Earth observation.

Acknowledgements

First and foremost I thank my thesis advisors Mercè Vall-llossera and Adriano Camps who were very supportive throughout the entire journey.

I would like to thank my UPC CommSensLab team Miriam Pablos, Gerard Portal, David Chaparro, and Carlos López Martínez, and the NanoSat Lab team David Llavería and Juan-Francesc Muñoz Martin.

I would also like to thank Cristina Gonzáles Haro, Verónica Gonzáles and Estrella Olmedo Casal with whom I had the pleasure to share an office at the Barcelona Expert Centre, as well as Carolina Gabarró Prats, Marcos Portabella and Antonio Turiel Martínez, and to my PhD fellows and friends Niclas Rieger and Gerard Llorach Tó.

I am grateful to the La Caixa foundation and its coordinators, to my cohort fellows staying in Barcelona who have become good friends.

Thank you to my collaborators Florian Wellmann (CGRE Aachen), José Martínez Fernández (CIALE Salamanca), and Luisa von Albedyll (AWI Bremerhaven).

A special thank you to my academic and doctoral thesis examination committee Jens Wickert (GFZ Potsdam) as chair, Ignasi Corbella (UPC) as secretary, Juan Manuel Lopez-Sanchez (Universidad de Alicante), Núria Duffo (UPC) and Carolina Gabarró Prat (CSIC-ICM).

Table of Contents

Abstract . . . . . **i**

Acknowledgements . . . . . **v**

Nomenclature . . . . . **xiii**

Acronyms . . . . . **xx**

1 Introduction **1**

1.1 Relevance of Soil Moisture and Sea Ice in the Earth system 1

1.2 Monitoring Surface and Root-Zone Soil Moisture 5

1.3 Monitoring Sea Ice Thickness and Concentration 9

1.4 Objectives 14

I Relating Satellite-Based Surface to In-Situ Profile Soil Moisture **17**

2 Remote Sensing of Soil Moisture **19**

2.1 Soil Moisture Acquisition Methods 19

2.2 Satellite-Based Surface Soil Moisture 22

2.3 Root-Zone Soil Moisture Estimation 24

3 Time Series Analysis of Satellite-based and Subsurface Soil Moisture **27**

3.1 Exponential Filter 27

3.2 Dynamic Time Warping 30

3.2.1 General Concept 30

3.2.2 Customization 33

3.2.3 Discussion 35

4 Estimation of Response Time between SMOS and In-Situ Soil Moisture at Different Depths **37**

4.1 Time Series Data sets 38

4.1.1 SMOS Soil Moisture 38

4.1.2 REMEDHUS Soil Moisture Network and Climate Data 38
4.1.3 Comparison of SMOS and In-Situ SM 40
4.2 Analysis of Soil-Moisture Related Factors 42
4.2.1 Temporal Variability of Climate Factors 42
4.2.2 Spatial Heterogeneity of Land Coverage 43
4.3 Application of DTW Technique 46
4.3.1 Intermediary Results of DTW and Customization 46
4.3.2 Final Results of the Evolution of Time Lag 49
4.4 Seasonal Time Length Estimates Based on Exponential Filter 52
4.5 Discussion 57

II Sea Ice Segmentation and Parameter Retrieval 61

5 Remote Sensing of Sea Ice 63
5.1 Sea Ice Physics 63
5.1.1 Formation and Development of Sea ice 63
5.1.2 Physical and Radiometric Properties 65
5.1.3 Sea Ice Across Spatial and Temporal Scales 68
5.1.4 Changes in Sea Ice Thickness Distribution 69
5.2 Satellite Observations over Polar Areas 71
5.2.1 Passive Remote Sensing 71
5.2.2 Active Remote Sensing 74
5.3 Sea Ice Parameter Retrieval 76
5.3.1 Sea Ice Concentration and Extent 76
5.3.2 Melt Ponds 78
5.3.3 Sea Ice Thickness 79
5.3.4 Ice Charts 80
5.4 Discussion 82

6 Segmentation of Sea Ice 87
6.1 Bayesian Unsupervised Learning Approach 89
6.1.1 Bayesian Inference Framework 89
6.1.2 Segmentation Algorithm 92
6.1.3 Extension of the Approach into Three Dimensions 94
6.2 Discrimination between Sea Ice and Closed Water using Sentinel-1 SAR data 99
6.2.1 Angular Variation of SAR backscattering coefficient 102
6.2.2 Estimation of the Number of Significant Classes 102
6.2.3 Bayesian Segmentation of SAR Images 103
6.3 Spatial Segmentation of Arctic Sea Ice Using SMOS Data 106
6.3.1 Input Feature Selection 106

6.3.2 Segmentation Results . . . 109
6.3.3 Cluster Analysis . . . 112
6.4 Spatio-temporal Segmentation of Sea Ice using SMOS and AMSR2 Data . 116
6.4.1 Input Feature Selection . . . 117
6.4.2 Segmentation Results . . . 120
6.4.3 Class Analysis and Interpretation . . . 124
6.5 Discussion . . . 135

7 Sea Ice Thickness Retrieval . . . 141
7.1 Inference of Sea Ice Thickness using FSSCat Data . . . 141
7.1.1 Ancillary Data . . . 142
7.1.2 Implementation of the Regression Neural Network . . . 145
7.1.3 Inference of Arctic and Antarctic Sea Ice Thickness . . . 150
7.2 FSSCat Sea Ice Products . . . 155
7.3 Discussion . . . 157

III Conclusions and Future Research 163

8 Conclusions . . . 165

9 Future Work . . . 171

IV Back of the Thesis 175

Appendices . . . 177

A Application of DTW to Relate Gaussian Distributions . . . 179

B Implementation of the Bayesian Segmentation Algorithm . . . 181

C Preliminary Comparison between SAR images and Airborne EM . . 183

D Distribution of SIT . . . 187

Publications and Conference Contributions . . . 189

Bibliography . . . 191

List of Figures

1.1 Projected changes in drought frequency by the mid-21st century 3
1.2 Minimum and maximum Arctic sea ice extent from 1979-2021 5

3.1 Dynamic Time Warping customization scheme 34
3.2 Sample-wise allocation between surface and in-situ SM 36

4.1 REMEDHUS soil moisture network and the examined stations 39
4.2 Monthly accumulated precipitation and estimated PET over REMEDHUS 43
4.3 16-day MODIS NDVI time series at 1 km from 2016–2018 44
4.4 Sentinel-2 NDVI mean and StDev within the SMOS L4 pixel 44
4.5 Sentinel-2 NDVI mean and stDev as a function of the parameter `delta` . . 45
4.6 Illustration of the intermediate steps of the DTW 47
4.7 Results of customization of DTW 48
4.8 Three-days accumulated precipitation and normalized cumulative sum . . . 49
4.9 SMOS and in-situ at `M5` and the resulting time lag 50
4.10 SMOS and in-situ at `E10` and the resulting time lag 50
4.11 SMOS and in-situ at `J12` and the resulting time lag 51
4.12 Validation metrics between SWI retrievals after applying exponential filter 54
4.13 Retrieved SWI and in-situ at `L3` at 25 cm using NSE 56
4.14 Retrieved SWI and in-situ at `E10` at 50 cm using R^2 57

5.1 Sea ice types at different stages of development 64
5.2 Regional sea ice chart from the Greenland and Barents Seas 83
5.3 Polar-wide ice charts for stages of development 84

6.1 Set of 2D cliques comprising the central pixel and its neighboring pixels . . 92
6.2 Coordinate system for spatio-temporal analysis of satellite images 95
6.3 Set of cliques of a central voxel 96
6.4 Synthetic data set to verify the 3D segmentation approach 98
6.5 Segmentation diagnostics of the spatial and statistical model parameters . 99
6.6 Comparison of the initial latent field and the estimated field 100
6.7 Study area for SAR image segmentation 101

6.8 Spatial distribution and cumulative sum of Sentinel-1 backscatter 101
6.9 Angular dependence of the backscattering coefficient 103
6.10 Expectation-Maximization result after 100 iterations 104
6.11 Segmentation result to discriminate water from sea ice 104
6.12 Comparison between the class results and optical Sentinel-2 images. 105
6.13 Estimated concentration of intact sea ice in comparison to OSI-SAF SIC . 105
6.14 Relationship between PR and SIT as a function of incidence angle 108
6.15 Distribution of PR values at 56° incidence angle 109
6.16 Segmentation result between 24 October and October 28, 2016 110
6.17 Comparison of the obtained latent field result with SIT products 112
6.18 Distribution of PR and segmentation result in feature spac 113
6.19 Temporal evolution of class mean values and StDevs 115
6.20 Temporal evolution of class membership and separability 116
6.21 Relationship between SIT and T_B observations 118
6.22 Kernel density chart of the SMOS and AMSR2 input features 119
6.23 Segmented spatial patterns from September 2016 to September 2017. . . . 121
6.24 Clustering result in marginal feature space. 122
6.25 Temporal evolution of classes for a one-year segmentation period 123
6.26 Features-specific T_B mean values and StDev for all classes 125
6.27 Intra-class cohesion in terms of absolute values of Pearson correlation . . . 127
6.28 Temporal evolution of classes for a 7.5-year segmentation period 128
6.29 Spatial patterns compared to operational sea ice products in November 2016130
6.30 Spatial patterns compared to operational sea ice products in March 2017 . 131
6.31 Class-specific evaluation of medians and percentiles of SIT products 133
6.32 Boxplot of the class-specific associated SIT 134
6.33 Latent field compared to SIT-CS2SMOS with adapted bounds 134

7.1 Maps of the NN input features 143
7.2 Relationship between T_B and SIT as a function of T_{Ph} and ice types . . . 144
7.3 Principle architecture of the implemented NN 146
7.4 KDE charts of the NN training sets used to train the thin sea ice model . . 148
7.5 KDE charts of the NN training sets used to train the full-range model . . . 149
7.6 Convex hulls around point clouds in 2D sub-feature space of Arctic data . 151
7.7 Evaluation of training and prediction of the Arctic thin SIT model 153
7.8 Weekly maps of predicted Arctic thin SIT 154
7.9 Evaluation of training and prediction of the Arctic full-range SIT model . . 154
7.10 Comparison between the weekly composites of Arctic full-range SIT maps . 155
7.11 Distribution and monthly composite of Antarctic full-range SIT predictions 156
7.12 Maps of Arctic and Antarctic SIC product 157
7.13 Maps of the weekly Arctic L3 thin SIT product 158

7.14 Maps of the weekly Antarctic L3 thin SIT product 158
7.15 Maps of the Arctic L4 weekly full-range SIT product 158
7.16 Maps of the weekly Antarctic L4 full-range SIT product 159

A.1 DTW technique explained on the basis of a synthetic example 180

B.1 Scheme of the parallel Gibbs sampler 181
B.2 Scheme of the parameter estimation using a Metropolis-Hastings algorithm 182

C.1 EMI-derived SIT and SAR images in the Ross Sea 184
C.2 Diagnostics of the 1D segmentation 185
C.3 Results of the 1D segmentation in feature space 185
C.4 Results of the 1D segmentation in physical space 186

D.1 Class-specific SIT distribution regarding the thin SIT-SMOS product . . . 187
D.2 Class-specific SIT distribution regarding the merged SIT-CS2SMOS product 188

List of Tables

4.1 Land use, soil type and depth-specific SM-related properties 41
4.2 Estimated SM seasons from monthly accumulated precipitation and PET . 42
4.3 Results of the analysis of land use variability 46
4.4 Mean and maximum time lag obtained within the estimated SM seasons . 53
4.5 Optimal characteristic time length for each station and depth 55
4.6 Representative SM-season-specific characteristic time lengths 58

5.1 Stages of development and associated SIT intervals 70
5.2 AMSR2 channel specifications 74

6.1 Independent directions of the heterogeneity coefficient 96
6.2 Summary of the temporal evolution of classes 111
6.3 Statistics of SIT and SIC corresponding to the class spatial patterns 135
6.4 Summary of the segmentation result and class interpretation 135

7.1 Summary statistics of the NN training set 149
7.2 Summary of training and prediction characteristics 152

C.1 Statistical and spatial class interpretation 186

Acronyms

AARI Russian Arctic and Antarctic Research Institute.

Adam Adaptive Moment Estimation.

AIC Akaike Information Criterion.

AMSR-E Advanced Microwave Scanning Radiometer for Earth Observing Systems.

AMSR2 Advanced Microwave Scanning Radiometer-2.

ASCAT Advanced Scatterometer.

AWI Alfred Wegener Institute for Polar and Marine Research.

BEC Barcelona Expert Centre.

BIC Bayesian Information Criterion.

CDF Cumulative Distribution Function.

CIMR Copernicus Imaging Microwave Radiometer.

CIS Canadian Ice Service.

CRISTAL Copernicus Polar Ice and Snow Topography Altimeter.

CS2 Cryosat-2.

DMI Danish Meteorological Institute.

DTW Dynamic Time Warping.

EASE Equal-Area Scalable Earth.

ECMWF European Centre for Medium-Range Weather Forecasts.

ECV Essential Climate Variable.

EM Expectation-Maximization.

EMI Electromagnetic Induction.

EO Earth Observation.

ERT Electrical Resistivity Tomography.

ESA European Space Agency.

EUMETSAT European Organisation for the Exploitation of Meteorological Satellites.

FAO Food and Agriculture Organization of the United Nations.

Fb Sea Ice Freeboard.

FC Field Capacity.

FMI Finnish Meteorological Institute.

FMPL-2 Flexible Microwave Payload-2.

FSSCat Federated Satellite Systems CubeSat.

FYI First-Year Ice.

GCOS Global Climate Observing System.

GMM Gaussian Mixture Model.

GNSS Global Navigation Satellite System.

GNSS-R Reflected Global Navigation Satellite System.

GPR Ground Penetrating Radar.

GR Gradient Ratio.

GSI Geometric Separability Index.

HMRF Hidden Markov Random Field.

ICESAT Ice, Cloud, and land Elevation Satellite.

IFOV Instantaneous Field of View.

IPCC Intergovernmental Panel on Climate Change.

ISMN International Soil Moisture Network.

ITACyL Agrarian Technological Institute of Castilla y León.

JAXA Japan Aerospace Exploration Agency.

KDE Kernel Density Estimation.

MAE Mean Absolute Error.

MCMC Markov Chain Monte Carlo.

MIRAS Microwave Imaging Radiometer with Aperture Synthesis.

MODIS Moderate Resolution Imaging Spectroradiometer.

MOSAiC Multidisciplinary drifting Observatory for the Study of Arctic Climate.

MPF Melt Pond Fraction.

MYI Multi-Year Ice.

NASA National Aeronautics and Space Administration.

NDVI Normalized Difference Vegetation Index.

NetCDF Network Common Data Form.

NIC U.S. National Ice Center.

NN Neural network.

NSE Nash Suthcliffe Efficiency.

NSIDC National Snow and Ice Data Center.

NT2 NASA Team-2.

OW Open Water.

PAW Plant Available Water.

PET Potential Evapotranspiration.

PR Polarization Ratio.

RCP Representative Concentration Pathway.

ReLU Rectified Linear Unit.

REMEDHUS Red de Medición de la Humedad del Suelo.

RFI Radio Frequency Interference.

RMSE Root-Mean Squared Error.

ROSE-L Radar Observing System for Europe – L-band.

RTM Radiative Transfer Model.

RZSM Root-Zone Soil Moisture.

SAR Synthetic Aperture Radar.

SIRAL Synthetic Aperture Radar Interferometric Radar Altimeter.

SM Soil Moisture.

SMAP Soil Moisture Active Passive.

SMMR Scanning Multichannel Microwave Radiometer.

SMOS Soil Moisture and Ocean Salinity.

SMRT Snow Microwave Radiative Transfer.

SSM/I Special Sensor Microwave/Imager.

SSMIS Special Sensor Microwave Imager/Sounder.

StDev Standard Deviation.

SVD Singular Value Decomposition.

SWI Soil Water Index.

T_B Brightness Temperature.

TDR Time Domain Reflectometry.

TDS Transpolar Drift Stream.

TSA Time Series Analysis.

TWC Total Water Capacity.

ubRMSE Unbiased Root-Mean Squared Error.

VWC Volumetric Water Content.

WMO World Meteorological Organization.

WP Wilting Point.

1 Introduction

No single sensor can provide comprehensive information on a geophysical parameter of interest in a complex environment and it is necessary to exploit synergies from complementary Earth Observation (EO) data. Accurate and efficient process-based models are required to include the relevant processes and physical relationships. In complex environments where observations are sparse or only available at different scales, these models are very difficult to obtain and are therefore based on several assumptions. Soil moisture (SM) – especially in the root zone – and sea ice are two examples of very complex environments, where the adequate observations are not available for direct inference. Data-driven approaches are increasingly being used to extract patterns from remote sensing and geospatial data. The main challenge is to develop suitable algorithms capable of analyzing measurements from multiple instruments in a common retrieval framework. I dedicate my doctoral thesis to the retrieval of SM and sea ice-related variables on the basis of advanced data-driven modelling techniques used for analysis and segmentation of the geophysical quantities.

The work is divided into two main parts consisting of inference methods to estimate subsurface SM and sea ice parameters. Part I focuses on time series analysis techniques to relate surface-sensitive satellite-based SM time series to in-situ profile SM at different depths. Part II focuses on a Bayesian inference framework to exploit the joint effect of multi-source satellite observation for the segmentation of sea ice into classes which can be related to different sea ice properties, and a regression neural network approach for the sea ice parameter retrieval based on data of the first results of the Federated Satellite Systems CubeSat (FSSCat) mission.

1.1 Relevance of Soil Moisture and Sea Ice in the Earth system

SM is recognized as an essential climate variable (ECV) by the Global Climate Observing System (GCOS) [Bojinski et al., 2014], a body of the World Meteorological Organization (WMO), which evaluates the maturity and provides guidance for the development of the required observing system. SM plays an important role in agricultural applications including drought monitoring and rainfall estimations and in weather forecasting and

climate models across different spatial and temporal scales [Bojinski et al., 2014]. In a porous medium it is defined as the water contained in the pore spaces between soil grains, often expressed as volumetric water content (VWC) which is the ratio of water to soil volume. Surface SM is the water content of the topsoil that includes approximately the top 5 cm of soil. Root-zone SM (RZSM) is the water available to the root zone of cropping systems, assuming that most of the root biomass is in the top 50 cm to 100 cm of soil [Fan et al., 2016]. SM is highly variable in space and time, with characteristic length scales ranging from a few centimeters to several kilometers, and characteristic time scales ranging from minutes to years [Vereecken et al., 2014]. The surface water balance includes processes such as infiltration, runoff, evaporation, and transpiration, as well as subsurface water movement, including recharge and runoff.

In regions where water can be seasonally scarce and therefore cannot be used for irrigation, crop yield depends solely on the soil water content available to the plants. Drought affection in agricultural fields manifests itself in adverse reactions of the plants, leading to yield losses or even total crop failures. Meteorological conditions set the boundary conditions at the atmosphere-soil interface for topsoil moisture [Basara and Crawford, 2002], but rainfall often has no immediate impact on the underlying RZSM and the effectiveness of drought monitoring for the agricultural sector is highly dependent on the availability of SM measurements. Modern cropping systems are adapted to short dry spells to a certain degree. However, low SM content can damage crops even in a relatively short period of time. Plants are particularly vulnerable if they do not have sufficient access to water during their main growth phase, which can lead to SM-stress and agricultural losses. Knowing the dynamics of SM is critical to determine the growing season and for optimal timing of irrigation effectively [Jiménez-Martínez et al., 2009]. For this reason, drought indices are based on both anomalies in atmospheric conditions and SM on time scales of a few days or months.

Continuous monitoring of surface and RZSM is essential to predict water shortages and droughts [Batool et al., 2019, Falkenmark, 2013], and comprehensive knowledge on SM content has substantial socio-economic relevance for food security. As climate variability increases with climate change, events such as heat waves and the absence of precipitation will become prolonged and more frequent [Kang et al., 2009]. Drought is an insidious phenomenon that develops over several time scales with regional differences. A global temperature increase of only a few tenths of a degree because the anthropogenic greenhouse effect encompasses large local and seasonal anomalies. Due to the effects of global warming and unsustainable land management, the frequency, intensity and duration of summer droughts will increase in the next decades, whereas countries are differently exposed to the consequences [Miyan, 2015, Poljansek et al., 2017]. Altering global precipitation patterns due to climate change favor the drying of the soils and water shortage. Higher temperatures are accompanied by more energy in the atmosphere, leading to higher evaporation, which causes not the infiltration-friendly land rain, but heavy down-

pours. Paradoxically, more heavy rain leads to more drought, because – similar as in sealed surfaces – water runs off rapidly over streams and rivers with no impact on subsurface SM, resulting in negative water balance. There is little time left for the freshwater droplets to percolate, which is required for long-term recharge of the soil, and ultimately the groundwater. More frequent extreme events – such as the severe summer droughts observed in Europe in 2003, 2012, and 2018, and on the West Coast of the United States from 2012 to 2016 – can disrupt the balance of groundwater storage, which also affects irrigated agriculture. Based on different climate emission scenarios, an increase in the frequency of droughts is projected for the entire European continent – according to different Representative Concentration Pathways (RCP) – described by the Intergovernmental Panel on Climate Change (IPCC) [Van Vuuren et al., 2011]. Figure 1.1 illustrates the change in the number of drought events per decade for the period 2041–2070 relative to the period 1981–2010 in the moderate emission scenario (RCP 4.5) and the most severe emission scenario (RCP 8.5) [Spinoni et al., 2018]. Droughts become more frequent in the Mediterranean area and Western Europe towards the mid-21st-century due to reductions in precipitation and increasing temperatures.

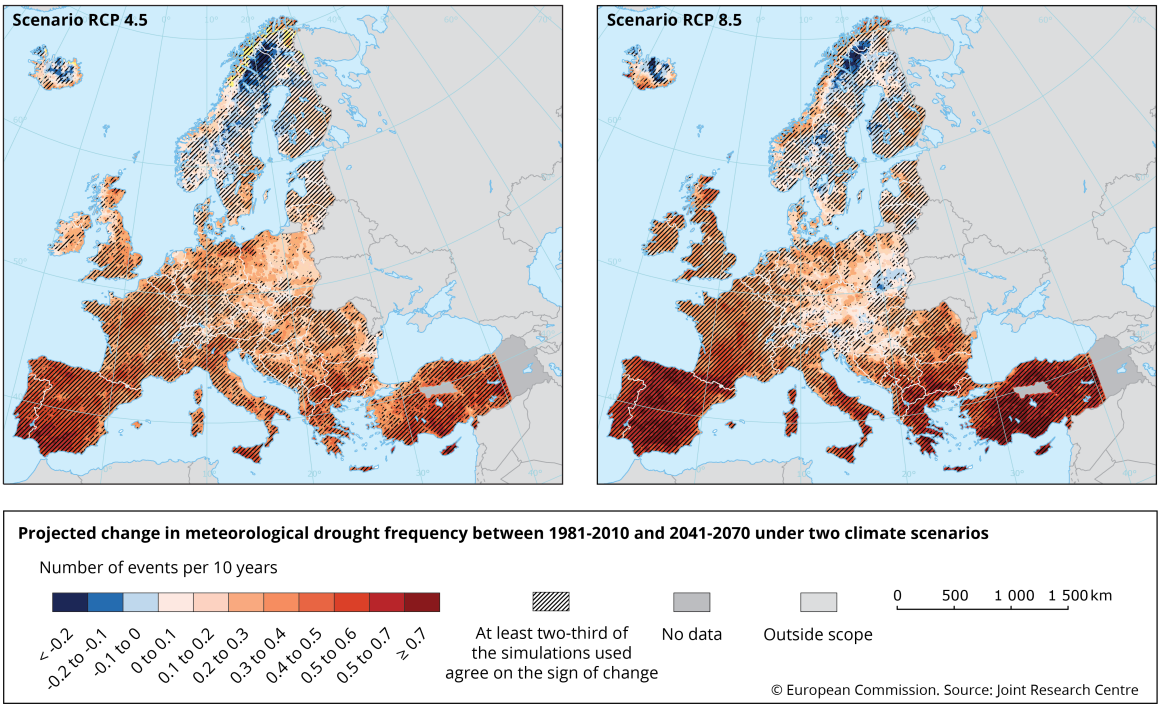

Figure 1.1: Projected changes in drought frequency in number of events per decade by the mid-21st-century (2041–2070) relative to 1971–2010 for the IPCC- medium emission scenario (RCP 4.5) (left) and the worst-case scenario (RCP 8.5) (right) [Spinoni et al., 2018].

In addition to the relevance of SM monitoring over land, sea ice is an important indicator of climate variability in polar environments. The state of sea ice is also recognized as an ECV [Hollmann et al., 2013] and determines the exchange of heat, momentum, moisture and gases between the atmosphere and the ocean. Sea ice has a significant impact

on the Earth's albedo, and therefore, changes in sea ice affect the global energy budget. Global ocean dynamics are strongly influenced by the timing of freezing and melting as well as the total amount of sea ice present in polar regions. The state of sea ice can be monitored based on a set of indicating parameters, including sea ice concentration (SIC), sea ice extent (SIE), sea ice thickness (SIT) and drift. SIC is defined as the ice-covered fraction of an area. SIE refers to the total area covered by sea ice of an entire polar region composed of the individual ice-covered areas – with a minimum SIC threshold of typically 15 % set due to technical modelling reasons.

Sea ice is subject to an annual cycle of freezing and melting and depends on the distribution of continents, and atmospheric and oceanic currents. Arctic and Antarctic sea ice are composed differently in terms of age and the distribution of SIT and the regions respond differently to climate change. Antarctic sea ice is largely seasonally stable – even with a slight recent increase – showing regional warming between +1–1.5 °C (global temperature rise: +1.1 °C) since the beginning of industrialisation. In contrast, the average SIE of the Arctic has decreased significantly, especially since the turn of the millennium, accompanied by a stronger regional warming of +2 °C. Both Arctic and Antarctic sea ice are subject to a strong seasonal cycle, with the Arctic reaching its minimum in September and its maximum in March, and vice versa for the Antarctic. While the Southern Ocean melts almost completely every year and freezes over again, the Arctic sea ice can last up to 5 years – only 14 % (Antarctic) and 32 % (Arctic) of sea ice persisted in summer 2021 compared to winter of the same year.

The Arctic is one of the fastest changing environments due to climate change. Figure 1.2 visualizes the minimum and maximum Arctic SIE since polar-wide satellite imagery became available in 1979 (data available at the National Snow and Ice Data Center (NSIDC) at `https://nsidc.org/arcticseaicenews/sea-ice-tools`. During the last 43 years of recording, the downward linear trend of the annual minimum SIE is about 13 %, in comparison to an average decline of 3.5 %. Furthermore, the timing of the extrema in extent shifts towards earlier dates for the Arctic sea ice minimum in September. The decline is alarming as global warming in the Arctic could be further amplified by the ice-albedo feedback resulting from the higher reflectivity of the ice compared to the ice-free ocean – causing the sea ice to become thinner and younger. If this process continues until the more resilient older ice is largely gone, the planet is going to seasonally loose the insulating boundary that limits heat exchange between the ocean and the atmosphere – and eventually, a cycle similar to that in the Antarctic might settle in.

Arctic sea ice is one of the stable 'cooling anchors' of our climate and mid-latitude weather system, and SIE in the Arctic can be linked to atmospheric circulation and the periodicity of planetary waves, which leads to changes in duration of dry and wet conditions [Mann et al., 2017]. The large decline of Arctic sea ice can drive a decrease in precipitation in mid-latitude's climate, such as in Europe, the southwest of the United States, and Asia. This can have worrisome effects in the form of anomalously high tem-

peratures that increase potential evapotranspiration (PET, which decreases SM, leading to more long-lasting heat waves and droughts in the summer [Comiso, 2012, Tang et al., 2014, Cvijanovic et al., 2017, Spinoni et al., 2018, Zhang et al., 2020]. The monitoring and retrieval of the sea ice parameters is crucial in order to get a continuous and comprehensive picture of the variability of the fast-changing Arctic environment.

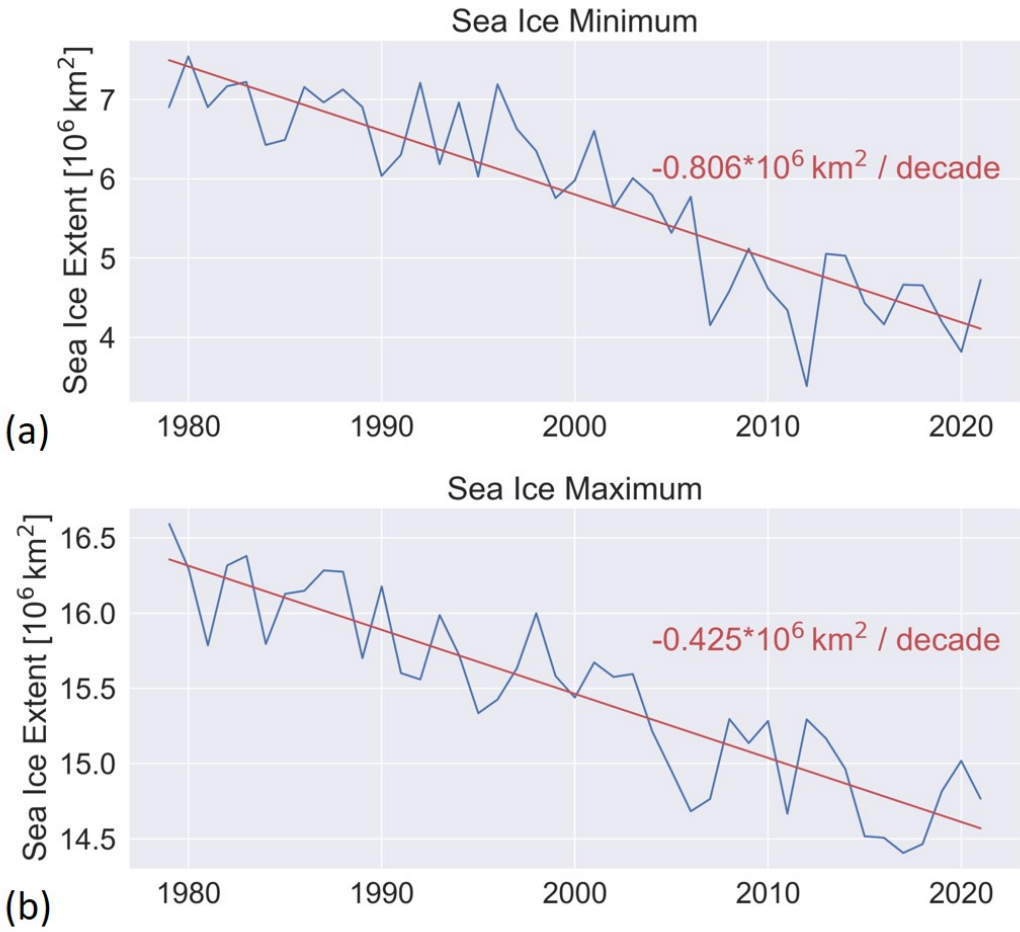

Figure 1.2: Minimum and maximum Arctic sea ice extent from 1979-2021. (**a**) annual minimum extent around mid-September; (**b**) annual maximum extent at the end of March (data downloaded from the NSIDC at `https://nsidc.org/arcticseaicenews/sea-ice-tools`)

1.2 Monitoring Surface and Root-Zone Soil Moisture

The unsaturated (or vadose) zone is the soil layer between the land surface and the groundwater table, including the capillarity fringe. Its thickness varies from zero meters in the lakes, to hundreds of meters in arid regions. The hydraulic conductivity, which describes the water movement through the soil porous media, depends on soil properties including porosity, permeability and saturation. Except for water uptake by roots, SM tends to move mainly downward due to gravity. The rate of SM exchange can be defined

by two separable fluxes corresponding to advection and diffusion terms [Ogden et al., 2017]. The diffusive term describes the exchange of SM due to the shape of the soil water capillarity profile and becomes important under long-lasting dry conditions, where hydraulic conductivity is low. In case a sharp wetting front enters the soil after heavy rains, the diffusive term becomes negligible, and the advective SM exchange dominates during water infiltration. Estimation of SM along the soil depth profile requires knowledge of natural SM-related processes such as precipitation, evapotranspiration, infiltration and surface runoff, soil layering and man-made processes, such as irrigation. For instance, the distribution of SM and soil properties determines how much precipitation infiltrates into the soil or results in runoff. These two related processes affect the near-surface soil layer at relatively large spatial scale and at different timescales [Skøien et al., 2003, Rosenbaum et al., 2012]. Additionally, small-scale variations in topography and soil properties (local heterogeneity) are important factors regarding the local distribution of SM, which makes surface SM highly variable. Consequently, surface SM observations are mainly characterized by short-term fluctuations, while RZSM is less dynamic, more affected by long term atmospheric conditions and dominated by seasonal trends.

SM acquisition methods can be generally divided into invasive in-situ observations, non-invasive geophysical measurements such as Ground Penetrating Radar (GPR) and electromagnetic induction (EMI), and air- and spaceborne remote sensing techniques [Bell et al., 2001, Jol, 2008, Wang and Qu, 2009, SU et al., 2014]. In-situ observations enable the continuous monitoring of SM from multi-depth measurements at point-scale and with high temporal sampling.

Spaceborne remote sensing techniques for SM retrieval are relatively inexpensive and provide high spatial coverage on a regular basis, which cannot be achieved using labor-intensive geophysical measurements [Jackson, 2002]. The Soil Moisture and Ocean Salinity (SMOS) mission, launched in 2009 by the European Space Agency (ESA), is the first space mission specifically dedicated to estimate SM. It uses an L-band interferometric radiometer to provide global SM, derived from brightness temperature (T_B) observations, with an equatorial revisit time of three days, and a spatial resolution of $\sim$ 40 km [Kerr et al., 2016]. The Soil Moisture Active Passive (SMAP) is the second spaceborne mission devoted to monitor SM [Chan et al., 2016]. It was launched in 2015 by the National Aeronautics and Space Administration (NASA) and carries on board an L-band real aperture radiometer. It was also equipped with a radar, but it failed after three months in orbit. SMAP and SMOS provide global SM at $\sim$ 40 km spatial resolution every three days.

Satellite microwave sensors are sensitive to SM content within a certain layer and over a particular area. The depth range of this layer within the soil profile is defined by the penetration depth and the extension of the area is determined by the sensor footprint size. Thus, the validation of satellite measurements requires several assumptions. Firstly, frequencies at L-band (1–2 GHz) are sensitive to SM at approximately the top 5 cm of

the soil [Escorihuela et al., 2010]. However, the penetration depth does not only depend on the frequency of the electromagnetic signal, decreasing as frequency increases, but also on the attenuation of the signal due to changes in the soil temperature and the SM. It is larger in dry than in wet soils [Owe and Van de Griend, 1998]. Secondly, satellite-based SM is usually compared against in-situ observations acquired by sensors installed at 5 cm depth, using collocated and concurrent data.

Both SMOS and SMAP SM respond more quickly to wetting up and dry down events – similar to the precipitation pattern – revealing a response time between satellite and in-situ measurements at the top 5 cm [Rondinelli et al., 2015, Shellito et al., 2016, Pablos et al., 2017, Colliander et al., 2020]. In addition, satellite SM measurements are assumed to have low intra-pixel variability. To address the problem of data comparison at different spatial scales, several strategies for upscaling in-situ SM have been employed [De Lannoy et al., 2007a, Crow et al., 2012, Wang et al., 2015]. Another assumption in validating SM with in-situ observations is that point measurements are considered representative of a surrounding homogeneous area observed by the satellite.

Continuously changing atmospheric conditions and corresponding processes are supposed to be reflected in the time series of satellite observations. Nowadays, satellite SM retrievals are widely used to monitor surface SM [Ochsner et al., 2013, Petropoulos et al., 2015, Mohanty et al., 2017], but observations within a preceding time span contain useful information about the temporal SM variability of the underlaying soil profile to infer RZSM. Satellite imagery in combination with more accurate point-scale observations contain information about the spatio-temporal variability of SM at the surface and along the depth profile. Surface-sensitive observations can be used to retrieve RZSM using process-based or data-driven approaches. Common SM acquisition methods and relevant missions to estimate surface SM, and approaches to retrieve subsurface SM from surface-sensitive observations are described in Chapter 2.

The exponential filter is a simple time series analysis (TSA) method that has been successfully applied to remotely sensed surface SM time series to retrieve subsurface SM, without requiring knowledge of local soil properties and complete drainage information [Wagner et al., 1999]. This method estimates the SM in the subsurface by optimizing a characteristic time length, which is considered as a surrogate parameter and includes all relevant processes and soil properties that affect SM variability at different temporal scales. RZSM was estimated from different active and passive satellite SM retrievals (including European Remote Sensing – satellite scatterometer, Advanced Scatterometer (ASCAT), Advanced Microwave Scanning Radiometer - Earth Observing System (AMSR-E), and SMOS, and estimated RZSM time series were evaluated at several in-situ SM networks over Europe [Wagner et al., 1999, Ceballos et al., 2005, Albergel et al., 2008, Brocca et al., 2011, Ford et al., 2014, González-Zamora et al., 2016]. Hereby, the characteristic time length was optimized to be constant over the course of a year, and over several years for specific location and depth level. However, the response time in which subsurface

SM is affected by atmospheric forcing varies, being shorter around precipitation events and longer during dry events [Wu et al., 2002]. Consequently, the characteristic time length cannot be assumed as constant, but seasonally variable. This variability could be particularly notable if the water balance becomes perturbed in case of high rate of water introduction or removal due to pronounced precipitation (or irrigation), or strong evaporation and transpiration.

There are different approaches to quantify the time lag between non-linearly related time series, which can be divided into representation methods and similarity methods [Wang et al., 2013]. In the first case, shorter sub-sequences can be approximated from longer time series, with the aim to identify representative patterns, which relate the fundamental features of different observations [Liu, 2003, Grinsted et al., 2004]. Wavelet transforms can be analyzed to decompose time series into similarly shaped sub-sequences. As an example in hydrology, singular value decomposition (SVD) was applied to identify complex spatial response modes of temporal sequences, and phase information of the cross-wavelet was evaluated to study the response of groundwater levels to precipitation [Qi et al., 2018]. Their time series were related to extract anomalies and extreme events, like heavy rainfall, and local time lags were effectively approximated. In contrast, similarity methods aim for sequence alignment based on a distance measure, which describe the point-to-point alignment between two time series rather than relating single pronounced events or representative sequences. Dynamic Time Warping (DTW) is a method capable of evaluating the similarity between two time series. It analyses local variations, distortions and shifts between the time series and quantifies the time lag by finding the optimal match between them. DTW and derived versions provide the most effective similarity measure to align time series data in a wide variety of applications [Rakthanmanon et al., 2012, Wang et al., 2013]. Time lag may provide information on the mutual dependencies or causal relationships between the time series. Originally, DTW was applied in speech recognition to identify a particular word within a longer, more distorted signal [Berndt and Clifford, 1994, Sakoe and Chiba, 1978]. In the remote sensing community, DTW was mostly used for land cover classification purposes [Maus et al., 2016, Belgiu and Csillik, 2018, Csillik et al., 2019]. In addition, it has been used to analyze the similarity of different satellite SM estimations to in-situ near-surface SM observations [Lee et al., 2019]. TSA methods to relate surface and subsurface SM time series are presented in Chapter 3.

In Chapter 4, the relationship between satellite-based and subsurface SM is investigated based on TSA using DTW. The DTW technique is applied to the SMOS L4 SM data product at 1 km resolution provided by the Barcelona Expert Center (BEC) [Portal et al., 2018] and in-situ SM measured at several depths over the SM sensor network 'red de medición de la humedad del suelo' (REMEDHUS) in Western Spain [Sanchez et al., 2012]. Satellite time series were compared to SM observations at 5, 25 and 50 cm depth at four representative in-situ stations to estimate the time lag between surface and RZSM, respectively. Since the temporal resolution of SMOS is limited by its revisit time, time

series were averaged to obtain regular sampling. They were normalized to account for differences in dynamic ranges between area-averaged satellite and point-scale in-situ observations. The time series are linked based on the most prominent common features to quantify the evolution of the time lag. The typical response time was determined according to the previously estimated SM seasons for all stations and depth. Similarly, the exponential filter is applied to the same time series, and optimized to determine a representative characteristic time length according to each SM season, to verify the findings with an independent method.

1.3 Monitoring Sea Ice Thickness and Concentration

Polar spaceborne microwave radiometry observations have been available since 1979, starting with the launch of the Scanning Multichannel Microwave Radiometer (SMMR) and follow-on missions carrying sensors such as the Special Sensor Microwave Imager/Sounder (SSMIS), and the Advanced Microwave Scanning Radiometer-2 (AMSR2). T_B observations in the microwave spectrum is sensitive to sea ice properties and can be used to retrieve SIC and SIT. The emissivity in the microwave spectrum depends on the dielectric properties of sea ice which is a function of its physical composition including salinity, density, surface temperature, and surface roughness. The collected signal is emitted from a radiating layer which depends on the penetration depth at sensor frequency. A snow layer on top of sea ice influences the radiation properties of sea ice and the energy received by the sensor. The contribution of snow to the emitted signal is lower in the lower microwave spectrum and the separability of surface properties, such as open water and sea ice including SIT, is – in theory – feasible. Low-frequency microwave radiometry observations at L-band (1.4 GHz) are sensitive to thin sea ice up to ~ 0.6 m depth [Steffen, 1992, Naoki et al., 2008]. Among the most important missions for sea ice monitoring, the SMOS mission [Font et al., 2009, Kerr et al., 2010] provides multi-incidence angle full-polarization T_B maps at L-band. Various products have been developed based on SMOS data retrieving thin SIT at Arctic scale [Huntemann et al., 2014, Tian-Kunze et al., 2014, Kaleschke et al., 2016, Ricker et al., 2017, Gupta et al., 2019]. SIT above 1 m has been successfully derived based on sea ice freeboard (Fb) estimates from satellite altimeters [Laxon et al., 2013, Guerreiro et al., 2017]. Sensors operating at higher microwave frequencies have smaller penetration depth into sea ice and enable discrimination of sea ice and water at the surface, which allows the monitoring of SIC and SIE. Algorithms are based on the contrast of T_B using observations at frequencies ~ 19 GHz and ~ 37 GHz [Parkinson et al., 1999, Comiso and Nishio, 2008, Lavergne et al., 2019]. This methods allowed to generate satellite-based maps of SIC with polar coverage on an operational basis. The new Copernicus Imaging Microwave Radiometer (CIMR) mission, expected to be launched in 2028, is intended to provide T_B at L-band (similar to SMOS and SMAP) and higher microwave frequencies (similar to AMSR2 channels) with at least daily revisit and increased spatial

resolution in the polar regions [Kilic et al., 2018, Donlon et al., 2019].

Applications in the Arctic environment, like navigation through sea ice, require data at high resolution and ideally at real time. The large amount of ice cover detail found in Synthetic Aperture Radar (SAR) imagery holds enormous potential for high-resolution sea ice modelling, and ice classification and charting in several national ice services are based on SAR images [Zakhvatkina et al., 2019]. One of the major tasks using SAR imagery is to accurately determine the boundaries between sea ice and water and to discriminate different ice types. Reliable classification of ice types and water requires the expertise of sea ice analysts, while models still lack sufficient generality and robustness to realize their full potential for automatic assimilation. The intensity of radar reflections on the ice surface is given by the backscatter coefficient which shows high angular variability – especially over the open ocean.

Today, nanosatellite technology has matured to the point that it can be used for scientific missions and the number of instruments deployed in space has steadily increased over the past decade [Kulu, 2020, Camps, 2019]. CubeSats are miniature satellites that are composed of small unit cubes (U) of $10\times10\times10\,\mathrm{cm}^3$ with a maximum weight of 1.33 kg. Their payloads have an advantage over those carried by traditional missions (i.e. large passive optical and microwave payloads) due to their smaller dimensions in terms of size, mass, power consumption and downlink capability. Markedly reduced expenses in development, construction and satellite launch make them more accessible to universities and research institutes, and their use is increasing to broaden the scope of Earth observation. Commercial companies, like 'Planet' and 'Spire', operate constellations of hundreds of 3-U CubeSats ($\sim 30\times10\times10\,\mathrm{cm}^3$), carrying optical imagers or Global Navigation Satellite System (GNSS)-Radio Occultation payloads [Kramer, 2014, SpaceNews, 2020]. The FSSCat mission, launched on 3 September 2020, is formed by two federated CubeSats with one of them (^{3}Cat-5/A) carrying the Flexible Microwave Payload-2 (FMPL-2) on board, combining a Reflected GNSS (GNSS-R) reflectometer and the first radiometer operating at L-band ever deployed on a CubeSat [Munoz-Martin et al., 2020]. It is designed to provide maps of SIE and SIT over both poles on a five-day basis and soil moisture over land at low-moderate resolution, and it is the first CubeSat mission contributing to the Copernicus system (Land and Marine Environment Monitoring Services). Both FMPL-2 instruments have been successfully validated in orbit and the first set of nominal acquisitions are available from 1–13 October 2020 [Munoz-Martin et al., 2021a].

Inversion methods for estimating geophysical parameters such as SIT can be divided into statistics-based and process-based modelling. The choice of a suitable technique depends directly on the modelling applications and the available data. Process-based techniques are based on thermodynamic or radiative transfer models (RTM), with the goal of reproducing sea ice growth processes. They require detailed knowledge of the sea ice composition, including stratification and potential snow load. Sea ice is undergoing continuous transformation showing regional and seasonal variability. Algorithms to infer sea

ice parameters rely on strong model assumptions and empirically determined sea ice properties of different ice types. Information about the sea ice heterogeneity is not available and accurate models need collocated and concurrent observations from multiple sources to prevent ambiguous inversion. The main uncertainties in sea ice products originate from long revisit times and coarse spatial resolution of satellites. Models can be oversimplified, and model uncertainty is difficult to estimate. Knowledge on the distribution of sea ice is limited due to sparsely available in-situ and airborne data for validation. SIT retrieval algorithms perform well during Arctic freeze-up [Kaleschke et al., 2016], while the high heterogeneity of sea ice during summer melt and the limited spatial resolution of satellite observations make SIT estimation highly ambiguous. Therefore, current SIT products show sufficient accuracy during the Arctic freeze-up period from mid-October to mid-March, but they do not perform well during the Arctic melting season. The relevant physical properties of sea ice, current passive and active missions, and inference techniques for satellite-based retrieval of sea ice parameters, particularly for SIT and SIC, are described in Chapter 5. Irrespective of the modelling technique, sufficient details on the modeled metrics are required to understand the hidden link between input data sets and sea ice parameters. Ideally, the model parameters provide information to evaluate the joint effect of a combination of data sets that allows the study of both spatial heterogeneity and temporal variability of sea ice. This knowledge is important for informed feature selection and refinement decisions to be made to achieve sensitivity enhancement to sea ice properties. Of particular importance to ensuring continuous monitoring of sea ice parameters in polar regions is the identification of data gaps and limitations for an assessment of existing satellite missions and products. The method is a tool for understanding the utility of data from new sensors and future missions and their suitability for integration into new products.

Data-driven approaches – being the complementary to process-based modelling – have provided promising results by harnessing the sensitivity ranges of multi-source satellite data for sea ice parameters by extracting the information contained in the various observations. However, these approaches often comprise a purely statistical analysis of images where information is retrieved from a temporal pixel-based consideration only. Without considering the semantic meaning of the data sets during the analysis, the data collected by multiple sensors with different resolutions cannot be merged easily and converted into information for physical interpretation. As a result, automated models are not general enough to obtain consistent solutions with sufficient stability. Thus, given the dynamic nature and complexity of sea ice, geostatistical analysis is required to integrate both the temporal and the spatial interactions into the model.

In Chapter 6, a Bayesian unsupervised learning approach, developed at the Computational Geoscience and Reservoir Engineering at RWTH Aachen University [Wang et al., 2017], is investigated to segment Arctic sea ice into a number of separable classes based on the synergy of multi-source satellite data. The aim is to yield a framework to reveal

spatial pattern from differences and similarities in the sensitivity between sea ice properties and T_B observations from different sensors operating at different frequencies and incidence angles. The statistical relationships between the observations are accounted for by a Gaussian Mixture Model (GMM), and spatial interactions of images are reflected using Hidden Markov Random Fields (HMRF). Spatial information is provided in terms of a latent field in physical space and statistical information is indicated in the means and covariances of the obtained classes in feature space. Aim is to reduce information of multiple satellite images to a relevant number of spatial classes, which are related differently to sea ice parameters, while keeping the probabilistic distribution for subsequent cluster analysis and uncertainty quantification. The automated data-driven segmentation approach opens up a new scope to improve current retrieval algorithms based on the combined information contained in a multitude of observations.

The Bayesian segmentation is applied to three different data sets: SAR imagery for high-resolution discrimination of water and sea ice, multiple-incidence angle T_B data from SMOS to exploit angular differences in sensitivity to thin sea ice, and multi-frequency observations from SMOS and AMSR2 after extending the algorithm to three dimensions to obtain consistent class patterns that can be compared to ice maps and SIT products.

In a first application the segmentation of sea ice-covered areas based on high-resolution images of multi-angular SAR backscattering coefficient. Low-resolution microwave radiometry data have limited penetration depth and are unable to resolve surface characteristics of sea ice in sufficient detail. As a consequence, current retrieval algorithms often underestimate the SIC of areas that are completely covered by sea ice. Important information on the surface roughness conditions are contained in the distribution of radar backscattering signals which are useful to discriminate surface water such as melt ponds from different sea ice types. Surface roughness for closed water and sea ice is significantly smaller as compared to the mainly wind-forced open ocean, which enables to classify surface types based on its intrinsic surface conditions. Sentinel-1A/B SAR images are available on a daily basis at medium resolution ($\sim 40\,\mathrm{m}$). The goal is to segment SAR images into a number of separable classes using the Bayesian segmentation algorithm. The approach considers the angular variations and the spatial correlations of the SAR images. Surface water fraction is estimated based on annual images at a selected area in the Northern Barents Sea from September 1, 2019 to August 31, 2020. A second application involves the segmentation of Arctic sea ice from SMOS data, assuming that independent information on sea ice properties, particularly thin SIT, are captured in the multi-incidence angle T_B observations. In order to increase the sensitivity to the composition of sea ice by reducing the effect of physical surface temperature, the polarization ratio (PR) between horizontally and vertically polarized values is selected for segmentation. The combination of PR at different incidence angles may give better insights into the distribution of thin sea ice along the freeze-up period. Model uncertainty can be quantified using information entropy from the class probabilities to distinguish well-determined

from uncertain regions in the resulting spatial patterns. The optimal number of separable classes can be determined when compared to thin SIT of existing products during sea ice formation.

To include the fact that observations over sea ice can be essentially linked in both space and time through the non-negligible drift of the ice pack, the implementation of purely spatial correlations between pixels of 2D images can be complemented by considering the temporal and spatio-temporal interactions between volume pixels in 3D space. The two-dimensional Bayesian algorithm to segment spatial data is extended to a third dimension to segment Arctic sea ice in a complete spatio-temporal context. In a third application, channels of SMOS and AMSR2 T_B data are used as input features to examine the joint effect of set of passive microwave observations at 1.4, 6.9, 10.6, 18.7, and 36.5 GHz – equivalent to those of the planned CIMR mission. Aim is to segment the Arctic region into a set of relevant classes based on the synergy effects of the multiple observations and to verify the developing class patterns for the common operational sea ice products SIT and SIC. Then, the segmented classes can be analyzed in terms of their statistical distribution (means and covariances) and spatio-temporal patterns (class probability) to assess their temporal stability, robustness, and spatial representativity, and to verify the solution's general sufficiency for automated application.

Machine learning can often perform better on complex problems where traditional approaches miss out hidden links between the model parameters among large amounts of data. Algorithms have been successfully applied to segment sea ice based on the distribution of surface signatures of satellite observations to recognize patterns of sea ice properties among different scales [Lee et al., 2016, Shen et al., 2017]. Data-driven neural networks (NN) approaches were developed decades ago and can adapt to new ice conditions, changing sea ice types and intermittent periods of freeze up and melting. Before Arctic-wide L-band observations from SMOS were available, NNs were used to infer SIT based on SIC maps from satellite radiometry observations at higher bands, and ancillary geophysical parameters, including surface air temperature and ice drift velocity [Belchansky et al., 2008]. The time series of SIC maps were analyzed on the basis of NNs to forecast SIC by assessing the time-varying characteristics of previous observations [Lin and Yang, 2012, Chi and Kim, 2017]. Snow depth is an important factor with regard to the inference of SIT from both microwave radiometry and Fb observations, and its estimation is particularly complicated due to the complexity of the radiation properties of the snow layer. Therefore, regression NN approaches have been developed to invert snow depth using data from multi-frequency satellite microwave radiometer measurements, including the Special Sensor Microwave/Imager (SSM/I), SMMR, AMSR2, and SMOS [Tedesco et al., 2004, Maaß et al., 2013, Liu et al., 2019, Braakmann-Folgmann and Donlon, 2019]. NNs are efficient and often easy to implement. As an advantage they are capable of recognizing the principal forcing mechanisms contained in the non-linear relationships between geophysical parameters and they provide similar or better results when compared

to those of conventional models. Chapter 7 focuses on a predictive regression NN framework approach to infer SIT based on the first FMPL-2 T_B acquisitions provided by the FSSCat mission. Two separated models were trained on Arctic data to estimate thin ice up to a thickness of 0.6 m and full-range thickness. The models were applied to retrieve Arctic and Antarctic maps of SIT and disseminated products are publicly available under `https://catalogue.nextgeoss.eu/`. In addition to the SIT products, maps of the SIC and SIE over both poles, and global SM over land were also created on the basis of a NN approach using data from both sensors on the FSSCat FMPL-2 payload – the GNSS-R instrument and the T_B L-band radiometer.

1.4 Objectives

This dissertation focuses on the development and application of advanced data-driven modelling techniques for determining SM at the root zone and sea ice parameters – thickness and concentration – using data from various space-based observations. In current retrieval methods, there is a need to extract the information of the ever-increasing amount of satellite data in sophisticated ways to resolve ambiguities and overcome ill-posed problems. The overall goal is to obtain robust solutions with sufficient generality to elaborate evaluation metrics and analysis approaches that allow the joint effect of combining different satellite observations to be exploited. Accounting for spatial correlations and the representativity of observations in the context of geostatistical modelling are among the key challenges of this work. Emphasis is placed on the adaptability of the methods to provide model parameters that reveal information about the physical properties and prevailing processes in the environment under study.

The first objective was to establish a method which allows the characterization of the response time between satellite-based SM data and multi-depth in-situ SM measurements based on the common features contained in their time series – a topic of great relevance for the improvement of the RZSM estimation. The response time between the subsurface SM and satellite observations represents the time span that includes the relevant preceding atmospheric forcing at the surface and initial SM conditions. An appropriate method requires flexibility to account for a time lag, which may be warped in time due to the temporally variable coupling of surface and profile SM, caused by alternating strong wetting fronts and gradual drying of the subsurface. The DTW technique applied in speech recognition allows local mapping between time series data and is a suitable method to characterize the similarity between two time series on a local level. The goal was to implement the method on a new basis so that it is adaptive to the particular time series to obtain a physically meaningful evolving warping path and resulting time lag from which to identify the relevant processes related to the SM dynamics in the subsurface. Patterns of depth-specific alternation in temporal delay and alignment between subsurface SM with respect to surface-sensitive observation are assumed to be represented in the

warping path.

The objective was to apply the DTW to analyze the relationship between point-scale multi-depth and areal satellite observations, and to customize the method and constrain the warping path accordingly, that SM-related processes such as infiltration and drying, as well as water uptake by roots during the growing season are well-reflected in the evolution of the time lag. This thesis examines how land use heterogeneity affects the representativity of in-situ stations with respect to SM variability to be captured in satellite data and how temporal variability of SM is related to climate factors precipitation and PET. Particularly in semiarid regions, cropping periods, precipitation and temperature are clearly seasonal, and are assumed to be reflected in the response time. Greater consideration was given to the fact that the model is based on input data – such as Sentinel-2 channels and meteorological observations – that are available over most areas and with suitable temporal resolution, so that the methodology can be easily applied to other studies. It was expected that common TSA methods such as the exponential filter result in more accurate estimation of profile SM when retrieval periods were divided into SM seasons – rather than assuming a constant relationship between surface and subsurface SM.

The second major goal of the thesis is on the investigation of a Bayesian Unsupervised learning approach to segment multi-dimensional satellite data over sea ice for sea ice parameter retrieval. Due to the dynamics of sea ice and its complex multi-scale structure that includes different ice types with distributed SIT below satellite resolution, sea ice models must be flexible enough to account for both the statistical characteristics and the spatial correlations of the observations. The segmentation algorithm, which was originally developed for segmenting only spatial data sets, was extended to three dimensions in the scope of this work to allow for significant temporal and spatio-temporal correlations. Semi-automatic classification of SIC and developmental stages is currently still based on the experience of ice analysts. The objective was to use the probabilistic approach to quantify model uncertainty based on class probabilities and to evaluate the spatial and statistical model parameters to relate the segmented classes to the underlying ice physical properties. The method presented allows combined sensitivities of a selected set of satellite observations to the seasonally predominant composition of sea ice to be examined and the additional value of including data, e.g., from new satellite missions, to be determined.

The Bayesian segmentation algorithm was applied to different sets of satellite observations. A two-step approach to spatially segment Sentinel-1 SAR data was used with the aim to retrieve high-resolution SIC, while overcoming common underestimation of SIC in current retrieval methods, which are based on low-resolution T_B observations. In a second application, multi-incidence T_B data from SMOS was spatially segmented during freeze-up to investigate classes based on their different sensitivity to thin ice due to variations in optical path lengths through the ice. In a third application, aim was to segment multi-frequency T_B data in a complete spatio-temporal context based on SMOS and AMSR2 data to obtain classes with multi-year consistency which can be seasonally

related to ranges of SIT and SIC. A major advantage of the approach is that it is not limited to single sensor data, but serves as a tool for combining multi-sensor data automatically that can be used to analyze their joint sensitivity to sea ice based on evaluation metrics derived from model parameters.

In addition, the potential of using data from the successfully launched low-cost FSSCat mission to determine SIT and SIC – a topic of great importance for continuous monitoring of sea ice – was investigated. The objective was to evaluate whether low-resolution CubeSat data could be used as an alternative to the data from large satellite missions to provide SIT products of similar quality to operational products. A regression NN approach was selected to be able to incorporate the T_B data from the FMPL-2 payload in combination with a set of suitable auxiliary observations to train two separate models, aiming to provide thin SIT based on the direct sensitivity of the L-band T_B data to thin ice, and to estimate full-range SIT by complementing freeboard data from the CryoSat2 mission to the model. Because SIT products are currently limited to the Arctic, both models were trained with Arctic data and were initially used to predict Arctic SIT, but were also applied to Antarctic data to conditionally estimate Antarctic SIT.

Part I

Relating Satellite-Based Surface to In-Situ Profile Soil Moisture

2 Remote Sensing of Soil Moisture

This chapter focuses on common SM acquisition methods which can be divided into small-scale on-site measurements and spaceborne observations to provide SM on global scale, and retrieval techniques to infer SM in the subsurface from available surface-sensitive observations. Direct in-situ measurements and non-invasive geophysical methods which allow estimation of local SM are presented in Section 2.1. The multiple satellite sensors and respective retrieval algorithms to generate satellite-based SM products are described in Section 2.2. Space-based observations are sensitive to the water contained in the uppermost soil layer, and the products are validated against in-situ SM observations at ~ 5 cm depths – which are pooled in international sensor networks. For characterization of SM in the underlying subsurface, the current process-based and data-driven techniques to estimate RZSM based on the surface-sensitive satellite products and auxiliary data are given in Section 2.3.

2.1 Soil Moisture Acquisition Methods

Current methods to estimate the SM content include in-situ measurements such as gravimetric analysis [Reynolds, 1970] and time domain reflectometry (TDR) [Evett, 2003, Walker et al., 2004], and non-invasive geophysical methods such as ground penetrating radar (GPR) [Lunt et al., 2005], electromagnetic induction (EMI) [Callegary et al., 2007], and electrical resistivity tomography (ERT) [Samouëlian et al., 2005]. These methods differ in terms of their feasibility and representativity in capturing SM dynamics at different temporal scales and their variability at different spatial scales – also with respect to RZSM along the depth profile. In-situ measurements provide SM at the local scale, geophysical observations at the field scale, while regional and global coverage can only be achieved through space-based observations.

Local In-Situ Methods

Gravimetric methods are the most direct techniques to determine the SM content by decomposing a soil sample into water and dry material quantitatively. Hereby, the soil bulk is continuously oven-dried and weighed, and the loss of weight of the remaining

constituents is indicative of the SM content. Gravimetric methods are invasive and tedious to perform under laboratory conditions.

TDR is a transient method which involves injecting a fast pulse into the soil. It measures the velocity through the porous medium, which depends on the apparent dielectric constant, largely determined by the water content. The graphical evaluation of the reflected waveform allows to relate the velocity pattern to the SM content, with a shorter pulse travel time through the porous medium indicating a wetter soil. It is less invasive and representative to the SM content of a small volume of a few centimeters with limited spatial coverage. Periodic and automatic acquisition of subsurface SM can be obtained by distributing multiple buriable-type TDR sensors along the soil profile.

The integrated in-situ sensors, based on techniques such as the gravimetric method and electromagnetic methods, are subjected to a rigorous quality control process to achieve a common and high standard for data dissemination. They have been a indispensable source of information used for validation and calibration of land surface models and satellite-based SM retrievals [Dorigo et al., 2021].

GPR is a subsurface imaging technique to estimate the local spatial variability of SM content with a resolution of meters [Huisman et al., 2002, Huisman et al., 2003]. An antenna emits electromagnetic waves at frequencies in the MHz range and the received energy of the transmitted groundwaves through the subsoil depends on the contrast in the dielectric properties in the subsoil. The electromagnetic wave velocity can be related to the vertical SM distribution because most changes in the effective dielectric constant in soils are caused by changes in the water content in the unsaturated vadose zone.

EMI systems consist of a pair of coils, where the first coil generates a primary magnetic field that induces an electric current in conductive subsurface layers, which in turn generate a secondary magnetic field that is measured by the second coil [McNeill, 1980]. The combined information of the coil transmitter and receiver reflect the distribution of apparent electrical conductivity which has been used to estimate SM [Sherlock and McDonnell, 2003, Callegary et al., 2007].

ERT relates resistivity measurements to SM content and is used to estimate the distribution of subsurface SM, in particular in the RZSM dynamics [Samouëlian et al., 2005, Garré et al., 2011]. The resistivity distribution of the sounded soil volume pseudo sections is inverted by injecting electric currents into the soil and measuring the resulting potential differences along a transect with electrodes.

Non-invasive geophysical methods work best under homogeneous conditions and with high contrasts in the soil horizons. They become inaccurate for fine-grained, clay-rich soils as the signals have a low signal-to-noise ratio. The temporal variability of the SM profile can be determined using sounding data collected at different times. They are of limited use to monitor the spatial variability and dynamics of the SM beyond local scale and field scale.

The International Soil Moisture Network (ISMN) is an open access database containing

global in-situ SM networks that guarantees a standard of data sets for validation and calibration of air- and spaceborne remote sensing [Dorigo et al., 2011, Dorigo et al., 2013].

Remote Sensing Observations

Both in-situ automated techniques for point measurements and geophysical methods require continuous and labour-intensive maintenance and are therefore not suitable for SM monitoring at regional and global scales. Large spatial coverage and regular temporal sampling for the operational provision of SM can only be achieved through spaceborne measurements. Several sensors operating in different electromagnetic spectra suitable for satellite-based detection were investigated for their application for retrieving SM. Initially, observations of short-wave radiation and thermal inertia monitoring were tested understanding that a soil with a high moisture content appears optically darker and cooler than a dry soil. Since satellites measure radiation at the top of the atmosphere, interactions along the transfer through the gas- and aerosol-filled tropospheric and stratospheric column become relevant. These measurements turned out to be unsuitable for all-sky retrieval due atmospheric effects, potential cloud coverage, and vegetation cover opacity [Kerr, 2007]. Thermal infrared images were considered, but they do not reflect the SM contained in the topsoil, as they are most sensitive to the skin layer of the surface, which is strongly coupled to the atmosphere. Hereby, short-term fluctuations predominate and an accurate retrieval would require knowledge on the atmospheric forcing, such as the effects of wind speed on evaporation. An ideal system set up for operational capability hence needs to be ready to use regardless of the local time, under most weather conditions, with high vegetation transparency, and sensors require a shallow penetration depth so that measurements are representative of topsoil moisture.

Observations in the microwave spectrum can be directly related to SM, as they are sensitive to the dielectric properties and the respective hydraulic conductivity, which in turn varies with volumetric SM content. Active and passive microwave systems were evaluated by simulating the SM sensitivity of radiometers, radars such as SAR and scatterometers regarding potential satellite-based global systems [Pellarin et al., 2003]. In particular, observations are independent of daylight, and in the lower microwave spectrum they are largely unaffected by the atmosphere, and with less impact of vegetation cover [Srivastava et al., 2014]. Besides the frequency range constraint, several technical challenges had to be overcome with regard to the implementation of satellite systems to achieve sufficient revisit time, and spatial resolution to adequately capture the hydrological dynamics of surface SM. These systems need to be designed in a way that SM retrieval products can reach the maturity to capture spatio-temporal dynamics of SM to enable the development of new drought monitoring and agricultural products and applications.

2.2 Satellite-Based Surface Soil Moisture

There are several ongoing spaceborne missions suitable for SM retrieval using radiometry sensors at microwave frequency including SMOS and SMAP (L-band at ~ 1.4 GHz) [Kerr et al., 2001, Entekhabi et al., 2010a], and AMSR2 (frequencies ranging between 6.9 GHz to 89 GHz) [Owe et al., 2008]. The Advanced Scatterometer ASCAT instrument (C-band at 5.255 GHz) was originally designed to monitor wind speed and direction but has also been used to retrieve SM [Wagner et al., 2013]. These active and passive observations are used to provide SM products with a spatial resolution of several tens of kilometers at global coverage [Rodriguez-Fernandez et al., 2019]. For observations in the higher microwave spectrum, such as for AMSR2, both the influence of the atmospheric effect and the vegetation cover increase. The two Copernicus Sentinel-1 satellites (C-band at 5.405 GHz) achieve higher spatial resolution to retrieve SM down to 5 m, using SAR with a revisit time of six days. Besides being sensitive to surface SM, their back-scattered signal depends on multiple parameters such as the dielectric constant of the soil, surface roughness, and the composition of the vegetation canopy and biomass, and it is often strongly attenuated due to surface and volume scattering [Paloscia et al., 2013]. Therefore, the accurate determination of SM from SAR backscatter remains an open task fraught with ambiguity. To address this ill-posed problem, either prior knowledge of soil and vegetation parameters or multiple-configuration SAR observations, i.e., multi-temporal, multiple incidence angles, multiple polarizations, are required.

Change detection-based methods are based on the assumption that temporal changes in surface roughness, canopy structure, and vegetation biomass occur on a larger temporal scale than changes in SM [Rignot and Van Zyl, 1993]. Alpha approximation is a change detection method commonly used to estimate SM from time series SAR data over agricultural fields [Balenzano et al., 2010]. Given time series of SAR measurements are collected over bare soil, assuming that the surface roughness of consecutive observations does not change and volume scattering does not dominate, changes in multi-temporal backscatter are largely a result of changes in SM. Vegetation and surface roughness can be effectively decoupled from SM effects by considering the ratio of consecutive radar backscatter measurements which can be approximated as the squared ratio of correspondingly defined alpha coefficients. These coefficients are a function of the dielectric constant, incidence angle, and polarization, and the original alpha approach requires an initial estimate of the upper and lower bound soil moisture values to constrain the estimated range. The method was extended by considering dynamic, spatially explicit boundaries obtained from the SAR data themselves, or by using multiple rather than single polarizations (HH or VV) and higher incidence angles [He et al., 2017, Palmisano et al., 2020].

In addition to satellite-based direct methods, ERA-Interim/Land generated by the European Centre for Medium-Range Weather Forecasts (ECMWF) – among other land surface parameters – provides SM through reanalysis of observations and land surface

model simulations [Balsamo et al., 2015].

ESA's SMOS mission was launched in November 2009 and it is the first spaceborne mission specifically designed to provide global maps of SM and sea surface salinity [Font et al., 2009,Kerr et al., 2010]. SMOS is equipped with the Microwave Imaging Radiometer with Aperture Synthesis (MIRAS), an interferometric radiometer that acquires multi-angular full polarization brightness temperatures in ascending and descending orbits with equator crossings at 06:00 and 18:00 local times [Corbella et al., 2005]. It has a nominal accuracy of $0.04\,\mathrm{m}^3\,\mathrm{m}^{-3}$ and a spatial resolution of $\sim 40\,\mathrm{km}$, and a 2–3 days revisit time at the Equator [Kerr et al., 2010].

The SMOS L2 retrieval algorithm was developed to create global surface SM maps [Kerr et al., 2012]. It is based on an iterative approach that minimizes a cost function by finding an optimum set of SM, and vegetation characteristics using multiple incidence angles T_B. Hereby, the extraction of SM from T_B consists of the following steps: The observations are normalized to emissivity using a RTM to account for effective surface temperature and the effects of soil surface roughness. A tau-omega model is used to correct for the attenuation of soil emission due to the vegetation layer. The emissivity measurement is related to the soil dielectric properties [Kerr et al., 2012]. In a final step, the corresponding properties are related to SM.

The sensitivity of L-band T_B observations to land surface SM is particularly strong with a total dynamic range of about 100 K [Shi et al., 2006, Wigneron et al., 2017]. This is the case for the aforementioned SMOS L2 product, where the effects of surface temperature, vegetation and surface roughness are accounted for [Kerr et al., 2012]. Information about heterogeneity below the 40-km-resolution of L-band radiometers need to be extracted from parameters obtained from additional maps or forecasts. An observed pixel may contain a variety of surface types including water bodies, different land uses such as forests and cropping systems, transition areas with snow cover, urban areas, and topography, and additional information about them determines the meaningfulness of the retrieval. The retrieval is applied only to the percentage of the pixel consisting of the surface area where surface SM can be determined. For the remaining percentage, a predefined fixed specific reference value – determined by a set of auxiliary parameters – is assigned regarding the surface type.

Radio Frequency Interference (RFI) is a known issue causing performance degradation of SM retrievals and eventually the total loss of the data. It is mainly affecting regions in Europe, Asia and the Middle East [Daganzo-Eusebio et al., 2013]. The effect of RFI on SMOS T_Bs leads to or loss of information or underestimation of SM due to unwanted energy. Active RFI emissions are usually stronger than the natural radiation emitted by the Earth, and interference originates from adjacent bands or from man-made illegal emissions in the protected 1400–1427 MHz passive band. They must be detected and flagged in the T_B observations to avoid erroneous retrievals [Oliva et al., 2016].

Satellite-based observations at L-band are sensitive up to the top $\sim 5\,\mathrm{cm}$. Therefore,

RZSM cannot be inferred directly from remotely sensed data. Direct observation would potentially require lower frequent observations – such as P-band (250–500 MHz) [Ye et al., 2020] or much lower frequencies – to increase the penetration depth or, ideally, even penetrate the entire vadose zone to the water table. However, these measurements are not yet technically feasible for satellites today, because the already large footprint (∼40 km for L-band) would be even larger at lower frequencies, up to hundreds of kilometers. Therefore, SM beyond the penetration depth of regular surface-sensitive SM observations can only be inferred using an indirect approach. In the next section, methods that relate SM retrievals to subsurface SM based on process- and data-driven modelling and assimilation techniques are described.

2.3 Root-Zone Soil Moisture Estimation

Accurate inference of subsurface SM along the soil profile from surface-sensitive observations is challenging because observations are widely non-linearly related. The time scale of processes relevant to variations in surface SM is generally shorter and responsive to changing atmospheric conditions, whereas factors that determine the state of the SM in the underlying subsoil are arranged on longer time scales [Vereecken et al., 2014]. Regarding observations, satellite data are available regularly at relatively high temporal resolution in the order of days or weeks, and profile SM is usually acquired on sub-daily basis. Although active and passive systems in the microwave spectrum are sensitive to near-surface because of their shallow penetration depth, and the capability to resolve the spatial variability of SM through remote sensing measurements is limited, observations provide the spatial coverage needed for exhaustive inversion approaches.

The goal of SM inference methods is to understand the relationship between surface SM measurements and in-situ SM along the depth profile in order to find a realization of the subsurface SM through inversion which is in agreement with the observed data. If methods are too simplistic, they do not add value or miss out fundamental characteristics of the underlying problem, whereas too complex models can have limited applicability, because they require conceptual understanding and information on the hydraulic properties. Basically, a distinction can be made between data-driven and process-based methods, each exhibiting its own advantages and drawbacks in terms of the required information of the described system (input data and model parameters), computational efficiency, geophysical realism (plausible and realistic picture, i.e. heterogeneity captured), and generalizability of the solution (robustness and temporal stability).

The physical properties and processes responsible for the changes in SM state can be described by directly accounting for the partial flow and transport differential equations using process-based methods. In dynamic system theory, state-space models fully describe the evolution of a dynamic system in terms of the smallest set of internal independent variables, called state variables, and its response to certain inputs as a set of

first-order ordinary differential equations. For a given state-space model, the number of state variables is equal to the order of the differential equations describing the system and the number of initial conditions required to fully solve the model, while the set of state variables is not unique and can be defined in terms of directly measurable or indirectly determinable physical variables. Hereby, soil water balance models can be applied to simulate profile SM by computing the spatial and temporal mass and energy fluxes, where simple hydrological models based on the soil water balance equation can be used to capture the subsurface SM dynamics [Manfreda et al., 2014, Baldwin et al., 2019].

However, the 'true' states, such as of the SM, cannot be observed directly because variables evolve over time and measurements contain noise and can be highly ambiguous. Thus, the goal of a state space model is to retrieve information about the states by continuously updating the model which enables to exploit newly available information from recent observations. Aim is to integrate time series of measured surface data into hydrological models to obtain more accurate estimates of SM content through data assimilation techniques. A widely used approach is the Bayes' theorem-based Kalman filter, which has been adopted for state variable estimation by implementing a feedback loop that assimilates a representative set of observations in real time [Welch et al., 1995]. Both observations and model background state contain unknown errors which makes estimation a statistical problem, and state variables of the system are described by probability density functions rather than single values. Versions of the original method – such as the extended Kalman filter and the ensemble Kalman filter – have been adapted to estimate SM, the latter being widely used due to its ability to handle nonlinear systems and its computational efficiency [Huang et al., 2008]. In addition, numerical weather prediction includes information on the land surface from satellite measurements to integrate SM into the operational forecast system [Drusch et al., 2009].

Land data assimilation methods have been applied to improve process-based model estimates [Sabater et al., 2007, Al-Yaari et al., 2014]. An integrated hydrological model is used for rigorous simulation of surface and subsurface flows by including the relevant vegetation-soil interactions [Kuffour et al., 2020]. Retrievals based on these conceptual models are especially beneficial in regions where observations are sparsely available and SM changes are determined by boundary conditions in addition to the physical laws. They provide the most sophisticated techniques to produce realistic models and obtain the basic framework for predictions. The feasibility of these methods can be limited by the fact that many input parameters are needed to adequately model the soil-physical properties, which are often unavailable or of poor quality, and missing information is filled with empirical assumptions. Also, inversions may be computationally time-consuming and large-scale solutions of physical models require the use of supercomputers.

The goal of data-driven methods for profile SM estimation is to evaluate observations in terms of their variability to recognize patterns in the data sets. These methods can be separated into statistical modelling and time series analysis (TSA) methods. Statistical

models are fully data-driven, and they can be used to find the relationship based on regression models. Machine learning techniques such as Deep Learning algorithms and Random Forest approaches can be used to estimate RZSM, while accounting for non-linearity in the statistical distribution of a set of input features [Kornelsen and Coulibaly, 2014, Carranza et al., 2021]. These techniques have the common advantage that assumptions on the model parameters are not necessary. Although geophysical reasoning is limited, machine learning techniques can be useful for pattern recognition, and often achieve results of similar quality as those provided by e.g. data assimilation techniques. Nonetheless, these methods assume that the relevant subsurface processes are represented in the input features, and the retrieval accuracy is often poor for extremely wet and dry conditions – also due to limited learning capability in case of these rare events.

TSA methods are used to determine the functional relationship between surface and subsurface SM observations. Cumulative Distribution Function (CDF) matching follows a simple and efficient stochastic technique to extract the systematic differences between different measurement techniques such as point-scale in-situ and areal satellite SM observations for subsequent retrieval. The original methodology has been extended to account for representativity errors between them [Reichle and Koster, 2004, Gao et al., 2013, Gao et al., 2019, Zhuang et al., 2020].
The current profile SM content can be inferred by exponentially filtering previous surface SM observations based on a optimal time length, which is characteristic for each location, depth and soil properties [Wagner et al., 1999, Albergel et al., 2008]. The exponential filter technique is often referred to as an independent method to compare results obtained using statistical and physics-based approaches. In comparison to process-based models, analytical models rely only on a few assumptions, require a small number of input features and are computationally efficient. However, the coupling between surface and subsurface SM may vary by climate, and methods that are robust for a particular region may not lead to general solutions to be applicable to other regions. Since these approaches rely exclusively on the relative behaviour of time series, the performance often depends on the temporal sampling and the data length. The influence of soil properties and meteorological conditions can cause SM time series obtained from surface-sensitive remote sensing techniques and subsurface in-situ observations to be related in a highly non-linear way.

DTW is a dynamic programming technique capable of dealing with temporal distortions with the aim to find the optimal match between time series. It can be used to provide a time lag evolution as a continuous dissimilarity measure comprising the main temporal variability features of surface and subsurface SM time series. In Chapter 3, the exponential filter and DTW technique are introduced. In Chapter 4, the DTW technique is applied to observation the SMOS L4 product – developed at BEC [Portal et al., 2018] – with in-situ measurements at top- and subsoil-representative depth levels at stations that are located in the Soil Moisture Measurements Station Network of the University of Salamanca (REMEDHUS) in a semi-arid region in Western Spain.

3 Time Series Analysis of Satellite-based and Subsurface Soil Moisture

In this chapter, two TSA techniques are presented to relate satellite-based SM to RZSM time series. The exponential filter is a simple and commonly used method to estimate RZSM from previous surface-sensitive SM observations according to a constant characteristic time length, and it is explained in Section 3.1. The SM content is sensitive to external forcing such as climate conditions, land use and soil properties, which cause subsurface SM to be seasonally variable. The DTW technique (Section 3.2) enables to quantify a variable time lag between non-linearly related and distorted time series, and has more flexibility than the exponential filter which is based on a constant time length. Its fundamentals are explained in Section 3.2.1. The principle of the method is explained and the technique is verified in Appendix A, based on a synthetic example using DTW to estimate the time lag between two random variables. Customization of the method including warping path step-size condition, maximum allowed time lag, and the determination of the onset dates of pronounced precipitation events are presented in Section 3.2.2.

3.1 Exponential Filter

A soil profile can be divided into a surface layer and an underlying sub-layer. The surface layer is considered the soil horizon where observations are sensitive to SM content Θ_S. The sublayer lies beyond the penetration depth of the satellite sensors and contains the subsurface SM Θ_2. Both layers are connected by a vertical water flow that is proportional to the SM differences, expressed by

$$\frac{d\Theta(t)}{dt} = \frac{C}{L}\left(\Theta_S(t) - \Theta_2(t)\right), \tag{3.1}$$

where L is the depth of the subsurface layer, and C is the hydraulic pseudo-diffusivity constant that controls the flow between the soil layers. The differential equation can be

solved for Θ_2 by integrating the preceding SM values over time at the surface as follows

$$\Theta_2(t) = \frac{1}{T}\int_{-\infty}^{t} \Theta_S(\tau)\, \exp\left(-\frac{t-\tau}{T}\right) d\tau. \tag{3.2}$$

where $T = L/C$ denotes the characteristic time length representing the time scale of SM variability which describes the degree of smoothing applied to the observed SM at the surface. This time length is considered as a surrogate parameter that includes all relevant hydrological processes and soil properties at different time scales that affect SM dynamics at various depths.

Remote sensing observations have a discrete revisit time and the continuous formulation for Θ_2 can be described by the soil water index (SWI)

$$\mathrm{SWI}(t_n) = \frac{\sum_i^n \mathrm{ms}(t_i)\, \exp\left(-\frac{t_n - t_i}{T}\right)}{\sum_i^n \exp\left(-\frac{t_n - t_i}{T}\right)} \tag{3.3}$$

a SM trend indicator – dimensionless and normalized between 0 and 1 – resulting from a series of previous surface-sensitive satellite measurements $\mathrm{ms}(t_i)$ at the times t_i contributing to the current SWI at the time t_n. For facilitating the computation of the exponential filter, the SWI can be represented in a recursive formula as

$$\mathrm{SWI}(t_n) = \mathrm{SWI}(t_{n-1}) + K(t_n)\left(ms(t_n) - \mathrm{SWI}(t_{n-1})\right), \tag{3.4}$$

where $K(t_n)$ is the gain to update the current SWI, given by

$$K(t_n) = \frac{K(t_{n-1})}{K(t_{n-1}) + \exp\left(\frac{\Delta t}{T}\right)}. \tag{3.5}$$

To obtain the actual subsurface SM, the SWI needs to be re-scaled according to the soil-physical and hydrological properties that determine the SM dynamic range. SM content can be expressed in terms of plant available water (PAW) [Wagner et al., 1999], which can be determined based on the estimated SWI and empirical observations of soil properties field capacity (FC), wilting point (WP), and total water capacity (TWC) as follows

$$\mathrm{PAW} = \mathrm{SWI}\left(\frac{\mathrm{FC} + \mathrm{TWC}}{2} - \mathrm{WP}\right). \tag{3.6}$$

Performance metrics and indicators to quantify the applicability of the approach are essential. The goal is to optimize T to obtain the most accurate estimates of SWI for

a given location and depth, after its validation with representative in-situ observations. Different validation metrics, such as the coefficient of determination (R^2), the Root-Mean Squared Error (RMSE), Nash Suthcliffe model efficiency coefficient (NSE), and unbiased Root-Mean Squared Error (ubRMSE), which are defined as

$$R^2 = \left(\frac{\sum^N (x - \overline{x})\,(y - \overline{y})}{\sqrt{\sum^N (x - \overline{x})^2 \, \sum^N (y - \overline{y})^2}} \right)^2, \tag{3.7}$$

$$\mathrm{RMSE} = \sqrt{\frac{\sum^N (x \breve{} y)^2}{N}}, \tag{3.8}$$

$$\mathrm{NSE} = 1 - \frac{\sum^N (x - y)^2}{\sum^N (x - \overline{x})^2}, \text{and} \tag{3.9}$$

$$\mathrm{ubRMSE} = \sqrt{\mathrm{RMSE}^2 - \mathrm{bias}^2} = \sqrt{\mathrm{RMSE}^2 - (\overline{y} - \overline{x})^2}, \tag{3.10}$$

have been used to determine the optimal parameter T [Albergel et al., 2008, González-Zamora et al., 2016, Tobin et al., 2017]. RZSM was estimated from different active and passive satellite SM time series including the European Remote Sensing scatterometer, ASCAT, AMSR-E and SMOS, and the obtained SWI was evaluated at several in-situ SM networks over Europe [Wagner et al., 1999, Ceballos et al., 2005, Albergel et al., 2008, Brocca et al., 2011, Ford et al., 2014, González-Zamora et al., 2016]. Hereby, the characteristic time length was optimized as being constant over the course of a year or even some years for specific location and depth level.

Scale differences between surface and subsurface observations can strongly depend on the measurement techniques, and the representativity of, for example, point-scale in-situ and areal satellite observations. If in-situ observations have been acquired over a sufficiently long period of time to cover the entire dynamic range of SM at a given depth, the SWI can be re-scaled according to the range of in-situ observations $[\Theta_{obs,min}, \Theta_{obs,max}]$ by

$$\mathrm{SWI}([\Theta_{obs}]) = \frac{(\mathrm{SWI} - \mathrm{SWI}_{min})\,(\mathrm{SWI}_{max} - \mathrm{SWI}_{min})}{\Theta_{obs,max} - \Theta_{obs,min}} + \Theta_{obs,min}. \tag{3.11}$$

This can lead to more accurate estimates compared to the approach based on PAW in case knowledge of soil physical properties is limited.

In the exponential filter approach, the diffusivity C is considered constant, and thus the hydraulic conductivity is also assumed to be constant. In reality, hydraulic conductivity is highly variable, spanning several orders of magnitude for different soil types with differences under saturated SM conditions. This variability could be particularly notable if the water balance becomes perturbed in case of high rate of water introduction or removal due to pronounced precipitation and irrigation, or strong evaporation and transpiration. The response time in which subsurface SM is affected by atmospheric forcing varies, be-

ing shorter around precipitation events and longer during dry events [Wu et al., 2002]. Consequently, the characteristic time length may exhibit strong seasonal variations, and considering this parameter as a constant may considerably limit the estimation accuracy of the derived SM.

3.2 Dynamic Time Warping

DTW is used to study dissimilarities between time series by determining the optimal match between two observations [Müller, 2007]. It is a dynamic programming technique which breaks down a complex problem into easier solvable sub-problems [Berndt and Clifford, 1994]. Hereby, the initial problem is optimized in a way that the solution of the corresponding sub-problem produces the identical result with a considerable reduction of computational effort. This is particularly beneficial when data sets become large or highly dimensional. The DTW algorithm is based on a local distance measure, which contains the distortions and shifts between the analyzed time series. Its main objective is to find the optimal warping path by minimizing a local distance measure between the series within a particular observation period. Two general cases can be pursued – (1) finding a repetitive sub-sequence within a longer sequence and (2) aiming for the optimal global match of two time series within an entire period of observation. Regarding the first case, it was applied in speech recognition and to improve the assessment of electrocardiograms to recognize essential heartbeat patterns within a longer sequence of waveforms [Ainsworth, 1988, Berndt and Clifford, 1994, Laguna et al., 1994, Zifan et al., 2006]. The algorithm has the advantage to account for the relative warping speed between the time series by considering their local changes. The temporal evolution obtained by DTW can be analyzed to retrieve information about mutual dependencies or causal relationships between the time series. In reality, these time series can represent regularly sampled, continuous geophysical or meteorological parameters which are considered to have a variable time lag over an observed period.

3.2.1 General Concept

The DTW algorithm evaluates two input time series which consist of a sequence $\mathcal{X}$ of length M and a second sequence $\mathcal{Y}$ of length N with not necessarily the same length as $\mathcal{X}$:

$$\mathcal{X} := x_i \quad \text{with} \quad i \in \{1, ..., m, ..., M\}\,; \quad \mathcal{Y} := y_j \quad \text{with} \quad j \in \{1, ..., n, ..., N\}. \tag{3.12}$$

The absolute values of two regularly sampled sequences are pairwise compared on the basis of a local distance measure. A criterion to select an adequate distance measure is the dimensionality of the time series [Houle et al., 2010]. Since only two series are

compared, Euclidean distance is used as a local distance measure. The more time series are considered, the less is the total distances between them. This effect is less distinctive considering other measures such as Manhattan distances [Hinneburg et al., 2000]. The aim of the technique is to find the warping path, which represents the maximum alignment between the two time series. The optimal warping path between two series corresponds to the minimum global cost over the entire period. The global cost gc is defined as the sum of local costs of the L pairwise elements $\mathrm{d}_l = \mathrm{d}(x_{m_l}, y_{n_l})$ in a local cost matrix along a warping path p:

$$gc_p(X, Y) = \sum_{l=1}^{L} \mathrm{d}_l. \tag{3.13}$$

Accordingly, gc indicates the global dissimilarity between time series, that is, the higher the value, the more distinctive the features of the input time series. Its absolute value depends on both the total length and the sampling (temporal resolution) of the time series. Therefore, it is difficult to generally ascribe a physical meaning to this absolute quantity. The warping path can be defined by a set of (X, Y)-tuples that correspond to the L pairwise elements $x_i \in X$ and $y_j \in Y$ along its trajectory. It represents the relationship between samples of time series $\mathcal{X}$ with samples of time series $\mathcal{Y}$:

$$p = \{p_1, ..., p_l, ..., p_L\}\,;\; p_l = (p_i, p_j) \in [1:M] \times [1:N] \quad \text{with} \quad l \in [1:L]. \tag{3.14}$$

The warping path is implemented by satisfying the following criteria:

(i) boundary condition: $p_1 = (1, 1)\,;\; p_L = (M, N)$

(ii) monotonicity condition: $m_l \leq m_{l+1} \leq ... \leq m_K\,;\; n_l \leq n_{l+1} \leq ... \leq n_L$

(iii) step-size condition (simple version): $p_{l+1} - p_l \in (1, 0), (1, 1), (0, 1) \quad \forall \quad l \in [1, L-1]$.

The boundary condition defines the initial and final states of the warping path. As indicated in (i) the time series are forced to be aligned at the beginning and the end of the observed period. The monotonicity condition ensures causality and particularly refines the path to exclusively advance forward in time. The continuity condition requires the path to go through every sampled point in time. Hereby, a step-size condition is introduced and chosen in a way that both monotonicity is guaranteed and no samples are skipped (continuous path). In a simple version, two consecutive samples either maintain the present time lag (1,1) or change in relative delay or alignment (1,0), (0,1). The optimal warping path is successively obtained by following three steps:

(i) Computation of the **local distance matrix** D_E

(ii) Building the **accumulated cost matrix** C_{acm}

(iii) Retrieval of the **optimal warping path** p^{opt}

First, D_E is computed from the pairwise local distances d at every point in time:

$$D_E := d_{i,j} = ||x_i - y_j|| \,; \quad i \in [1:M]\,,\; j \in [1:N]. \tag{3.15}$$

Determination of the optimal warping path by comparison of the global cost of all possible paths is computationally expensive (complexity $\mathcal{O}(N \cdot M)$, that is, exponentially increasing cost for an increasing length of time series). Since the optimal warping path is obtained based on a single constant distance matrix D_E and satisfies the criteria (i)–(iii) (time series evolve positively monotonous), a successive calculation of the warping path also yields the optimal solution. An accumulated cost matrix C_{acm} is computed from D_E by summing up the partial costs given by the corresponding distances of each path section. C_{acm} can be obtained using a simple step-size condition (criterion (iii)) with the elements computed as follows:

$$C_{acm} := c_{i,j} = \begin{cases} \sum_{k=1}^{i} d(x_k, y_j),\; i \in [1:M]; & j = 1 \\ \sum_{k=1}^{j} d(x_i, y_k),\; j \in [1:N]; & i = 1 \\ d_{i,j} + min\{c_{i-1,j},\, c_{i-1,j-1},\, c_{i,j-1}\}; & i,j > 1. \end{cases} \tag{3.16}$$

The left and bottom boundaries in C_{acm} are set to infinity, and the first element is initialized with the corresponding value of the bottom-left element of D_E. The matrix C_{acm} is then successively calculated from (1,1) to (M,N). An intermediate value at element (m,n) is obtained by summing up the distance in element (m,n) of D_E and the minimum accumulated cost of the corresponding element according to the step-size condition. Once C_{acm} is obtained, the optimal warping path is retrieved by backtracking the entries along the 'valley' of the minimum accumulated cost from (M,N) to (1,1). The sum of the distances of all warping path tuples (X, Y) in D_E yields the minimum global cost.

Relative changes of global cost between time series at different locations or at different times can be used to describe temporal and spatial variability of the observed parameters. However, being a global quantity over an entire period, it can miss out local information which is needed to understand the behaviour of the warping path and investigate the underlying processes. Therefore, this study is focused on the extraction of a meaningful warping path evolution rather than optimizing the global cost. Geophysical parameters can be retrieved using measurement techniques with differences in data quality as well as temporal and spatial resolution. DTW allows to compare time series of either the same or different parameters which can be extracted at different locations. In case the same geophysical parameter is observed and compared at different locations, temporal variations of the warping path may contain spatial variability of the governing processes. Additionally, local warping behaviour between series measured at the same location may reflect their temporal variability. The local information at a particular sample is given by the

relative time lag between time series at a specific time. In Appendix A, the unconstrained DTW technique is applied in an example to relate two Gaussian distributions. Aim of this work is to investigate the time lag evolution between SMOS and in-situ SM observations. Since the observed parameters have a geophysical meaning, both the evolution and range of the time lag are naturally constrained by their underlying properties and mechanisms. Importance of the resulting time lag in terms of the reflection of prominent features of the input time series and computational efficiency can be improved through customization of the DTW technique (Section 3.2.2).

3.2.2 Customization

In this section, possible customization to the DTW technique are explained. They comprise a maximum allowed time lag, the adjustment of the step-size condition and the computation of the dates of onset of pronounced precipitation events [Herbert et al., 2020]. Results of the intermediate steps after application of customized DTW to SMOS and in-situ SM are presented in Section 4.3.1.

Maximum allowed time lag

The standard implementation of DTW requires the computation of the entire C_{acm} (Equation (3.16)). With basic knowledge about the temporal relation of geophysical observations, the range of the warping path can be roughly estimated beforehand. A Sakoe-Chiba band is a global constraint that adjusts a time interval in C_{acm} in which the warping path can freely evolve [Sakoe and Chiba, 1978]. It has been widely used in DTW to define the range of maximum allowed time lag (Figure 3.1a) [Müller, 2007]. After applying a Sakoe-Chiba band, all off-diagonal elements of C_{acm} outside a certain interval around the main diagonal are set to infinity. The evolution of the warping path is limited to a reasonable predefined time lag interval as follows:

$$\{p_l = (p_i, p_j) \in [i - lead : i + delay] \times [j - lead : j + delay] \,|\, i, j > lead \wedge i, j + delay \leq M, N\}, \tag{3.17}$$

where *lead* and *delay* represent the maximum allowed lead and delay of series $\mathcal{Y}$ with respect to series $\mathcal{X}$, respectively. Short-term fluctuations in SM observations typically are responses to certain events (e.g., precipitation). In cases where temporal sampling is insufficient, SM fluctuations originating from different events may be incorrectly attributed to the same event. Also, without the Sakoe-Chiba constraint, the warping path can skip important temporal features and, as a consequence, unnaturally long delays are accumulated. SMOS SM is more sensitive to meteorologic conditions. In contrast, in-situ SM observations appeared to be more damped depending on the soil properties [Wagner et al., 2007] and long-term climate factors. Furthermore, recharge of subsurface SM content via infiltration is a gravitationally driven process. Therefore, the in-situ SM is expected to

lag behind the SMOS observations and no *lead* is expected.

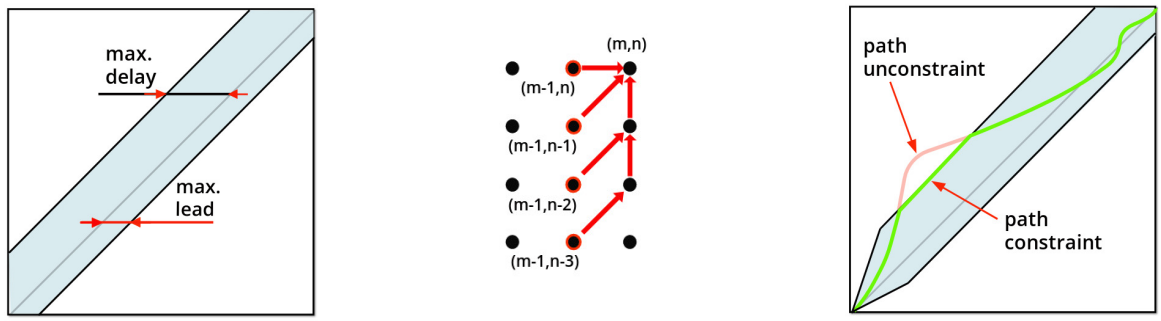

(a) (b) (c)

Figure 3.1: Dynamic Time Warping (DTW) customization scheme: (**a**) Sakoe-Chiba band for maximum allowed time lag; (**b**) adapted step-size condition: $p_{l+1} - p_l \in \{(1,0),(1,1),(1,2),(1,3)\}$; (**c**) warping path evolution with applied constraints.

Adjustment of step-size condition

Uncustomized DTW allows the warping path to freely evolve under satisfaction of criteria (i)–(iii). The step-size condition controls the slope of the warping path and defines the sensitivity level to relative changes between observations. It is important to note that the simple version of criterion (iii) corresponds to an uncontrolled slope, which permits the assignment of an infinite number of samples of series $\mathcal{Y}$ to one sample of $\mathcal{X}$, and vice versa. An instantaneous accumulation of high time lag between two consecutive samples is unphysical. Conversely, when the slope is controlled, the number of assigned samples per sample is limited and the warping path is forced to advance in time within a maximum defined rate.

The slope control also serves as a low-pass filter to account for highly variable or noisy observations which would lead to overaccumulation of time lag. Additionally, the temporal sampling of the input series affects the time lag evolution for a particular step-size condition. As an example, in case of an uncontrolled slope and fine-sampled series are compared, small fluctuations between the series may already cause unreasonably high variations in time lag. For this reason, it is necessary to control the slope to find a trade-off between the temporal sampling limit, the noise level, and the expertise on the temporal scale of the processes to be resolved.

The 2–3 days revisit time of SMOS defines the sampling limit for application. While the topsoil moisture time series are characterized by a rapid increase during recharge after precipitation and a somewhat exponential decrease during a dry period [Albergel et al., 2008], subsurface SM is mainly governed by intrinsic SM properties and the exposure to continuous atmospheric forcing. Therefore, only pronounced precipitation events lead to notable short-term increase in SM at deeper levels, whereas weaker events cause gradual increase over the long term [Martínez-Fernández et al., 2015]. The positive and negative

slope of the step-size condition can be customized differently. Figure 3.1b illustrates the step-size condition between two warping path tuples $p_{l+1} - p_l \in \{(1,0),(1,1),(1,2),(1,3)\}$. The corresponding elements of the C_{acm} are given by

$$c_{m,n} = d(m,n) + min \begin{cases} c_{m-1,n} \\ c_{m-1,n-1} \\ c_{m-1,n-2} + c_{m,n-1} \\ c_{m-1,n-3} + c_{m,n-2} + c_{m,n-1} \end{cases} . \tag{3.18}$$

In the step-size condition in Equation (3.18) the relative rate of reduction and accumulation of time lag between the input series are of 3 and 2 samples per sample, respectively. As an example, step-size interval can be determined by considering the rate of reduction of time lag in case a pronounced precipitation event leads to fast SM increase and the rate of accumulation of time lag during SM decrease with the absence of precipitation.

Determination of onsets of pronounced precipitation events

Surface processes often affect subsurface SM over long periods of time. However, pronounced precipitation events can lead to a rapid increase in both SMOS SM and in-situ SM down to a certain depth. In this case SM time series are sensitive to the same event. Regarding DTW, the warping path is assumed to be aligned at these particular dates of high precipitation. Subsequently, it further evolves depending on the prominent features as before. A function was developed based on the cumulative sum of precipitation to automatically detect the dates of onset of the k most pronounced precipitation events within a given period of time. To obtain the dates, the precipitation is first discretized with a predefined bin rate with respect to the temporal sampling of the time series. Bin edges are determined by considering an equal amount of precipitation within each bin (fixed bin density) and a variable bin width. Hereby, a small and a wide bin width correspond to a period with a high and a low precipitation rate, respectively. The change from low to high precipitation is indicated by a sharp increase in convexity of the cumulative sum of precipitation. The higher the change in curvature, the more pronounced is a precipitation event. The date of onset of a pronounced event is given at the bin edge, where the differences in adjacent bin widths show a local maximum. Subsequently, the local maxima are sorted to obtain the onsets of the k most pronounced events.

3.2.3 Discussion

The DTW technique requires customization to obtain a robust and meaningful warping path that contains the most important features represented in the response time between the surface and profile SM observations. In the next chapter, DTW is used to relate time series of the SMOS L4 SM product to multi-depth REMEDHUS in-situ observations. Fig-

ure 3.2 shows a preliminary results of customized DTW, which illustrates the time lag in terms of the individually mapped samples between SMOS surface and in-situ observations at different depth – similar to Figure A.1d in Appendix A. It is observed that the common features in the input series are well captured by the warping path.

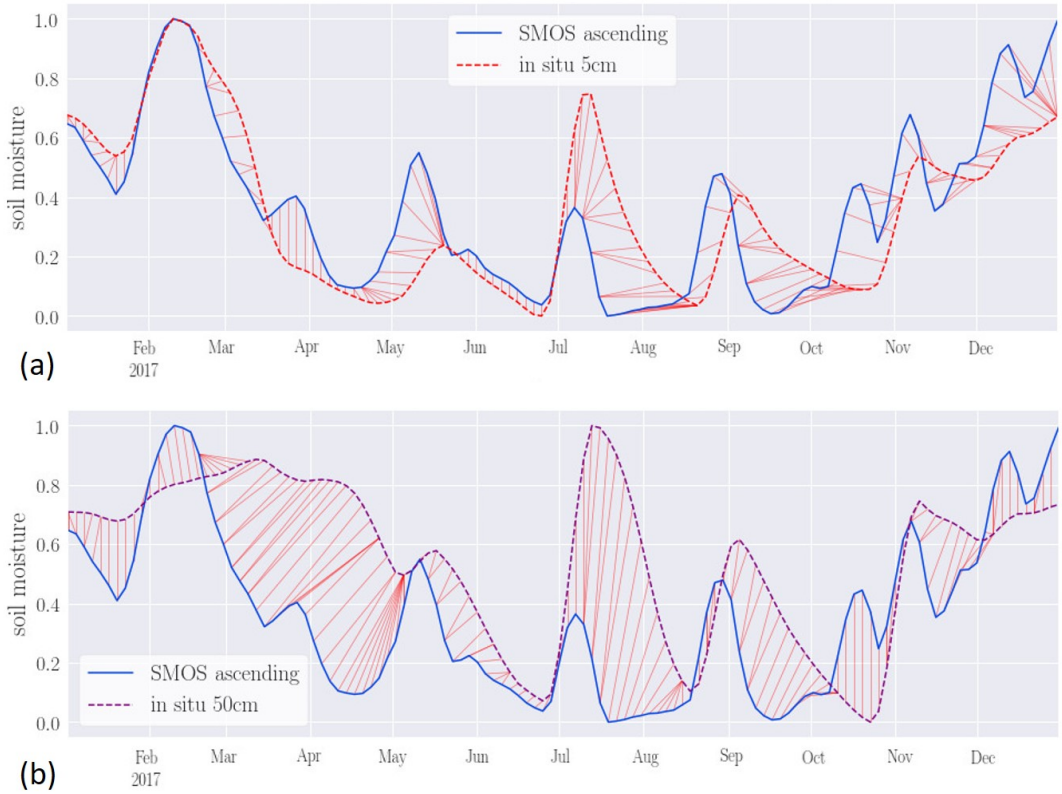

Figure 3.2: Sample-wise allocation – represented by thin red lines – between surface and in-situ SM time series at station `E10` in 2017, obtained using customized DTW. Allocation between samples of SMOS surface and in-situ SM trend series at (**a**) topsoil 5 cm depth with a maximum allowed time lag of 30 days with a step-size $\in [-\infty, 3]$, and (**b**) root-zone 50 cm depth with a maximum allowed time lag of 50 days and a step-size $\in$ [-∞,2], and forced alignment at the dates of onset of the heaviest precipitation events.

However, the factors affecting SM are required to be analyzed and the time series need to be prepared for the DTW technique to perform properly. Processing steps prior to DTW, consisting of normalization and smoothing, ensure a consistent dynamic range and is used to remove irrelevant short-term fluctuations. This leads to a more robust and reliable warping path that highlights the common features of the related time series. Taking into account the heterogeneity of land cover is important to understand the similarity of SM observations and to determine the representativity between the point in-situ and areal SMOS observations. Relevant climate factors, including precipitation and PET, are sources and sinks of SM, and their typical seasonal patterns for the study region may have implications for the temporal variability of the time series.

4 Estimation of Response Time between SMOS and In-Situ Soil Moisture at Different Depths

This chapter focuses on the analysis of the spatio-temporal factors to relate satellite-based surface-sensitive and in-situ SM measurements at different depths [Herbert et al., 2020]. Among the several in-situ SM networks available worldwide and included in the ISMN [Dorigo et al., 2011], the (REMEDHUS) network of the University of Salamanca in Western Spain provides SM observations at multiple depths with excellent temporal resolution [Martínez-Fernández and Ceballos, 2003, Pablos et al., 2016]. This network has been widely used for calibration and validation of both passive and active remote sensing SM data [Pablos et al., 2018, Brocca et al., 2011, Sanchez et al., 2012, Colliander et al., 2017, Portal et al., 2020]. It is located in a semiarid region which consists of cultivated fields and the interaction between SM and vegetation is non-negligible regarding the influence of crops during their growing season [Masialeti et al., 2010, Atchley and Maxwell, 2011]. Therefore, spatial heterogeneity of land use was analyzed to provide information about the level of representativity of SMOS observations to each in-situ station. Land use impact was investigated by means of the Normalized Difference Vegetation Index (NDVI) using composite time series data from the Moderate Resolution Imaging Spectroradiometer (MODIS), and high-resolution images from Sentinel-2 L1C [Sinergise, 2020]. To support the interpretation of the time lag evolution, SM seasons were estimated from precipitation and evapotranspiration recordings to categorize sub-periods in which similar SM-related processes occur. The evolution of the quantified response time was analyzed considering the results of the spatio-temporal analysis of the study area to recognize seasonal and spatial patterns, and to give insight into the variability of the characteristic time length.

The high-resolution SMOS L4 SM product is described in Section 4.1.1. The REMEDHUS SM network including multi-depth observations under consideration of the predominant climate factors is described in Section 4.1.2. Results of the estimation of SM seasons as part of the analysis of temporal variability of climate factors and the evaluation of the spatial heterogeneity of land use are given in Section 4.2. The intermediate steps of the DTW technique and its customization are demonstrated in Section 4.3.1, for the

particular case of comparing SMOS with in-situ SM at station `E10` in 2017. Customized DTW was applied to the time series of all stations and depths, and the evaluation of time lag evolution is presented in Section 4.3.2. In Section 4.4, the exponential filter is applied to the time series to determine a seasonally representative characteristic time length by averaging values obtained for the sub-periods belonging to the same SM season. The potential of the DTW technique regarding the interpretation of SM processes and the inference of subsurface are discussed in Chapter 4.5.

4.1 Time Series Data sets

4.1.1 SMOS Soil Moisture

For the last 10 years, several SM products with enhanced spatial resolution have been developed [Pablos et al., 2019]. In this study, high-resolution 1 km SMOS L4 SM time series provided by the BEC have been used [Portal et al., 2018]. They are obtained by a linear downscaling algorithm – similar to Reference [Piles et al., 2014] – merging data from microwave, visible, and near-infrared sensors with different spatial resolutions, and modeled data. The relationship between SMOS L3 SM product and auxiliary data is derived from the so-called universal triangle method in the vegetation-land-surface temperature space, using an adaptive moving window to ensure homogeneous climate conditions. The auxiliary data comprise SMOS L1C T_B, NDVI from MODIS, and land surface temperature provided by ECMWF. Previous research revealed a slight difference between SMOS T_B measured at ascending and descending orbits over the same homogeneous scene [Martín-Neira et al., 2016], resulting in non-negligible differences in SMOS SM retrievals. Therefore, both orbits are only compatible for specific applications. In the following, high-resolution SM maps of only the ascending orbits were used.

4.1.2 REMEDHUS Soil Moisture Network and Climate Data

The REMEDHUS network is located in the Duero basin comprising a relatively flat area of 35 km $\times$ 35 km between 41.1–41.5°N and 5.1–5.7°W (Figure 4.1) with small slopes and an altitude ranging between 700–900 m above sea level. Land use has remained broadly stable along the last decade, and it consists predominantly of rainfed cereals (80%) (winter wheat and barley), forest pasture (12%), irrigated crops (5%) and vineyards (3%), with occasional legumes and sugar beet. The growing season of winter wheat is usually between October and July, but it can vary by several weeks depending on the meteorological conditions. The main soil texture is sandy loam and sandy clay loam, with the topsoil becoming sandier at the shallow foothills to the east of the network. REMEDHUS consists of four automatically recording meteorological stations and about 20 SM monitoring stations among which more than 10 stations record multi-depth SM. It has already been

used for validation of SM content and variability of previous SM products from SMOS and SMAP mission [Sanchez et al., 2012, González-Zamora et al., 2015, Colliander et al., 2017]. The stations are equipped with HydraProbe® (Stevens Water Monitoring Systems Inc., Oregon, USA) and EnviroSMART® (Sentek Pty. Ltd., Stepney, Australia) sensors. The frequency sensors measure the soil impedance automatically by taking into account the energy storage and energy loss in the soil, and provide SM content on an hourly basis at 5 cm, and 25, 50 and 100 cm, with a nominal accuracy of 0.01 $m^3\,m^{-3}$. The REMEDHUS network is part of the ISMN and comprises a homogeneous area and provides favourable conditions in terms of topography and climate conditions for validating large-scale satellite imagery with the in-situ measurements.

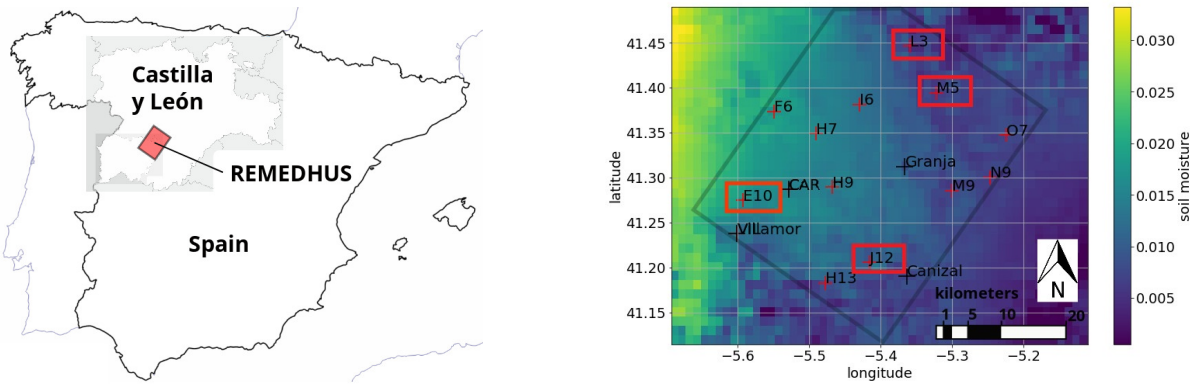

(a) (b)

Figure 4.1: (**a**) Location of the REMEDHUS network; (**b**) snapshot of the high-resolution SM and Ocean Salinity (SMOS) L4 SM over the area. The SM stations `E10`, `J12`, `L3` and `M5`, which are used in this study, are marked in red. Black crosses indicate the 4 meteorological stations.

The region is characterized by a semiarid continental climate with an average annual temperature of ∼12 °C. The annual precipitation has been 385 ± 100 mm in the last 10 years and it is homogeneous among the network. However, intensity and timing of meteorologic conditions vary over the course of the year. Climate factors in combination with present growing and dormant periods can be used to define SM seasons, which are accompanied by similar patterns of SM recharge and consumption processes. In this work, SM seasons were estimated based on the relationship between PET – the net SM demand if water was potentially available—and precipitation. Results of the comparison of PET and precipitation are given in Section 4.2.1. Hereby, PET was computed on the basis of the Penman-Monteith equation [Allen et al., 1998], and was used as a reference to directly estimate the actual crop evapotranspiration. It was obtained using solar irradiance, relative humidity, mean temperature, and wind speed. The average of PET over all four meteorological stations was computed. This approach has been shown to accurately estimate evapotranspiration for cropped surfaces in various climates and has been used as the standard method by the Food and Agriculture Organization of the United Nations

(FAO) [Allen et al., 1998].

4.1.3 Comparison of SMOS and In-Situ SM

Among the different REMEDHUS stations, four stations were selected regarding land use, soil texture and the availability of multi-depth SM measurements (marked in the red boxes in Figure 4.1). 2017 was an anormal year, showing the lowest annual values ever recorded since the REMEDHUS network was installed in 2006 regarding both precipitation (250 mm) and SM average ($0.10\,\mathrm{m}^3\,\mathrm{m}^{-3}$). In contrast, 2016 and 2018 received considerably more precipitation (129 % and 136 %) as compared to the average recorded annual mean, respectively. Therefore, the period from 2016 to 2018 is representative enough to reflect the climate variability of REMEDHUS.

Satellite observations at L-band are known to be sensitive to the SM profile within the first 5 cm profile. In croplands, vegetation root zone is estimated to be within the first 50 cm depth, where most of the root biomass is present [Pietola and Alakukku, 2005, Fan et al., 2016]. For these reasons, in-situ SM measurements at 5, 25 and 50 cm were selected to encompass both topsoil and RZSM. Land use, soil type and depth-specific SM-related properties of stations `E10`, `J12`, `L3` and `M5` are shown in Table 4.1. These properties include FC and WP of the soil bulk at the corresponding depths. FC defines the amount of SM which eventually gets retained subsequent to infiltration, after water has completely drained away (after 2–3 days), and WP estimates the minimum SM content a plant is capable to utilize against the soil matric potential, i.e. the force by which the water is retained in the soil [Or et al., 2005]. These parameters were obtained from the sand-silt-clay composition of the soil and vary with soil texture. In case these parameters are vertically heterogeneous, they may indicate differences in SM dynamic range as well as different rates of recharge and dry out. Additional information on the predominant soil type of the uppermost soil horizon at the four study sites were obtained from the Agrarian Technological Institute of Castilla y León (ITACyL) [ita, 2020].

Since the low spatial variations between SMOS L2 pixels over REMEDHUS found in a previous study were in agreement with in-situ site-specific characteristics [Sanchez et al., 2012], the SMOS L4 pixels at 1 km also correspond. However, how accurate SMOS L4 SM represents a single station over the course of a year is not clear. A non-negligible part of SM consumption is due to root-water uptake which is a particularly important process during the growth of vegetation. Similar to timing and quantifying the amount of precipitation in SM recharge, root-water uptake depends on the land use, which in turn depends on water availability and stage of plant development. Stations `M5` and `J12` comprise rainfed winter cereals, which is the principal land use of REMEDHUS. Since stations `E10` and `L3` are located in vineyards, the corresponding SMOS pixels are likely representing a mixed land use. Thus, it is important to know the typical field scale of land use (heterogeneous length scale) at the REMEDHUS network, especially at the

Table 4.1: Land use (2016–2018), soil type and depth-specific SM-related properties including soil texture, WP and FC of stations `E10`, `L3`, `J12` and `M5`.

Station	Land Use / Soil Type	Depth [cm]	Sand [%]	Silt [%]	Clay [%]	WP [$m^3\,m^{-3}$]	FC [$m^3\,m^{-3}$]
E10	Vineyard / Gleyic and albic luvisol	5	75.11	16.35	8.54	0.028	0.088
		25	73.74	15.71	10.55	0.047	0.108
		50	66.79	4.96	28.25	0.099	0.193
L3	Vineyard / Cambic arenosol and calcaric cambisol	5	82.25	6.44	11.31	0.040	0.125
		25	82.45	6.27	11.28	0 .056	0.146
		50	80.20	11.90	7.90	0.043	0.130
J12	Fallow (2016), winter cereals (2017/2018) / Gleyic luvisol	5	60.94	16.85	22.21	0.096	0.236
		25	59.10	16.76	24.14	0.113	0.228
		50	59.99	14.97	25.04	0.168	0.265
M5	Winter cereals / Calcaric and eutric cambisol	5	81.64	8.31	10.05	0.057	0.100
		25	81.41	7.87	10.72	0.042	0.125
		50	84.75	5.37	9.88	0.043	0.071

surrounding area of the SM stations. This includes knowledge to which level SM at 1 km resolution can represent point-scale observations and, whether crop-related processes are supposed to be captured in their time series.

In this study, the NDVI was used to quantify the variability of land cover in the REMEDHUS network. Temporal variability of land use was studied using 16-day time series composite from MODIS within the three-year study period. High-resolution (10 m) NDVI maps are computed using near-infrared and red bands of Sentinel-2 L1C satellite images with a maximum cloud coverage of 30 % [Sinergise, 2020]. The following steps were carried out, and the results are presented in Section 4.2.2. The temporal variability of land use was studied using the Terra MODIS NDVI from 2016 to 2018, particularly the 16-day composite at 1-km resolution (MOD13A2 product of collection 6), derived from atmospherically-corrected reflectances at red (band 1: 620–670 nm) and near-infrared (band 2: 841–876 nm). The spatial variability of land use within the corresponding SMOS L4 pixel was investigated using Sentinel-2 NDVI images at 10 m at a representative date within the growing season of winter wheat (21 February 2017), when differences in land use were particularly pronounced. The NDVI was computed from Sentinel-2 L1C reflectances at 10 m in red (band 4: 665 nm) and near-infrared (band 8: 842 nm) with a maximum cloud coverage of 30 %. The mean and variation of NDVI were studied around the stations to understand the level of representativity of SMOS L4 at 1 km to each of the four in-situ stations.

High-resolution SM from SMOS is compared to in-situ observations at different depths from 2016 to 2018. A three-days average was applied to all SM time series to obtain regular sampling from irregularly sampled SMOS observations. Subsequently, a low-pass filter (Gaussian smoothing $\sigma = 22$) was applied to all series to smooth out high magnitude peaks of short-term SM fluctuations and to obtain the comparable trend series. To account

for different dynamic ranges of the observations, input time series were calculated by applying min-max normalization to the trend series.

4.2 Analysis of Soil-Moisture Related Factors

The results of the temporal variability of climate factors in terms of SM seasons are presented in Section 4.2.1. The estimated levels of spatial representativity of each station from the analysis of spatial heterogeneity of land cover due to the presence of crop growing seasons are given in Section 4.2.2.

4.2.1 Temporal Variability of Climate Factors

Figure 4.2 shows the monthly accumulated precipitation recordings and PET estimation, averaged over eight years (2011–2018). The three distinct SM seasons (recharge, utilization, deficit) are defined by comparing monthly averages of PET and precipitation. The recharge season starts as soon as monthly accumulated precipitation exceeds PET around November, and it coincides with the approximate crop sowing date. While evaporation decreases during the winter months, SM begins to recharge and be used in part by early plant development and the transpiration that accompanies it. The utilization period starts once monthly accumulated PET exceeds precipitation around mid-February. Water availability from precipitation cannot compensate for the losses due to increasing evapotranspiration, and vegetation mainly utilizes stored subsurface water. Due to decreasing precipitation and continued water consumption during the growing season, soil starts to dry out. The limit between utilization and deficit is defined to be around mid-June when RZSM gets intensively taken up by plants, with interannual variation. Crops are harvested shortly after, when water becomes scarcer. Summer months are very dry and the associated subsurface SM deficit is not suitable for crop cultivation on a purely rainfed basis. Information about the main features of the SM seasons are summarized in Table 4.2.

Table 4.2: Estimated SM seasons from 8-year averaged monthly accumulated precipitation and PET, and the typical growing season within REMEDHUS, including the prevailing processes of SM change.

SM Season	Recharge	Utilization	Deficit
Period	November–Mid-February	Mid-February–mid-June	Mid-June–October
Criterion	Precipitation > PET; initial plant growth	Precipitation < PET; main growing season	Precipitation << PET; crops are harvested
Prevailing Processes	Precipitation	Strong root-water uptake and evapotranspiration	Evaporation at maximum
SM Condition	SM storage increases	SM decreases due to consumption	Continuous drying; SM at minimum in the end

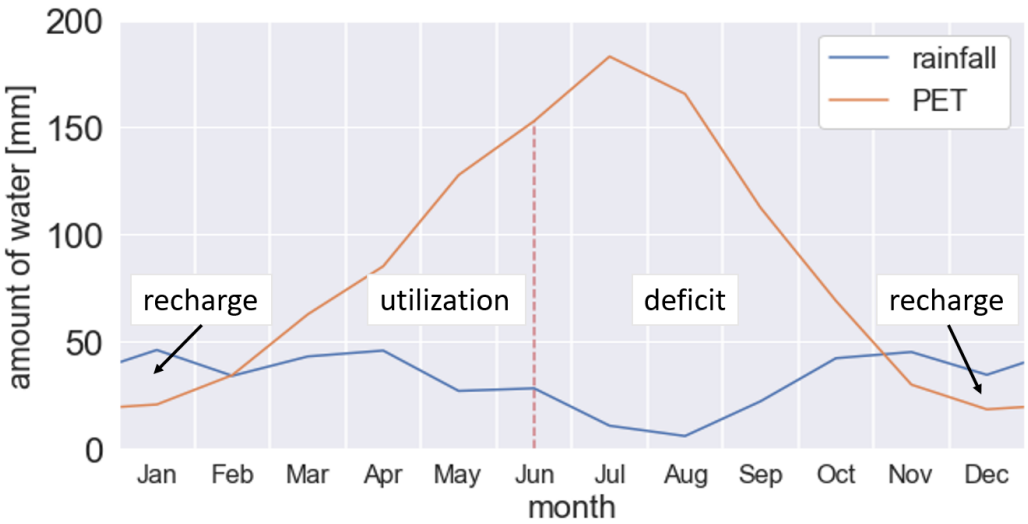

Figure 4.2: Monthly accumulated precipitation and estimated PET over REMEDHUS averaged from 2011–2018. A comparison of the amount of water which is added to the soil in terms of precipitation and released to the atmosphere via evapotranspiration defines SM seasons, including periods of recharge, utilization and deficit.

4.2.2 Spatial Heterogeneity of Land Coverage

Figure 4.3 shows the MODIS NDVI time series at 1 km resolution for all stations from 2016 to 2018. Albeit land use differs among the locations of the stations, all NDVI time series generally indicate the phenological characteristics and timing of a winter cereal growing season [Masialeti et al., 2010]. After the sowing date around October and subsequent germination, a small green-up peak at the turn of the year represents plant emergence and growth. After a short crop dormancy due to the low winter temperatures, indicated by a local NDVI minimum, rapid plant growth is reinitiated until peak greenness is reached around April. The harvest date is around June/July depending on meteorological conditions and crop maturity. Although total water consumption is high due to the relatively long growing season, summers in the REMEDHUS region are very dry to cultivate summer crops. Due to the high irradiance and temperature, an estimated 350 mm of the approximately 500 mm of integrated PET over the entire growing season will occur during the main growing season from May to July (see Figure 4.2). In this main growing period the water consumption by root-water uptake is the highest. Winter cereals reach a considerable rooting depth in the initial phase and a possible final rooting depth of more than one meter. Thus, the accessibility of deeper soil layers guarantees yield stability even in regions with low rainfall (annual precipitation lower than 600 mm) [Guddat et al., 2015]. To better understand the spatial variability within the SMOS L4 pixel, Sentinel-2 NDVI images at 10 m are shown in Figure 4.4a–d for the four in-situ stations, respectively.

The selected images with full coverage correspond to a representative date within the crop growing period (21 February 2017), when vegetation of the agricultural fields is already sufficiently developed to distinguish a variety of land covers. The typical field scale

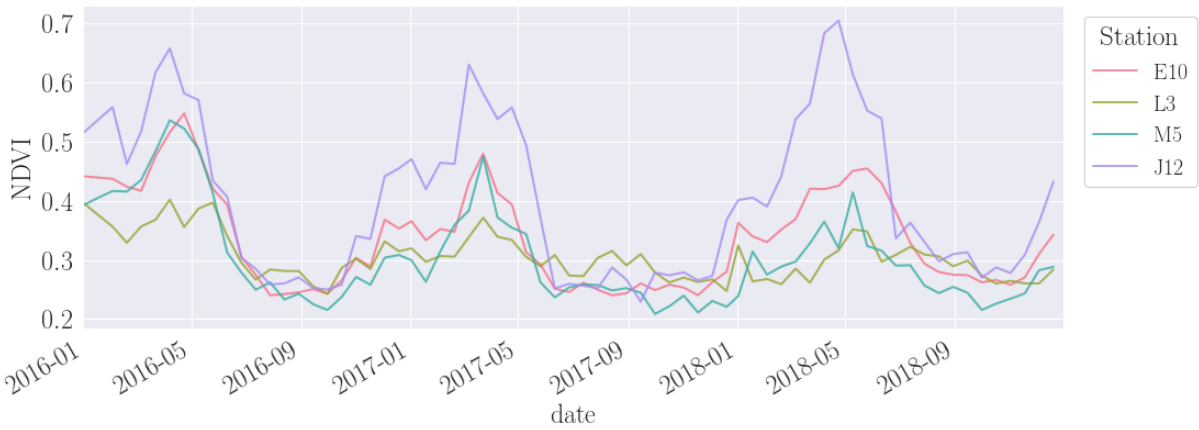

Figure 4.3: 16-day MODIS NDVI time series at 1 km from 2016–2018 encompassing the stations `E10`, `L3`, `J12` and `M5`.

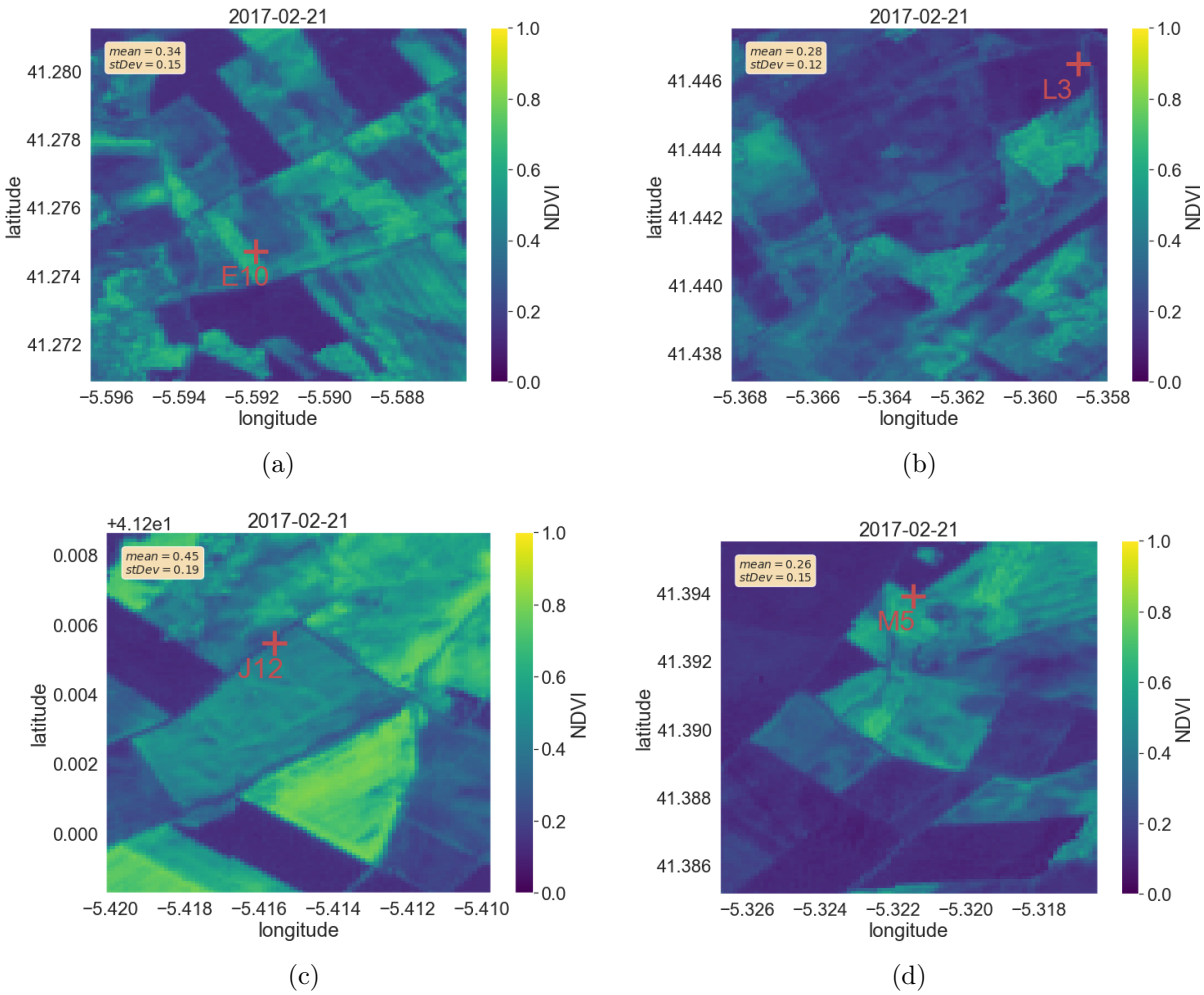

Figure 4.4: Sentinel-2 NDVI image at 10 m including mean and StDev within the corresponding SMOS L4 pixel encompassing station `E10` (**a**), `L3` (**b**), `J12` (**c**) and `M5` (**d**), for a representative date (21 February2017).

of cultivation in the REMEDHUS network is significantly smaller than 1 km. Figures 4.5a–d show the NDVI mean and StDev of Sentinel-2 NDVI as a function of the square area around the corresponding station. It is worth noting, that in all cases, NDVI in a square

area of 1 km × 1 km (`delta` of 500 m) resembles the mixed land use over the entire REMEDHUS network, which was observed to be of 0.32 ± 0.18 at that particular date. The typical NDVI values for vineyard and rainfed cereals were determined to be around 0.15 and 0.45, respectively.

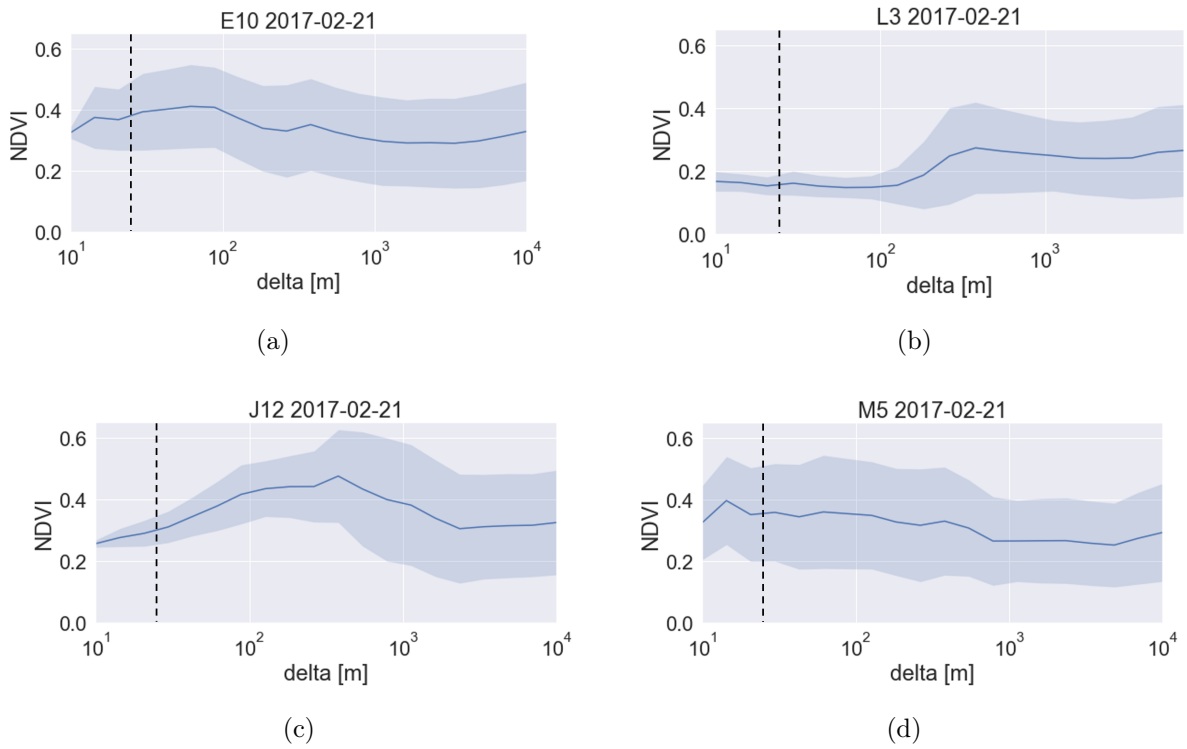

Figure 4.5: Sentinel-2 NDVI mean and stDev as a function of the parameter `delta` around the stations `E10` (**a**), `L3` (**b**), `J12` (**c**) and `M5` (**d**) for a representative date (21 February 2017). The extent of the square area is determined by `delta` being half the side length from the station location along latitude and longitude directions. The black dashed line corresponds to `delta` = 25 m (50 m resolution).

Station `E10` is located in a vineyard area next to a field with cereal crops. Accordingly, a fast increase of NDVI values for increasing `delta` and higher variability are given in the close surrounding of `E10`. Station `L3` is more centrally located in vineyard, and resembles its typical NDVI of 0.15 up to about 100 m resolution. The increase of mean and variation of NDVI beyond that scale indicates that different land uses are incorporated in the wider surrounding. Station `J12` shows an increase in both mean and variation of NDVI for larger resolution, while including crop fields at different stages of development. Regarding both mean and variation of NDVI, among all stations, `M5` overall resembles the values at SMOS resolution best and represents similar land use within the entire resolution ranging from a scale of 10 m to 10 km. The high NDVI standard deviation (StDev) at station `M5` at small resolution is due to its location near the border of different land uses. Albeit knowledge of soil texture, spatial variability and distribution of land cover are necessary, additional information of climate factors and the presence of crops are crucial to further understand the plant-moisture relationship, and to eventually point out regions with similar SM

dynamics. All information about the level of spatial representation of land use of single stations within the corresponding SMOS L4 pixel is summarized in Table 4.3.

Table 4.3: Results of the analysis of land use variability in the surrounding of the in-situ locations (`delta` = 25 m) and at 1 km resolution (`delta` = 500 m), including an estimated level of spatial representativity of SMOS and the corresponding in-situ station. NDVI Images (mean values and StDev) are evaluated at a representative date during a growing season (21 February 2017).

Station	Local Land Use / NDVI	SMOS Land Use / NDVI	Spatial Heterogeneity	Representativity (SMOS to In-Situ)
E10	Vineyard 0.38 ± 0.12 *	Mixed land use 0.34 ± 0.15	Homogeneous up to ± 20 m, then heterogeneous	Given; but station bordering on cereals!
L3	Vineyard 0.17 ± 0.04	Mixed land use 0.28 ± 0.12	Homogeneous up to ± 100 m, then heterogeneous	Not given
J12	Rainfed cereals 0.31 ± 0.05	Rainfed cereals 0.45 ± 0.19	Prop. increasing heterogeneity with resolution	Conditionally given; variability is diverging
M5	Rainfed cereals 0.34 ± 0.17 *	Mixed land use 0.26 ± 0.15	Heterogeneous	Given

* values resemble the overall distribution at REMEDHUS of 0.32 ± 0.18.

4.3 Application of DTW Technique

Intermediate steps of the application of the DTW technique, and its customization to SMOS and in-situ time series are assessed and presented in Section 4.3.1. The resulting evolution of time lag is presented and interpreted in section 4.3.2.

4.3.1 Intermediary Results of DTW and Customization

DTW was applied to SMOS and in-situ SM observations, and the single steps are explained for station `E10` in 2017. For this station, the SMOS and in-situ time series at different depths, together with the final results for the entire study period, are shown in Figure 4.10 in Section 4.3.2. As an example, the intermediate steps of the application of DTW to SMOS and in-situ 5 cm depth time series are illustrated in Figure 4.6. Included are the computation of the local distance matrix D_E from the normalized trends, the accumulated cost matrix (C_{acm}) with a particular step size $\in [-\infty,3]$, and a maximum allowed time lag of 10 samples (30 days). The time lag evolves along the optimal warping path for the given customization, indicated by a red line.

Figure 4.7 illustrates the customization of DTW for station `E10` at 50 cm depth in 2017. The particularly dry year with intermittent pronounced precipitation events in summer

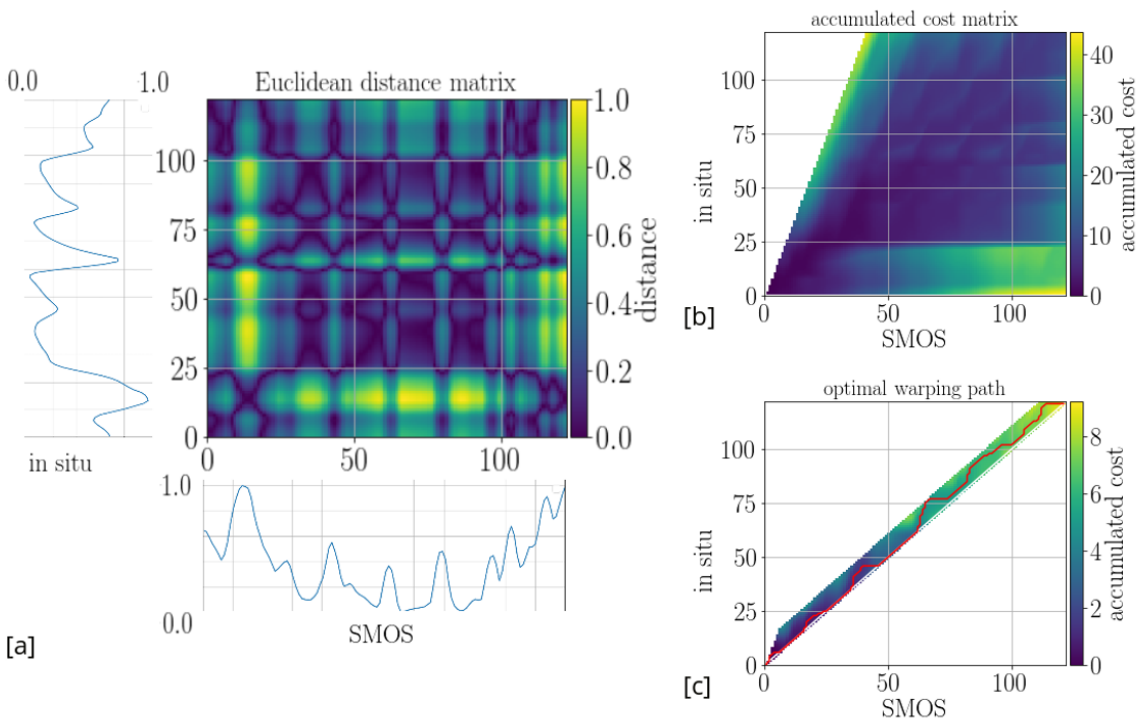

Figure 4.6: Illustration of the intermediate steps of the DTW, applied to SMOS and in-situ 5 cm time series at station `E10` in 2017: (**a**) Computation of D_E from the normalized trends; (**b**) C_{acm} with step size $\in [-\infty,3]$; (**c**) Optimal warping path (red line) with a maximum allowed time lag of 30 days.

clearly led to short-term recharge at 50 cm depth. Figure 4.7a shows the corresponding normalized trends in combination with the three-days accumulated precipitation. SMOS SM increases at almost all precipitation events, while in-situ SM is only sensitive to the most pronounced events, such as to those in the beginning of the July, September and November, when the soil was initially dry. SMOS SM decreases several days after the absence of precipitation, whereas in-situ SM is only characterized by gradual drying.

Figure 4.7b shows the time lag evolution, corresponding to a maximum allowed time lag of 60 days under customization of the negative slope and fixed maximum positive slope of two samples per sample. Irrespective of the customization of the negative slope, the time lag runs into the maximum allowed value between May and mid-July. Thus, the time lag does not reflect the observed alignment of the input series at the onsets of the most pronounced precipitation events in the beginning of May and July, when both trend series resemble clearly. For a finite negative slope of -2 or -3, the time lag gets further trapped at high accumulated values until mid-October. The customization with an infinite negative slope performs best, but is not sensitive enough to lead to a prompt reduction of time lag, if necessary.

To enhance the sensitivity to common features of the input series, the alignment of time series are forced at the onset dates of the most pronounced precipitation events. Both SMOS and in-situ SM show significant increase after the occurrence of pronounced

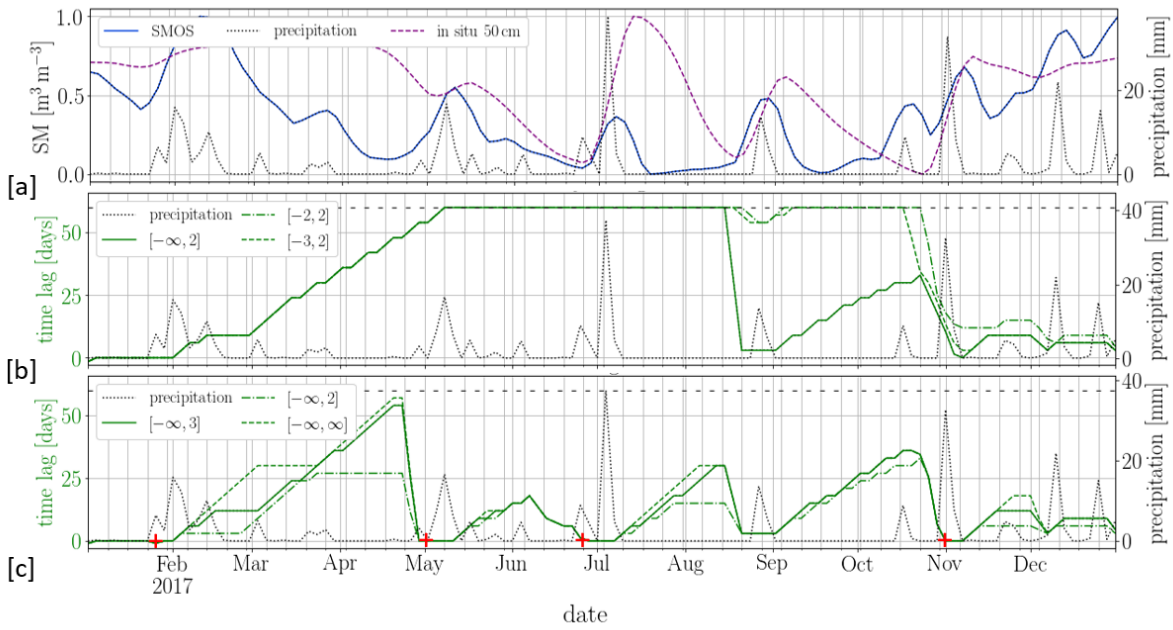

Figure 4.7: Results of customization of DTW applied to SMOS and in-situ SM at 50 cm depth at station `E10` and in 2017 as an example: (**a**) normalized trends of SMOS and in-situ time series; (**b**) time lag for different negative slopes – maximum positive slope of two samples per sample; (**c**) time lag for different positive slopes – maximum negative slope fixed is $-\infty$ and forced alignment at the dates of onset of the four most pronounced precipitation events in 2017 (26 January, 2 May, 22 June and 29 October).

precipitation during summer, precipitation events which initiate SM recharge after the mostly dry summer, and heavy precipitation during the wetter winter. The number of pronounced events was selected according to the precipitation pattern, and the most prominent features of SMOS and in-situ SM along the study period (2016 to 2018). The selection of the nine most pronounced events was sufficient to capture the dates of the most prominent features, without overcontrolling the evolution of time lag. The corresponding dates of onset are illustrated

DTW was subsequently applied to the resulting sub-periods in 2017, which are limited by the four onset dates. The corresponding time lags of the sub-periods were eventually merged. Figure 4.7c shows the time lag evolution after forced alignment, including different customization of the positive slope and infinite negative slope. The dates when alignment is forced are marked by red crosses. It can be seen that the main features of the input series are reflected in the evolution of time lag. Features which are only visible in SMOS SM (e.g., SM increase after a rain event in mid-October) correctly lead to further accumulation of time lag. Therefore, the automatized implementation to force the alignment increases the sensitivity of DTW; the customization with an infinite negative and finite positive slope showed the overall best performance for all depths.

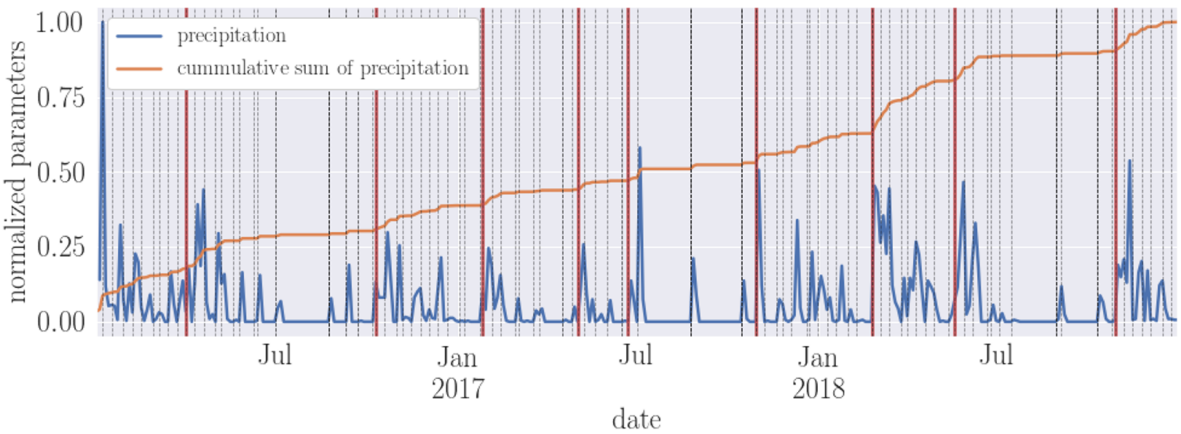

Figure 4.8: Three-days accumulated precipitation (blue line), and normalized cumulative sum of precipitation (brown line). Binning with fixed bin density is applied to the cumulative sum of the precipitation. The bin edges (dashed black lines), where the contrast between periods of sparse and strong precipitation is the highest, are defined as dates of onset of the nine most pronounced precipitation events (red lines) from 2016 to 2018 (1 April 2016, 10 October 2016, 26 January 2017, 2 May 2017, 22 June 2017, 29 October 2017, 29 February 2018, 18 May 2018 and 27 October 2018).

4.3.2 Final Results of the Evolution of Time Lag

In this section, the results of time lag evolution between SMOS and in-situ SM time series at the depths of 5, 25 and 50 cm of the representative stations `M5`, `E10` and `J12` from 2016–2018 are presented. In all cases the time lag is determined from customized DTW using a step size $\in [-\infty,2]$ and forced alignment of the time series at the onsets of the nine most pronounced precipitation events within the study period. Customization of a maximum allowed time lag was not applied. The results for each station are given in Figures 4.9–4.11. The time lag evolution of the corresponding time series are displayed below. The onset dates at which time lag gets reseted to zero are depicted by red lines in the distribution of precipitation along the study period (Figure 4.8, previous section) and by red crosses at the resulting time lags (Figures 4.9b, 4.10b and 4.11b). The results were assessed in terms of SM time series, the previously defined SM seasons (Table 4.2 in Section 4.2.1), and the level of spatial representativity of the SMOS observations (Table 4.3 in Section 4.2.2). The best results have been obtained for stations `M5` and `E10`, where land use between SMOS and in-situ station is well-represented. For these particular stations, the following general observations can be made regarding the amount and timing of accumulation of the time lag.

A similar evolution of the time lag is given in 2016 and 2018, resembling the typical observed precipitation pattern among REMEDHUS. The time lag is characterized by seasonal variations, which can be attributed to the summarized SM seasons and the presence of growing seasons. Deeper observations generally show longer time lag. This phenomenon becomes more pronounced at stations `M5` and `E10` during the deficit season,

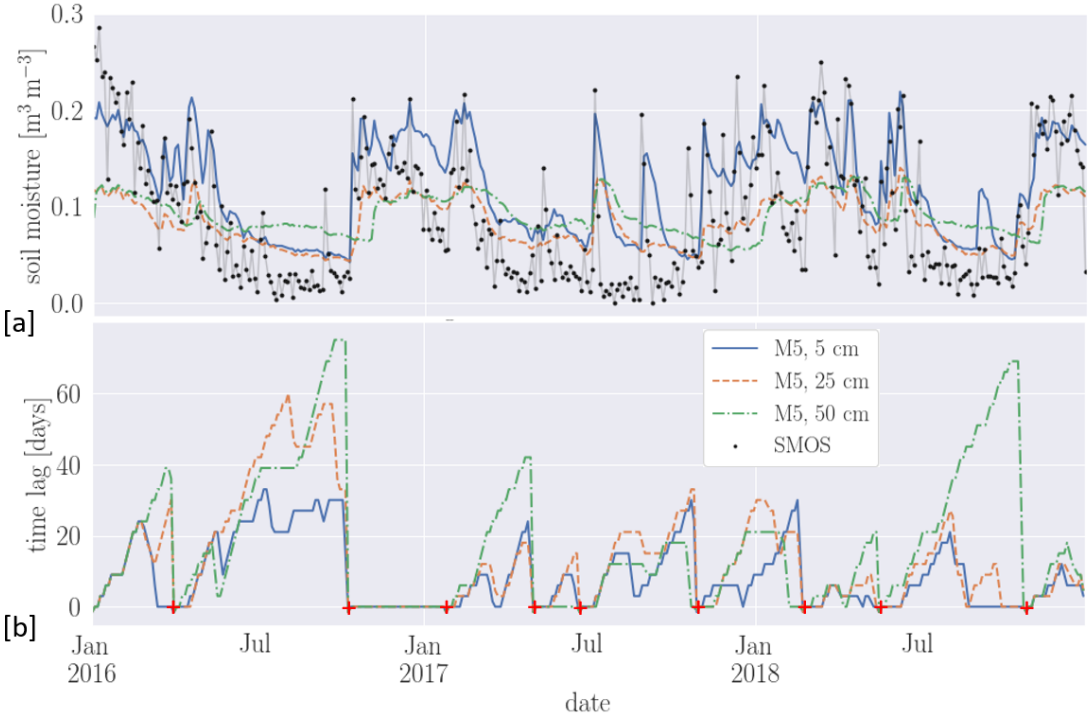

Figure 4.9: (**a**) SMOS and in-situ SM time series at station `M5` at 5, 25 and 50 cm depth from 2016 to 2018; (**b**) Evolution of time lag between SMOS and the respective depths. Dates when alignment was forced are indicated by red crosses.

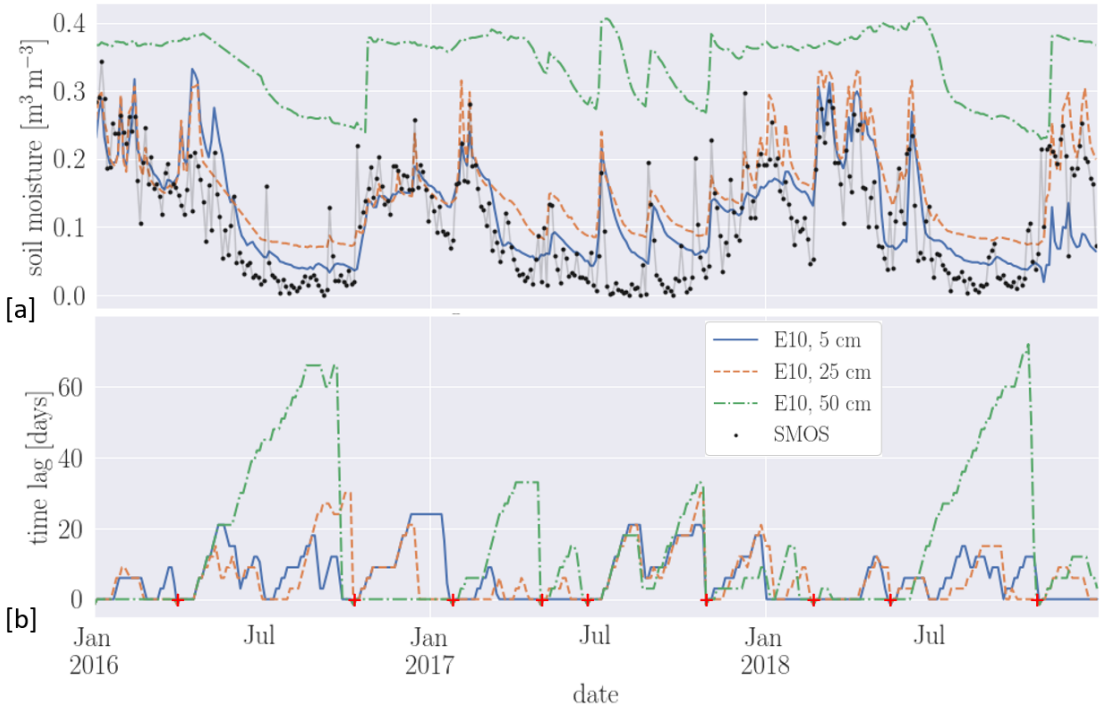

Figure 4.10: (**a**) SMOS and in-situ SM time series at station `E10` at 5, 25 and 50 cm depth from 2016 to 2018; (**b**) Evolution of time lag between SMOS and the respective depths. Dates when alignment was forced are indicated by red crosses.

Figure 4.11: (**a**) SMOS and in-situ SM time series at station J12 at 5, 25 and 50 cm depth from 2016 to 2018; (**b**) Evolution of time lag between SMOS and the respective depths. Dates when alignment was forced are indicated by red crosses.

when the time lag for 50 cm SM reaches values up to 60 days. In this season, the exchange of SM with the atmosphere occurs mainly through evaporation at the uppermost layer, resulting in a reduced drying rate at 50 cm. Less accumulation of time lag is observed during recharge and utilization in comparison to deficit season. One of the most pronounced precipitation events occurs in the beginning of each recharge season, that is, 10 October 2016, 29 October 2017 and 27 October 2018 (see Figure 4.8), when dry conditions are followed by abundant rains. This leads to an increase in subsurface SM, and to more frequent alignment of the time series within the recharge season. Thus, almost no time lag is observed in the period from October to January, and both subsurface and SMOS SM follow the same pattern. A small time lag implies that SM changes mainly depend on shortly preceding atmospheric conditions, which is in agreement with the fact that in this case the increase of SM in the recharge process cannot be referred to a low initial SM content in the beginning of the recharge season.

After sufficient recharge occurred at all depths, continuous precipitation and moderate consumption are barely changing the SM content. As a consequence, RZSM becomes widely insensitive to changes at the surface, which results in less accumulation time lag. With increasing water consumption and evapotranspiration during utilization, SM gradually starts to dry. This dry out gets interrupted by intermittent precipitation, which results again in low accumulation of time lag. In the beginning of the deficit season, SM decreases substantially due to both absence of precipitation and strong root-water uptake.

After crops are harvested, less-intense, but continuous SM decrease is recorded close to the WP, where water becomes unavailable for roots. From now on, evapotranspiration becomes too high for effective infiltration and less frequent rain events marginally influence SM. These circumstances lead to high accumulation of time lag up to the length of the entire deficit season, especially for deeper observations, and the actual SM content is more influenced by initial SM conditions.

The year 2017 was an anormal one regarding both timing and amount of precipitation with overall dry conditions (annual rainfall only half the usual average), which had consequences for the time lag evolution. Firstly, due to the absence of precipitation, high accumulation of time lag could be already observed in March. Furthermore, the two occasional strong rainfall events in the deficit season led to SM recharge and hence time lag was reduced.

Regarding soil texture, clay-rich soils with high FC are characterized by less pronounced SM changes in comparison to sandy soils. This can be seen at station `J12` consisting of clay-rich soils, where SM recharge at 50 cm only occurs at the very end of the recharge season. It is important to note that the presence of crops can influence the time lag significantly. This can be especially seen at station `J12` towards the end of the main growing season. In the absence of precipitation around July 2016 and 2018, strong root-water uptake leads to a fast decrease of RZSM at 25 and 50 cm depth, which is unusual for clay-rich soils. SM at 5 cm is less utilized and remains more sensitive to atmospheric forcing. This has a reverse effect on the time lag showing the highest accumulation for 5 cm SM along the depth profile. Station `L3` was categorized as the least representative among the four stations. Due to limited validity, results of this station are presented, but the time lag evolution is not further analyzed in detail. The time lag within the estimated SM seasons are summarized in Table 4.4 for each station and depth. Mean and maximum values in each period are averaged over the representative years 2016 and 2018.

4.4 Seasonal Time Length Estimates Based on Exponential Filter

The variation in the average estimated time lag among SM seasons in Table 4.4 indicates a substantially larger response time for the deficit season. This demonstrates that the relationship between satellite-based SM and profile SM in the observed semi-arid region is seasonally dependent. The time length T used to for the retrieval of subsurface SM by means of an exponential filter is widely considered as characteristic for each station and depth. Instead of considering T as a constant, it can be further optimised in regard to the SM seasons, which can be estimated in terms of monthly accumulated precipitation and PET (see Figure 4.2). The exponential filter (Section 3.1) is applied to the corresponding

!htb]

Table 4.4: Results for mean and maximum time lag obtained within the estimated SM seasons recharge, utilization and deficit, respectively, averaged over 2016 and 2018.

Station	Depth [cm]	Time Lag [d]					
		Recharge		Utilization		Deficit	
		Mean	Maximum	Mean	Maximum	Mean	Maximum
E10	5	5	12	4	16	6	16
	25	6	18	3	13	7	22
	50	3	7	4	19	38	69
L3	5	7	24	7	22	11	34
	25	4	19	5	18	8	25
	50	1	4	3	13	23	45
J12	5	3	13	6	22	26	51
	25	8	19	4	15	7	21
	50	1	4	8	24	13	21
M5	5	6	22	6	27	13	27
	25	8	24	9	25	23	43
	50	7	19	11	30	38	72

SMOS L4 SM series covering stations `E10`, `L3`, `J12` and `M5`. Similar to previous studies of [Wagner et al., 1999, Albergel et al., 2008, González-Zamora et al., 2016] the profile SWI series are first of all optimized considering a constant characteristic time length from 2016 to 2018. In a second step, the exponential filter is optimized seasonally within sub-periods along the three years and representative SM-season-specific characteristic time lengths are determined for each station and depth. The two approaches, i.e. optimizing the time length as constant or seasonally varying, are compared in terms of their differences in accuracy in retrieving SWI.

Constant Time Length

The exponential filter is applied to the representative SMOS time series with a constant characteristic time length varying between 0–100 days with a step size $\Delta T = 1$ day. Since the soil-physical properties to describe the SM sensitivity range along the soil profile are often unknown; and the resulting SWI series are re-scaled according to long-term dynamic ranges of the targeting in-situ SM series at the corresponding station and depth. If long-term in-situ observations are available without registering a considerable trend, this leads to a more realistic estimate of the variability of the SM content then re-scaling SWI to obtain PAW from information on WP and FC. These properties are often determined only once, and they can vary horizontally. Subsequent to normalization, the validation metrics (Equations 3.7–3.10) coefficient of determination (R^2), NSE, RMSE and ubRMSE are determined between the re-scaled SWI and the corresponding in-situ SM series at 5, 25 and 50 cm depth.

The computed validation metrics as a function of characteristic time length for the SWI

compared to in-situ observations at 25 for all stations are presented in Figure 4.12. The optimal T extracted according to the best values for each validation metric are summarized for each station and depth in Table 4.5. Maximum NSE and minimum RMSE correspond to the same T, while different values are obtained for optimum R^2 and ubRMSE. The maxima of the R^2 and NSE metrics corresponding to the optimal T show better contrast then the other metrics. It is important to note that the absolute values of the individual metrics differ regarding its applied normalisation. For example, both the RMSE and the bias are determined from the absolute differences in volumetric water content between the two SM series, and therefore the deviations are larger as their dynamic ranges become more unequal. R^2 and NSE are normalised to the average of the respective time series and therefore react most sensitively to their relative fluctuations.

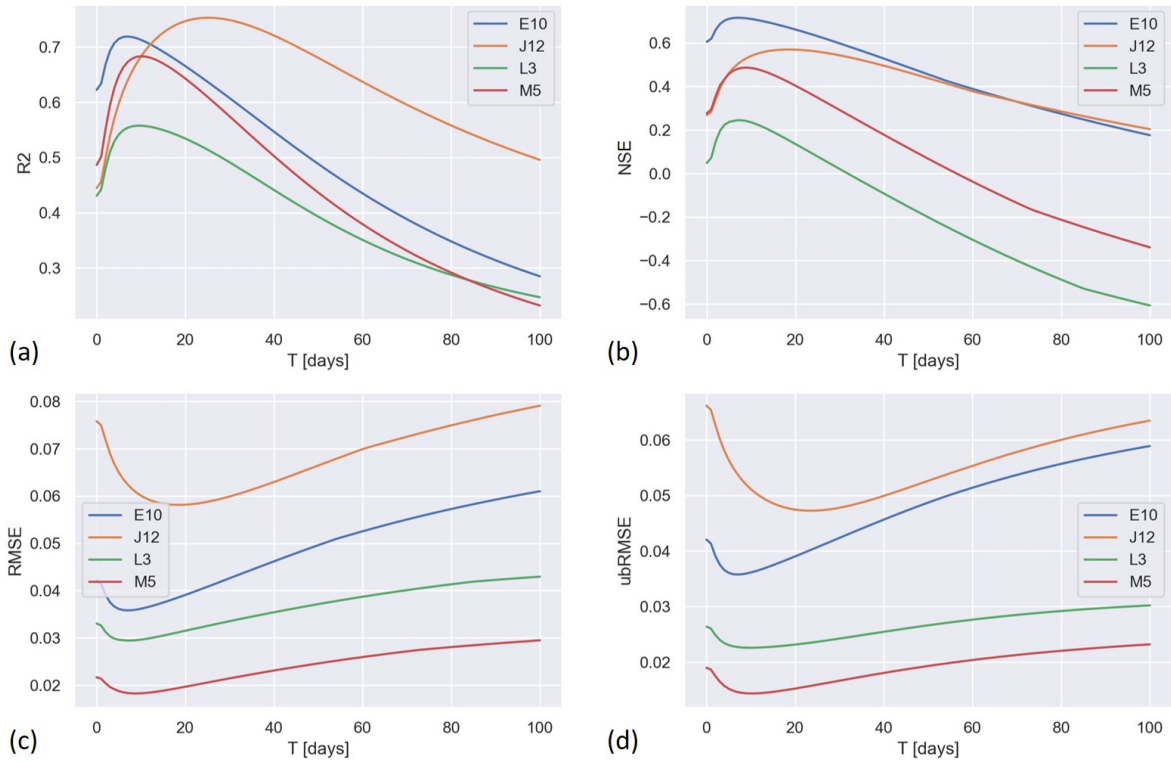

Figure 4.12: Validation metrics (**a**) R^2, (**b**) NSE, (**c**) RMSE, and (**d**) ubRMSE, computed between the SWI retrievals after applying an exponential filter to SMOS time series with a constant characteristic time length T varying between 0–100 days and the corresponding in-situ observations at 25 cm for the stations `E10`, `L3`, `J12`, and `M5` in the period from 2016–2018.

Figures 4.13a and 4.14a show the SMOS time series and corresponding SWI after applying the exponential filter with $T = 7$ days and $T = 24$ days after validation based on NSE and R^2 with the in-situ series at station `L3` at 25 cm and station `E10` at 50 cm, respectively. Figures 4.14b and 4.13b illustrate the PAW which is equal to the re-scaled SWI according to the in-situ dynamic range, respectively. The red dashed lines indicate the WP (lower bound), and the average between FC and TWC (upper bound) as a natural thresholds for the SM content. Regarding the determined SM range based on

]

Table 4.5: Optimal constant characteristic time length T corresponding to the optimal values of the validation metrics R^2, NSE, RMSE, and ubRMSE for the stations `E10`, `L3`, `J12`, and `M5` at 5, 25, and 50 cm in the period from 2016 to 2018.

Station	**Depth [cm]**	T **[d]**	$\mathbf{R^2}$	T **[d]**	**NSE**	T **[d]**	**RMSE** $[\mathbf{m^3\,m^{-3}}]$	T **[d]**	**ubRMSE** $[\mathbf{m^3\,m^{-3}}]$
	5	19	0.642	20	0.605	20	0.045	22	0.045
E10	25	7	0.719	7	0.716	7	0.036	7	0.036
	50	24	0.504	14	-0.722	14	0.064	25	0.035
	5	20	0.461	9	-0.26	9	0.049	22	0.033
L3	25	10	0.558	7	0.245	7	0.029	10	0.023
	50	26	0.535	12	0.018	12	0.017	6	0.012
	5	11	0.748	10	0.395	10	0.057	11	0.037
J12	25	25	0.753	18	0.57	18	0.058	23	0.047
	50	86	0.636	69	0.523	69	0.07	81	0.064
	5	6	0.765	6	0.522	6	0.036	6	0.025
M5	25	10	0.683	9	0.487	9	0.018	10	0.014
	50	31	0.404	19	-0.236	19	0.022	33	0.016

soil-physical properties, the variability of in-situ observations at 25 cm at `L3` (Figure 4.13 is in agreement, whereas in-situ observations at 50 cm at `E10` (Figure 4.14) show a large offset with respect to the defined boundaries. In the latter case, the SWI re-scaled based on soil-physical properties would not reflect the variability of the corresponding in-situ range, and the retrievals of subsurface SM would become inaccurate.

Season-Specific Time Length

So far, the exponential filter was applied to SMOS time series by means of a constant characteristic time length to find the global optimum value based on various validation metrics to yield the most accurate SWI estimate which overall matches the in-situ observations best. Seasonal variation of the response time between SMOS and in-situ observations – particularly high for the deficit period – suggesting that the time length can be also considered characteristic with regard to SM seasons. SWI retrievals based on the time length considered as constant along the entire period are compared to those determined by finding the optimal characteristic value individually for the respective sub-periods, which are separated by the onset of the subsequent SM season (i.e. mid-Feb/mid-Jun/Nov). In the first case, validation metrics are computed once again by comparing the time series segments of in-situ observations and SWI retrievals within each sub-period (as subsets of the three-year SWI obtained for a constant T). In the latter case, subsequent to the aforementioned application of the exponential filter to the SMOS time series (T between 0–100 days, $\Delta T = 1$ day), the optimal T is determined for the best most accurate SWI retrieval for the specific sub-period. Representative SM-season-specific time length is obtained by averaging the results of the sub-periods which correspond to the same SM

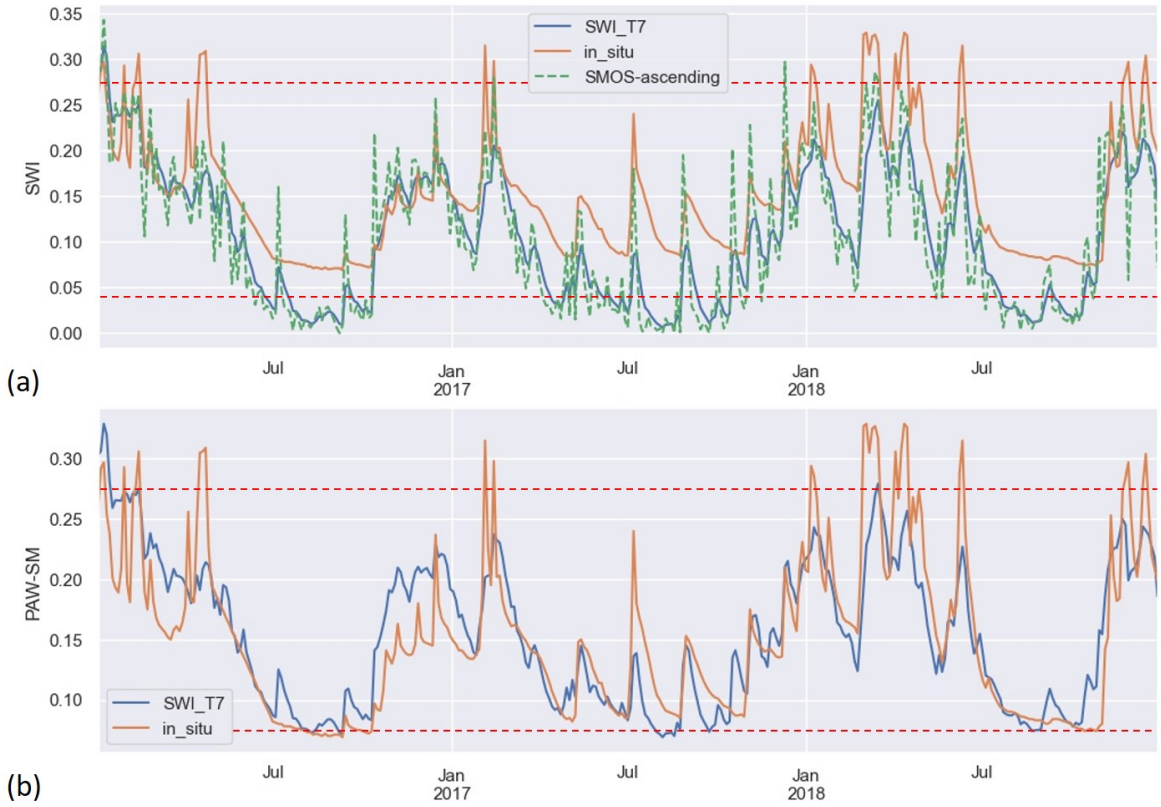

Figure 4.13: Comparison between the retrieved SWI for $T = 7$ days, obtained by maximizing NSE, and the corresponding in-situ observation at station `L3` at 25 cm. (**a**) SMOS, in-situ, and retrieved SWI series; (**b**) in-situ series and SWI retrievals, re-scaled according to the dynamic range of in-situ observations. In-situ observations are largely within the range spanned by the red dashed lines, which correspond to the lower and upper natural bounds of subsurface SM according to the WP and the average between the FC and the TWC, respectively.

season.

The results of the T obtained for each SM season and the differences in ΔR^2 between the two approaches, i.e. T optimized for each sub-period individually and T optimized once along the entire three-year period, are presented in Table 4.6. Similar to the findings in Table 4.4, the obtained values for T are widely situated between the mean and maximum estimates of the response time in the years 2016 and 2018. In addition, the representative time lengths of the deficit season are mostly longer than the optimal values for the recharge and utilization seasons. The retrieval accuracy improves overall with SM-season specific optimization of T, showing increasing R^2 between 0.05 up to almost 0.3 in the special case of station `E10` at 50 cm for the utilization period. Hereby, the SM season-specific optimal T of 5 days is much lower than the one using a constant T (24 days; see T for R^2 at station `E10` at 50 cm in Table 4.5), which is biased, and broadly representative of the deficit season.

Figure 4.14: Comparison between the retrieved SWI for $T = 24$ days, obtained by maximizing R^2, and the corresponding in-situ observation at station `E10` at 50 cm. (**a**) SMOS, in-situ, and retrieved SWI series; (**b**) in-situ series and SWI retrievals, re-scaled according to the dynamic range of in-situ observations. In-situ observations are outside the range spanned by the red dashed lines, which correspond to the lower and upper natural bounds of subsurface SM according to the WP and the average between the FC and the TWC, respectively. This justifies the re-scaling of SWI with respect to the dynamic range of available long-term in-situ observations.

4.5 Discussion

SM maps with regional and global coverage can only be achieved by using satellite-based sensors, which are commonly operated at the lower microwave spectrum (L-band). These sensors are directly sensitive to topsoil moisture, and subsurface SM – in particular at the root zone – can only be indirectly inferred. Among the aforementioned methods for obtaining subsurface SM based on process- or data-driven approaches, TSA techniques are useful for investigating how the areal satellite surface-sensitive are linked to in-situ profile observations at different depths. SM observations of the downscaled SMOS L4 product were related to in-situ time series from a suitable set of stations at the REMEDHUS network on the basis of a DTW method. DTW is a similarity method that takes into account spatial variability of non-linear, temporally distorted time series with the aim of quantifying the typical response time that reflects their transient SM dynamics. The approach was customized to obtain the time lag between their trend series – which is

Table 4.6: Representative SM-season-specific time length T for differences in R^2 for SWI retrievals obtained through sub-period optimization of T and optimization with constant T along the entire period from 2016 to 2018 regarding the stations `E10`, `L3`, `J12`, and `M5` at 5, 25, and 50 cm.

Station	**Depth**	**Recharge**		**Utilization**		**Deficit**	
	[cm]	T **[d]**	$\Delta\mathbf{R^2}$	T **[d]**	$\Delta\mathbf{R^2}$	T **[d]**	$\Delta\mathbf{R^2}$
	5	8	0.142	7	0.109	21	0.013
E10	25	6	0.132	5	0.037	21	0.135
	50	5	0.213	5	0.293	36	0.029
	5	9	0.151	10	0.168	17	0.02
L3	25	12	0.19	8	0.073	14	0.025
	50	16	0.15	7	0.168	26	0.078
	5	8	0.236	10	0.137	39	0.156
J12	25	11	0.317	9	0.145	33	0.182
	50	34	0.012	14	0.277	24	0.046
	5	7	0.081	6	0.079	17	0.047
M5	25	24	0.162	9	0.067	17	0.144
	50	36	0.117	31	0.024	30	0.275

assumed to be a dynamic quantity rather than a constant – describing the relationship of their common prominent features.

The focus was on assessing whether repetitive patterns of alignment and accumulation of time lag can be attributed to SM-related processes on the basis of additional information about climatic factors, soil properties and heterogeneity of land use among the stations of the studied SM network. Differences in the evolution of time lag could be referred to specific SM seasons recharge, utilization, and deficit, and variations due to the level of spatial representativity of land use between SMOS and in-situ observations. The results suggest that causality information about processes can be reflected in the time lag. In previous studies, the response time of subsurface SM observations to satellite time series were assumed to increase along the depth profile [Ceballos et al., 2005, Albergel et al., 2008, Brocca et al., 2011, González-Zamora et al., 2016]. However, during the main growing season of cereals, root-water uptake led to an inversion of the typical response time, showing longer time lag for shallow depths. Further investigation is required to quantify the observed phenomena. The semiarid REMEDHUS region investigated consists mainly of a seasonal continental climate with cultivated winter cereals. The scope of this work was not to quantify causality of targeted variables. To do so, the evolution of the time lag has to be evaluated regarding different climates, topographic characteristics and land covers to understand how dependencies and certain processes are eventually reflected in its local behaviour.

SM dynamics depend on atmospheric conditions, local soil properties, and the initial SM state. The availability of precipitation data is crucial to estimate both amount and timing of SM infiltration and to distinguish between rain events of different intensities. In case subsurface SM reaches values close to saturation or dry-end of the soil, the contri-

bution of atmospheric conditions is limited and the time lag becomes less representative. During the deficit season for example, the SM release towards the atmosphere through evaporation is particularly high. Consequently, SM in the topsoil increases in response to moderate-intense rainfall events, but water is not infiltrated into deeper layers and hence, SM dynamics at 50 cm are not captured in the satellite observations. After intensive recharge, water can be retained in the soil for weeks, and subsurface SM values reach their maximum close to saturation. Thus, even in cases of ongoing rains, no significant changes of subsurface SM are expected, and the time lag becomes insensitive to the recorded SM changes at the surface. The matching process between the time series was improved by separating the study period into sub-sequences by determining the dates of pronounced precipitation events, to which both time series are sensitive to. Conversely, wavelet transforms of the time series can be analyzed to relate the prominent features of the observations and to approximate representative sub-sequences. This approach could be used as an alternative to customization prior to DTW to improve the matching process by considering the local structural information of the observations.

The time lag evolution can be used to assess whether remotely-sensed SM is in agreement with the corresponding ground-truth acquisitions. Studies have shown that satellite SM showed a clear bias in both mean value and amplitude of fluctuations in comparison to ground-truth SM [Dorigo et al., 2015, González-Zamora et al., 2015, Colliander et al., 2017]. In-situ observations generally show a smaller dynamic range than satellite observations, due to limitation of intrinsic SM-related soil properties [Entin et al., 2000]. The more a pixel is spatially extended, the more constrained is the dynamic range of the area-averaged satellite observation. Biased values can have non-negligible seasonal variation [De Lannoy et al., 2007b]. Furthermore, penetration depth of satellite measurements is not constant, but depends on the attenuation of the signal due to changes in the SM content in the uppermost soil layers, and hence affects its validation [Monerris et al., 2006]. As a result, the choice of an appropriate metric should be based on the nature of the retrieved variables (dynamic range and fluctuations) including advantages and drawbacks for a particular application [Entekhabi et al., 2010b]. The time lag evolution provided in this work relies on the relative behaviour of the input series rather than on absolute values only and has the advantage of accounting for temporal shifts and non-stationary biases between time series.

In previous studies, estimates of the RZSM by applying an exponential filter to the remote sensing observations while optimising a depth-specific characteristic time length over a period of time showed good results [Wagner et al., 1999, Ceballos et al., 2005, Albergel et al., 2008, Brocca et al., 2011, Ford et al., 2014, González-Zamora et al., 2016]. However, in critical periods of sudden SM changes, the assumption of a constant time length may lead to oversmoothing of the estimated values depending on the weighting criteria of preceding SMOS measurements. The exponential filter was applied to the SMOS L4 time series – initially with a constant characteristic time length – and the inferred SWI was

validated against the multi-depth measurements. The results of the constant filter approach were compared with the cases where the characteristic time length was optimised according to the previously determined SM seasons. Similar to the estimated average seasonal lag between SM time series based on the DTW method, the optimal characteristic time length for the deficit season exhibited much higher values in comparison to the other seasons. The findings imply that knowledge of the climate factors, information on the presence of growing seasons, and the accompanied root-water uptake and the level of spatial representativity of the satellite observation to field scale are beneficial to infer subsurface SM more accurately. An upfront determined time lag, which is tailored to a corresponding target climate, can be utilized as a measure similar to the characteristic time length to improve performance in the inference of RZSM from satellite observations.

The DTW technique is computationally efficient with a complexity of $\mathcal{O}(N \cdot M)$ in space and time. In this study, spatial complexity is not an issue since satellite data is compared with point-scale in-situ observations. However, the technique becomes inefficient for long time series. Performance can be increased if a multilevel approach (Fast DTW) is considered, where a warping path is initially computed with a coarse approximation of the time series and eventually obtained on the basis of a finer sampled time series after refinement of the beforehand obtained result [Salvador and Chan, 2007]. This could be of special advantage for investigating time series with higher temporal resolution. Hereby, the time lag of finer sampled time series could help to interpret hydrogeophysical processes which take place in small temporal scale such as evapotranspiration and infiltration. An application of DTW to high-resolution time series can include short-term fluctuations like sub-daily meteorological events.

Part II

Sea Ice Segmentation and Parameter Retrieval

5 Remote Sensing of Sea Ice

This chapter is an introduction to remote sensing of sea ice. Sea ice is a complex environment which is subject to an annual cycle of melting and refreezing, leading to the formation of different types of sea ice distributed and observable at different spatial and temporal scales. The thermodynamic and dynamic processes of sea ice development and the relevant ice physical and radiometric properties that allow the characterization of sea ice from remote sensing observations are discussed in Section 5.1. The various remote sensing techniques for continuous monitoring of polar regions from space, including active and passive methods, are presented in 5.2. Common retrieval methods for estimating relevant sea ice parameters SIC and SIE, SIT, and for detecting melt ponds in summer are described in section 5.3. Also explained is the nomenclature standard for sea ice charts published by WMO, based on many years of effort by national services to summarize sea ice parameters into different stages of sea ice development.

5.1 Sea Ice Physics

5.1.1 Formation and Development of Sea ice

The freezing and melting cycle of sea ice can be divided into a series of stages, starting with the initial formation of the ice, consolidation, vertical and lateral growth, drift and deformation, and, finally, melting and desintegration. The freezing process is initiated at higher latitudes in the Arctic around mid-September. Then, the upper layer of relatively warm seawater is cooled down to below the freezing point of saline water, and fresh ice is formed by the continuous release of heat into the colder atmosphere. The way sea ice forms and thickens depends on the prevailing atmospheric and ocean conditions. The rate of thermodynamic growth of sea ice depends mainly on the air temperature, ice thickness, snow cover on the ice surface, and the amount of solar irradiation. Under calm ocean conditions new sea ice forms homogeneously into nilas, and subsequently grows into thin layer of young ice. Under turbulent conditions, more irregular pancake ice forms until it consolidates into a fully-covered area of sea ice, leading to larger variety of thin sea ice in the early development of sea ice. Images of the types of sea ice at different stages of development are given in Figure 5.1.

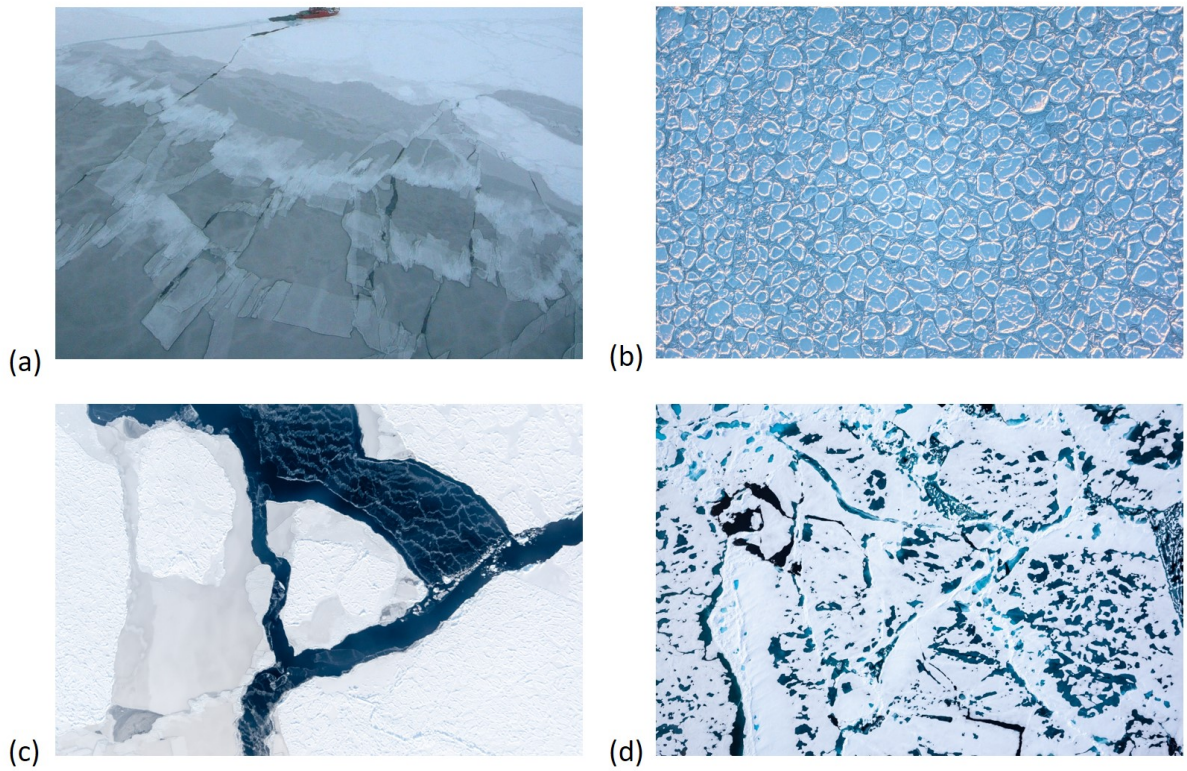

Figure 5.1: Sea ice types at different stages of development: (**a**) overlapping nilas; (**b**) Antarctic pancake ice; (**c**) opened lead between ice floes; (**d**) melt ponds on Arctic sea ice during summer (images downloaded from the NSIDC and AWI photo galleries under `https://nsidc.org/cryosphere/photo-gallery` and `https://www.awi.de/en/focus/sea-ice/sea-ice-photo-galleries`.

First-year ice (FYI) is then formed by vertical ice growth as water continues to freeze at the bottom of the ice layer. Around June, the melting period in the Arctic begins when the amount of absorbed solar radiation and air temperatures increase so that the ice surface begins to decay. On snow-covered surfaces, melt ponds start to form, and they subsequently expand in width and depth due to their relatively low albedo in comparison to the surrounding, still intact ice. Whereas most of the FYI is seasonal and vanishes in summer, the residual FYI that survives at least one summer melt period is referred to as old ice. According to the WMO sea ice nomenclature, old ice is also defined as second-year ice or multi-year ice (MYI) if it has survived exactly one summer or more than two summers, respectively. In the Arctic Ocean, the rate of expansion of sea ice and its ultimate extent largely depends on the distribution of the surrounding land masses, the weather system and ocean currents. Sea ice can be confined in the Arctic Ocean for up to 5 years, where it ages until it is eventually transported to lower latitudes by currents such as the transpolar drift stream (TDS). In contrast, in the Antarctic Ocean almost all sea ice drifts annually to lower latitudes and melts during the austral summer, so most of the sea ice present is FYI.

5.1.2 Physical and Radiometric Properties

An understanding of the physical and dielectric properties of sea ice is critical for radiation modelling and interpretation of remote sensing observations. Ice temperature influences all variables such as salinity, density, and the evolution of brine inclusions in the ice. Saline water gets initially entrapped as inclusions in the ice bulk during formation and successively desalinates as it ages, containing both more abundant and also substantially larger air bubbles. Density, brine volume fraction and salinity are lower for old ice. Sea ice properties also vary along the vertical profile and as sea ice thickens and ages, its physical and complex dielectric properties change. The older the ice becomes, the more its characteristics depend on weathering through aging and less on the historical heterogeneous processes of its original formation. Thus, with the exception of the uppermost layer and in the presence of snow, the physical properties are less affected by actual atmospheric conditions and can be better regarded as a function of the aging process. Years of intensive work have identified a set of typical values of key variables that serve as references for sea ice modelling.

Saline sea ice is a non-ideal dielectric, with non-zero conductivity due to its brine inclusions, which contain a small amount of free charges. Therefore, sea ice is an absorbing medium that looses energy through interaction with electromagnetic radiation and it is characterized by the dielectric constant $\epsilon = \epsilon' - i\,\epsilon''$. It can be represented as a complex number containing the permittivity ϵ' as the real part, and the loss factor ϵ'' as the imaginary part. The permittivity describes the part of the energy that propagates through the medium (reflection and transmission at interfaces). The loss factor is a function of the electrical conductivity and describes the energy attenuation due to dissipation of heat or scattering (absorption inside the material). Thus, dielectric properties (permittivity and loss) – together with surface roughness, ice thickness, and the temperature profile – determine the radiometric properties of the ice including microwave emission and scattering.

The dielectric properties of two media 1 and 2 can be described by their refraction indexes $n_{1,2}$. If radiation coming from medium 1 propagates towards medium 2, and the interface between them is perfectly flat, then the relationship between incidence angle Θ_1, and transmission angle Θ_2 is given by the ratio of the refractive indexes of the two media (Snell's law) as

$$\frac{\sin(\Theta_1)}{\sin(\Theta_2)} = \frac{n_2}{n_1}, \quad \text{with} \quad n_{1,2} = \sqrt{\epsilon_{1,2}} = \sqrt{\epsilon'_{1,2}} \tag{5.1}$$

The Sun's short wave radiation gets partly absorbed by the Earth's surface and re-emitted in form of long wave radiation. This natural thermal radiation impinging on a surface can either be absorbed, transmitted or reflected. Emissivity e is the ability of a material to emit energy as thermal radiation. If a material is in thermodynamic

equilibrium, it emits and absorbs the same amount of radiation, while the energy exchange due to transient processes is negligible. Thus, its absorptivity is equal to its emissivity, and emissivity and reflectivity R are related as $e = 1 - R$. The reflectivites for radiation at the boundary of a flat surface between medium 1 and 2 depend on the incidence angle Θ_i and polarization (vertical V or horizontal H), through the Fresnel Equations:

$$R_V = \left| \frac{n_1 \cos(\Theta_i) - \left(n_2 \sqrt{1 - \left(\frac{n_1 \sin(\Theta_i)}{n_2} \right)^2} \right)}{n_1 \cos(\Theta_i) + \left(n_2 \sqrt{1 - \left(\frac{n_1 \sin(\Theta_i)}{n_2} \right)^2} \right)} \right|^2 , \text{ and}$$

$$R_H = \left| \frac{\left(n_1 \sqrt{1 - \left(\frac{n_1 \sin(\Theta_i)}{n_2} \right)^2} \right) - n_2 \cos(\Theta_i)}{\left(n_1 \sqrt{1 - \left(\frac{n_1 \sin(\Theta_i)}{n_2} \right)^2} \right) + n_2 \cos(\Theta_i)} \right|^2 . \tag{5.2}$$

A blackbody perfectly absorbs and emits all incident energy with zero reflection. The total radiation P emitted by a blackbody at temperature T is given by the Stefan-Boltzmann law $P = \sigma A T^4$, where $\sigma = 5.670374\,\mathrm{W\,m^{-2}\,K^{-4}}$ is the Stefan-Boltzmann constant and A the area. The Planck's equation describes the radiation flux density distribution at frequency f and physical temperature T as

$$R(f) = \frac{P(f)}{A} = \frac{2\,h\,f^3}{c^2} \frac{1}{e^{h\,f/k_B\,T-1}}, \tag{5.3}$$

with the speed of light $c = 2.997925 \cdot 10^8$ m/s, Planck's constant $h = 6.626070 \cdot 10^{-34}$ Js, and the Boltzmann's constant $k_B = 1.380649 \cdot 10^{-23}$ J/K. The wavelength where the maximum amount of radiation is emitted by the Earth's surface with ~ 300 K average physical temperature is about 9.66 μm (~ 30 THz).

The parameters of interest – such as those representing the underlying physical composition of sea ice – cannot be measured directly with remote sensing instruments. Thus, indirect inferences are made by measuring other variables and knowing how they relate to the target parameters through sensitivity analysis, imposing requirements on both the dynamic range of the measured variable and its sensitivity to the target parameter for unambiguous determination. Passive microwave radiometry collects electromagnetic radiation in the microwave spectrum with frequencies between 1–300 GHz, for which Planck's equation can be approximated by the Rayleigh-Jean's equation

$$R(f) \approx \frac{2\,h\,k\,T\,f^2}{c^2}, \tag{5.4}$$

showing linear relationship between the radiation and the physical temperature. In addition, physical objects are imperfect blackbodies, and the emissivity is the ratio between the actually emitted radiation R_g, and the ideal blackbody radiation R_b, given by

$$e = \frac{R_g}{R_b} = \frac{T_B}{T}, \tag{5.5}$$

where T_B denotes the brightness temperature which is the key quantity measured by passive microwave radiometers. The emissivity contains the actual information about the physical composition of sea ice, whereas the physical temperature largely depends on external factors such as atmospheric forcing. In the microwave spectrum, T_B is as function of the emissivity and the physical temperature T, integrated over the radiating layers of the medium. At higher frequencies, small changes of T have much a larger effect on T_B than changes in sea ice composition and any inference about ice-physical properties based on radiometric properties are no longer possible.

Satellite observations measure T_B at the top of the atmosphere as the net emitted radiation traveling upward through the atmosphere. Apart from the surface emission $\epsilon\,T$, the observed radiation also comprises the reflected space radiation T_{sp}, the upwelling radiation T_{up}, and the surface-reflected downwelling radiation $T_{r,down}$ from the atmosphere. The radiative transfer equation is given by

$$T_B = \epsilon\,T\,e^{-\tau} + T_{up} + T_{r,down}\,(1-\epsilon)\,e^{-\tau} + (1-\epsilon)\,T_{sp}\,e^{-2\tau}, \tag{5.6}$$

with τ being the total atmospheric opacity which attenuates the radiation. Sea ice properties are observed at microwave frequencies ($< 30\,\mathrm{GHz}$) where the atmosphere is fairly transparent ($\tau \to 0$) and continuous monitoring is possible independent of daylight. To reduce the influence of atmospheric composition, corrections are implemented in the RTM from profile information on temperature, water vapor and cloud liquid water to estimate the effective bottom-of-the-atmosphere radiation.

Since ice crystals radiate more energy than water molecules, the emissivity of sea ice is higher than that of water, which easily allows to distinguish open water (OW) from sea ice. The dynamic range of the T_B observations allows us to further discriminate different types of sea ice, and infer continuous sea ice parameters such as snow and SIT in a type-specific manner. Extinction of the radiation in a medium is caused by absorption and scattering. The penetration depth is defined as the representative depth where radiation is attenuated by the factor of 1/e, referring to the range within which observed radiometric properties actually contain information about the physical composition. It varies with microwave frequency, salinity and surface wetness – showing differences for water,

among ice types and snow-covered sea ice. In the lower microwave spectrum ($< 20\,\mathrm{GHz}$), scattering processes are less relevant for the energy loss, and the penetration depth is given by

$$d_P = \frac{c\sqrt{\epsilon'}}{2f\pi\epsilon''}, \tag{5.7}$$

which is inversely proportional to frequency and the loss factor ϵ''. The permittivity ϵ' is largely frequency independent, while ϵ'' depends on both temperature and frequency, and model simulation show substantial differences in the estimation of ϵ''. The penetration depth into FYI is limited by number of brine inclusions. In comparison, less salty MYI has larger penetration depth than FYI. However, especially at large microwave frequencies scattering phenomena and surface roughness cannot be neglected. Because of high conductivity and associated large loss factor, the penetration depth into saline and freshwater is in the order of mm. Thus, although sea ice is easy to discriminate from OW, it is difficult to distinguish from ice with a wet surface or with a small layer of water on top. As a consequence, microwave penetration into sea ice from radiometry measurements enables the derivation of some sea ice properties that allow to discriminate different sea ice types, and to estimate the thickness of thin sea ice.

5.1.3 Sea Ice Across Spatial and Temporal Scales

Sea ice contains a multi-scale structure and can be parametrized at different spatial and temporal scales. The importance of providing appropriate sea ice parameters at specific scales based on sea ice properties is suggested by their applicability and the structure of interest being studied, and whether these parameters are used operationally or scientifically. For instance, navigation through the ice requires near-real time information on local sea ice conditions (SIC and SIT) at a small scale ($\sim$100 m). Melt ponds can be parametrized by geometry, depth and size, and additionally by its number and distribution. However, knowledge on the sea ice conditions at small scale cannot be provided due to the relatively large footprint from satellites. Satellite observations – based on passive microwave radiometry or SAR – are usually indirectly related to the sea ice parameters. In case parameters cannot be determined due to the limited spatial resolution, they need to be estimated from previous observations or auxiliary data using prediction models. In contrast to the study of small-scale features such as sea ice deformation, the precise timing of measurements is less important for large-scale features of sea ice, and the application purpose of studying regional weather phenomena or global climate monitoring requires SIT estimates from daily imagery at a larger scale of $\sim$10 km. Hereby, different sea ice types are mixed and the discrimination of areas with uniform ice conditions becomes ambiguous. Structures of ice floes and leads appear to be homogeneous due to the big difference in scales and the features are no longer recognizable. Shape and distribution of

melt ponds are no longer discernible, but can be expressed by the fraction of melt ponds to the total area of an observed cell (MPF). At 10-km scale, SIC is a continuous variable between 0 and 1, and apart from areas at the ice margin, distributions tend to peak near the bounds. At smaller scales, SIC is expected to only have discrete values of 0 and 100 %, which makes a representation of sea ice conditions by SIC at high resolution problematic.

5.1.4 Changes in Sea Ice Thickness Distribution

Sea ice is continuously changing due to both thermodynamic and dynamic processes. A key objective in sea ice modelling is the prediction of the evolution of SIT distribution in space and time [Thorndike et al., 1975]. The distribution can be defined and analyzed at a characteristic length scale similar to the resolution of polar-orbiting satellites acquiring data in the microwave spectrum (∼10–50 km). The large-scale consequences of the small-scale processes need to be understood to relate satellite observations to sea ice properties. Most of the physical properties of the sea ice bulk depend upon SIT and its changes. Sea ice undergoes an annual thermodynamic cycle of melting and re-freezing depending on the shortwave radiation from the sun which is a function of time and latitude, the thermal conditions of the ocean and the atmosphere, and the presence of already existing sea ice. An important characteristic of sea ice is that its rates of growth and melt, and lateral transport depend on the actual ice thickness. Thinner ice both grows and melts faster because heat exchange is more feasible due to a higher vertical temperature gradient within the ice column, and thinner ice floes are also more prone to break under stress. This is why accurate SIT prediction models, relying on knowledge about changes in SIT require the consideration of the distribution of SIT rather than assuming a uniform distribution.

Changes in SIT can be described by the ice thickness distribution equation [Thorndike et al., 1975, Toppaladoddi and Wettlaufer, 2015, **?**]

$$\partial_t p = -\nabla \cdot (p\,\mathbf{v}) + \Psi - \partial_d\,(g\,p)\,, \tag{5.8}$$

consisting of the three main components:

(i) Advection into and out of an observed area through horizontal motion of sea ice,

(ii) Mechanical opening of leads and the formation of pressure ridges, and

(iii) Thermodynamic growth and melt at the upper and lower sea ice boundaries.

The distribution of thickness h is described by the probability density function $p = p(h, \mathbf{x}, t)$, which changes with space $\mathbf{x}$ and time t. It depends on the ocean and atmosphere-driven velocity $\mathbf{v}$ of the ice pack, a so called redistribution function Ψ which summarizes the deformation processes, and a growth rate function g, describing the balance through thermodynamic growth and melt on the bottom and the top of sea ice caused by atmosphere-ocean heat flux and shortwave radiation. Therefore, g varies strongly with

thickness and season. The cumulative probability function is obtained by integration of p over all thickness intervals smaller than h, and can be approximated by it cumulative sum as

$$\int_0^{d_{max}} p(h, \mathbf{x}, t)\, dh \approx \sum_{l=1}^{N} p(h_l, \mathbf{x}, t)\, \Delta h_i \approx 1, \tag{5.9}$$

where the sum of p over all thickness intervals is 1. N is the total number of thickness intervals with irregular width $\Delta h_i = (h_i - h_{i-1})$, $h_{l=0} = 0$ refers to OW and $h_N = h_{max}$ to a maximum observed thickness, which can vary depending on the considered length scale and the sensor sensitivity. The term $p\,\Delta h_i$ is the fraction of an observed area covered by thickness within the interval h_i and $h_i + \Delta h_i$. Sea ice analysts assign the most plausible SoD category to a region according to the predominant SIT range and the historical evolution of the sea ice. Table 5.1 shows higher-level SoD categories and associated SIT ranges, which are determined based on the analyst's capability of discriminating SoD based on the satellite data. In total only a few thickness intervals are defined, and more categories are assigned to thinner ice due to the higher level of discrimination based on the spaceborne observations (e.g. Sentinel-1 SAR and AMSR2 T_B).

Table 5.1: SoD and associated SIT intervals (Δh) according to the WMO Sea Ice Nomenclature [WMO, 2014].

SoD	Nilas	Young ice	Thin FYI	Medium FYI	Thick FYI	Old ice
Δh [cm]	0–10	10–30	30–70	70 - 120	>120	>120

The aforementioned theoretical considerations represented in the ice thickness distribution equation 5.8 including the components (i)–(iii) raise some key requirements for the implementation of a consistent SIT prediction model. The sea ice pack can move at a non-negligible rate of several kilometers per day, which is in the order of the resolution of temporally-composed satellite data sets. Therefore, an exclusively spatial consideration of present-time features – as done in common inference algorithms – does not capture the essential history of sea ice dynamics. Information on the development of sea ice cannot be retrieved purely statistically from the time series in a pixel-based consideration either. Ice drift causes neighboring pixels of observations to be correlated in both space and time. Especially at the boundaries where sharp contrasts between different ice types can occur, SIT estimation may contain large errors. Thus, a spatio-temporal approach is necessary to create a model which fully integrates the temporal evolution of satellite data embedded in the geo-statistical context. Current operational sea ice charts are based on the manual or semi-automatic determination of the fraction of sea ice with a specific SoD to a region. These products rely on long-standing experience to obtain significant and temporally stable classes, which include knowledge about growth and advection phenonmena, and annual variability. Thus, a reliable automated segmentation of the polar region requires physically meaningful classes with multiple-year consistency, similar to those assigned by trained sea ice analysts as recurring SoD and associated SIT intervals.

A probabilistic approach enables to include the distribution of SIT for each pixel rather than assigning a single value by assuming mostly homogeneous conditions, which is particularly important with regard to SIT-dependent sea ice growth. It should be pointed out that information on the thickness at small-scale deformations is often not sufficiently captured in the satellite data. Current approaches aim to understand changes of the distribution of SIT through recognition and tracking of the major features like pressure ridges and leads, and they still lack the accuracy and capability to generate an automated workflow. Knowledge about the redistribution of sea ice for a particular SoD can be retrieved from in-situ or airborne observations, which are capable of revealing the small-scale distribution of SIT. This may help to parametrize the deformation behavior to accounts for missing information beyond the observable range of satellite measurements and to apply necessary corrections to current sea ice models.

5.2 Satellite Observations over Polar Areas

Spaceborne remote sensing is the only technique to continuously observe the polar regions in order to allow operational sea ice monitoring. Satellite observations of the polar regions at the operational level have been available since the late 1970s. Data in the electromagnetic spectrum are collected at different frequencies within the three major ranges – microwave ($\sim$ 1–300 GHz), infrared ($\sim$ 300 GHz to $\sim$ 400 THz), and visible optical ($\sim$ 400–700 THz) – by recording the reflected, scattered, and emitted radiation. Different types of platforms and instruments – either passive or active – are providing complementary information about sea ice at different temporal and spatial scales with resolutions from tens of meters to tens of kilometers. Most products for sea ice applications are based on data from a few selected satellite missions – mainly passive and active sensors operating in the microwave spectrum, because they are insensitive to clouds and illumination conditions. Passive microwave radiometry acquire the emitted radiation, while active sensors measure the backscattered signal. Sea ice parameters can be determined using data from a single or from multiple sensors, such as SIC and SIE from coarser passive observations, or ice drift from fine SAR imagery.

5.2.1 Passive Remote Sensing

Passive remote sensing instruments operating in the visible optical and near-infrared range collect the solar radiation reflected of the Earth's surface, whereas thermal infrared and microwave radiometers measure the naturally emitted electromagnetic radiation.

Visible and Near-Infrared Radiometry

Optical sensors mostly cover the visible range ($\sim$ 400–700 THz), and are sensitive to the Earth's surface albedo. Due to their contrast in color, they can distinguish between OW,

melt ponds, and sea ice. However, because they record sunlight reflected from the surface, images can be obtained during the day, and they can only be used when the sky is clear. Thus, optical imagery is not appropriate for operational sea ice products, but commonly serve as auxiliary information and in data validation when available. Sensors in the thermal infrared range ($\sim$ 20–400 THz) acquire thermal emission and are used to sense the physical temperature and can allow the discrimination of different surfaces of sea ice, and the surrounding warmer ocean with temperatures slightly above the freezing point. Both the optical and infrared bands are affected by the presence of clouds, which prevent the satellites from detecting the radiation emitted by the surface of the Earth. Besides that, observations in the thermal infrared have limited capability to unambiguously discriminate between water and sea ice, because both thin sea ice during formation and melting ice show temperatures close to the freezing point of saline water.

Microwave Radiometry

Microwave radiometry is more suitable for continuous monitoring, since it is independent of daylight and at the lower microwave frequencies it is largely unaffected by atmospheric conditions – except for specific bands, where the transmittivity of radiation through the atmosphere is limited due to absorption or scattering by certain gases, aerosols, or hydrometeors. It determines the emitted amount of radiation sensitive to the physical composition of crystalline sea ice structure and water molecules, allowing to effectively discriminate radiometrically warmer sea ice from the radiometrically colder ocean. However, the energy level of radiation in the microwave spectrum is rather low, requiring the integration of measurements over a large area. The size of the antenna footprint defines the spatial resolution and it depends on the wavelength of the instrument. For frequencies in the upper microwave spectrum, the footprint is smaller whereas the signal is more affected by the water vapour contained in the atmosphere. This lowers the overall resolution of images and limits the discrimination of small-scale objects. Therefore, a trade-off has to be found to appropriately resolve small signatures, while maintaining sufficient sensitivity range of the measurements to the actual sea ice properties.

Current passive microwave instruments acquire daily images of polar regions and the data continuity of records over the last 40 years enable the monitoring of long-term trends of sea ice parameters. There are only few satellite missions available that are suitable for providing sufficient coverage to retrieve SIT at polar scale. Both NASA's SMAP and ESA's SMOS missions are carrying a radiometer operating at L-band (1.4 GHz), whereas the AMSR2 collects T_B at multiple microwave frequencies from 6.9–89 GHz. The upcoming CIMR mission, which is expected to be launched in 2028 – observing bands from 1.4–36.5 GHz – is intended to replace the SMOS and SMAP missions and provide continuous data collection. One of the main objectives of the CIMR is to monitor the polar regions with at least daily revisit [Kilic et al., 2018, Donlon et al., 2019]. The

FSSCat mission carried the first L-band radiometer onboard a CubeSat for sea ice and SM monitoring. In addition to these satellite missions, CubeSats can also make an important contribution to the continuous monitoring of the polar regions, and data can be utilized to fill capacity gaps. In the following, the technical details of the satellite missions that serve as radiometric data basis for the determination of sea ice parameters, and which are used in this work, are presented.

The AMSR2 onboard the Japan Aerospace Exploration Agency's (JAXA) Global Change Observation Mission 1st – Water 'SHIZUKU' (GCOM-W1) spacecraft was launched on May 18, 2012. The mission was designed for global, long-term observation of ECV and geophysical parameters including sea surface temperature, wind speed, precipitation, SIC, snow depth, soil moisture, vegetation water content, atmospheric water vapor and cloud liquid. It is located in near-polar orbit, at an altitude of 700 km, and has twice a day temporal coverage (ascending and descending phase) of more than 99 % of the Earth's surface every 2 days – allowing daily revisit of the polar regions above 70° latitude. Similar to its predecessor missions AMSR and AMSR-E, the follow-on instrument AMSR2 is a dual-polarized, conical scanning, passive microwave radiometer with a sensor swath width of 1450 km. AMSR2 measures microwave emissions from the Earth's surface and the atmosphere at an incidence angle of 55°, and provides multi-frequency T_B observations at vertical and horizontal polarization.

The spatial resolution depends on the Instantaneous Field Of View (IFOV), which is the angular cone of visibility determining the area of the Earth‘s surface (resolution cell), visible from a particular sensor platform altitude at a particular moment. The IFOVs of the different AMSR2 channels vary substantially in size – with smaller values at higher frequencies. For more accurate geophysical parameter retrieval, the T_Bs need to be remapped to the footprint of a low-frequency channel. A unified target IFOV is obtained by computing the weighted sum after the application of smoothing factors to the different high-resolution footprints from the higher frequency channels [Maeda et al., 2015]. The specification of the 12 channels in terms of frequency, ground resolution and sensitivity to specific geophysical parameters are summarized in table 5.2. Because of the small footprint of the 89 GHz channels, two scans (A and B) are combined to cover the gaps in between them. JAXA provides a modified L1R product containing the resampled T_Bs. Regarding polar regions, the NSIDC and the University of Bremen provide products at several processing levels based on AMSR2 data such as SIC, sea ice motion, and snow water equivalent.

Table 5.2: AMSR2 channel specifications including frequency at vertical (V) and horizontal (H) polarization, ground resolution corresponding to the -3 dB ellipse diameters of the beam width (cross-track x along-track), and geophysical parameters based on the relative sensitivity of T_B observations.

Frequency [GHz]	Resolution [km]	Geophysical parameters
6.925 V,H	35 x 62	Soil moisture, sea surface temperature
10.65 V,H	24 x 42	soil moisture
18.7 V,H	14 x 22	SIC, snow depth, precipitation
23.8 V,H	15 x 26	Water vapor
36.5 V,H	7 x 12	SIC, snow depth, wind speed, cloud liquid vapor
89.0 A/B V,H	3 x 5	SIC, precipitation

The CIMR mission (Sentinel 11) is one of the three future polar EU High Priority Copernicus Missions from ESA with a passive microwave sensor payload. It is conceived to collect T_B at the microwave frequencies 1.41, 6.9, 10.65, 18.7, and 36.5 GHz at an incidence angle of 55° with full coverage of the polar regions, i.e. no polar observation hole, and sub-daily revisit. It was designed as a follow-on mission of SMOS, SMAP, and AMSR2, with improved capability to retrieve sea ice parameters including SIC, thin SIT, snow depth, sea ice drift velocity, ice types, and surface temperature over the polar ice-covered oceans with increased accuracy and spatial resolution [Kilic et al., 2018]. Due to atmospheric effects, high-resolution AMSR2 observations at 89 GHz are the main error source in current in SIC retrieval methods. CIMR's larger antenna reflector (diameter > 7 m) will provide a higher spatial resolution for all low-frequency channels. These channels have the advantage of being capable of replacing high-frequency observations, and provide high-resolution sea ice parameters (in particular SIC) with high accuracy at all weathers [Scarlat et al., 2020]. Operational sea ice products suffer from accuracy losses due to sea ice drift and changing weather phenomena, and synergy of multi-source observations is challenging because instrument footprints show temporal and spatial mismatches.

5.2.2 Active Remote Sensing

Active instruments emit radiation to gain information about the physical properties by evaluating the energy of the signal reflected back to the sensor (backscattering) after interaction with the Earth's surface. Active sensors can be separated into microwave-based radars (radio detection and ranging), and optical laser-based lidars (light detection and ranging).

Scatterometers receive the back-scattered energy of the Earth's surface with a similar resolution to that of passive radiometry (10-km scale). They typically operate in the lower microwave spectrum at C- or Ku-band (4–8 GHz and 12–18 GHz, respectively), where they are sensitive to surface roughness, and provide insight into the composition of sea ice and snow through volume scattering. Instruments such as ASCAT are mainly

utilized to measure the wind-induced roughness in ocean waves to retrieve wind speed and direction.

Imaging radars such as SAR provide detailed high-resolution images by using the relative motion of the antenna over an observed region. The movement of the antenna creates an aperture equivalent to a large physical antenna that cannot be deployed in space due to its size. Images are created by illuminating a target area with successively transmitted pulses, receiving their reflection, and recording the duration of the echo window – related to the swath width. The position of the antenna on-board the moving satellite changes relatively to the observed area over time. SAR can be used in different scanning modes, with different transmitter and receiver polarizations, resolutions and swath widths. ESA's Sentinel-1 mission, launched in April 2014, is composed of two polar-orbiting satellites, Sentinel-1A and Sentinel-1B. They operate at C-band (5.405 GHz), and data are collected in ascending and descending orbit direction independent of daylight under all weather conditions. SAR systems are considered the most important data source for monitoring and mapping sea ice and in terms of the analysis of small-scale features such as ridges and leads.

In radar altimetry, pulses are sent to the surface and the distance between the satellite and the object can be determined from the two-way travel time. Then, the elevation of an object is determined with respect to a known reference, such as sea ice freeboard (Fb), which is the height of sea ice above the reference sea level. Spaceborne radar altimeters such as ESA's CryoSat-2 (CS2) mission, launched in 2010, are specialized to monitor the thickness of land and see ice through estimating the elevation of ice sheets and Fb, which in turn is used to infer SIT [Wingham et al., 2006]. Hereby, information about the ice thickness d_I is contained in the Fb measurements d_{Fb} by following Archimedes' principle of buoyancy

$$SIT_I = \frac{\rho_W \, d_{Fb} + \rho_S \, d_S}{\rho_W - \rho_I}, \tag{5.10}$$

where a snow column with thickness d_S and density ρ_S on top of sea ice with density ρ_I are partially immersed in water with density ρ_W. This equation is valid for radar altimeters, which operate in the microwave spectrum and can penetrate snow to some degree to obtain the Fb. In contrast, laser-based lidars are only surface sensitive and measure the total Fb of snow and ice. Therefore, they provide complementary measurements that are used, for example, to estimate snow depth on ice.

Laser altimeters use laser pulses to measure the distance between the instrument and the surface of the target. Due to the limited penetration depth of the optical signal into the ice, data can be used to provide accurate maps of ice-surface topography. NASA's Ice, Cloud, and land Elevation Satellite (ICESAT) mission – operating from 2003 to 2009 – acquired the first large-scale measurements of sea-ice Fb based on laser altimetry to infer SIT of the Arctic. The follow-up ICESat-2 mission, launched in 2018, uses laser pulses

to detect single photons to produce detailed maps of the Earth's surface and its changes, such as those observed in the ice sheets of Antarctica and Greenland.

5.3 Sea Ice Parameter Retrieval

5.3.1 Sea Ice Concentration and Extent

Satellite-based maps of SIC have been generated since 1979 starting with the launch of the SMMR and follow-on missions carrying sensors such as the SSM/I, the SSMIS, and the AMSR2. Common algorithms rely on the differences between radiometry data at different polarization and frequencies, while they aim to reduce effects due to the physical temperature and atmospheric losses. The choice of the frequency to achieve a high sensitivity range to distinguish different ice types and OW is then a compromise. For lower frequencies ($< 10\,\mathrm{GHz}$), higher penetration depth may lead to incorrectly assigning thin sea ice as low SIC. If the frequency is much higher ($> 50\,\mathrm{GHz}$), the penetration depth is too shallow to distinguish between different ice types, and in addition, observations are more affected by atmospheric composition. Comparing observations in the intermediate frequency range allows us to distinguish between OW, FYI and MYI due to the different microwave signatures – for example, volume scattering is stronger at higher frequencies. Thus, most algorithms are based on the contrast between T_B observations at the frequencies $\sim 19\,\mathrm{GHz}$ and $\sim 37\,\mathrm{GHz}$ [Parkinson et al., 1999, Comiso and Nishio, 2008, Lavergne et al., 2019].

Current methods used by the US NSIDC to provide SIC are obtained using passive microwave observations based on the NASA Team-2 (NT2) algorithm or the Bootstrap algorithm [Cavalieri et al., 1984, Comiso, 1995, Cavalieri et al., 1997, Markus and Cavalieri, 2000, Comiso and Nishio, 2008, Markus and Cavalieri, 2009]. The NT2 algorithm takes advantage of the fact that the T_Bs at horizontal (H) and vertical (V) polarization differ significantly between the observations at 19 and 37 GHz with respect to different ice types. It is based on the PR and gradient ratio (GR), which are computed from observations at 18V, 18H, and 36V and is defined as follows:

$$\mathrm{PR} = \frac{T_{B\,(18V)} - T_{B\,(18H)}}{T_{B\,(18V)} + T_{B\,(18H)}} \quad \text{and} \quad \mathrm{GR} = \frac{T_{B\,(36V)} - T_{B\,(18V)}}{T_{B\,(36V)} + T_{B\,(18V)}}. \tag{5.11}$$

GR and PR span a feature space with data points clustering around surface types related to OW, FYI, and MYI. The typical values for the three different types define tie-points, which form a unique set for each hemisphere (N, S) and sensor used to retrieve SIC in the final product. A weather filter is implemented based on GR observations between 18 and 22 GHz at vertical polarization, but tends to misclassify grid cells with SIC values below 15 % as OW.

The Bootstrap algorithm analyzes the scatter plots of observed data points in the

marginal T_B feature spaces with regard to contrasts in a comparison in frequency mode between 18V and 36V, and polarization mode between 36V and 36H, respectively. The frequency mode is used to estimate SIC along the sea ice margin, because the contrast between OW and sea ice is more pronounced. The positions in feature space corresponding to OW and sea ice with a concentration of 100 % are determined as tie points, respectively. Hereby, observations of OW are largely distributed around a point, while observations representing pixels that are completely covered with ice – but different ice types – are arranged along a line. The SIC between 0 and 100 % is obtained by interpolation. Unlike the NT2 algorithm where the tie-points are fixed, in the Bootstrap algorithm, the calculated tie-points to distinguish between OW and sea ice and ultimately to estimate SIC, are dynamic, i.e., they change daily, and are different for each hemisphere. The polarization mode is used to obtain more accurate estimates for higher SIC within the ice edge, assuming that the air column is dryer above areas covered with sea ice, and measurements are therefore influenced by the atmosphere, while observations at 37 GHz have higher spatial resolution. Further methods exploit the contrasts of similar T_B observations as the Bootstrap algorithm. The Bristol algorithm overcomes possible discontinuities between low and high SIC by evaluating clusters of data points in the three-dimensional scatter plot (between 18V, 36V, and 36H) and estimating SIC through performing a principal component analysis.

Since the NT2 algorithm uses the T_B observations, it is less affected by changes in surface temperature than the bootstrap algorithm. However, the ratios PR and GR are sensitive to the presence of snow and SIC of thin sea ice is underestimated due the low salinity. The Bootstrap algorithm shows the opposite effect, it is less affected by the presence of snow or thin ice but depends on the seasonal variation of surface temperature. Both algorithms are cluster-based methods; uncertainties may be introduced near the threshold between low-concentrated ice and OW and between different ice types. The SIC is underestimated in areas where sea ice is younger and thinner. This is not only visible at lower frequencies due to a higher penetration depths, but also at higher microwave frequencies because younger and thinner ice also has overall smoother surface conditions and higher salinity. During summer periods, algorithms are unable to separate melt ponds and OW, because the emitted radiation dissipates already at the water surface, and sea ice below melt ponds is invisible at microwave frequencies.

One ongoing challenge in common SIC algorithms is the erroneous assignment of wind-roughened ocean as sea ice. Atmospheric contamination which often results in spurious ice can be corrected using a weather filter or data from Numerical Weather Prediction, but it often removes low-concentrated ice. This leads to high uncertainties of concentrations below 15 %. In this range estimations are not reliable, and are usually removed from operational products. Both the generally large footprint of satellite passive observations and the potential footprint mismatch effect by combining observations at different frequencies makes accurate detection of the sea ice margin difficult. Particularly during

freeze-up when snow on FYI can be present, the variability of the microwave signature of snow dominates over that of the ice, which complicates accurate discrimination. Combine microwave observations at different frequencies and polarizations to reduce the effect of the physical temperature of the ice, increasing the sensitivity for reliable ice-water discrimination.

The convention for determining the extent is that the total area is the sum of all individual grid cells or pixels with a concentration greater than 15 %. After applying atmospheric correction, higher uncertainties in the resulting emissivities involve a risk of confusing water- and ice-covered surfaces, and below this threshold, rough ocean is sometimes misclassified as false ice. Also, this assumption results in more accurate estimations of sea ice extent in summer, when the surface of sea ice is partially covered by melt ponds. Pixels that contain ponded ice are then correctly classified as sea ice, which prevents underestimation of the extend by doing the integral sum of the individual concentration of all pixels. Except for areas at the edge of the sea ice, SIC values over the ocean are mostly close to 0, and over the sea ice around 100 %. This trend is even more pronounced in high-resolution measurements, because the smaller an observed grid cell is, the fewer pixels comprise the sea ice edge, and the definition of the SIC as a continuous variable only applies to observations with sufficiently low resolution. Thus, models to retrieve SIC or that are based on SIC, require consideration whether SIC should be treated as a continuous or categorical parameter by taking into account the spatial resolution.

5.3.2 Melt Ponds

The penetration depth of microwave radiometers into ice at frequencies above 5 GHz is on the order of a few mm to tens of cm considering sea ice under wet conditions to dry non-saline MYI, respectively. Water on top of the ice cannot be distinguished from sea water based on the radiometric properties. Thus, current SIC estimates exclusively reflect the two-dimensional surface, and leave out necessary information about sea ice conditions, which are in turn directly related to the surface. Especially in Arctic summer, sea ice is considered a heterogeneous medium consisting of various surface structures such as melt ponds and slushes, composed of wet snow and sea ice. Melt ponds need to be monitored because they influence the albedo and therefore have consequences on the overall melting process in summer. An example of ponded ice is given in Figure 5.1d. Melt ponds occur at multiple scales and are difficult to detect from low-resolution images. A melt pond cycle from its origin to re-freeze up can be divided into discrete stages [Eicken et al., 2002]. They start to form on top of the snow and sea ice covering up to half of the sea ice area in the end of summer, leading to substantial underestimation of SIC products derived from microwave radiometry.

A more specified distinction between fractions of intact sea ice, melt ponds, and closed sea water is required to eliminate ambiguities in models and retrieval algorithms which are

build on these estimates. High-resolution SAR images can be used to distinguish between different types of sea ice – including MPF under certain conditions [Li et al., 2017] – by evaluating backscatter signatures that respond to differences in surface roughness. The intensity of the back-scattered signal is variable which allows to detect different surface types such as deformations, leads, and melt ponds, if sufficient contrast between sea ice and surface water is given. It also depends on the incidence angle which makes robust and automatic discrimination particularly challenging, but is beneficial when combining with auxiliary data in the visible spectrum (such as Sentinel-2) in a manual classification.

5.3.3 Sea Ice Thickness

Sea ice thickness at polar scale can be derived from satellite observations using direct and indirect methods, which have different sensitivities to the target parameter. First, SIT can be directly computed from Fb measurements using radar altimetry. Several approaches have been implemented to provide maps of Arctic SIT from CS2 altimetry data [Ricker et al., 2014, Kurtz and Harbeck, 2017, Tilling et al., 2018]. Second, thin SIT can be indirectly retrieved from passive observations at the low-microwave spectrum on the basis of RTM. The penetration depth of T_B observations highly depends on the sea ice properties such as salinity, density and the physical temperature. Temperature and salinity differ among sea ice types, and vary both seasonally, and along the depth profile. Thus, L-band radiometry based SIT retrievals are in principle only reliable up to about 0.6 m depth.

Several methods have been developed to estimate the distribution of thin SIT at Arctic scale while using SMOS T_B data at multiple incidence angles and polarizations [Kaleschke et al., 2012, Gupta et al., 2019]. An approach based on the combination of a thermodynamic model, and a RTM was used to infer SIT from variations in the physical properties of ice, including temperature and salinity, and to further extend the maximum sensitivity range of retrievals [Tian-Kunze et al., 2014, Kaleschke et al., 2016]. T_B polarisation differences were combined in growth models, together with empirical assumptions about sea ice properties [Huntemann et al., 2014]. A thin SIT product was developed based on data from the SMOS and SMAP missions [Paţilea et al., 2019]. In addition, SMOS and CS2 observations were merged according to their sensitivity ranges and uncertainties in a combined method to generate weekly Arctic SIT [Kaleschke et al., 2015, Ricker et al., 2017].

The above methods are only applicable under certain conditions. The limited footprint of radar altimeters requires several weeks to cover the entire pole, which in turn implies that SIT maps are often highly interpolated due to the coarse temporal and spatial resolution of the observations. Because of the limited penetration depth, passive microwave radiometry at L-band can only be used in regions completely covered with ice and under predominantly cold conditions. Beyond this range, the observations are not

sensitive enough to allow direct inference. Process-based retrieval algorithms to infer SIT rely on strong model assumptions and empirically determined sea ice properties. These simplifications are required due to limited knowledge of the distribution of sea ice, exhibiting large spatio-temporal variability. Passive microwave sensors often do not capture all of the necessary information about SIT, but they also require ancillary data. The main uncertainties originate from long revisit times and large spatial resolution of satellites. Current SIT products show sufficient accuracy during the Arctic freeze-up period from mid-October to mid-March, but they do not perform well during the Arctic melting season.

Ancillary data such as atmospheric conditions and the relationship between sea ice properties and additional monitored sea ice variables such as ice type or age can be used as proxy information to indicate SIT. Although there is no direct physical link, previously empirically determined relationships between the variables can be used. The development of specific ice types with changing surface conditions may contains sea ice with a typical average thickness range. Ice age derived from ice drift maps based on backscatter data from SAR or scatterometers allows to determine specific tie points which allows to relate the surface information to SIT. During the summer months, the various types of ice of different ages show different resilience to external influences, especially with regard to the development of wet surface conditions, which in turn can be used to infer SIT. As sea ice formation recurs annually, these known relationships between the growth rate of specific ice types along the freeze-up period or the summer melting properties can be used in combination with atmospheric conditions to relate to SIT.

Validation of the SIT retrieval models is particularly challenging, because in-situ observations in polar areas are irregular and sparsely available. The collected sensitivity range of measurements – covering the seasonal and type-specific variations in the development of sea ice – is often not sufficient to determine uncertainties and biases from statistical analyses. The relatively large satellite footprints are troublesome because sea ice can be locally homogeneous and the averaged values differ from the actual distributions, which may contain deformations and can change within short distances away from locations of the in-situ observations. Satellite observations smooth out the true local SIT distribution, and reduce the dynamic range of retrievals. Satellite and in-situ observations are often not collocated in space and time – additional mismatches in scales, differences in recording time, and shifts due to sea ice drift – can lead to potential biases in inversion methods. Thus, direct comparison between in-situ and satellite observations is problematic, and it can lead to significant representativity errors in the final gridded product.

5.3.4 Ice Charts

The need to ensure safety of navigation and establish reliable shipping routes encouraged interaction between sea ice information systems of different countries which were initially

generated independently by nations for specific areas of interest. Methods commonly used in ice analysis were used to integrate information from various sources of observations into ice charts. Ice charts are determined manually by trained ice analysts from operational ice services of different states adjacent to the Arctic including Canada, USA, Russia, Norway, and Denmark. With the progress in development and processing techniques, the countries involved had discussions about an international sea-ice symbology and dissemination method. The 'egg' code to describe the state of sea ice concerning SIC and thickness-related SoD had been initially suggested by the Canadian ice forecasting agency and endorsed later by the WMO. Sea ice was divided into one of six main categories: nilas and new ice, grey ice, grey-white ice, FYI, second-year ice, and MYI.

Beginning with the first edition of Sea-Ice Information Services in the World published by WMO in 1981, satellite imagery and the availability of decent computer power revolutionized sea-ice products in terms of increasing complexity. Since then, national services such as the U.S. National Ice Center (NIC), the Danish Meteorological Institute (DMI), the Canadian Ice Service (CIS), the Finnish Meteorological Institute (FMI), and the Russian Arctic and Antarctic Research Institute (AARI) provide consistent ice charts following widely a standard provided by the WMO, and have developed in a collaborative effort a process for joint dissemination for operational ice monitoring and climate-related purposes. All ice services consist of an integrated observational system, which includes the observation network of in-situ and satellite data, a communication system where information about sea ice is collected and distributed, and a system for data integration, analysis and production. Currently, the Global Digital Sea Ice Database stores historical and updated information electronically at two archival centers, the AARI (`http://wdc.aari.ru/`) and the NSIDC (`http://nsidc.org/noaa/gdsidb`), and has mapped 7- or 10-day ice data for the Arctic from the 1950s and for the Antarctic from the 1970s to the present. Examples of a regional chart between Greenland and Barents Seas – used during the Multidisciplinary drifting Observatory for the Study of Arctic Climate (MOSAiC) expedition on 10 June 2020 – is given in Figure 5.2a, and polar-wide charts showing the SoD in for the Arctic and Antarctic is illustrated in Figure 5.3.

Although the majority of data integrated into the observing system are obtained with space-based instruments such as visible and infrared imagers, passive microwave radiometers, scatterometers, laser and radar altimeters, and SAR, observations from land stations, ships, and aircraft remain an important source of data for producing 'ground truth' information. Satellite sensors based on low-resolution (6–70 km) passive microwave radiometry and scatterometry such as AMSR2 and ASCAT, and high-resolution (10–100 m) active microwave SAR observations such as RADARSAT-2, Sentinel-1, and TerraSAR-X, are the main sources of information, providing full daily or even sub-daily coverage of the polar regions. In addition, visible and infrared sensors are being used, and radar altimeters have also begun to be included. SAR images are the main source of information to provide partial SIC and types (e.g. ratio between FYI and MYI) at high-resolution, and

to detect deformations and the presence of leads and – to some degree – also melting ponds. Manual analysis and interpretation of visible and SAR images requires a certain level of expertise about both the existence of ambiguities and how to eliminate them by evaluating auxiliary data set from ship reports and growth history. In recent years, automated or interactive processing techniques based on image recognition and classification have been developed to support the interpretation of satellite data from single or multiple sources to the implementation of prediction systems.

The 'egg-code' depicts information of the total SIC of an observed cell, and the partial SIC of a variety of ice types with its respective predominant floe size and thickness range and its common nomenclature is given in Figure 5.2b [WMO, 2014]. The discrimination of sea ice into patterns of types with uniform ice conditions requires expert knowledge on sea ice physics and atmospheric and oceanographic forcing and entails a certain degree of subjectivity. Ice charts are commonly used for evaluation of new model approaches and satellited-based retrieval algorithms. However, constrained actuality and spatial continuity of satellite imagery in combination with sea ice drift and fast evolving sea ice conditions limit the applicability of any ice chart product. SIT is described using data from multiple satellites and – as mentioned in the previous section – sea ice conditions in the form of ice type and age as surrogate parameters to indirect specification. In addition, atmospheric conditions such as freezing degree days can also be useful in specific regions. Unlike in common SIT products where a single value per grid cell is specified, SIT in ice charts is treated as a categorical variable. This approach is more realistic since an observed cell contains a distribution of SIT with strong variations in sub-grid scale. The categories established can therefore be understood as a compromise between the information required for the user's purpose (e.g., navigation, oil and gas exploration), the ability to unambiguously distinguish sea ice based on the resolution and sensitivity characteristics of the satellite observation techniques used, and the nature of sea ice regarding the occurrence of the most common types.

5.4 Discussion

Algorithms for Sea ice parameter retrieval have been successfully developed to produce maps of SIC, SIE, SIT, drift and surface temperature, which are needed for climate-related studies as well as for operational activities such as shipping that rely on the knowledge of sea ice variability. Process-based algorithms depend on empirical type-specific assumptions about sea ice properties and auxiliary data. Especially for high-resolution applications, operational retrieval still hinges on the expertise of sea ice analysts, who must consider historical sea ice trends and atmospheric indicators. The uncertainty of satellite-based sea ice products is dominated by model uncertainty, while the satellite observations themselves are quite accurate. For these reasons, it has been difficult to develop reliable algorithms under all possible ice conditions.

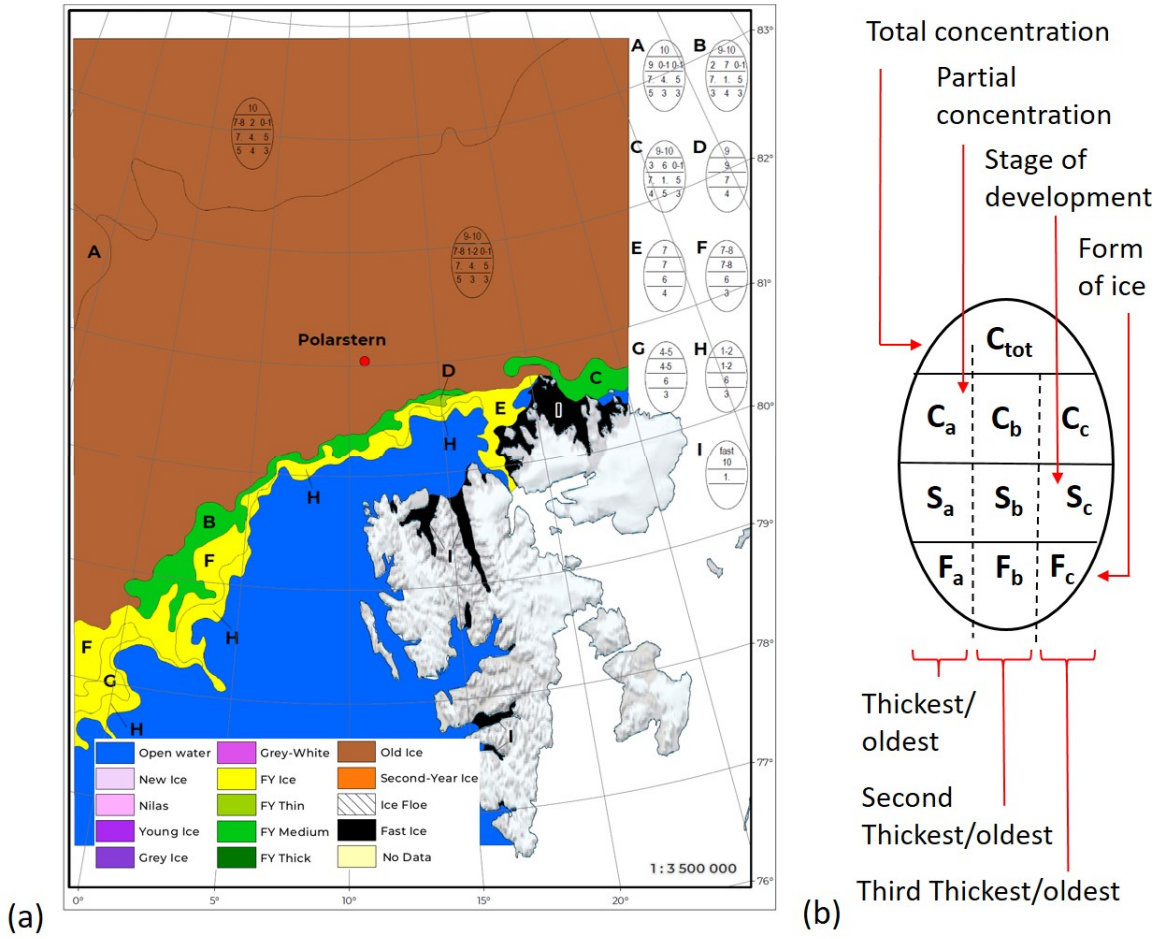

Figure 5.2: (**a**) Regional sea ice chart from the Greenland and Barents Seas in the surrounding of the Polarstern (marked with red dot) during the Multidisciplinary drifting Observatory for the Study of Arctic Climate (MOSAiC) expedition on June 10, 2020; (**a**) Common 'egg-code' nomenclature used for ice chart categorization.

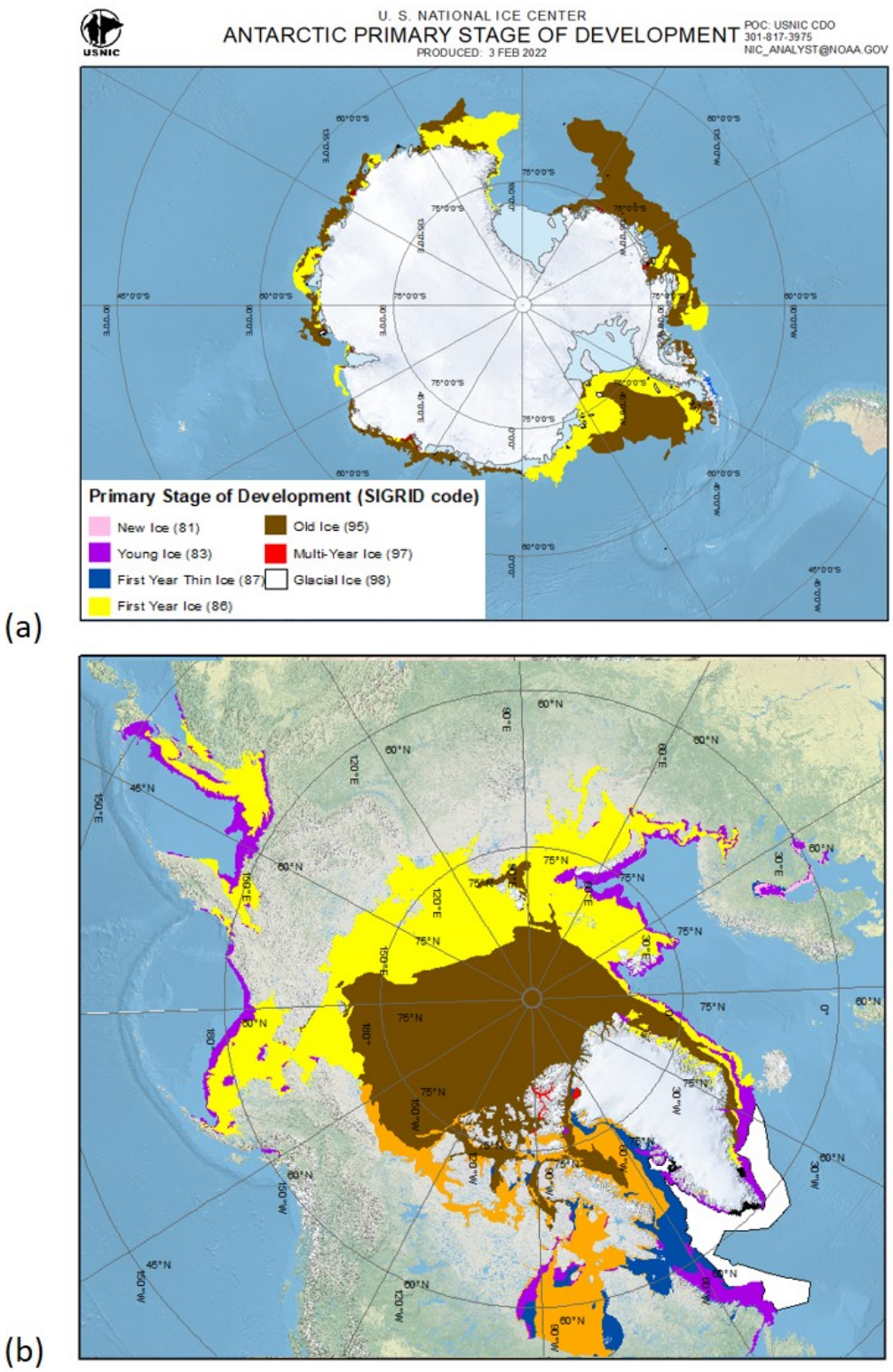

Figure 5.3: Ice charts showing the stages of development on February 3, 2022, for (**a**) Antarctic and (**b**) Arctic, provided by the NIC available under `https://usicecenter.gov/Products`.

Data-driven modelling techniques to combine satellite imagery derived from various sensors with multiple configurations is critical for including information on the different conditions, which is essential to resolve ambiguities to overcome ongoing challenges such as the underestimation of SIC for thin ice, and errors due to the presence of melt ponds and snow cover. Microwave radiometry provides to most suitable observations which are all-sky, largely unaffected vegetation, and independent of daylight. Common models usually try to correct for unwanted sensitivity effects in the data instead of providing performance metrics to evaluate them in more detail. The scientific community needs robust tools to exploit the joint effect of multi-source data more in depth by harnessing their different sensitivity ranges to sea ice properties, developing algorithms capable of analyzing measurements from multiple instrument in a common retrieval framework.

In addition to that, automatic and robust retrieval methods require the flexibility to fully describe the complexity and dynamics of sea ice. During the formation and melting, sea ice undergoes certain SoD that are associated with changes in the physical properties through thickening and aging. Nearby locations in sea ice are exposed to similar atmospheric conditions and neighboring pixels of satellite observations are therefore spatially correlated. Gradual thermodynamic growth under calm conditions makes consecutive observations to be also temporally correlated, whereas strong sea ice drift velocities lead to both correlation in space and time. Thus, data-driven modelling requires evaluating sea ice in its full spatio-temporal context, rather than a mere statistical data analysis.

The next chapter focuses on sea ice segmentation based on an unsupervised learning algorithm that exploits the synergistic effects of satellite observations from multiple sources. A Bayesian inference framework is aimed at investigating the link between a set of observations and the ability to relate the resulting class patterns to sea ice parameters SIT and SIC.

6 | Segmentation of Sea Ice

Clustering methods aim for dividing a given input data set of features into a number of clusters that can be assigned a particular label or class membership. Data points that have similar physical properties are assigned to the same class, while dissimilar data points result in a different class. Unsupervised learning algorithms and the associated process of data clustering are used in various geoscientific disciplines like earthquake studies or land use determination. They have been developed for more than 30 years [Dubes and Jain, 1988, Köhler et al., 2010, Gonçalves et al., 2017]. Unlike supervised clustering, in unsupervised clustering the number of clusters used to classify the data or the actual properties of the classes is initially unknown. Clustering methods can be further divided into hard and soft clustering [Omran et al., 2007]. In hard clustering, each data point is exclusively assigned to a specific cluster, resulting in sharp boundaries between the clusters. Soft clustering is a probabilistic approach where data points have a cluster membership probability. The observations have a probability to belong to each cluster, which allows determining the model uncertainty of the clustering results. Satellite observations are spatial images that are combined to extract spatial patterns, hence clustering is referred to as segmentation.

This chapter focuses on a segmentation approach to investigate the synergy of combining multiple satellite observations. In Section 6.1, a Bayesian unsupervised machine learning algorithm, originally developed at the Computational Geoscience and Reservoir Engineering at RWTH Aachen University [Wang et al., 2017], is used for soft clustering of a high-dimensional data set based on a Bayesian inference framework. In a Gibbs sampling process [Geman and Geman, 1984], the spatial and statistical model parameters are considered using Hidden Markov Random Fields (HMRF) and finite multivariate Gaussian Mixture Models (GMM). The method allows the combination of high-dimensional set of observations and was developed for segmentation of data in one- and two physical dimensions in the field of geological modelling and geophysics. The segmentation algorithm has already been applied to 1D data geophysical well logging to automatically obtain stratigraphic units from a variety of borehole observations [Giesgen, 2018], and to 2D data sets, for example for pattern recognition between satellite and geophysical measurements to study plant-soil interaction [Wang et al., 2019]. The implemented 2D version of the algorithm is publicly available on the GitHub repository, and can be downloaded

from `https://github.com/cgre-aachen/bayseg`.

The objective of this work encompasses the application of the Bayesian segmentation algorithm to the field of sea ice modelling, and on extending the 2D approach by a third physical dimension to account for the complexity and dynamics of the sea ice environment (see Sections 5.1.3 and 5.1.4). Sea ice consists of a multi-scale structure with distributed ice types with thickness ranges – varying at scales below the resolution of satellite imagery. The novelty is on providing an automated data-driven approach that can adequately characterize sea ice by meeting the following requirements: The segmentation needs to be robust, with resulting classes that can be consistently related to sea ice parameters SIT and SIC; and which is of probabilistic nature to account for mixed sea ice conditions to reveal model uncertainties. It is aimed to consider interaction between the physical dimensions of the multiple observations to account for the dynamics and thermodynamics of sea ice in a complete spatio-temporal context. The goal is to obtain a model that combines different data sets to reduce ambiguities in the retrievals and to provide evaluation metrics derived from the model parameters to assess the respective sensitivity and complementary information of each input feature to the respective sea ice properties.

In a first application of the method, it is investigated how to estimate high-resolution SIC by spatially segmenting SAR images to better discriminate between surface water including melt ponds and sea ice types (Section 6.2). The goal is to obtain stable classes which describe surface water in a two-step procedure, and by finding a new way of properly addressing the known challenge of the angular variation of the backscatter coefficient for different ice types and the ocean. The method aims to first determine statistically whether an image contains a significant amount of surface water to be formed as a separate class, and to subsequently estimate SIC by means of the 2D Bayesian segmentation, which has the advantage of considering the spatial correlations between the image pixels. In addition, Appendix C describes a preliminary study in which SIT data derived from 1D airborne EMI data are segmented together with SAR images to investigate the link between SAR backscatter signatures and SIT.

In Section 6.3, the 2D Bayesian segmentation algorithm is applied to spatially segment Arctic sea ice by combining multi-incidence angle SMOS T_B data. In common SIT retrieval algorithms, where T_B observations at low incidence angles are averaged to reduced the uncertainty, observations of high incidence angle are usually discarded. However, observations at high incidence angles are assumed to show differences in sensitivity to thin sea ice, which is mostly present in the Arctic during the period of early freeze-up. The segmentation is carried out for spatial images each time step individually to assess whether the obtained statistical model parameters of the segmented classes are temporally stable along the freeze-up period. The aim was to evaluate how the resulting spatial patterns can be linked to the corresponding values of the common SIT products, and whether classes are sufficiently separable to be consistently classified with SIT ranges for the individual time steps.

Considering an entire annual cycle in the Arctic consisting of sea ice formation, development, and melting, both the number of significant classes and their representation of sea ice parameters changes in the segmentation of T_B data. The dynamic and thermodynamic nature of sea ice limits the classification of the spatial patterns obtained for each individual time step – as considered in the second application. To address this limitation, the Bayesian approach, which originally only supported segmentation of observations up to two physical dimensions, was extended to three dimensions to also include the temporal component of satellite observations and allow direct segmentation of 3D data sets. This enables the algorithm to account for spatial and temporal correlations and classes are represented as spatio-temporally connected patterns. Unlike in purely spatial segmentation, where the number of classes is determined separately for each time step, classes can form freely throughout the three physical dimensions and the number of classes needs to be set only once for the entire time period. The implementation was verified based on a 3D synthetic data set (Section 6.1.3).

In Section 6.4, the 3D approach is applied to segment Arctic sea ice in space and time by combining multi-frequency T_B data from SMOS and AMSR2. They vary in sensitivity to sea ice due to different penetration depth and response to scattering phenomena. The goal was to analyze the classes for stability over time in terms of their temporal onset and multi-year recurrence. The corresponding sea ice conditions are related to the individual developmental stages of sea ice charts, and the consistency of the patterns is evaluated using common products of SIC and SIT.

6.1 Bayesian Unsupervised Learning Approach

6.1.1 Bayesian Inference Framework

Bayesian inference is a probabilistic method based on Bayes' theorem that essentially updates a prior distribution as more knowledge about probability functions becomes available. [Gamerman and Lopes, 2006]. With sufficient background knowledge about the physical composition and arrangement of the underlying structures, more targeted and faster predictions can be made. The Bayesian inference framework uses Gaussian distributions as prior information to minimize the influence of existing outliers. It is important to choose the background knowledge to avoid bias in the obtained model parameters. The fundamental approach in Bayesian inference to interpret the available observed data is given by Bayes' theorem:

$$P(\theta \,|\, y) \;=\; \frac{P(y \,|\, \theta)\, P(\theta)}{P(y)}, \tag{6.1}$$

where y denotes the field observations, and θ the model parameters, which are derived in an updating process. The formula can be unraveled into its respective probability components. $P(\theta)$ is the marginal probability distribution that contains the prior knowledge

gained to describe the model using expertise knowledge. $P(y \mid \theta)$ is the likelihood function that the measurement y occurred under the condition that a particular model (latent field with labels) is already given. $P(\theta \mid y)$ is called the conditional *a posteriori* distribution and the outcome one is mostly interested in. The marginal distribution $P(y)$ denotes the partition function which is a constant to normalize the integration of the *a posteriori* distribution.

Gaussian Mixture Models

A GMM addresses multidimensional data sets in feature space in a purely statistical manner. It is one of the mathematically and computationally simplest models to segment variables using unsupervised learning. As a starting point, N data points (measurements) in an M-dimensional space (M number of features) are given as input data. The aim is to fit the data for a total number L of multivariate Gaussian distributions, and to find the most appropriate set that represents the given observations best. The total number of distributions (or labels) L is predefined for the segmentation and can be estimated based on different statistical criteria (e.g. Bayesian or Akaike Information Criterion (BIC or AIC)). The Gaussian distributions are parameterized by its mean vector $\boldsymbol{\mu}$ and the covariance matrix $\boldsymbol{\Sigma}$. Initially, it is not obvious to which of the Gaussian distributions each of the data points belongs. The exercise of the method is to assign all data points to the distributions in an unsupervised manner. Unlike in hard conditioning algorithms such as K-means [Jain, 2010], in GMMs there is no sharp boundary between clusters, and the model outputs a probability estimate $P(l \mid j)$ that indicates the membership probability of each data point j to belong to the clusters $l \in L$. For an input matrix of size $N \times M$, the estimated parameters are the L mean vectors $\boldsymbol{\mu_l}$ of length M, the L covariance matrices $\boldsymbol{\Sigma_l}$ of size $M \times M$ and the probability estimate $P(l \mid j)$ of the size $N \times L$.

The likelihood $\mathcal{L}$ represents the posterior probability to obtain the observations for the given model parameters. The essence of the inference algorithm is to maximize the likelihood and to converge towards the highest probability by finding the most appropriate model parameters in accordance with the observations. The likelihood is given by

$$\mathcal{L} = \prod_{n \in N} P(\boldsymbol{y_j}), \quad with \quad P(\boldsymbol{y_j}) = \sum_{l \in L} f(\boldsymbol{y_j} | \boldsymbol{\mu_l}, \boldsymbol{\Sigma_l})\, P(l), \tag{6.2}$$

where $P(l)$ is the probability for a randomly chosen data point x_j being member of cluster l, $P(\boldsymbol{y_j})$ is the likelihood of finding a data point at observation $\boldsymbol{y_j}$, and f is a component density function in form of a multivariate Gaussian distribution

$$f(\boldsymbol{y_j} | \boldsymbol{\mu_l}, \boldsymbol{\Sigma_l}) = \frac{1}{(2\pi)^{\frac{M}{2}} |\boldsymbol{\Sigma}|^{\frac{1}{2}}} \exp\left[-\frac{1}{2} (\boldsymbol{y} - \boldsymbol{\mu})^T \boldsymbol{\Sigma}^{-1} (\boldsymbol{y} - \boldsymbol{\mu}) \right]. \tag{6.3}$$

The probability estimate can then be component-wise separated into

$$P(l|\boldsymbol{y_j}) = \frac{f(\boldsymbol{y_j}|\boldsymbol{\mu_l}, \boldsymbol{\Sigma_l})\, P(l)}{P(\boldsymbol{y_j})}. \tag{6.4}$$

First, the means and covariances of the multivariate Gaussian distributions and $P(l)$ need to be estimated and subsequently updated to obtain the maximum likelihood. This is commonly done using methods including Expectation-Maximization (EM) or Markov Chain Monte Carlo (MCMC). In standard GMMs, data points are assumed to be conditionally independent. Since in this case they originate from georeferenced satellite measurements and describe a 2D or 3D physical space, the observed data points are not easily separable and interactions between adjacent observations are expected. Therefore, a HMRF approach is used together with the GMM to also account for spatial interactions of images. [Wang et al., 2017].

Hidden Markov Random Fields

HMRFs are used to account for the spatial interactions in the physical space in addition to the statistical characteristics in feature space considered in the GMM. The aim is to indicate a latent field in physical space according to the surface signatures observed from different sensors or different configurations in terms of frequency, incidence angle and polarization. The field is based on a hidden variable, which can not be clearly assigned to a strictly physical quantity, but enables categorization of heterogeneous measurements on the basis of statistically an spatially correlated patterns. The goal is to find appropriate classes that segment the data into patterns in order to reveal useful information how the multiple observations are linked.

All data points in feature space are provided with their respective spatial coordinates in physical space. The 2D field $\mathbf{x}$ is composed of i pixels corresponding to the resolution of the measurements with a total number of pixels N. Using similar notation as in the categorization of data points to a specific clusters in the GMM, each pixel is further classified by a label l with a total number of labels L. ∂_i denotes that a pair of the central pixel with one of its eight nearest neighbours forms a clique in a grid with 8 connections (see figure 6.1). Spatial correlation essentially means that neighbouring pixels are likely to belong to the same cluster with label l. The probability of interaction between neighboring pixels is described by the local conditional probability $P(x_j \,|\, \boldsymbol{x_{\partial_j}})$. It is the probability of a central pixel i to have label l after evaluating the surrounding pixels ∂_i and is given by

$$P(x_j \,|\, \boldsymbol{x_{\partial_j}}) = \frac{P(x_j, \boldsymbol{x_{\partial_j}})}{\sum\limits_{x_j \in L} P(x'_j, \boldsymbol{x_{\partial_j}})} = \frac{exp[-U(x_j, \boldsymbol{x_{\partial_j}})]}{\sum\limits_{x'_j \in L} exp[-U(x'_j, \boldsymbol{x_{\partial_j}})]}, \tag{6.5}$$

where $U(x_j, \boldsymbol{x_{\partial_j}})$ is the local energy of the central pixel i with respect to the neighboring pixels. The local energy is obtained from potential functions $V_{i,j}(x_i, x_j)$ in a Potts

model [Koller and Friedman, 2009]) and is calculated as

$$U_j(x_j, \boldsymbol{x_{\partial_j}}) = \sum_{i \in \partial_j} V_{i,j}(x_i, x_j), \quad \text{with} \quad V_{i,j}(x_i, x_j) = \begin{cases} 0, & \text{if } x_i = x_j \\ \beta_d, & \text{if } x_i \neq x_j \end{cases} . \tag{6.6}$$

The local energy is parameterized by the directional heterogeneity coefficients $\beta_d \in \{\beta_0 = 0, \beta_1 = \frac{\pi}{2}, \beta_2 = \frac{\pi}{4}, \beta_3 = \frac{3\pi}{4}\}$, which introduce directional smoothing to the latent field to account for possible anisotropy (see Figure 6.1).

A positive heterogeneity coefficient indicates largely homogeneous conditions, which means that neighbouring pixels along that particular direction 'attract' each other. A negative coefficient, on the other hand, indicates heterogeneous conditions, such as discontinuities at the sea ice edge, and neighboring pixels are 'repelled' in that particular direction.

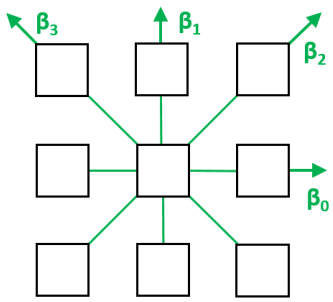

Figure 6.1: Set of cliques comprising the central pixel with one of its neighboring pixels in an 8-connected grid. The directional heterogeneity coefficients β_0–β_3 determine the local conditional probability of the latent field at the corresponding pixel position.

6.1.2 Segmentation Algorithm

The Bayesian segmentation algorithm [Wang et al., 2017] can be divided into three main parts: initializing the input parameters (consisting of the processed field measurements and the previous model estimates), updating the labels and the underlying latent field, and updating the statistical parameters of the GMM.

Initialization of Input Features and Model Parameters

The input data is given by the processed features provided with its physical coordinates. The features have to be scaled beforehand to make them comparable in the subsequent unsupervised algorithm. Hereby, the whole data set is standardized using the Z-score

$$Z = \frac{X - \mu}{\sigma}, \tag{6.7}$$

assuming the distributions to be of Gaussian origin, without considering significant skewness or kurtosis. In this process, the mean values of all input characteristics are shifted to zero and the variances are normalized to one to account for different scaling. The BIC score can be used to select the appropriate number of labels [Claeskens et al., 2008]. It is based on a purely statistical evaluation to find a trade-off between the GMM parameters and the number of clusters, and is given by

$$\mathrm{BIC} = L\,\ln(N) - 2\ln(\hat{\mathcal{L}}(\mathbf{y}|\boldsymbol{\theta})), \tag{6.8}$$

where N is the total number of data points, $\boldsymbol{y}$ the observations, L is the number of estimated labels and $\boldsymbol{\theta}$ is the set of all parameters $(\boldsymbol{\mu}, \boldsymbol{\Sigma})$. $\hat{\mathcal{L}}(\mathbf{y}|\boldsymbol{\theta})$ is the maximum value of the likelihood function $\mathcal{L}(\mathbf{y}|\boldsymbol{\theta})$ (similar to Equation 6.2), which corresponds to the optimal clustering result fitting the data best under the assumption of L labels. This approach follows Occam's razor to find the simplest scientific model to describe the data. Thus, more labels in the model lead to a higher penalization term $(L\,\ln(N))$ and to a higher BIC score. The most adequate model is given for the lowest score, and the corresponding number of labels enters the segmentation. Since no prior knowledge is given for the segmentation, the model parameters are initially chosen to be non-informative, i.e. arbitrary for $\boldsymbol{\beta}$ and $\boldsymbol{\mu}$ with large $\boldsymbol{\Sigma}$. The model parameters are determined in an iterative process and the segmentation leads to the final model parameters $\boldsymbol{\theta} = (\boldsymbol{\mu}, \boldsymbol{\sigma}, \boldsymbol{\beta})$ and the latent field $\mathbf{x}$ of the last iteration. The segmentation steps – including estimation and updating of the model parameters – are described below.

Segmentation of the Latent Field and Parameter Estimation

The aim of Bayesian segmentation is to obtain the latent field $\mathbf{x}$ in physical space in which for each pixel i the most probable label $l \in L$, i.e. the one with the highest label probability, is assigned. As aforementioned, the spatial correlations are considered using HMRF with the heterogeneity coefficient $\boldsymbol{\beta}$ as a model parameter, and the statistical characteristics of the random variables are included in a GMM with the corresponding model parameters $\boldsymbol{\mu}$ and $\boldsymbol{\Sigma}$. The marginal distribution of the entire field can be expressed using a mean field-like approximation $\widetilde{\boldsymbol{x}}_{\boldsymbol{\partial_j}}$ of $\boldsymbol{x}_{\boldsymbol{\partial_j}}$ [Celeux et al., 2003] as the sum of the local marginal distributions as

$$P(y_i;\, \boldsymbol{\mu}, \boldsymbol{\Sigma}, \boldsymbol{\beta}) \approx \prod_{j \in N} \sum_{l \in L} f(y_j; \boldsymbol{\mu_l}, \boldsymbol{\Sigma_l})\, P(l \,|\, \widetilde{\boldsymbol{x}}_{\boldsymbol{\partial_j}}; \boldsymbol{\beta}). \tag{6.9}$$

Hereby, $f(y_j; \boldsymbol{\mu_l}, \boldsymbol{\Sigma_l})$ is the component density function of the GMM, described in Equation 6.3. The conditional probability $P(l \,|\, \widetilde{\boldsymbol{x}}_{\boldsymbol{\partial_j}}; \boldsymbol{\beta})$ to obtain the specific label l locally according to labeling of the neighboring pixels and the directional heterogeneity coefficient of the HMRF is given by Equation 6.5. The conditional *a posteriori* distribution $P(\boldsymbol{x} \,|\, \boldsymbol{y}, \boldsymbol{\theta})$ to obtain the latent field for given observations and model parameters can be

computed with a Gibbs sampler [Geman and Geman, 1984]. To update the model parameters, the conditional *a posteriori* distribution $P(\boldsymbol{\theta} \,|\, \boldsymbol{y}, \boldsymbol{x})$ for given observations and latent field can be obtained by conditional MCMC sampling [Wang et al., 2017]. Both the model parameters and the latent field are iteratively sampled by the two conditional *a posteriori* distributions using a MCMC method.

In a first step, the *a posteriori* $P(\boldsymbol{x} \,|\, \boldsymbol{y}, \boldsymbol{\theta})$ (also called Gibbs distribution) is sampled parallel by a chromatic sampler [Wang et al., 2017]. Hereby, the local energy of the pixels can be computed by

$$P(x_j \,|\, y_j, \boldsymbol{x}_{\boldsymbol{\partial_j}}, \boldsymbol{\theta}_{\boldsymbol{x_j}}) \;\propto\; exp\Big[- [U(x_j, \boldsymbol{x}_{\boldsymbol{\partial_j}}) + U(y_j \,|\, x_j, \boldsymbol{\theta}_{\boldsymbol{x_j}})]\Big], \tag{6.10}$$

where the first component is the local energy (Gibbs energy) of the random field (Equation 6.6) and the latter part is given by the likelihood energy

$$U(y_j \,|\, \boldsymbol{\theta}_{\boldsymbol{x_j}}) = \frac{1}{2}(y_j - \boldsymbol{\mu}_{\boldsymbol{x_j}})^T \boldsymbol{\Sigma}_{x_j}^{-1}(y_j - \boldsymbol{\mu}_{\boldsymbol{x_j}}) + \frac{1}{2} log|\boldsymbol{\Sigma}_{\boldsymbol{x_j}}|. \tag{6.11}$$

Secondly, the model parameters $\boldsymbol{\theta} = (\boldsymbol{\mu}, \boldsymbol{\Sigma}, \boldsymbol{\beta})$ are iteratively updated with the conditional MCMC sampling process with the corresponding *a posteriori* distributions:

$$P(\boldsymbol{\mu} \,|\, \mathbf{y}, \mathbf{x}, \boldsymbol{\Sigma}, \boldsymbol{\beta}) \;\propto\; P(\boldsymbol{\mu})\, L(\mathbf{y} \,|\, \mathbf{x}, \boldsymbol{\mu}, \boldsymbol{\Sigma}, \boldsymbol{\beta}), \tag{6.12}$$

$$P(\Sigma \,|\, \mathbf{y}, \mathbf{x}, \boldsymbol{\mu}, \boldsymbol{\beta}) \;\propto\; P(\boldsymbol{\Sigma})\, L(\mathbf{y} \,|\, \mathbf{x}, \boldsymbol{\mu}, \boldsymbol{\Sigma}, \boldsymbol{\beta}), \text{ and} \tag{6.13}$$

$$P(\boldsymbol{\beta} \,|\, \mathbf{y}, \mathbf{x}, \boldsymbol{\mu}, \boldsymbol{\Sigma}) \;\propto\; P(\boldsymbol{\beta})\, L(\mathbf{y} \,|\, \mathbf{x}, \boldsymbol{\mu}, \boldsymbol{\Sigma}, \boldsymbol{\beta}), \tag{6.14}$$

with the likelihood function given by $L(\boldsymbol{y} \,|\, \boldsymbol{x}, \boldsymbol{\mu}, \boldsymbol{\Sigma}, \boldsymbol{\beta}) = \prod_{j \in N} P(y_j \,|\, \widetilde{\boldsymbol{x}}_{\partial_j}; \boldsymbol{\mu}, \boldsymbol{\Sigma}, \boldsymbol{\beta})$ (similar to Equation 6.2 for the statistical model). The implemented steps of the Gibbs sampler and the parameter estimation are illustrated in the Figures B.1 and B.2 in Appendix B [Wang et al., 2017].

6.1.3 Extension of the Approach into Three Dimensions

In spatial Markov model-based image segmentation, interactions between pixels in the latent field are included in a 2D lattice. The local interactions of a central pixel i, and its eight neighboring pixels ∂_i are evaluated by calculating the local energy in terms of its directional heterogeneity coefficients β_0–β_3 in four independent directions (see Figure 6.1). A small value of β indicates a noisy realization of the latent field with weakly constrained pixel interaction in that particular direction. Large values of β refer to a latent field with smooth conditions where constraints between pixels are strong. For positive values, neighboring pixels tend to be attracted and are encouraged to form the same class, whereas negative values cause repulsion and prevent clustering along a certain

direction. Anisotropic conditions result in high directional variation of β.

To include the fact that observations over sea ice can be essentially linked in both space and time through the non-negligible drift velocity of the ice pack, the 2D neighboring system needs to be extended by a third dimension. The implementation of purely spatial correlations between pixels of 2D images can be complemented by also including temporal and spatio-temporal interactions between volume pixels (voxels) in the 3D space. In analogy to the 8-connected spatial grid of pixels, a 3D realization accounts for the interactions between the central voxel i with its 26 neighboring voxels. Considering the fully spatio-temporal context, a total of 13 independent coefficients β_0–β_{12} are determined to allow the parameterization of heterogeneity independently in all directions. The direction d of the set of values β_d can be defined in terms of an azimuthal angle $\Phi \in [0, 2\pi]$ and polar angle $\Theta \in [0, \pi]$ in a spherical coordinate system in 3D space (see Figure 6.2a). Figure 6.3 illustrates the coefficients in form of cliques between the 27 voxels in an 26-connected grid in a 3D neighboring system. Hereby, β_0–β_3 and β_4 account for purely spatial and temporal interactions between voxels, and β_5–β_{12} represent correlations of voxels in both space and time, respectively. The directions d of all β_d in spherical coordinates (Φ, Θ) and the corresponding type of constraint are summarized in Table 6.1. Assuming that satellite data sets form a stack of consecutively collected observations of the same surface area of the Earth, the 3D space is spanned by two spatial (x, y) and a temporal coordinate z (see Figure 6.2b). Similar to the 2D case, the MRF energy of all neighboring voxels is calculated accordingly and considered in the iterative sampling process in the Bayesian inference framework.

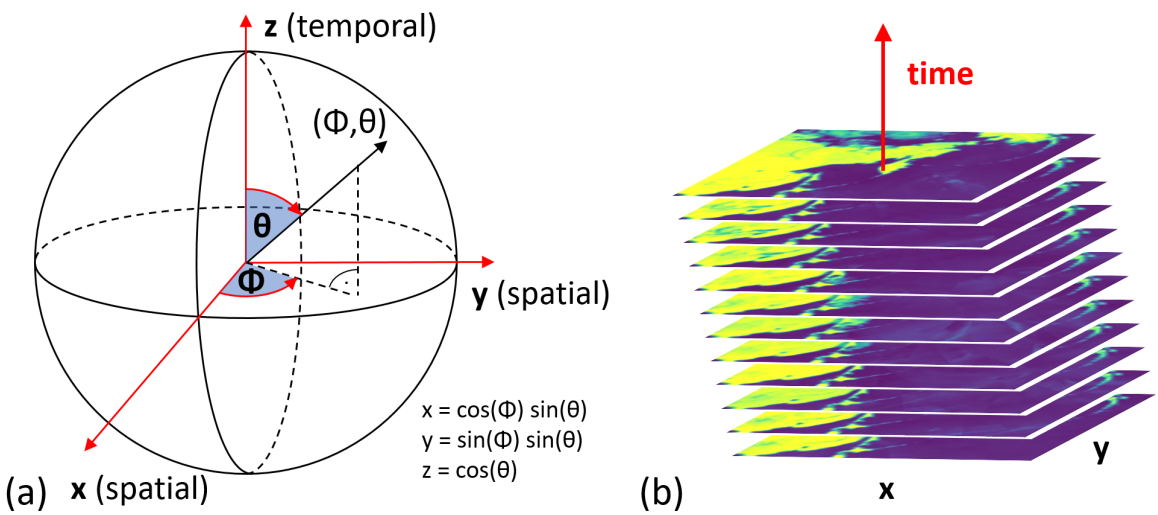

Figure 6.2: Coordinate system for spatio-temporal analysis of satellite images. (**a**) The spatial coordinates (x, y) and the temporal coordinate z span the 3D space, where any direction to a point at the unit sphere can be represented in spherical coordinates (Φ, Θ). (**b**) Stack of satellite data represented as regularly sampled time series of consecutive spatial observations of the same area.

For the most general case of anisotropic sea ice conditions, β_d are computed indepen-

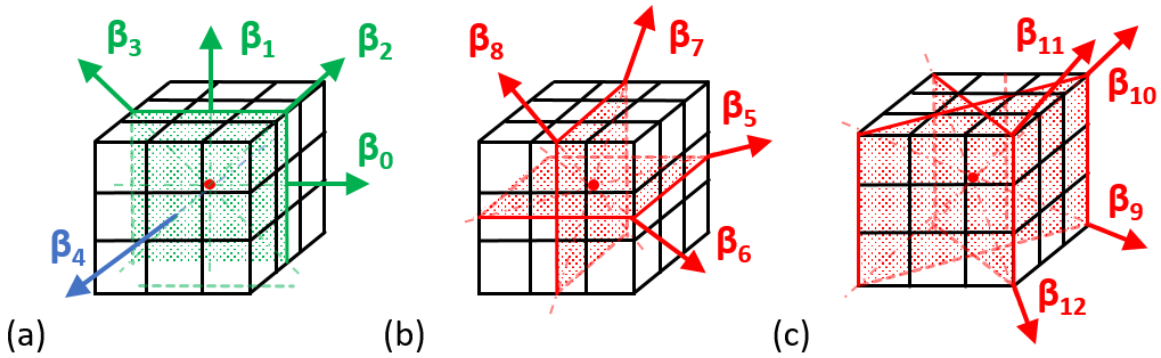

Figure 6.3: Set of cliques of a central voxel (with the red dot in the centre) paired with one of its neighboring voxels in a 27-connected grid. The correlation between voxels is parametrized in terms of 13 directional coefficients β_0–β_{12}. Without loss of generality in case the third dimension is considered as a temporal coordinate. (**a**) β_0–β_3 account for purely spatial and β_4 for purely temporal; (**b**) β_5–β_{12} for the spatio-temporal connections between voxels.

Table 6.1: Independent directions d of the heterogeneity coefficient β_d in terms of azimuthal angle $\Phi \in [0, 2\pi]$ and polar angle $\Theta \in [0, \pi]$ and the corresponding spatial and/or temporal constraints.

d	Φ	Θ	Constraint	d	Φ	Θ	Constraint
0	0	$\pi/2$	spatial	7	$\pi/2$	π	spatio-temporal
1	$\pi/2$	$\pi/2$	spatial	8	$\pi/2$	0	spatio-temporal
2	$\pi/4$	$\pi/2$	spatial	9	$3\pi/4$	$7\pi/4$	spatio-temporal
3	$3\pi/4$	$\pi/2$	spatial	10	$3\pi/4$	$\pi/4$	spatio-temporal
4	N/D	0	temporal	11	$\pi/4$	$\pi/4$	spatio-temporal
5	0	$3\pi/4$	spatio-temporal	12	$\pi/4$	$7\pi/4$	spatio-temporal
6	0	$\pi/4$	spatio-temporal				

dently for each direction d. However, structures can be oriented along specific directions at which neighboring voxels are attracted in the segmentation and are more likely to belong to the same class. At smaller scale for example, deformations can be governed by patterns of wind speed and temperature fields and the segmentation of the satellite observations may be preferred in the direction of linear structures such as leads and pressure ridges. When considering polar scale, observations usually cover sea ice at several SoD – with each sub-region consisting of a different level of anisotropy and heterogeneity. In case of the Arctic, the distribution of sea ice is complicated as it strongly depends on the distribution of land masses, ocean currents, atmospheric circulation, and the remaining sea ice of the previous season. Nevertheless, in the Antarctic sea, sea ice growth and melt are influenced to a larger degree by the seasonality of solar radiation, resulting in mostly a meridional expansion and reduction of sea ice from Antarctica towards lower latitudes. Thus, the boundaries between different SoD may be a function of latitude and season, and β values can be radially symmetric instead of directionally independent. This radial sym-

metry could be captured in the algorithm by transforming Cartesian coordinates (x, y) to Polar coordinates (r, ϕ) while facilitating the segmentation by reducing the number of implemented directions.

It is important to highlight that in case spatio-temporal data sets are analyzed, the interpretability of the values of β_d can strongly differ in terms of the corresponding direction d. The physical meaning of the intensities depends both on whether a constraint is purely spatial, temporal, or spatio-temporal, and on the spatial and temporal sampling of the segmented data set. The resolution capability of the input features needs to be put in context with the characteristic length scale of changes induced by dynamic and thermodynamic processes. Only a finite number of samples are available in finite time intervals, and the time scale of sea ice changes to occur needs to be set in causal relation with the revisit time of satellite data collection. The temporal sampling – ranging from sub-daily to monthly intervals – determines the pivotal processes which are the major reason for reported changes of sea ice properties at an observed area. Calm conditions generally favour thermodynamically-driven sea ice changes, leading to a continuous and long-term transformation of sea ice. Also, in case sea ice is observed at sparse time intervals, changes in properties due to continuous development of sea ice over longer periods can outweigh the changes originating from dynamic processes. In contrast, high variation between two consecutive measurements at daily revisit can be mainly associated with dynamic processes such as sea ice drift or the deformation of sea ice under rough conditions. Therefore, the data set needs to be critically examined in terms of spatial and temporal sampling, i.e. the choice of temporal composites as a stacks of spatial maps, in order to understand the physical meaning of $\boldsymbol{\beta}$ values as directional smoothing constraints.

Verification of the 3D Approach Based on a Synthetic Example

The 3D segmentation approach is verified on the basis of a synthetic example. A 3D lattice with 60×60×60 samples along the coordinates (x, y, z) is used to generate a synthetic latent field. For each voxel in the 3D space, the function $f(x, y, z) = \sin(x \cdot y \cdot z)$ is implemented for a definition range between 0 and 3 along each axis. The value range of $f \in [-1, 1]$ is separated into three discrete sub-ranges, where each voxel is labeled as follows: $l = 0$ for $-0.7 \leq f \leq 0.7$; $l = 1$ for $f < -0.7$; $l = 2$ for $f > 0.7$. A total of four 3D features are simulated as randomly sampled observations – which can be similar to those assumed to be measured by a satellite – by applying multivariate Gaussian emission functions (with different mean vectors and covariances) to the labeled 3D image. The latent field and the corresponding simulated features are shown in figure 6.4a–d as slices in the xy-plane for $z = 10$, 20, 40, and 60, respectively. The generated latent field of resulting patterns of labeled voxels is anisotropic, and the directionality of the boundaries between classes varies strongly throughout the 3D image. Widely homogeneous regions are located at smaller values of (x, y, z) and high spatial variability is given at larger

values.

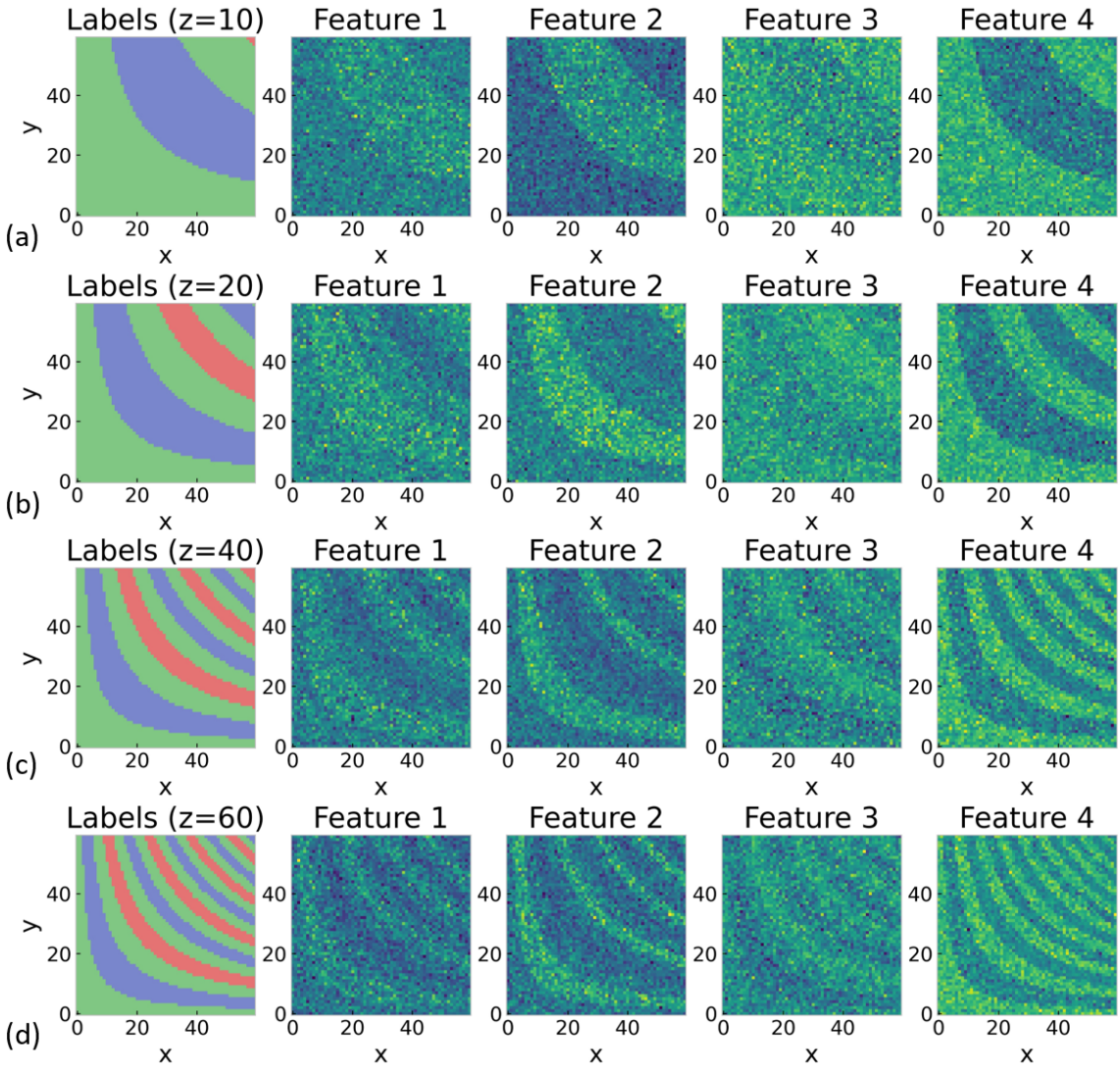

Figure 6.4: Synthetic data set to verify the 3D segmentation approach. The latent field comprises three classes from which a total of four features are generated by applying Gaussian emission functions to the labeled data. (**a**)–(**d**) Slices of the latent field and the features are visualized in the xy-plane for $z = 10$, 20, 40, and 60, respectively.

The four simulated feature fields are segmented into 3 classes by carrying out a total number of 200 iterations. The evolution of the spatial model parameters β_0–β_{12} and the class-specific Pearson correlation coefficients at each iteration step are shown in Figure 6.5. Figure 6.6 illustrates the initial field and the corresponding estimated latent field together with its uncertainty in terms of entropy in the xy-plane for $z = 10$, 20, 40 and 60, respectively.

The approach yields satisfying estimates for both the model parameters and the segmented latent field. The algorithm enables to account for the noise level contained in the features by introducing the 3D smoothness constraints β_d. The main structure of the underlying hidden pattern of homogeneous sub-regions could be extracted based on the

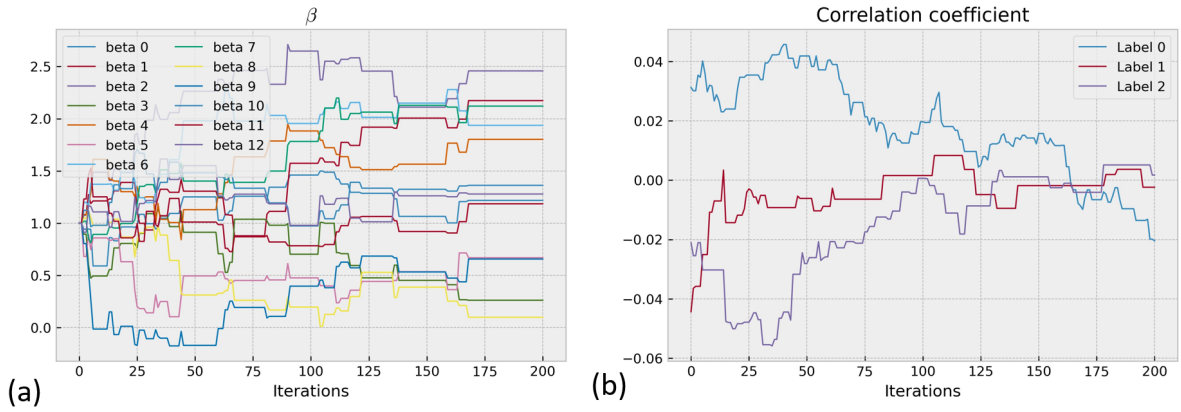

Figure 6.5: Segmentation diagnostics of the spatial and statistical model parameters for a total of 200 iterations. (**a**) Evolution of the directional heterogeneity coefficient β_0–β_{12} with an initial value of 1 (slight attraction) and the average jump length per iteration of 0.02; (**b**) Class-specific Pearson correlation coefficient computed from the covariance matrices after initial uniform distribution.

relationship between the input features. Since the pattern in the synthetic example does not represent a structured medium, the changing anisotropy throughout the 3D space is reflected by the high variation of values of β. Even though no clear structure in one particular direction can be observed in the generated synthetic pattern, the algorithm still manages to almost completely retrieve the original latent field, except for the finest structures pattern (see Figure 6.6d at the top-right corner).

6.2 Discrimination between Sea Ice and Closed Water using Sentinel-1 SAR data

Several methods have been developed to detect melt ponds based on air- and spaceborne observations among different scales using microwave radiometry, radar and optical data [Zege et al., 2015, Tanaka et al., 2016, Li et al., 2017]. This study presents a probabilistic approach to discriminate sea ice from surface water using Sentinel-1 A/B SAR images, which are available on a daily basis at medium resolution (~ 40 m) covering the entire polar area. The intensity of radar backscattering is sensitive to the surface roughness. Surface roughness for closed water and sea ice is significantly smaller as compared to the mainly wind-forced open ocean, which enables to classify surface types based on its intrinsic surface conditions. The goal is to segment SAR images into a number of separable classes using a two-step method, combining an EM step with Bayesian inference modelling. The approach considers the angular variations and the spatial correlations of the SAR images. This work focuses on the methodology and presents preliminary estimates of surface water fraction based on annual images at a selected area in the Northern Barents Sea from 1 September 2019 to 31 August 2020.

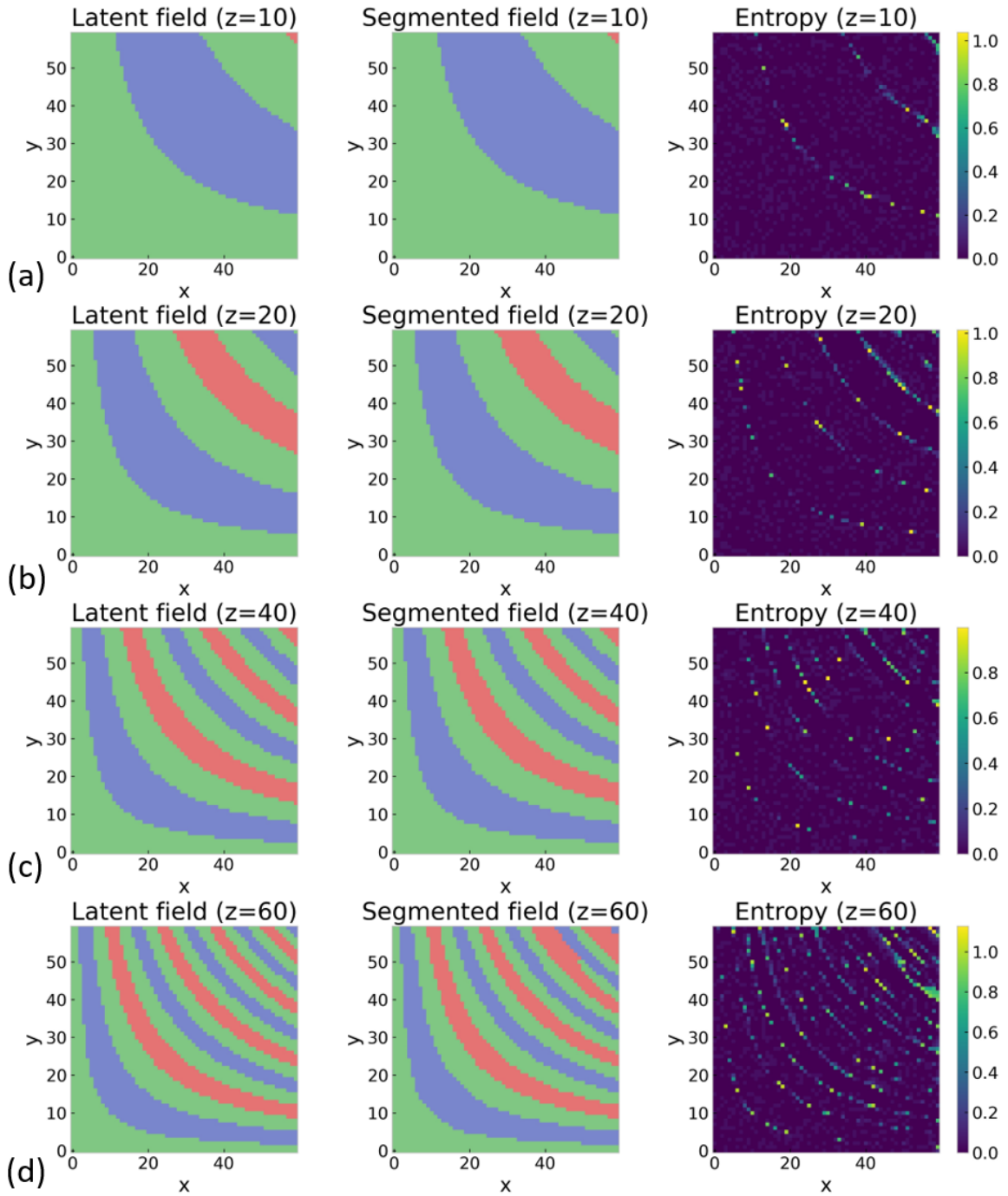

Figure 6.6: Comparison of the initial latent field and the estimated field including uncertainty in terms of entropy after 3D segmentation. (**a**)–(**d**) Slices of the latent field, segmented field, and entropy are visualized in the xy-plane for $z = 10$, 20, 40, and 60, respectively. The segmentation approach is capable of retrieving the initial pattern of labels, except for the fine structure at the top-right corner at the slice $z = 60$.

The Sentinel-1 mission – developed by ESA – was launched on April 2014, and it is composed of two polar-orbiting satellites, Sentinel-1A and Sentinel-1B, providing dual polarisation capability, very short revisit times and rapid product delivery [Nagler et al., 2015]. The SAR operates at C-band (5.405 GHz), and data are collected in ascending and descending orbits independently of daylight, under all weather conditions, with an

incidence angle ranging from 18.3 ° to 46.8 °. Data over sea and polar areas are acquired in a 12 or 6 day repeat cycle using one or both satellites, respectively, with a total coverage frequency of less than 1 day in the Arctic. This work is based on L1 Ground Range Detected HH-polarized observations in Extra Wide swath mode consisting of a 400 km swath at 20×40 m spatial resolution. It uses images of both the orthorectified backscattering coefficient γ_0 and the corresponding incidence angles. Data can be downloaded from any Copernicus service, e.g. at Sentinel Hub, `https://www.sentinel-hub.com/`, Sinergise Ltd.

The study area is given in Figure 6.7, and it encompasses a small area (10×20 km^2) located in the Northern Barents Sea, which is considered a warming hotspots in the Arctic [Lind et al., 2018]. The region passes an entire annual cycle of freeze up, melting, and ice-free ocean and consists exclusively of FYI during the Arctic winter months. Figure 6.8 shows an example of γ_0 image in decibels (left) including its distribution and cumulative sum (right), acquired on 20 June 2020 at an incidence angle of 37.4 °. The image indicates small low-valued patches which can be attributed to melt ponds.

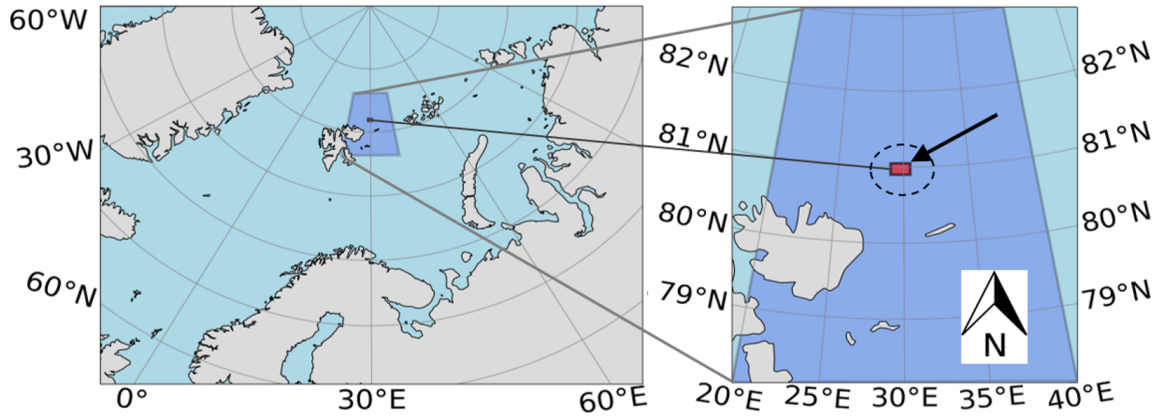

Figure 6.7: Study area consisting of ∼ 10 x 20 km^2 located in the northern Barents Sea between Svalbard and Franz Josef Land.

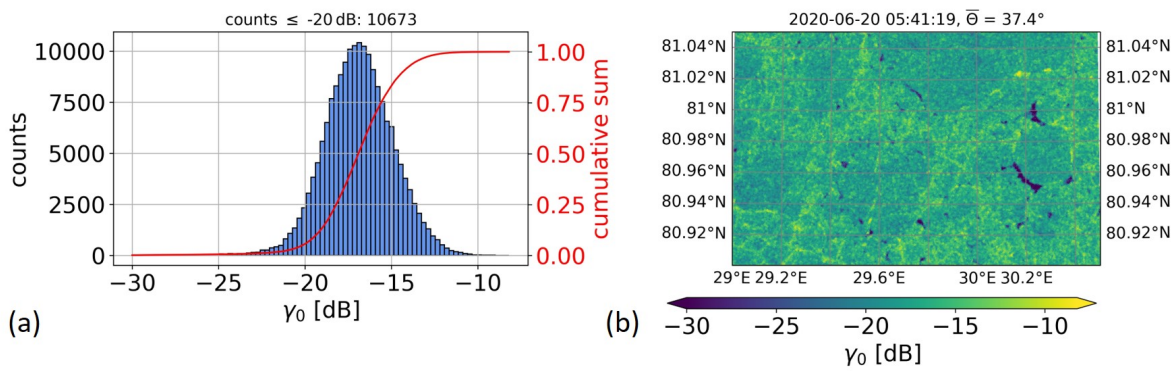

Figure 6.8: Sentinel-1 backscatter coefficient γ_0 acquired on 20 June 2020, at an incidence angle of 37.4 °. **(a)** distribution and cumulative sum of γ_0; **(b)** spatial distribution of γ_0.

The methodology consists of three main steps, a preceding angular normalization of

the SAR images, an estimation of the number of significant classes from information criteria obtained through EM, and the segmentation of the SAR images to extract the surface water fraction.

6.2.1 Angular Variation of SAR backscattering coefficient

SAR surface signatures of Arctic sea ice depend on the incidence angle [Mahmud et al., 2018, Lohse et al., 2020]. The intensity of γ_0 is smaller for observations at higher angles, and for smooth surfaces such as calm waters. The angular normalization of medium resolution SAR images has been considered in different approaches to detect sea ice types [Mäkynen and Karvonen, 2017, Komarov and Buehner, 2019, Cristea et al., 2020], but it remains challenging because of high sea ice drift velocities reaching up to several kilometers per day. The angular dependence of the backscattering coefficient is different for open water (OW) and sea ice, and it differs among several sea ice types such as FYI or MYI.

In this work, a single slope correction is determined from observations along the period when sea ice was present. A first examination showed that the angular dependence among the entire range of incidence angles of the Sentinel-1 images (18–47 °) is non-linear. Figure 6.9 shows the angular dependence of γ_0 for two consecutive observations at 43.1 ° and 31.3 ° on 5 July 2020. The highest deviations are given for observations at low incidence angles. Images at incidence angles $< 30\,°$ were discarded beforehand to be able to linearly correct for the angular dependence of the backscattering coefficient. Sentinel-1 provides images at at least daily coverage, but in many days it observes even multiple images per day (here at around 50 times per year). The angular difference in the backscattering coefficient was determined for each of the given multiple observations per day and a typical slope correction ($\Delta\overline{\gamma_0}/\Delta\Theta$) was obtained as follows

$$\frac{\Delta\overline{\gamma_0}}{\Delta\Theta} = \frac{1}{N}\sum^{N}\frac{\overline{\gamma_0}(\Theta_2) - \overline{\gamma_0}(\Theta_1)}{\Theta_2 - \Theta_1}. \tag{6.15}$$

This has the advantage that the surface structure of the sea ice has changed only marginally during two consecutive observations, and the main differences in the backscattering coefficient are caused by its angular dependence. All images were corrected according to its difference to the mean angle ($\sim 33\,°$) within the observed period.

6.2.2 Estimation of the Number of Significant Classes

EM is an unsupervised clustering method initially proposed by [Dempster et al., 1977] and is based on an iterative process which alternates between an expectation (E) step, and a maximization (M) step. It has been already applied to segment sea ice into areas of different sea ice types using multi-angular Sentinel-1 SAR images [Hänsch et al., 2020]. The likelihood of a GMM under variation of the number of classes and their expected

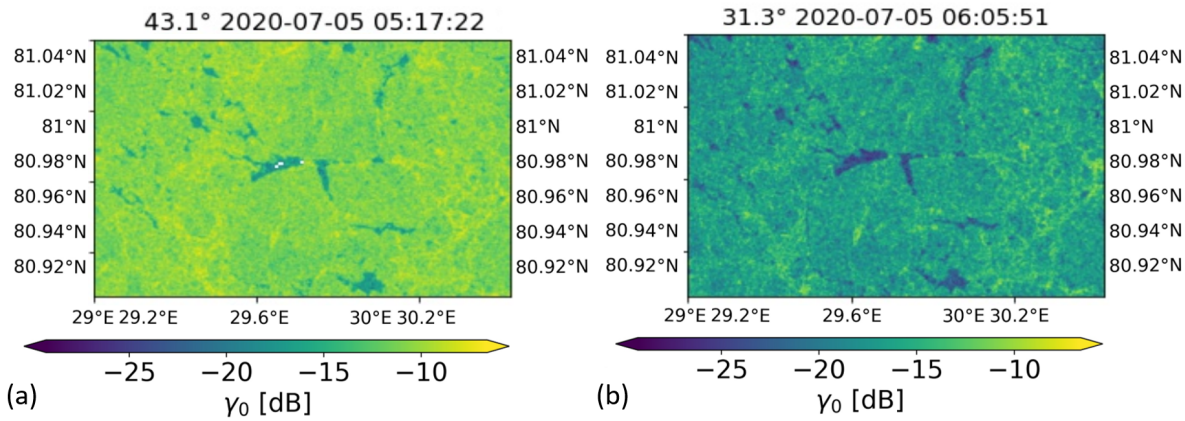

Figure 6.9: Angular dependence of the backscattering coefficient γ_0 of two consecutive observations on 5 July 2020. **(a)** at 43.1 ° and **(b)** at an incidence angle of 31.3 °.

weights is maximized for the respective distributions of γ_0. The best GMM with the optimal number of classes and their corresponding weights resulting in the largest likelihood is determined using AIC and BIC [Akaike, 1974, Schwarz et al., 1978].

6.2.3 Bayesian Segmentation of SAR Images

The weight and the mean value of the class belonging to the sub-distribution of the GMM with the lowest intensities of γ_0 are extracted and compared to an approximated intensity threshold. The threshold is used to assess whether the corresponding class contains a sufficient amount of low-intense values which can be attributed to surface water, and it is significantly large to form a separate class in the segmentation step. The Bayesian unsupervised learning algorithm was used to segment the SAR images, which are expected to contain significant amount of surface water, according to the predefined number of classes. The accuracy can be determined from the misclassification rate of the final segmentation step.

Figure 6.10 demonstrates the EM step applied to the angular-normalized SAR image acquired on 15 May 2020. BIC and AIC scores are determined after 100 iterations while fitting the GMM to the data using 1 to 5 classes, respectively. 3 classes result in the best fit with a minimum score for both criteria. The class-specific distributions of γ_0 are separable, and the weight corresponding to the lowest average value can be considered significant to be discriminable in the segmentation. Figure 6.11 shows the latent field result after segmentation with 3 classes, where every pixel indicates the class with the highest class membership probability. Patches of dark blue color belong to closed water and the remaining area is the concentration of intact sea ice.

In Figure 6.12, the segmentation results are compared to Sentinel-2 images in the visible spectrum. The class referred to 'closed water' can be associated with leads between and melt ponds on top of ice floes. The estimated SIC is compared to a reference SIC product OSI-SAF OSI-401-b in Figure 6.13 in the period from 1 September 2019 to 31

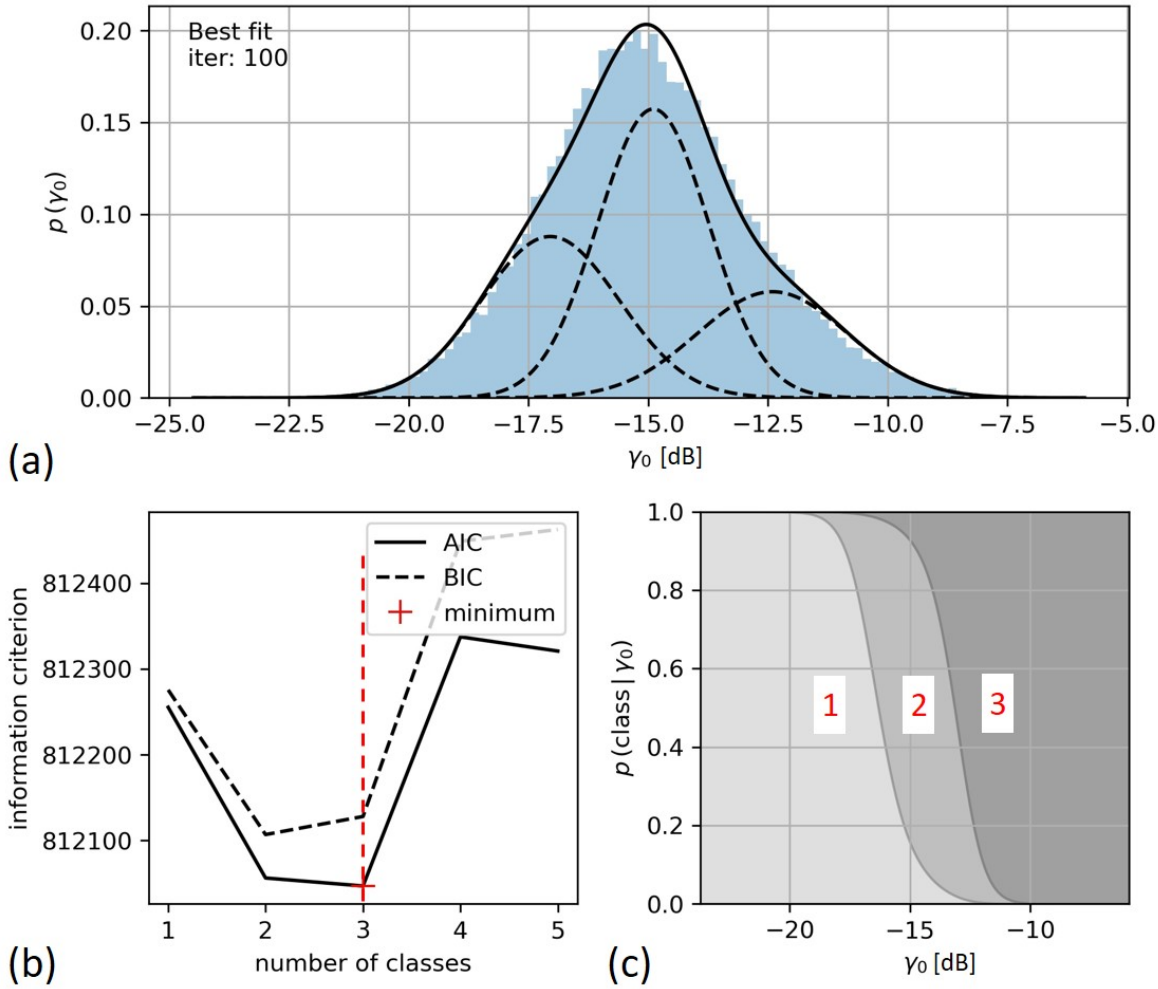

Figure 6.10: EM result after 100 iterations on 15 May 2020. **(a)** Distribution of γ_0 including the weights of the best fit; **(b)** AIC and BIC scores with its minimum value obtained for an optimal number of 3 classes; **(c)** class-specific probabilities as a function of γ_0.

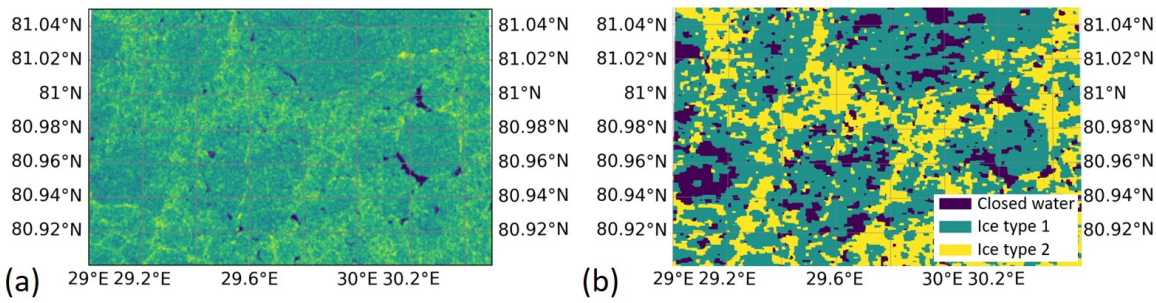

Figure 6.11: Segmentation result using 3 classes to discriminate surface water fraction from sea ice types based on a SAR image acquired on 20 June 2020.

August 31 2020. The reference product is known to underestimate SIC for thin ice and due the presence of melt-pond water [Lavergne et al., 2019]. This is in agreement with the estimated SIC showing higher values in the beginning of the freeze-up period, and during melting.

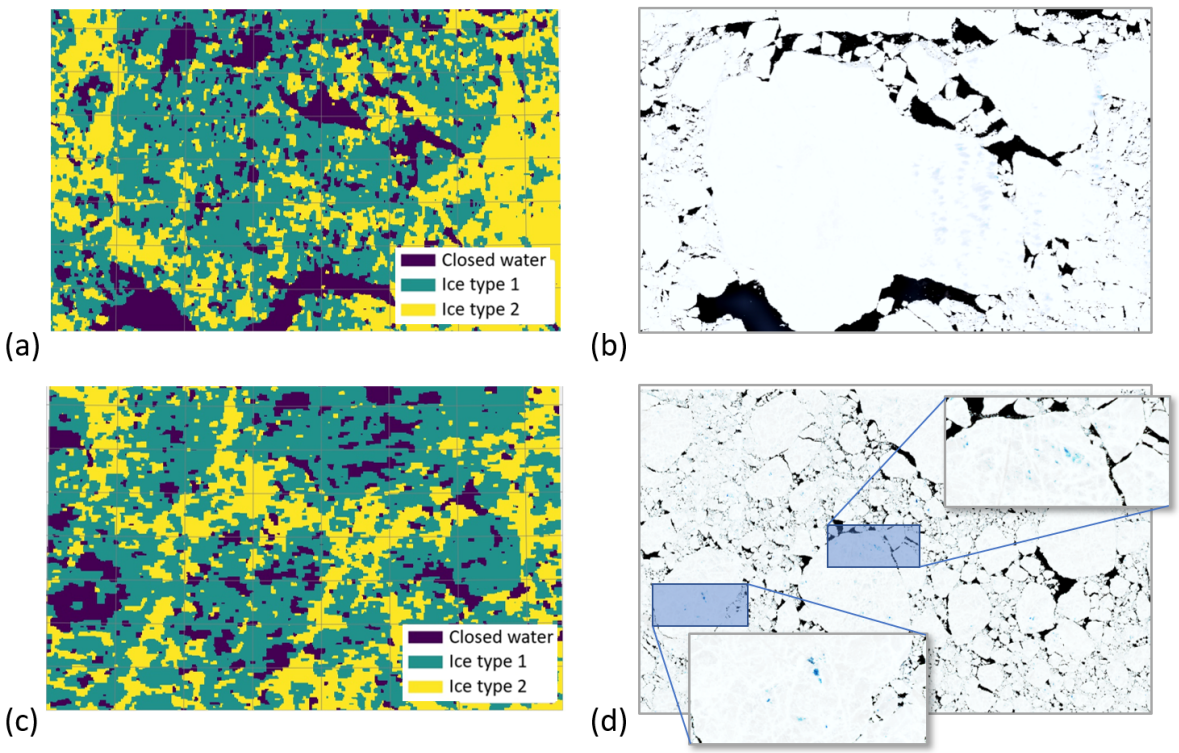

Figure 6.12: Comparison between the class results and Sentinel-2 images on two cloud-free days. The segmented class 'closed water' in **(a)** and **(c)** resembles the leads (dark black areas) and melt ponds (bright blue spots on the ice floes) which are visible in the optical images **(b)** and **(d)**.

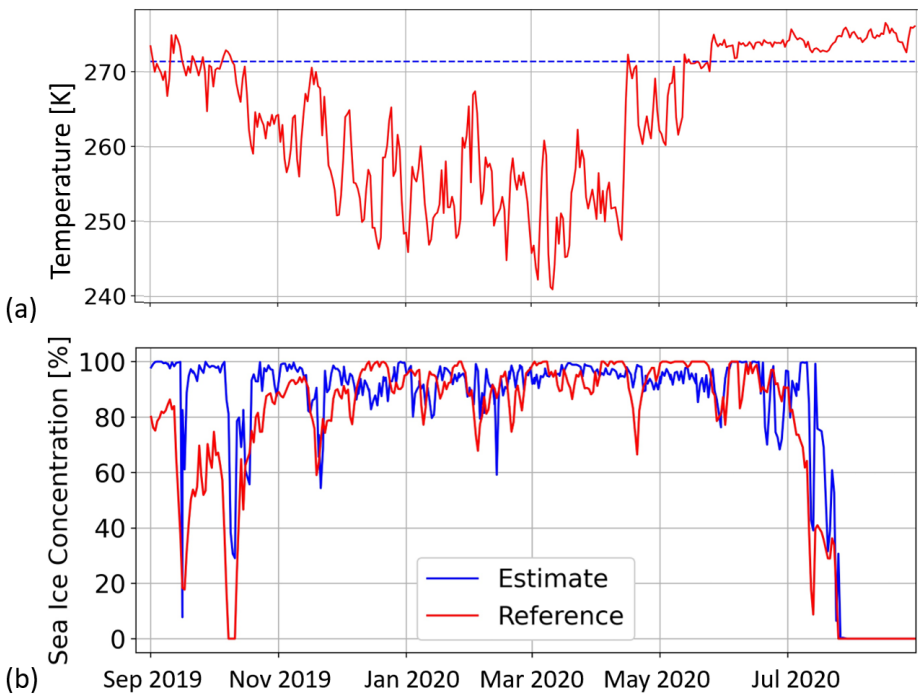

Figure 6.13: Estimated concentration of intact sea ice in comparison to OSI-SAF SIC from September 1, 2019 to August 31, 2020.

6.3 Spatial Segmentation of Arctic Sea Ice Using SMOS Data

The proposed unsupervised machine learning approach based on a Bayesian inference framework is applied to multi-incidence angle T_B data provided by the SMOS mission [Herbert et al., 2021a]. Hereby, maps of polarization ratio at multi-incidence angles are obtained from T_B observations and OSI-401-b SIC maps, and are used to segment the Arctic ocean into sub-regions based on different sea ice properties. The temporal evolution of these patterns can be analyzed in terms of cluster separability and correlation of the input features to investigate the corresponding sea ice signatures.

6.3.1 Input Feature Selection

The SMOS mission was originally designed to provide global and frequent maps of soil moisture and ocean salinity, but measurements also showed sensitivity to different sea ice properties (thin SIT and SIC). The satellite acquires multi-incidence angle (0–60 °) full polarimetric T_B in ascending (6 a.m. local time) and descending (6 p.m. local time) sun-synchronous orbit [Corbella et al., 2005]. The retrograde polar orbit (98.42 ° inclination and 758 km altitude) limits the observations to a maximum latitude of $\sim 84\,°$, resulting in missing values around the poles ('polar hole'). The input data set for this study is given by the SMOS Level 1B data product consisting of the Fourier components of T_B in the antenna polarisation reference frame. The strong discontinuities in T_B between land and sea observations lead to oscillations after image reconstruction at coastal areas (Gibbs phenomenon). These contaminated zones, as well as continental land mass, were removed in the data product. Ascending and descending SMOS observations show only small differences in T_B. Therefore, T_B of both orbits are averaged. A daily multi-angular data set with 2 ° sampling is created similar to [Gabarró et al., 2016] with T_B provided in horizontal and vertical polarizations.

The study period includes the late summer melt, and the first half of the freeze up period from 1 September to 31 December 2016. A 5-day composite of T_B is considered to guarantee full coverage of the Arctic ocean. Pixels of T_B images either consist of sea ice with ($0 < \mathrm{SIC} \leq 1$), or purely consist of OW ($\mathrm{SIT} = 0$). At frequencies < 117 GHz, Planck's equation can be simplified using the Rayleigh-Jeans approximation, and T_b is the product of the ice emissivity (ϵ) and the physical temperature (T_{Phys}) with an error $< 1\,\%$ [Ulaby et al., 1986]. T_{Phys} varies depending on the atmospheric conditions among the Arctic, and it is non-negligible in the lower microwave spectrum. Therefore, input data for segmentation are selected with the objective to correct for SIC, and to reduce the effect of spatial and temporal variability of T_{Phys} on T_B. In addition, direct inference of specific sea ice properties, particularly at the ocean-ice-boundary, is ambiguous by the fact that T_B can be sensitive to both SIC and thin SIT, and different ice types can be

mixed in low-resolution SMOS images.

In a first step, $T_{B_{(SI)}}$ was determined from the observed T_B, SIC, and the freezing point of seawater ($T_{B_{(OW)}}$) (Equation 6.16).

$$T_B = \alpha\, T_{B_{(SI)}} + (1-\alpha)\, T_{B_{(OW)}} \quad \text{with} \quad \alpha \in [0,1] \tag{6.16}$$

Hereby, OSI-401-b SIC maps are provided in a polar stereographic projection grid at 10-km resolution and are regridded and upscaled to SMOS resolution using k-d-tree resampling – a fast nearest-neighbour interpolation method [Bentley, 1975]. Images are resampled by recursively splitting the grid into subsets to evaluate the nearest neighbors within a defined radius of influence according to the resolution of the measurements. $T_{B_{(OW)}}$ are determined at different incidence angles and polarizations by evaluating the coldest values obtained for observations with low SIC located at latitudes above 75 °N. SIC is often underestimated with respect to SIT, resulting in an overestimation of T_B, which particularly influences the segmentation of areas covered by thin ice along sea ice edges. Therefore, a SIC threshold of $\alpha = 0.5$ was chosen to provide an OW mask, and to exclude observations classified with low SIC, which limits the overestimation error.

In a second step, to account for variations in T_{Phys}, the PR is computed as the normalized difference between vertically and horizontally polarized values ($T_{B_{(SI,V)}}$ and $T_{B_{(SI,H)}}$) as follows

$$\mathrm{PR} = \frac{T_{B_{(SI,V)}} - T_{B_{(SI,H)}}}{T_{B_{(SI,V)}} + T_{B_{(SI,H)}}} = \frac{\epsilon_{(SI,V)} - \epsilon_{(SI,H)}}{\epsilon_{(SI,V)} + \epsilon_{(SI,H)}}, \quad \text{with} \quad T_{B(SI)} = \epsilon_{(SI)}\, T_{phys}, \tag{6.17}$$

which leads to an expression of their emissivities that is independent of T_{Phys}, having the advantage of enhancing the sensitivity to the actual sea ice composition. $T_{B_{(SI,V)}}$ is higher than $T_{B_{(SI,H)}}$ with larger differences for increasing incidence angles. Also, the emissivity depends on the optical path length through sea ice, and PR increases for observations at higher incidence angles.

Figure 6.14 indicates the relation between PR and SIT obtained from vertically and horizontally-polarized T_B, as a function of incidence angle and sea ice type, determined using a RTM at 1.4 GHz. The model assumes a horizontally-layered column of sea ice above water (without snow on top) using empirically determined values for Arctic sea ice conditions [Menashi et al., 1993]. PR‘s obtained for high incidence angles show sufficient sensitivity range over ice-covered area with values reaching from 0 (thick ice, saturation) to ~ 0.4 (thin ice) and its distribution depends on the observed period. Selecting PR values for high angles increases the content of independent information on the sea ice, whereas values at lower angles are more likely to contain redundant information, which may lead to segmentation biases. The aim was to select an appropriate set of multi-incidence angle observations as input features for segmentation. PR‘s obtained for high incidence angles

show sufficient sensitivity range over ice-covered area with values reaching from 0 (thick ice, saturation) to ~ 0.4 (thin ice, and its distribution depends on the observed period). Below 30 °, PR almost does not vary with SIT, while there is a clear dependence between SIT and PR for higher angles. Changing the sea ice type does not lead to significant changes in PR. Selecting PR values for high angles increases the content of independent information about sea ice, whereas values at lower angles are more likely to contain redundant information, which may lead to segmentation biases. A total of three high angles with sufficient distance (here 8 °) covers a large range of PR without much overlap when considering a sensitivity up to $\sim$0.5 m of SMOS. The observations at 40 °, 48 ° and 56 ° were selected as relevant input features for segmentation.

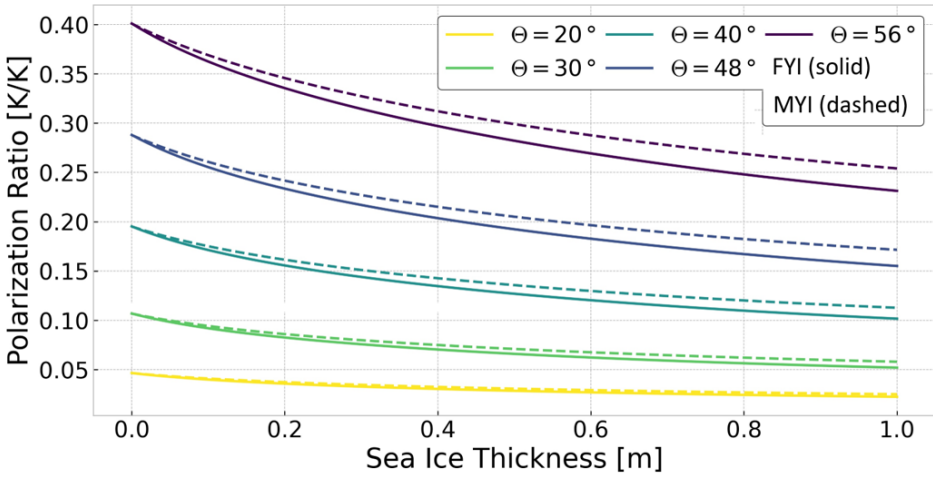

Figure 6.14: Relationship between PR and SIT as a function of incidence angle and sea ice type – FYI and MYI, using a RTM for emissions operating at L-band and empirically determined sea ice properties.

Prior to segmentation, the number of classes was predefined regarding the distribution of PR values. During late summer melt, only two significant classes are expected, comprising the remaining thick MYI and regions of thinner ice. With the start of the freeze-up period after mid-September, newly-formed sea ice and hence high PR values become more abundant to be captured in the segmentation. The choice of a new significant class is further approved by an evaluation of cluster separability subsequent to segmentation.

The choice of the appropriate number of classes is justified from the distribution of input features and the class separability. Figure 6.15 shows the marginal distribution of the PR at an incidence angle of 56° at 4 particular dates including the end of summer melt and the early freeze-up. PR distributions are shown for segmentation with 2 and 3 classes, respectively. During late summer melt until sea ice minimum (September 10, 2016), the choice of two classes was expected from the shape of the PR distribution. With the beginning of the freeze-up period, higher PR values become more frequent, and an additional class is expected. Class separability is indicated by the Geometric Separability Index (GSI) [Thornton, 1998], and was obtained subsequent to segmentation. As of the

segmentation step of 16 September 2016, the segmentation with a selection of 3 classes leads to a higher separability.

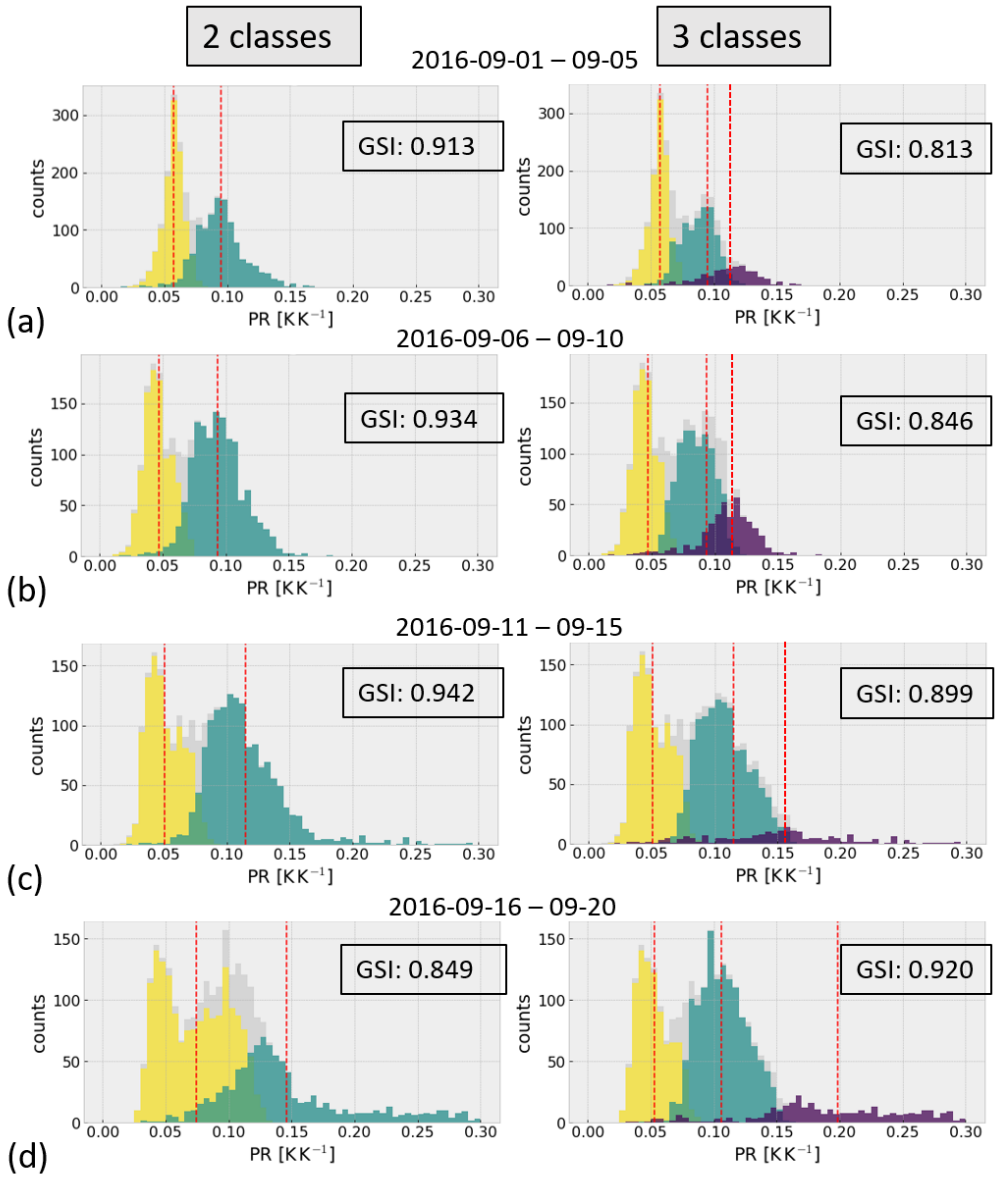

Figure 6.15: Distribution of PR values at 56° incidence angle for late summer melt and early freeze up from 1 September to 31 December 2016, regarding 5-day intervals (**(a)**–**(d)**) and segmentation with 2 classes (left-hand side) and 3 classes (right-hand side), respectively. Class mean values (red vertical lines) and global separability (GSI) validate the choice of the adequate number of separable classes.

6.3.2 Segmentation Results

Results of the Bayesian segmentation can be presented regarding the obtained patterns in physical space, and the location and orientation of clusters in feature space. The information-theoretic measure of entropy H is used to provide model uncertainty. It was initially defined by [Shannon, 1948] in the context of communication and since then has

been adapted to geosciences [Goodchild et al., 1994, Wellmann and Regenauer-Lieb, 2012]. It is used to distinguish well-classified from uncertain regions and is defined by

$$H(x_i) = -\sum_{l=1}^{L} p(x_i)_l \log\left(p(x_i)_l\right), \tag{6.18}$$

where $p(x_i)_l$ denotes the probability in the physical space of pixel i to belong to class l. H can reach values close to zero (pixel clearly assigned to one class) and $H_{max} = L[1-\log(L)]$ (uniform distribution for L classes).

Latent Field in Physical Space

Figure 6.16 shows and example of one of the PR input features at an incidence angle of 56 °, the resulting latent field and the model uncertainty quantified by information entropy, respectively. The latent field indicates spatial patterns, which are acquired from the final iteration of the segmentation by assigning the class with highest probability to every pixel. Pixels with the probability to belong to two or more clusters have larger entropy and reflect therefore uncertain pixels. These pixels comprise regions at the boundary between classes and pixels, which are generally difficult to assign to any cluster. In the latter case, these pixels may point out sub-regions with different sea ice properties (anomalies), which are characterized with high model uncertainty.

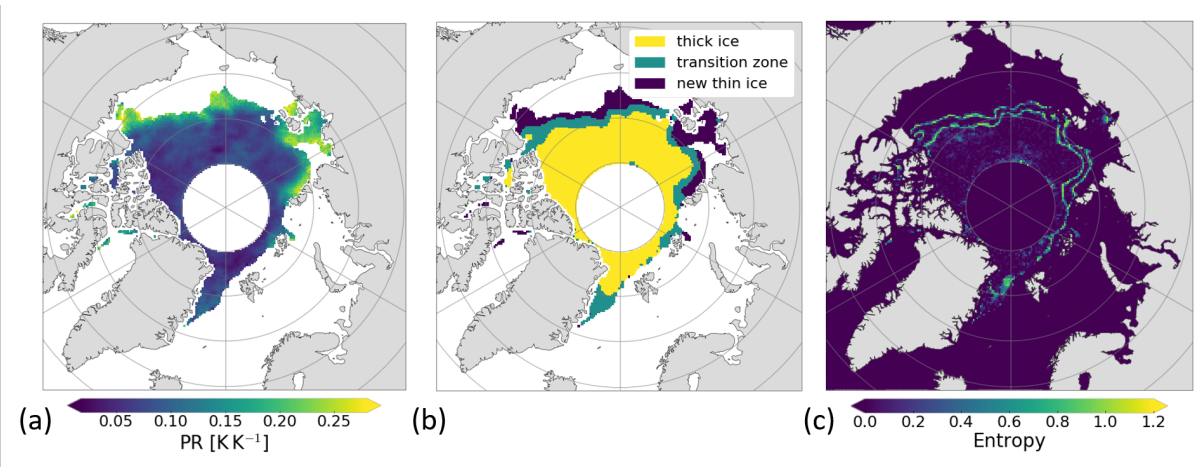

Figure 6.16: Segmentation result between 24–28 October 2016. **(a)** PR for an incidence angle of 56 °; **(b)** Latent field result for three classes; **(c)** Model uncertainty represented by information entropy based on label probabilities.

The segmented spatial patterns are compared to those of the SMOS L3 SIT product, provided by the Alfred Wegener Institute for Polar and Marine Research (AWI) for Polar and Marine Research [Tian-Kunze et al., 2014]. Figure 6.17 visualizes the latent field result in comparison to SIT-SMOS maps at the segmentation step intervals 19–23 October, 8–12 November, and 23–27 December 2016. SIT mean values were computed according to the indicated spatial classes in each segmentation step, and averaged values are deter-

Table 6.2: Summary of the temporal evolution of classes, evaluated within the freeze-up period from 15 October to 31 December 2016. Comparison of PR cluster mean values and StDev at 56° incidence angle, including GSI, with the SIT-SMOS product.

Class	Label	PR mean	PR StDev	GSI	SIT-SMOS [m]
0	Thick ice	0.061 ± 0.005	0.014 ± 0.004	0.95 ± 0.02	1.24 ± 0.010
1	Transition zone	0.112 ± 0.012	0.028 ± 0.006	0.83 ± 0.04	0.54 ± 0.24
2	New thin ice	0.187 ± 0.03	0.048 ± 0.009	0.83 ± 0.08	0.13 ± 0.07

mined during freeze up from 15 October to 31 December 2016. The three classes can be associated to different ice thickness (in meters) of 1.24 ± 0.10, 0.54 ± 0.24 and 0.13 ± 0.07, respectively. The classes are labeled as (0 $\widehat{=}$ thick ice up to sensor saturation), (1 $\widehat{=}$ transition zone with higher thickness variability, containing various ice types), and (2 $\widehat{=}$ newly-formed thin ice).

Table 6.2 summarizes the obtained class mean values and standard deviations, averaged over the freeze-up period from 15 October to 31 December 2016. At each segmentation step interval, SIT mean values for each class are calculated according to the spatial patterns of the latent field result. The obtained values at each segmentation step are then averaged over the freeze-up. The classes 0 and 2 show less variation and form stable clusters along the entire period, whereas class 1 contains higher variation. All three classes show sufficient separability along the entire period.

Clusters in Features Space

Figure 6.18 shows the distribution of the multi-incidence angle PR and the obtained clusters in the feature space. In Figure 6.18a, the distribution of the input features are presented for each incidence angle, showing an increasing dynamic range of PR for higher incidence angle. The means of the obtained clusters (Figure 6.18b) are generally increasing for higher incidence angles and show a different slope within the same class. The multivariate Gaussian distributions in marginal features space between 48 ° and 56 ° are illustrated in Figure 6.18c. The correlation between the input features is generally higher for thick ice, resulting in a well-determined cluster with high intra-cluster cohesion. In contrast, newly-formed thinner ice shows less correlation between input features. This enables discrimination of classes with similar surface characteristics, to which multi-incidence angle observations show a different signature. However, sea ice is a complex medium and sea ice growth can occur under rougher or calmer ocean conditions, causing newly-formed ice to be heterogeneous. These differences in the origin of sea ice formation might be captured in the input features, indicated by a broader distribution in marginal features space. On the contrary, the structures of multi-year thick ice appear more homogeneous.

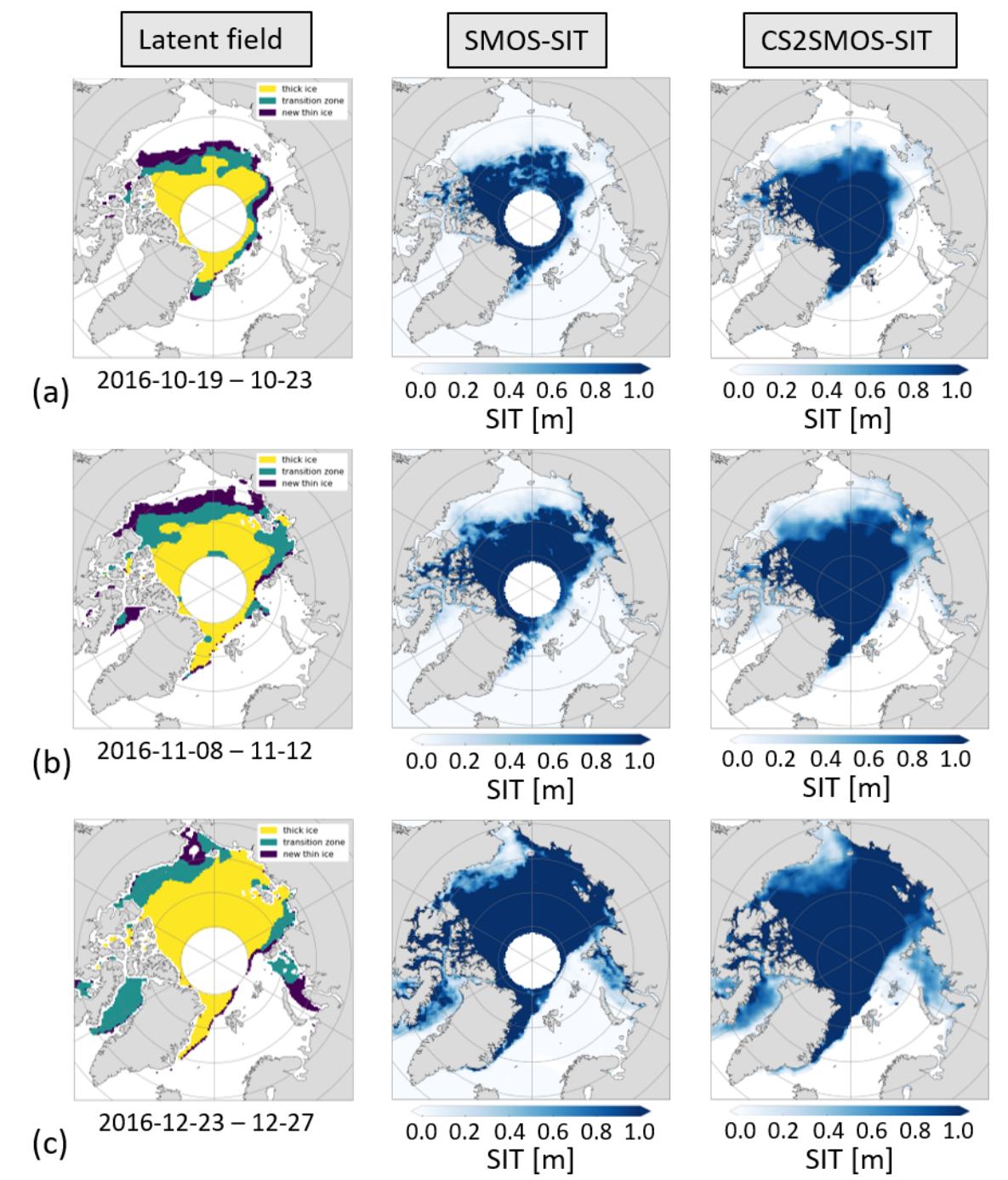

Figure 6.17: Comparison of the obtained latent field result with SIT maps of the products SIT-SMOS and SIT-CS2SMOS, averaged over the corresponding segmentation period (5-day interval). Class 0 predominately contains consolidated thick ice beyond the sensitivity range of L-band $>0.6\,\mathrm{m}$ (sensor saturation), class 1 refers to a transition zone of multiple thickness and types, and class 2 can be attributed to newly-formed thin ice.

6.3.3 Cluster Analysis

Sea ice properties, to which SMOS multi-incidence T_B are sensitive to, are dissimilar between classes and show similarities within the same class. Clusters in feature space can

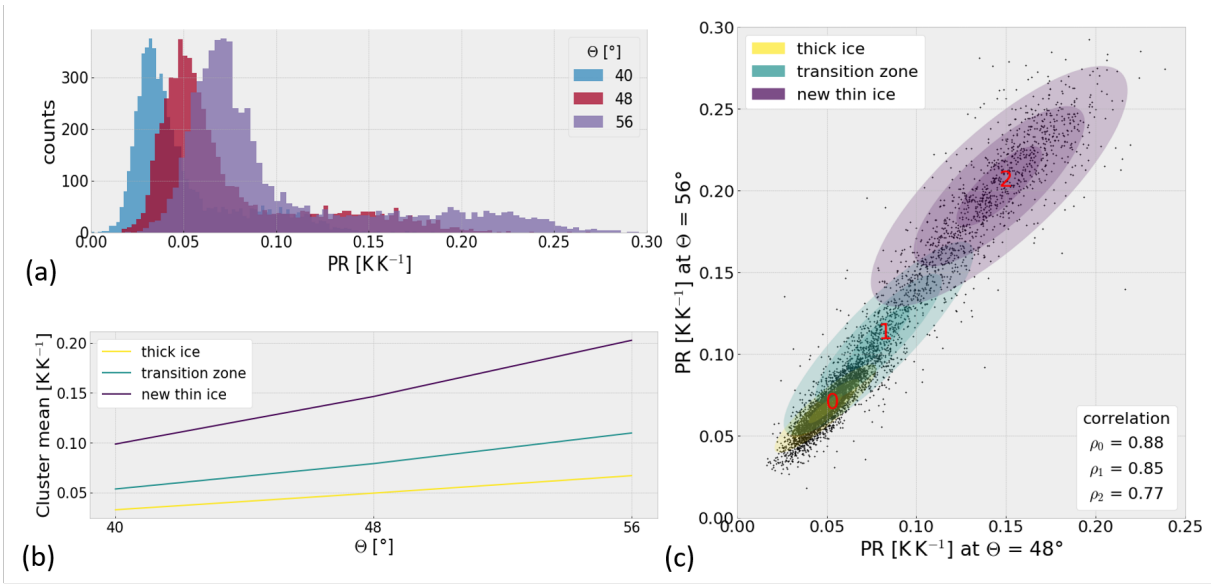

Figure 6.18: Distribution of PR and segmentation result in feature space for observations between 24–28 October 2016. **(a)** Incidence-angle specific distribution of PR. **(b)** Variation of PR cluster means with incidence angle. **(c)** Distribution of PR in marginal feature space between the incidence angles 48 and 56 ° and cluster-specific correlation.

be investigated regarding their location and orientation by analyzing the model parameters μ and $\mathbf{\Sigma}$. The correlation coefficient ρ quantifies the intra-cluster cohesion and can be used to distinguish between informative and redundant observations [Benesty et al., 2009]. It is derived for each cluster from $\mathbf{\Sigma}$ in 2D marginal space between features j and k $\in \{40°, 48°, 56°\}$

$$\mathbf{\Sigma}_l = \begin{bmatrix} \Sigma_{jj} & \Sigma_{jk} \\ \Sigma_{kj} & \Sigma_{kk} \end{bmatrix}_l = \begin{bmatrix} \sigma_j^2 & \sigma_j\,\sigma_k\rho_{jk} \\ \sigma_k\,\sigma_j\rho_{kj} & \sigma_k^2 \end{bmatrix}_l, \tag{6.19}$$

where $\sigma_{j,k}$ correspond to the standard deviations with respect to feature j, k and $\rho_{jk} = \rho_{kj}$ denote the correlation coefficients between two features, given by

$$\rho_{jk} = \frac{\Sigma_{jk}}{\sigma_j\sigma_k} = \frac{\Sigma_{jk}}{\Sigma_{jj}^{1/2}\Sigma_{kk}^{1/2}}, \quad -1 \leq \rho_{jk} \leq 1. \tag{6.20}$$

The Geometric Separability Index (GSI) [Thornton, 1998] is a distance-based measure to analyze inter-cluster separability and is widely used for cluster interpretation [Greene, 2001, Mthembu and Marwala, 2008]. GSI compares all N data points with their nearest neighbor regarding their class membership and is defined by

$$\mathrm{GSI}(f) = \sum_{i=1}^{N} \frac{(f(x_i) + f(x_i') + 1) \bmod 2}{N} \quad \text{with} \quad f(x_i) = \begin{cases} 1, & \text{if } x_i' = x_i \\ 0, & \text{if } x_i' \neq x_i \end{cases}, \tag{6.21}$$

where f is a binary target function, and x_i' is the nearest neighbor of x_i in the feature space of pixel i. GSI $\in [0.5, 1]$ and for values reaching its lower or upper limit, clusters

are completely entangled or ideally separable, respectively. In this study, both global and cluster-specific separability are estimated. GSI is computed based on Euclidean distance for all data points, and cluster-specific separability is obtained based on Mahalanobis distances $(x_i - \mu)\,\mathbf{\Sigma}^{-1}\,(x_j - \mu)^T$, considering the data points and covariances of the specific cluster [Mahalanobis, 1936]. GSI is investigated during the study period to evaluate the dynamics of the underlying sea ice properties, and the stability of the segmentation.

Arctic sea ice is segmented independently using 5-day composites into classes during the periods of late summer melt and early freeze up from 1 September to 31 December 2016. The latent field in physical space, and the corresponding multivariate Gaussian distributions of data points in feature space are presented as an example for the segmentation step interval 24–28 October 2016 (sections 6.3.2 and 6.3.2). The temporal evolution of the clusters is evaluated in section 6.3.3. Class membership and separability are assessed in section 6.3.3 to indicate cluster stability and performance of the algorithm.

Temporal evolution of clusters

Figure 6.19 shows the temporal evolution of cluster mean values and standard deviations (StDev) in marginal feature space for $\theta = 56\,°$, and the distribution of PR and the corresponding class membership at three particular dates. The late summer melt comprises two significant classes until annual SIE reaches its minimum (September 6, 2016). The evolution of clusters is compared to the mean Arctic temperature, computed from daily 2 m temperature ERA5 reanalysis data for latitudes above 75 °N and downloaded from ECMWF [C3S, 2017]. Once Arctic temperatures drop long enough below the freezing point of saline sea water ($\sim$-1.8 $°C$) to allow sufficient heat transfer towards the atmosphere, new sea ice starts to form. Hence, a third class can be determined, which is represented by a significant number of PR values above 0.15. The Thick ice class is widely stable over the entire study period. Two phenomena can be observed regarding new thin ice. Firstly, its mean value decreases and the class gradually closes up with that of the transition zone. Secondly, an overlap between clusters can be observed in relation to strong positive temperature anomalies in the Arctic. As sea ice gets thicker during freeze up, the relative amount of newly-formed ice decreases in comparison to the total SIE, and becomes less relevant in the segmentation.

Figure 6.20a shows the evolution of the number of pixels per class membership for filtered sea ice (SIC > 0.5) in comparison to the total. SIE comprises sea ice cover for SIC > 0.15 and daily data was downloaded from the data archive of the NSIDC [NSIDC, 2020]. Deviations and offsets between SIE and the total pixel counts are due to missing values within the 'polar hole' and contaminated zones at the sea-land boundary. The increase of the total number of pixels is equivalent to a monthly growth rate in SIE of about 2.5×10^6 km^2. The number of pixels consisting of newly-formed ice is broadly stable, whereas the number pixels classified as transition zone are slightly increasing during freeze

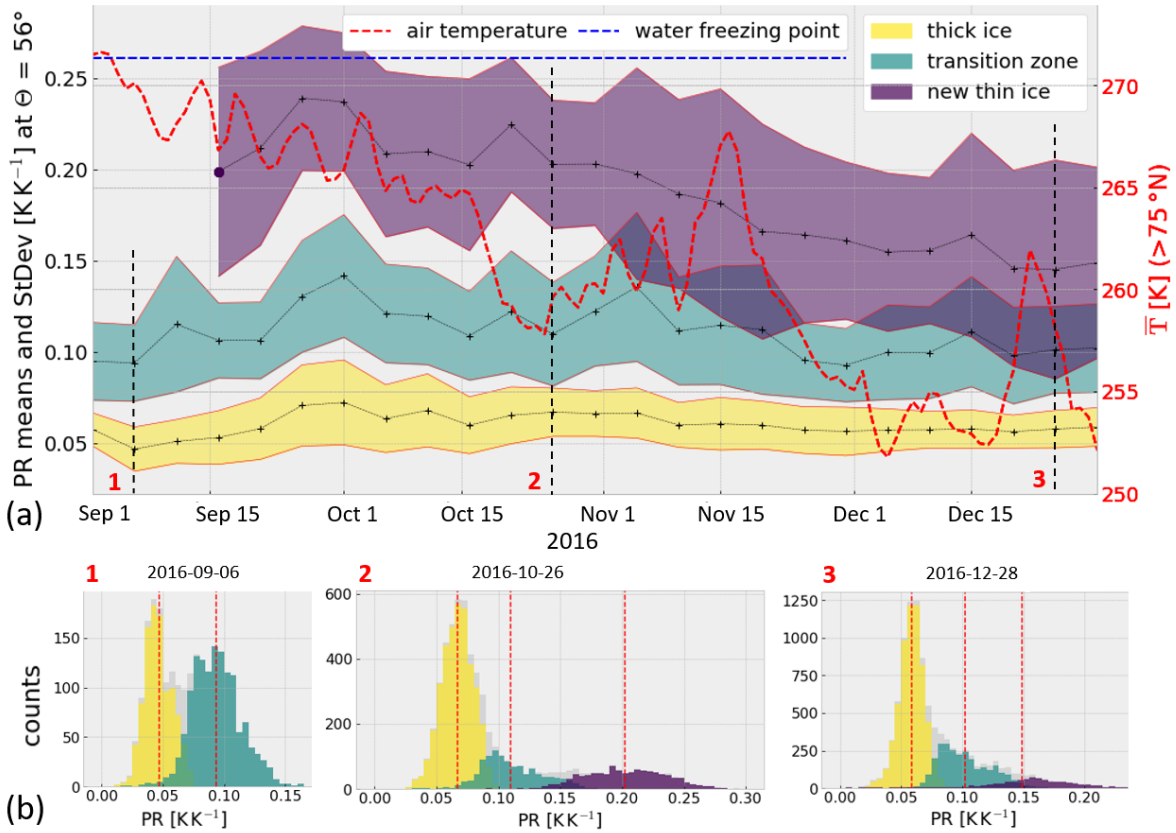

Figure 6.19: Temporal evolution of clusters. **(a)** Cluster mean values and StDevs at 56 ° and mean Arctic temperature for latitudes > 75 °N. **[b]** PR distribution with respect to class membership at three particular dates (4–8 September, 24–28 October and 24–28 December 2016).

up. As sea ice grows, thick sea ice becomes more abundant, leading to a log-normal-shaped PR distribution with increasing expected value (Figure 6.19b3). Although thin ice becomes less representative in the data during freeze up, the algorithm is still capable of separating three classes as long as sea ice formation continues.

Separability of clusters

Global and cluster-specific separability are shown in Figure 6.20b. The solid lines show the GSI for a choice of two classes in late summer melt and three classes during freeze up. High global separability is achieved during the entire study period with values around 0.9. The cluster-specific GSI indicates separable classes with mean values of 0.95, 0.83 and 0.83 for thick ice, transition zone and new sea ice, respectively. During the freeze up, thin ice starts to overlap with the transition zone and a threshold of minimum GSI needs to be defined to specify the appropriate number of classes for each segmentation step. For comparison, GSI is shown for the end of the summer melt for a segmentation with three classes (dashed lines). In this case, classes highly overlap and the choice of two initial clusters from the beginning of the study period leads to higher separability.

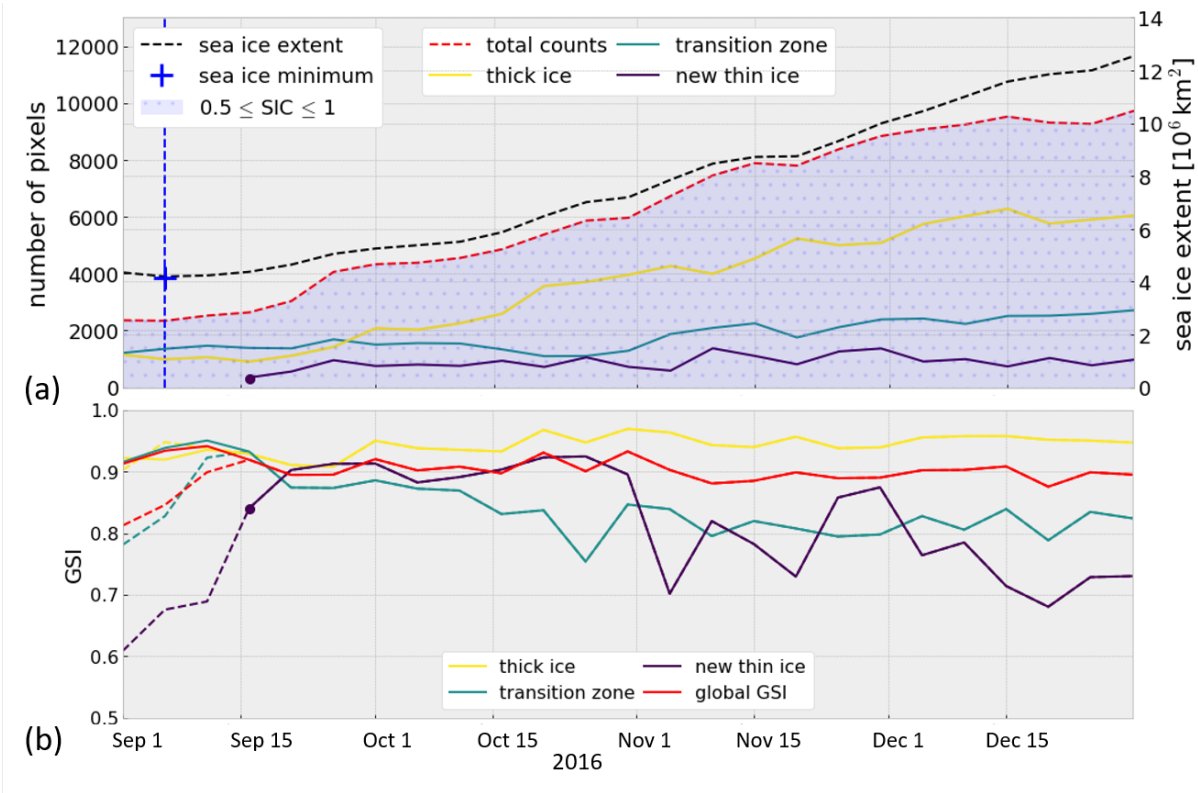

Figure 6.20: **(a)** Temporal evolution of class membership and SIE, with indicated sea ice minimum and SIC. **(b)** Global and cluster-specific GSI during the observation period, determined from nearest-neighbor evaluation using Euclidean and Mahanalobis distances, respectively.

6.4 Spatio-temporal Segmentation of Sea Ice using SMOS and AMSR2 Data

The Bayesian segmentation approach was extended to three dimensions in order to be able to analyze the joint effect of data sets from multiple sources in a complete spatio-temporal context (Section 6.1.3). Given the dynamic nature of sea ice, the algorithm is able to take into account relevant temporal and spatial correlations between consecutive observations, rather than segmenting spatial images of a temporal stack individually.

In this chapter, channels of SMOS and AMSR2 T_B data are combined to investigate the information contained in the multi-frequency observations of a CIMR-equivalent set of input features. The aim is to divide the Arctic region into relevant classes and compare the resulting spatio-temporal patterns for the common operational sea ice products SoD, SIT and SIC. Clusters are analyzed regarding their T_B mean values and intra-class cohesion in terms of correlation to understand the individual and combined sensitivity of input features to sea ice properties and related processes. The formation of classes during the freezing and melting period of sea ice is evaluated from the temporal evolution of class membership of a representative year. Class stability over time is assessed using several years of data to ensure that classes are significant in relation to their annual replicate

period. Since the algorithm is probabilistic, the class probabilities may contain relevant information for quantifying the SIT distribution for each voxel in space and time, which is of great importance for a more accurate prediction of SIT changes.

This section is structured as follows: The selection of the multi-frequency SMOS and AMSR2 T_B observations is explained in Section 6.4.1. Section 6.4.2 contains the segmentation results with the classes in feature space and the latent field patterns over time in physical space as well as the comparison with sea ice products. The analysis of the temporal evolution of classes and their physical interpretation in terms sea ice parameters is presented in Section 6.4.3.

6.4.1 Input Feature Selection

The data set for segmentation comprises the multi-frequency observations from AMSR2 and SMOS. The AMSR2 data are selected from the product 'AMSR-E/AMSR2 Unified L3 Daily 25 km Brightness Temperatures and Sea Ice Concentration' provided by the NSIDC [Markus et al., 2018]. T_B maps contain the full orbit averages at the six frequencies 6.9, 10.7, 18.7, 23.8, 36.5, and 89.0 GHz, projected on a 25-km polar Stereographic grid north provided with a total temporal coverage from July 2012 to present. Regarding SMOS low-frequency microwave observations at 1.4 GHz, measurements between 52.5–57.5° are averaged to obtain T_B maps at an incidence angle of 55°, similar to CIMR and AMSR2. As a remark, since SMAP operates at a fixed incidence angle of 40°, it is not considered as relevant input feature. Figure 6.21a shows the relation between T_B at vertical and horizontal polarization, and incidence angle for all selected frequencies, determined based on a RTM with an estimated SIT of 10 cm [Menashi et al., 1993]. Figure 6.21b indicates the relation between vertically polarized T_B and thin SIT up to 30 cm for an incidence angle of 55°. During the process of input features selection, preliminary segmentation revealed that PR values – even if the effects of the physical temperature of the sea ice are reduced – show high variability at low-concentrated areas. Also, both the observations at horizontal polarization and the first Stokes parameter do not provide sufficient information to identify old ice as a separate class along the freeze-up and are therefore not considered for segmentation. Observations at 23.8 GHz showed the highest redundancy among the potential set of input features.

The input features for segmentation consist of weekly maps of vertically polarized T_B observations at 1.4, 6.9, 10.7, 18.7, and 36.5 GHz, at an incidence angle of 55°, for a total period between July 2012 to December 2019. Prior to segmentation, the SIC images are applied to all T_B maps to mask out areas of purely OW. The number of classes for segmentation was selected so that they could be associated with superordinate categories of sea ice parameters that showed sufficient differences between classes and similarities within classes when verified with SoD, SIT and SIC, while achieving a good degree of temporal stability.

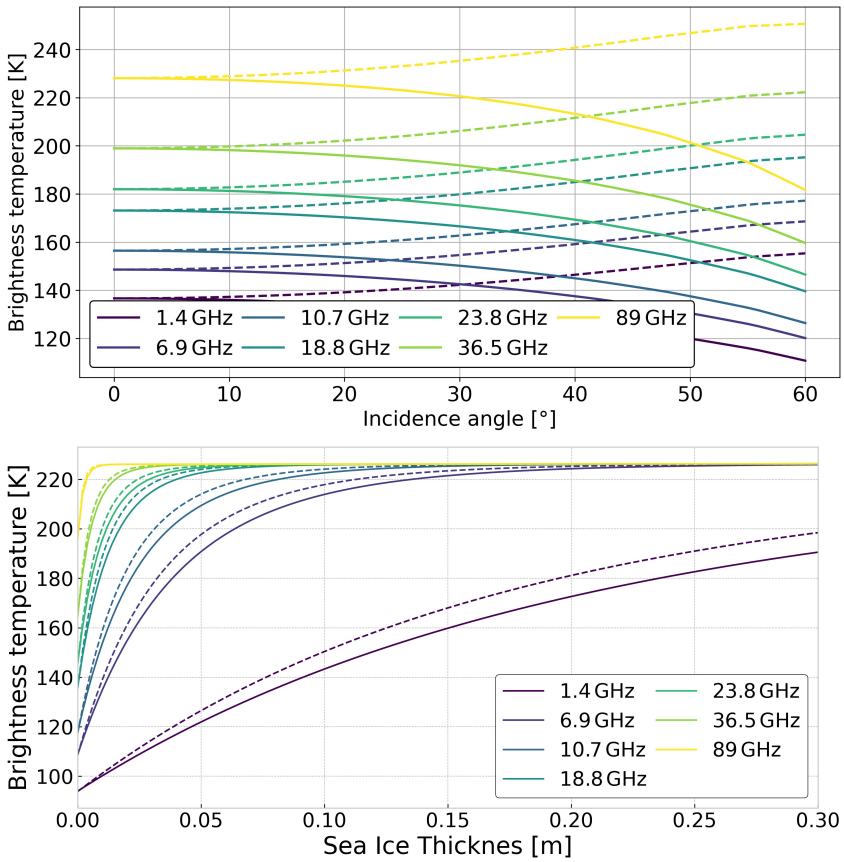

Figure 6.21: Relationship between SIT and T_B observations at different incidence angle, polarizations and frequency based on a RTM. (**a**) T_B at vertical (dashed line) and horizontal (solid line) polarization as a function of incidence angle and for multiple frequencies for SIT = 10 cm. (**b**) T_B as a function of thin SIT for multiple frequencies for FYI (solid line) and MYI (dashed line) ice.

The Kernel Density Estimation (KDE) charts of the input feature distributions in marginal features space are given in Figure 6.22 – consisting of the feature-specific density functions in the diagonal, the scatter plots representing the distributed data space between features in the upper right, and the qualitative density plots between features in the lower left. The highest correlation is given between observations at 6 and 10 GHz. These are considered the most redundant features. Observations at the lower microwave spectrum $<$ 15 GHz contain ambiguous information about sea ice, making it difficult to distinguish low-concentrated areas from regions of thin sea ice. Also, most of the data points are oriented along one linear-structured cluster with most of them located at the high-frequency ends.

If at least one higher frequency channel is considered, the distribution in marginal feature space opens up resembling a 'boomerang' shape, where a second cluster can be clearly identified. This is due to the fact that at the higher microwave spectrum the observed emissivitiy is influenced by surface scattering and volume scattering effects within the sea ice column. In addition, the penetration depth is already significantly lower than 10 cm. Thus, values oriented at the more diagonal branch represent data points of pixels

with partial SIC, and those at the steeper second cluster represent sea ice at 100 % SIC encompassing different ice types. The orientation of the second branch is tilted towards lower values, because at higher frequencies the emitted signal is more attenuated due to scattering.

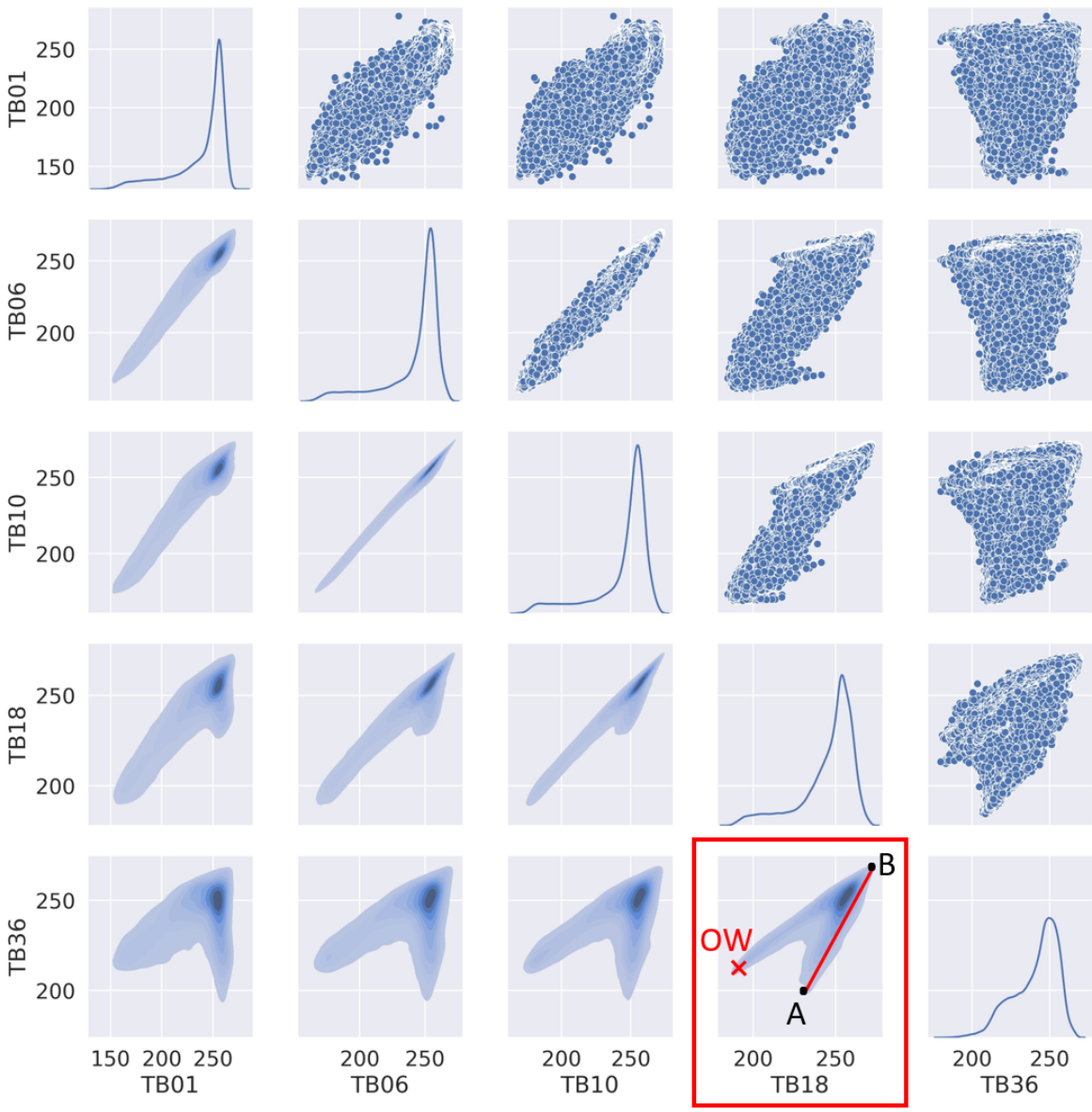

Figure 6.22: Kernel density chart of the input features consisting of the vertically polarized T_B observations at 1.4, 6.9, 10.7, 18.7, 36.5 GHz after applying an OW mask. The relationship between features is represented in terms of feature-specific density functions (diagonal elements), simple scatter plots of data points (upper right elements) and qualitative density plots (lower left elements). The distribution of data points between 18.7 and 36.5 GHz (element highlighted in red) is commonly used for evaluating SIC, where the red cross indicates the approximate position of values of OW and values along the red line between the points A and B correspond to SIC = 100 % with different sea ice types.

Current methods to provide SIC are obtained using passive microwave observations based on the NT2 algorithm or the Bootstrap algorithm [Cavalieri et al., 1984, Comiso,

1995, Cavalieri et al., 1997, Markus and Cavalieri, 2000, Comiso and Nishio, 2008, Markus and Cavalieri, 2009]. The Bootstrap algorithm mostly evaluates T_B observations at 18 and 37 GHz (see highlighted distribution in Figure 6.22) and determines which data points are associated to OW (values already masked prior to selection), SIC of 100 % with different ice types (red line), and the values in between corresponding to partial SIC. To obtain SIC, the scatter plot is evaluated by interpolating the distributions between two tie points (the center points of classes corresponding to OW and sea ice with SIC of 100 %), which are continuously changing due the sensitivity of observations to physical temperature of sea ice.

6.4.2 Segmentation Results

The Arctic region is segmented into 6 classes based on input features with a temporal resolution of two weeks covering a full year from 1 September 2016 to 30 September 2017. The segmented classes can be visualized in terms of the evolution of the latent field for each temporal slice in physical space, and the location (mean values) and orientation (covariances) of the clusters of data points in feature space. Temporal evolution of classes can be analyzed by looking at their periods of occurrence, where class membership is represented by the amount of voxels. Over the course of a year, classes grow or melt horizontally as they take area from or loose area to OW, or they may change to another class due to changes in thermal conditions. Two transition scenarios can be distinguished, a new class can emerge or an existing class can increase in terms of its class membership. The emergence of a new class is determined by a temporal onset, whereas two existing classes can merge gradually into one another.

The spatial representation of classes is presented in Figure 6.23 for 28-day intervals along the entire segmentation period. The top three rows contain the images associated with the freeze-up period between mid-September 2016 to mid-March 2017, and the bottom two rows show those along the summer melt from May to September 2017. First, the class labels are randomly assigned during segmentation and then classes are relabeled according to its ascending mean values of the SMOS input feature, i.e. label 0 corresponds to the class with the lowest and label 5 to the class with the highest T_B values obtained at 1.4 GHz.

Figure 6.24 shows the T_B observations in the marginal feature space between 18.7 and 36.5 GHz, which is a relevant configuration for common SIC retrieval algorithms (highlighted in Figure 6.22). The obtained class means are indicated by red numbers and the covariances by ellipses representing the corresponding 2D Gaussian distributions. Class 0 includes the data points near OW and represents areas of low SIC and predominantly thin ice. Classes 3–5 are situated on the red line corresponding to a SIC $\sim$ 100 % and represent different types of sea ice. Hereby, Class 3 covers areas with predominately younger sea ice, and Class 5 refers to older ice with more attenuated emissivity at higher microwave

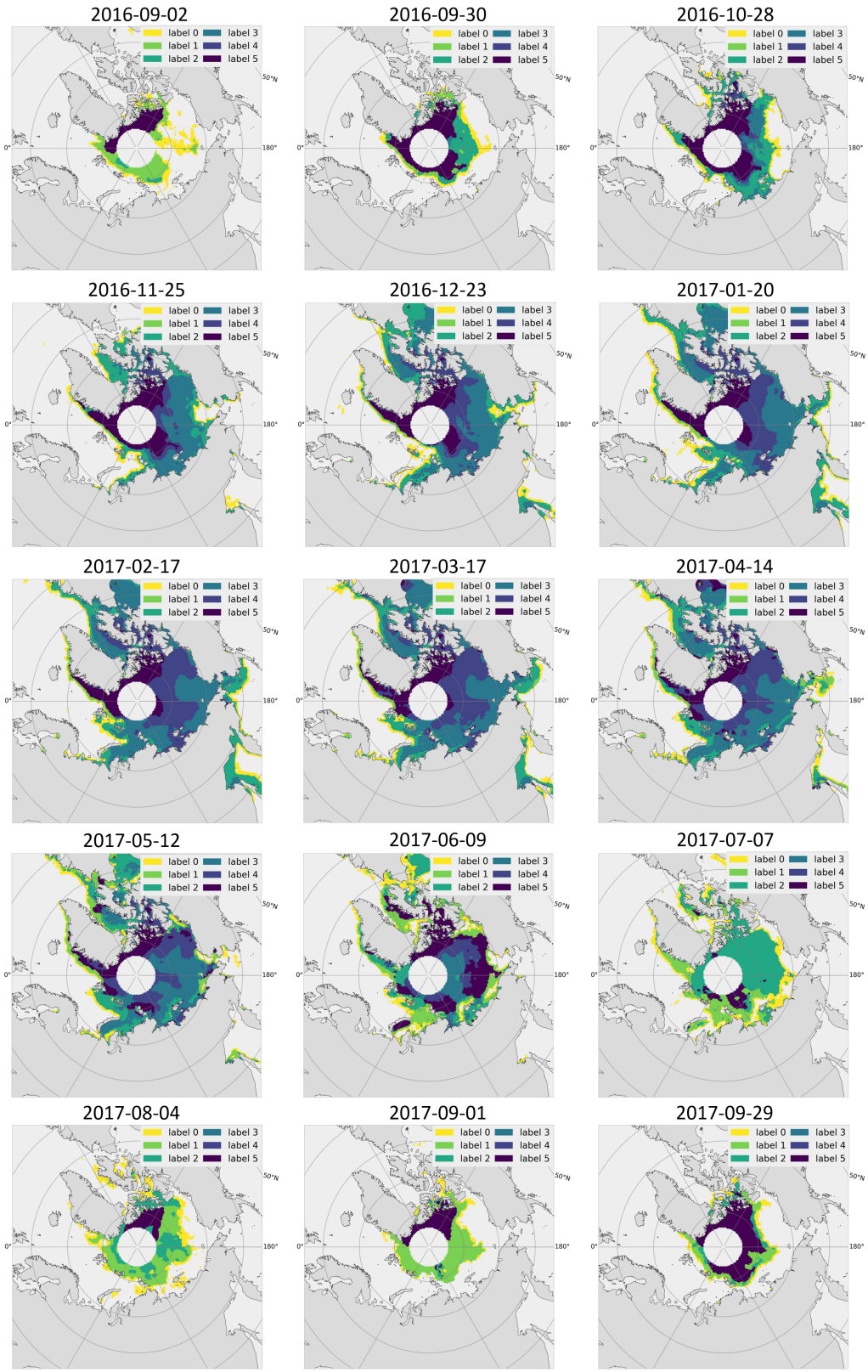

Figure 6.23: Latent field result in terms of spatial patterns represented in a four-week interval for a segmentation with 6 classes for the period from September 2016 to September 2017.

frequencies. Classes 1 and 2 represent observations over areas with partial SIC and presumably different SIT ranges. Class 1 contains observations encompassing a broad range

of 'mixed states' in terms of SIC, SIT and types – which can be typically associated with wet conditions during summer melt – and Class 2 follows the natural freezing of sea ice under dry and cold conditions.

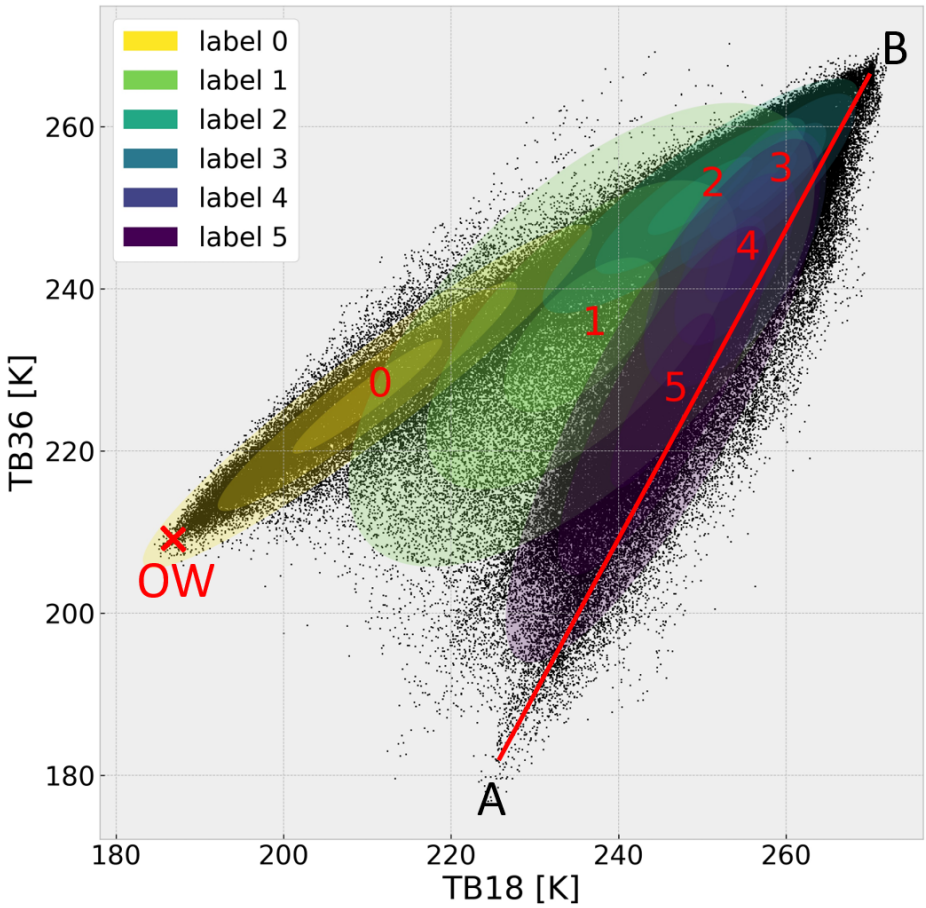

Figure 6.24: Clustering result in marginal feature space between T_B observations at 18.7 and 36.5 GHz with indicated class means and covariances. Values of OW and sea ice with SIC ∼ 100 % tend to be located close to the red cross and along the red line, respectively.

The temporal evolution of the number of data points belonging to each class is presented in Figure 6.25. Figure 6.25a shows the total amount of voxels for each class, where the sum over all classes represents the actual sea ice extent (remark: the amount of data points belonging to the polar observation hole is not considered here). Figure 6.25b illustrates the relative amount of class membership to better illustrate the evolution of classes. The emergence and transition of classes is compared with changes in average air temperature at lower latitudes between 70–75 °N and higher latitudes between 80–85 °N calculated from daily ERA5 reanalysis temperature data at 2 m [C3S, 2017].

During the segmentation period of one year, the classes can be related with the formation and melting of sea ice. As aforementioned, Class 0 indicates the low-concentrated areas and thin ice throughout the entire freeze-up. Class 5 represents the remaining old ice of the previous summer period. From mid-September, new ice is formed in the centre

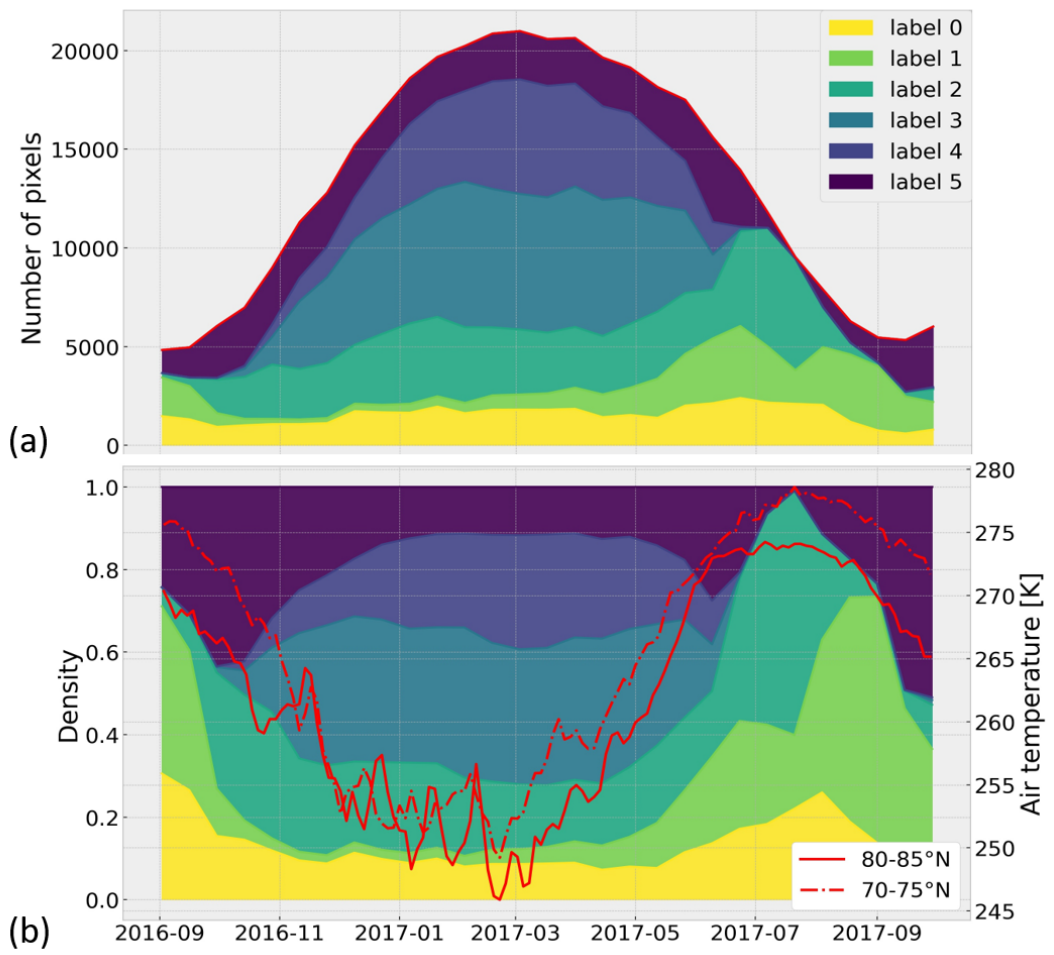

Figure 6.25: Temporal evolution of classes for a one-year segmentation period from September 2016 to September 2017, representing (**a**) the total amount and (**b**) the relative amount of voxels for each class membership. The red curve shows the average air temperature at 2 m in the latitude interval between 70 and 75°N (dashed line) and 80 and 85°N (solid line).

of the Arctic and thickens rapidly into thin FYI (Class 2). The classes 3 and 4 occur from October and November, when FYI continues to develop into medium and thicker FYI, respectively. Class 1 is only represented along the sea ice margin of the Greenland Sea during freeze-up. The physical characteristics of the classes during freeze-up remains similar under cold conditions until sea ice reaches its maximum extent in early March 2017, which is marked by the intrusion of higher temperatures into the Arctic.

During summer melt, classes 1, 2 and 5 can be qualitatively associated with three stages of wet surface conditions, in dependence of their prevailing temporal and latitudinal extent. Class 5 can be largely associated with thawing snow and initial melt of sea ice during the early summer (Stage 1). From mid-May to mid-June, air temperatures at lower latitudes between 70 and 75°N start to exceed the freezing point of saline water (~ 271.3 K) and Class 5 begins to expand (see Figure 6.24, 30 September 2016). From mid-June to the end of July, when air temperatures are above freezing throughout the Arctic, Class 5 largely shifts to higher latitudes – referring to similar wet conditions as initially observed

at lower latitudes. Around the same time, Class 2 begins to grow significantly in lower latitudes until it covers almost the entire central Arctic by mid-July and can be associated to sea ice under warmer conditions (Stage 2). In August, when temperatures again start to drop in the central Arctic, Class 2 transitions back to Class 5 in the area of the previous year's old ice. Class 1 spreads at lower latitudes where temperatures still remain high enough to cause further melting (Stage 3). Ultimately, from mid-September, Class 5 occupies the entire Arctic sea ice surface left after the summer melt, representing the refrozen old ice of the impending freeze-up. As temperatures continue to drop, new sea ice begins to form, creating new classes of thin sea ice with low concentrations.

6.4.3 Class Analysis and Interpretation

Classes can be analyzed to understand how the combination of a set of selected input features leads to the formation of classes and how these classes can be related to the underlying sea ice properties. For class interpretation the segmentation results have to be robust, i.e. classes need to be temporally stable and spatially consistent in terms of their physical characteristics. Thus, the segmented spatial patterns of classes are compared with values of sea ice parameters – including images of SIT, SIC and SoD – of operational products.

Cluster Analysis

Based on the similarities and differences of the observations and the radiometrical properties of sea ice, the algorithm segments the input features into a number of most significant classes. Figure 6.24 illustrates how these classes can be understood as multivariate Gaussian distributions of data points in marginal feature space. How the observations contribute to the formation of the classes can be inferred by the location and orientation of the clusters in the feature space, represented by the statistical model parameters (means and covariances). The cluster mean values can be analyzed in an absolute manner and relatively between classes to reveal information regarding the different radiation properties of the observations and how classes can be referred to the underlying composition of sea ice. The covariances quantify the relationship between observations and they indicate the level of redundancy and the significance of the selected set of input features and the resulting classes. The Pearson correlation coefficient obtained from the covariance matrix shows the linear dependence between the observations. In the following, the class-specific mean values and correlation are assessed for the corresponding set of input features and classes.

The observed T_Bs are affected by the emissivity of the radiating layer. The mean T_B values for each feature and individual class is shown in Figure 6.26. Class labels (0–5) are determined in ascending order regarding the class mean values of the T_B observations at 1.4 GHz (TB1), indicating the highest dynamic range due to its sensitivity to

both thin ice and SIC. All observations contribute to the formation of the Classes 0–2 with decreasing sensitivity ranges for higher frequencies and different dispersion of values. The information contained in the high-frequency observations at 10.7, 18.7, and 36.9 GHz enables the algorithm to distinguish between the Classes 3–5, where low-frequency observations at 1.4 and 6.9 GHz are saturated. At almost all frequencies, the highest T_B values are given for observations associated to Class 3, which can be related to intact FYI under cold conditions with a SIC $\sim 100\,\%$. For fully-concentrated sea ice, the higher the frequency, the more attenuated the emitted signal due to scattering processes. For instance, volume scattering from MYI observed at L-band is lower than for observations at higher frequencies. This is because the wavelength of the former exceeds considerably the typical air bubble size and emissions are less affected. In addition, the older the sea ice, the more pronounced the attenuation (transitioning from Class 3 to 4 and finally to 5), because more brine inclusions are gradually replaced by air bubbles, leading to a higher number of scattering events. Accordingly, Classes 0–2 correspond to sea ice of varying concentration or wet surface conditions, while Classes 3–5 represent completely covered areas whose emissivity changes due to scattering phenomena. Most of the ice parameters that affect the emissivity are explicitly dependent on the ice temperature – which influences the dielectric constant of the material – resulting in increasing absolute T_B values for higher temperatures.

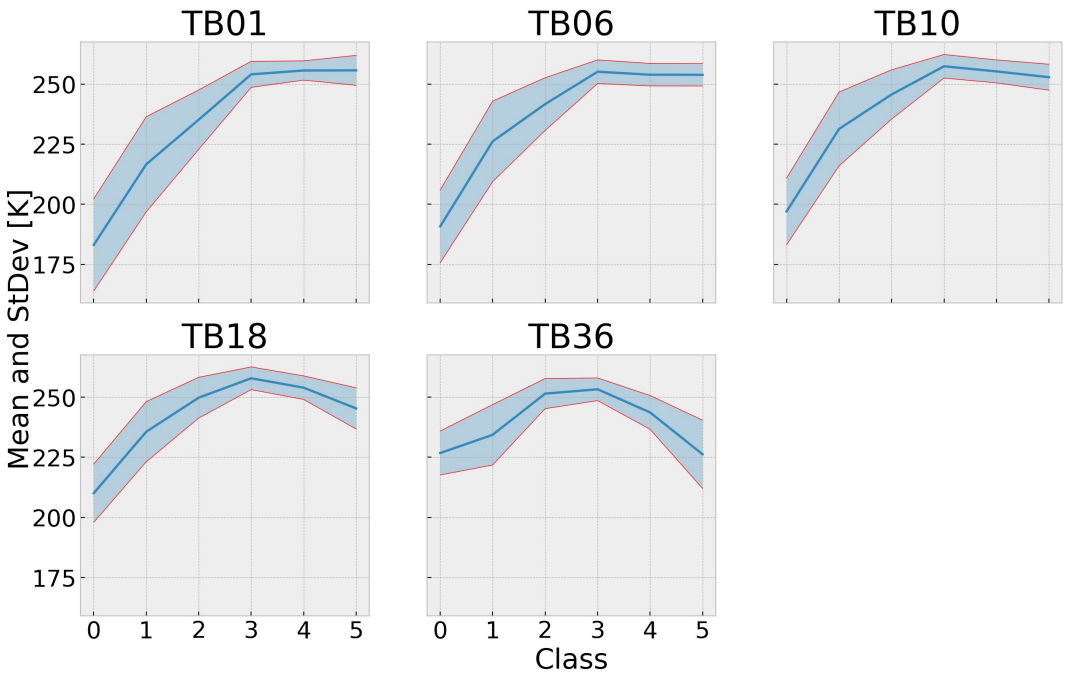

Figure 6.26: Features-specific T_B mean values and StDev for all classes, which are numbered according to ascending values of the feature corresponding to SMOS observations at 1.4 GHz. Classes 0–2 are formed based on the information contained in all input features, while Classes 3–5 can be separated mainly by the differences between the 18.7 and 36.9 GHz observations.

Since classes are formed based on the relationship between T_B values at different

frequencies, two data points whose observations differ in absolute values can be assigned to the same class, in case they are similarly sensitive to temperature changes. Information about how T_B observations are correlated allows conclusions to be drawn about which features are pivotal for the separability of a class. The feature-specific correlations for each class as a measure of intra-class cohesion are visualized in Figure 6.27. For all classes, observations at adjacent frequency bands are mostly strongly correlated with the highest between those at 6.9 and 10.7 GHz (above 0.9), whereas the correlation between the features decreases with increasing frequency difference. Classes 0, 2 and 3 have similar correlations between the input features, and the algorithm is able to distinguish the two based on the absolute T_Bs (see Figure 6.26). The absolute values of the input features for Classes 3 and 4 are similar, but the intra-class cohesion differs substantially, showing lower correlations between observations at 36.9 GHz and the other features for Class 4. Although Classes 1 and 4 emerge during summer melt and freeze-up, respectively, input features are similarly correlated. Except for Class 5, observations at 36.9 GHz are moderately or low correlated with the remaining features. The reason why the correlation of Class 5 is conceptually different may be because scattering phenomena in heterogeneous old ice vary essentially in intensity and observations at different frequencies have a different footprint. Therefore, observations cover a different variety of ice types the observed T_B values of each type and concentration are averaged and no clear relationship between the input features can be seen.

It is important to note that during the melt season the contrast between classes which rely on the observed emissivities is smaller than during freeze-up by the fact that sea ice in winter grows from the bottom of the ice column under cold conditions but in summer it melts largely from the top. The increase in both solar irradiation intensity and air temperature have the effect that a thin layer of water forms on the surface of the ice. As a consequence, surface-sensitive satellite observations during summer loose accuracy to the composition of sea ice, causing major ambiguities in the estimation of the underlying sea ice parameters. The penetration depth of microwave observations into the sea ice is limited, and depending on whether conditions are wet or dry, the underlying water is invisible, so that no direct inferences can be made about the thickness of the ice column. However, as sea ice ages, its composition at the surface and in the ice mass changes, as do the associated radiometric properties. Knowledge about sea ice age can serve as a proxy of the state of sea ice and can indicate a variety of sea ice parameters including surface roughness, melt pond fraction, and salinity. As sea ice also thickens with age, radiometric properties may be indirectly related to SIT ranges under cold conditions during freeze-up, although observations are only sensitive up to thin ice.

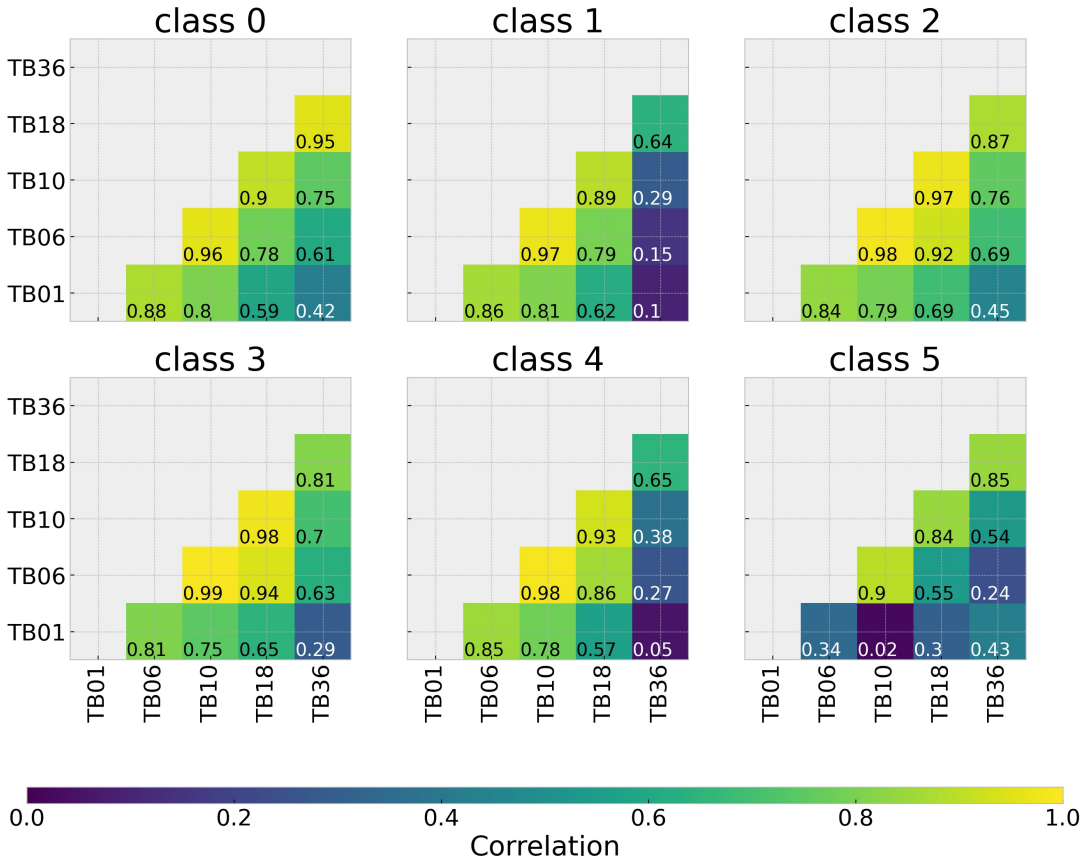

Figure 6.27: Intra-class cohesion in terms of absolute values of Pearson correlation. Classes 0, 2 and 3, as well as Classes 1 and 4 show similar correlation between features. With the exception of Class 5, the correlation between the features decreases with increasing frequency difference.

Temporal Stability

The Arctic region was segmented into 6 classes within a period of 7.5 years from July 2012 to December 2019 using input features with a temporal resolution of five weeks. Figure 6.28 shows the evolution of class membership (similar to Figure 6.25), where Figure 6.28a gives the total amount and Figure 6.28b gives the relative amount of voxels per class and time step. All classes occur in all years and overall match in terms of class size and same time period. Thus, the segmentation and the resulting classes are considered as temporally stable and significant in case at least one year of data is selected. The SIE declines approximately at a rate of 13 % per decade, relative to the 1981 to 2010 average [], and a slight decreasing trend is also visible in the sum over all classes in the observed 7.5-year period. If individual classes could be linked to SIT, then changes in the relative proportion of class membership could provide useful information about changes in SIT. However, during the observed period, there is no clear trend indicating a change in class membership in terms of loss from thicker to thinner sea ice.

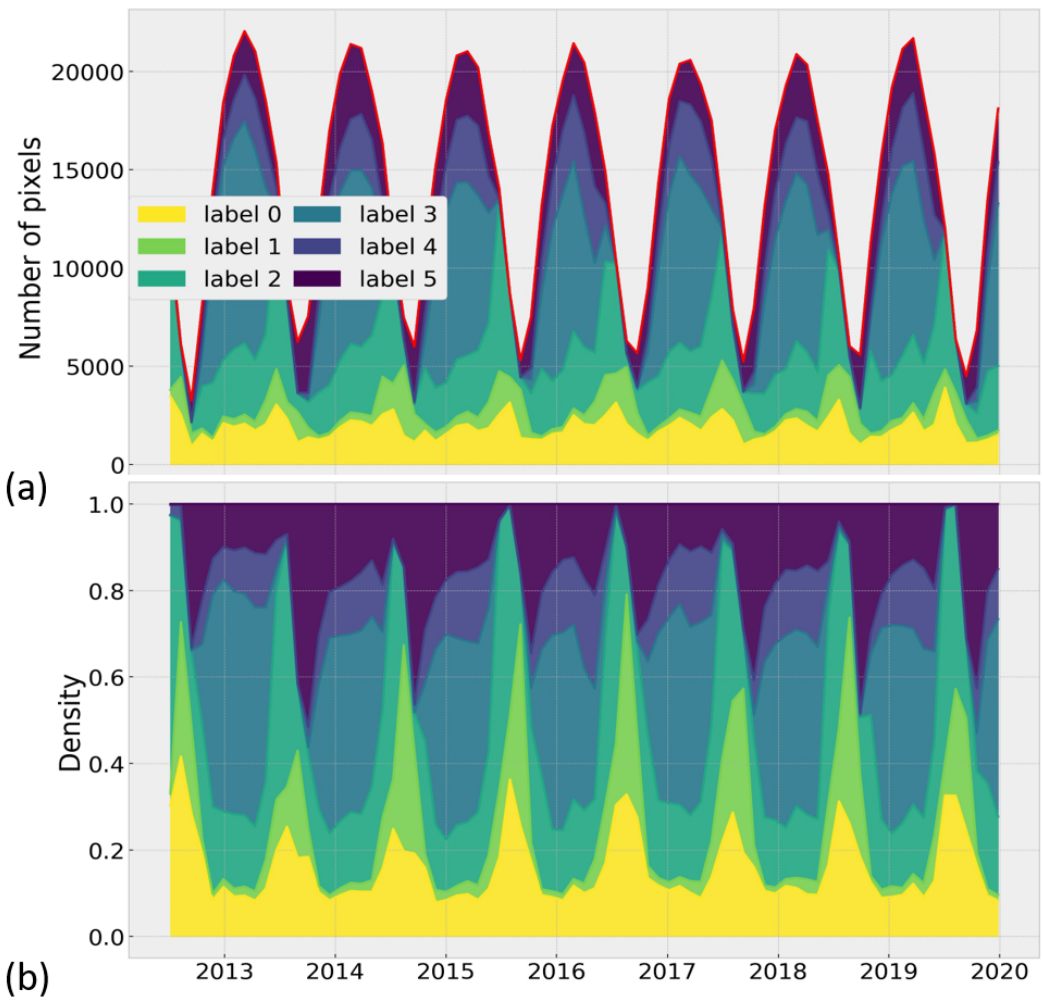

Figure 6.28: Temporal evolution of classes for a 7.5-year segmentation period from July 2012 to December 2019, representing (**a**) the total amount and (**b**) the relative amount of voxels for each class membership. The six classes clearly recur annually and can be considered significant regarding a one-year subperiod.

Spatial Consistency

The segmented patterns of the latent field result can be related to those of operational products including images of sea ice parameters (SIT and SIC) and sea ice charts of SoD and SIC obtained by sea ice analysts. The SIC maps were obtained from the same product used to mask out OW areas prior to segmentation. The following products were used to compare the classes with SIT, one for thin sea ice (SIT-SMOS) based on SMOS T_B observations and one for the entire SIT range based on SMOS data and altimetry data from CryoSat-2 (SIT-CS2SMOS) provided by the AWI. Both data sets are available during the freeze-up from 15 October to 15 April, respectively, and can be downloaded from `https://smos-diss.eo.esa.int/socat/L3_SIT_Open`, (accessed on 16 November 2021) and `https://smos-diss.eo.esa.int/socat/L4_SIT_Open`, (accessed on 16 November 2021). The State Scientific Center of the Russian Federation's Arctic and Antarctic Research Institute (AARI) provides weekly sea ice charts of SoD for the Arctic freeze-

up period from October to May, and SIC for the remaining months. The distribution of generalized categories covering the entire Arctic are determined from regional ice charts by analyzing images of additional institutions such as the NIC and maps can be downloaded from `http://wdc.aari.ru/datasets/d0040/arctic/`, (accessed on 16 November 2021).

The spatial classes are qualitatively compared to the shapes of SoD of sea ice charts, which are analyzed beforehand to determine a number of higher-order categories SoD during freeze-up, and the behaviour of sea ice during summer melt. The SoD and SIC ice charts were assessed over multiple years to draw general conclusions about the formation and development of sea ice. At the beginning of the Arctic freeze-up (mid-September), there is mainly old and young ice. A small area consisting of thin FYI begins to grow from mid-October until it becomes medium FYI from around mid-December. Grey ice and nilas are present throughout the entire freezing period (mid-September to late March). After that, no significant amount of new ice forms. Thick FYI is present from mid-January onwards (in some exceptional cases, such as 2018, it is generally classified as FYI (yellow label)). By the end of April, most of the sea ice extent consists of old ice and thick FYI. From June onwards (after freezing), the ice formed by then is generally referred to as MYI ice. At the beginning of June, the SIC of the ice-covered area is mostly above 0.9. The area with reduced SIC – due increasing melt pond fraction and wet surface conditions – increases in early July. From mid-August, the proportion of areas with high SIC decreases significantly. In early September, areas of low-concentrated sea ice are formed in the Greenland Sea and the Chukchi/Beaufort Sea. The five most abundant and superordinate SoD categories which are considered as significant during freeze-up are (I) nilas, young, gray and grey-white ice ($<$10 cm), (II) thin FYI ($\sim$ 10–30 cm), (III) medium FYI ($\sim$ 30–70 cm), (IV) thick FYI ($\sim$ 70–120 cm), and (V) MYI (ice formed after freeze-up) and old ice (remaining ice after summer melt).

Figures 6.29 and 6.30 show the segmented spatial patterns (a) compared to the sea ice products including SoD (b), SIT-CS2SMOS (c) and SIC (d), for the early freeze-up on 11 November 2016 and the late freeze-up on 31 March 2017, respectively. The relationship between the class distributions and the sea ice products shows that Class 0 represents largely newly formed thin ice, comprising mainly areas of nilas and grey ice and most of the low-concentrated ice. Class 1 largely comprises sea ice under wet conditions in summer and is observed during freeze-up almost exclusively at the sea ice edge in the Greenland Sea, where thicker sea ice drifts to lower latitudes and a mixture of ice types is expected. At early freezing, Class 2 resembles thin FYI and grey-white ice, and at late freezing it is more associated with medium FYI. Similar to Class 2, Class 3 also shows a trend towards thicker ice during the freezing period, mainly representing areas of thin FYI in November and thick FYI in March. Classes 4 and 5 in sum represent old ice and Class 4 also partially thick ice, with both classes showing a SIT above 1.5 m, respectively.

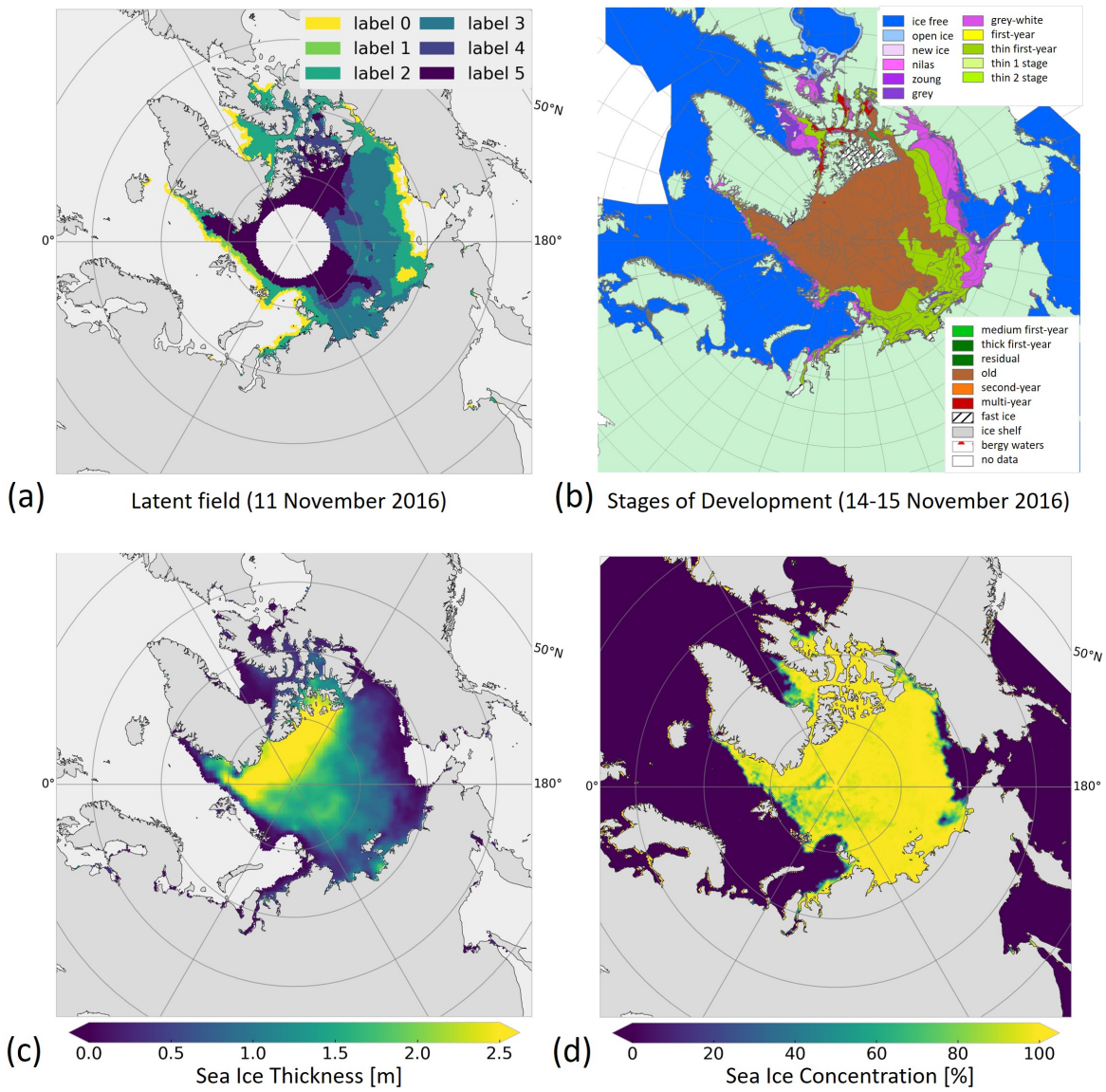

Figure 6.29: Comparison between segmented spatial patterns with operational sea ice products during early freeze up, comprising (**a**) latent field result, (**b**) SoD from AARI (determined on 14–15 November 2016), (**c**) SIT-CS2SMOS from AWI, and (**d**) SIC from NSIDC (estimated on 11 November 2016, respectively).

Class Interpretation

In order to evaluate the relationship between the resulting classes and SIT, the area covered by the individual classes were compared with the corresponding values of the two SIT products. Hereby, the values of the maps of both the thin and the merged SIT product contained in each specific class are considered at each time step along the entire freeze-up. This enables to assess the variability of SIT values covered by each class and its temporal stability. Individual distributions can be described in terms of its centre, spread and shape. Hereby, the centre of the distribution represented by the mean values are analyzed to understand whether the relationship between each class and SIT remains similar or may show a trend during freeze-up. The typical SIT range is identified from the

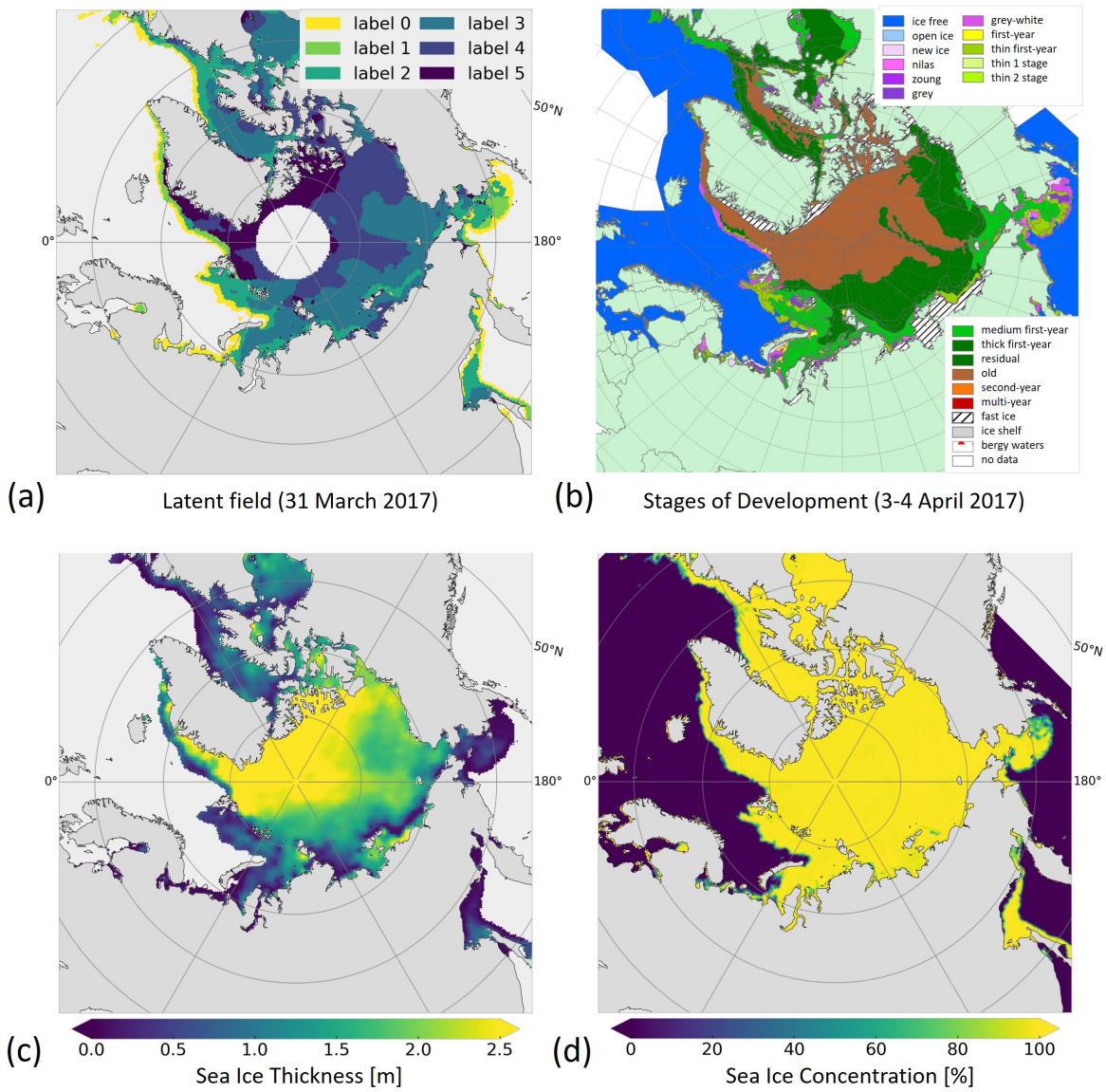

Figure 6.30: Comparison between segmented spatial patterns with operational sea ice products during late freeze up, comprising (**a**) latent field result, (**b**) SoD from AARI (determined on 3–4 April 2017), (**c**) SIT-CS2SMOS from AWI, and (**d**) SIC from NSIDC (estimated on 31 March 2017, respectively)

statistical dispersion of SIT values, and the shape of the distribution is analyzed to obtain information on symmetry and modality. The histograms of the individual distributions of the products SIT-SMOS and SIT-CS2SMOS at each time step are presented in Figures D.1 and D.2 in Appendix D, respectively. Figures 6.31a and b show the temporal evolution of medians and percentiles of SIT values of the products SIT-SMOS and SIT-CS2SMOS with respect to the corresponding pixels of each class, respectively.

Regarding SIT-SMOS, Class 0 refers to a sharp and temporally stable distribution representing SIT < 10 cm. Class 1 contains values of SIT < 30 cm at the beginning of freeze-up and includes also higher values over time. Class 2 comprises SIT values < 70 cm with the distribution being largely stable. It is important to note that SIT values as-

sociated with the Classes 0–2 follow a one-sided positively-skewed distribution (Figures D.1a–c). In contrast, the distributions associated to Classes 3–5 (Figures D.1d–f) contain higher SIT values, which are already beyond the sensitivity range of T_B measurements at L-band (~ 0.5 m), where the inference algorithm relies on the thermodynamic model (limited to 1.4 m). The SIT values for Class 3 are distributed over the entire dynamic range and follow a bimodal distribution. In conclusion, the SMOS-derived SIT maps can be linked to the spatial patterns of the Classes 0–2, with most of the values contained in the thin SIT range. No clear relationship is observed between Classes 3–5 and the SIT-SMOS product.

Because the merged product SIT-CS2SMOS includes altimetry data, it has the advantage of more accurately estimating SIT for thicker ice. The SIT distributions corresponding to Classes 0–2 shown in Figures D.2a–c have a similar shapes to those of the SMOS-derived product, except that they are spread toward higher values. This suggests that regions with isolated thicker ice but similar surface conditions are grouped in the same class because direct information about thicker ice is not included in the features selected for segmentation. For Class 2, the distributions of the SIT-SMOS and the SIT-CS2SMOS are most similar in shape and dispersion. The SIT values of the merged product associated with Classes 3–5 are mostly symmetrically distributed (Figures D.2d–f), in contrast to the bounded, negatively skewed distribution of values corresponding to the SMOS-derived product. Over time, a positive trend towards higher SIT values can be observed (Figures D.2d–f). This is consistent with the aforementioned relationship between spatial patterns and SoD, indicating that Classes 3 and 4 can be associated with increasing FYI along freeze-up.

The overall mean, standard deviation and skewness are determined to indicate the typical SIT range. Trend information is provided by the deviation of the means values along the freeze-up. The corresponding values for the products SIT-SMOS, SIT-CS2SMOS and SIC – computed for each class – are given in Table 6.3. In summary, Classes 0–2 can be associated with thin ice compared to SMOS-derived SIT values, indicating largely stable distributions with no upper limit along the freeze-up. Classes 3–5 are formed based on differences in observed surface conditions and contain information on progressively thicker sea ice during freeze-up, as they can be associated to largely symmetrically distributed SIT values of the merged product.

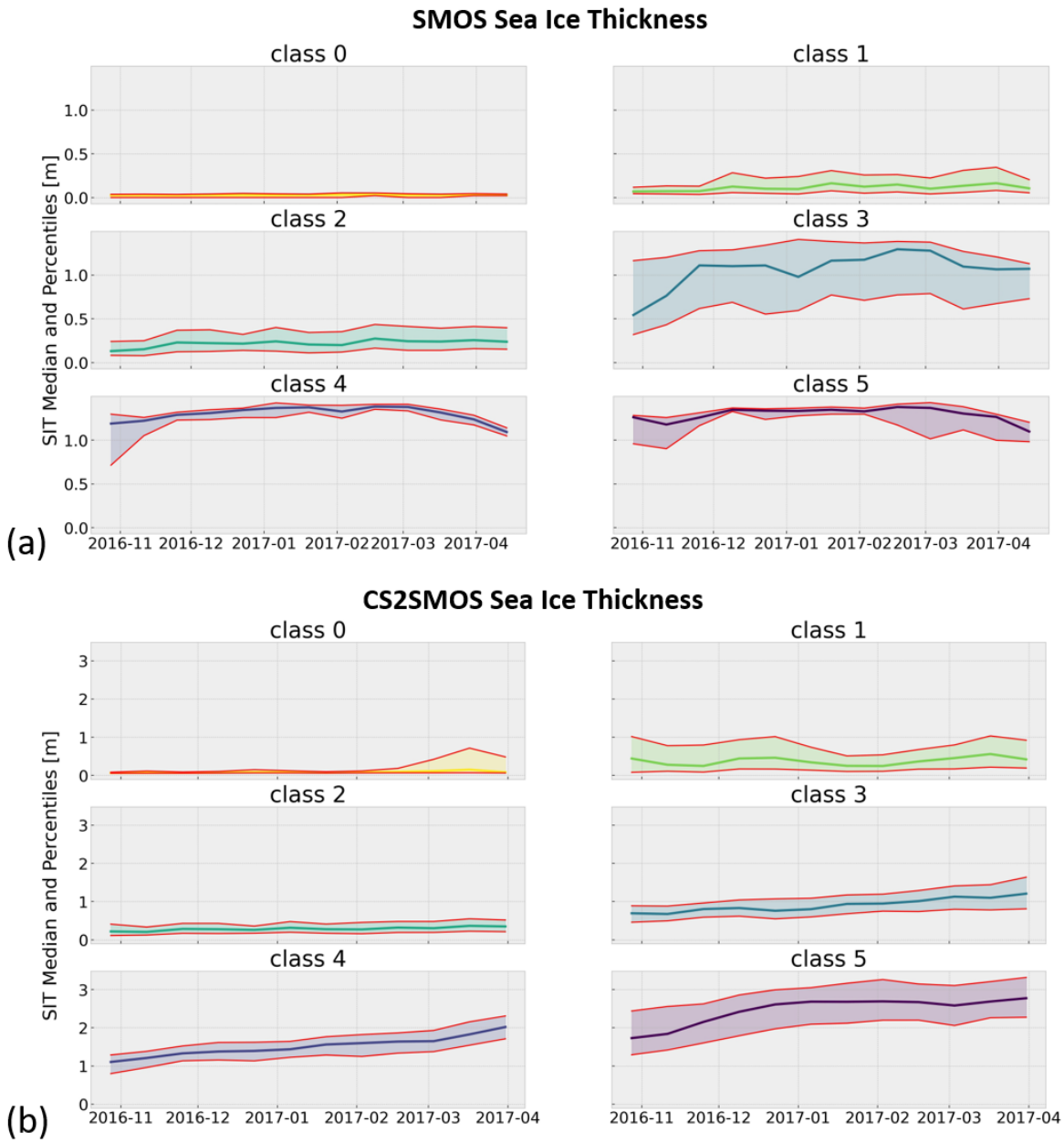

Figure 6.31: Class-specific evaluation of the spatial patterns with the median between the 25th and 75th percentiles of the SIT values of the corresponding SIT products along the freeze-up period from 15 October 2016 to 15 April 2017. Comparison with (**a**) the thin SIT product SIT-SMOS and (**a**) the merged full-range product SIT-CS2SMOS.

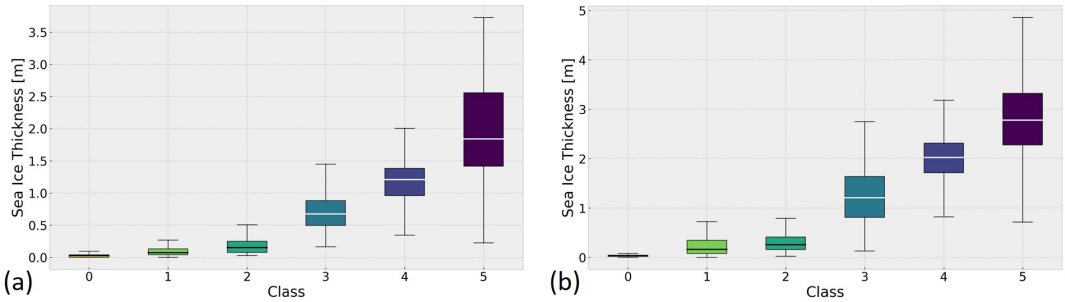

Figure 6.32: Boxplot of the class-specific associated SIT for (**a**) the beginning of freeze-up (11 November 2016) and (**b**) the end of freeze-up (31 March 2017). Classes 0 and 2 are associated with thin SIT (SIT-SMOS) and Classes 3–5 are related to values of the full-range product SIT-CS2SMOS.

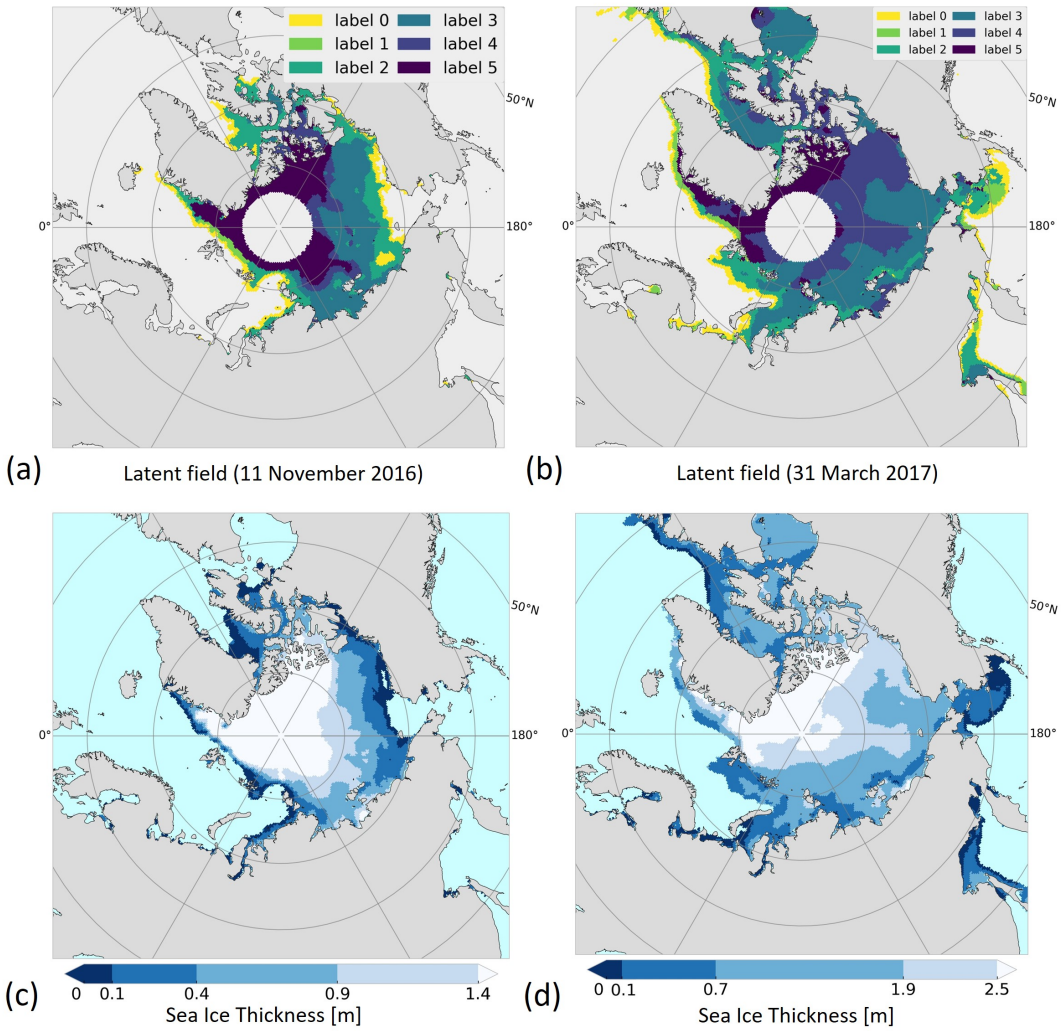

Figure 6.33: Comparison between the latent field and the SIT-CS2SMOS product with adapted bounds. The spatial patterns of the resulting classes in (**a**) and (**b**) are related to the corresponding SIT ranges in (**c**) and (**d**) at the beginning (11 November 2016) and at the end of freeze-up (31 March 2017), respectively. As sea ice thickens, the class-specifically associated ranges of SIT become extended and shifted towards higher values.

Table 6.3: Statistics of SIT and SIC values corresponding to the segmented spatial patterns of classes, evaluated at the beginning (11 November 2016) and the end of the freeze-up (31 March 2017). The 25th percentile (Q_1), Median (M), and 75th percentile (Q_3) of the SIT distribution are determined for each class, whereas Classes 0–2 are related to the SIT-SMOS and Classes 3–5 are related to the SIT-CS2SMOS product.

Date:		**11 November 2016**						**31 March 2017**					
Class		**0**	**1**	**2**	**3**	**4**	**5**	**0**	**1**	**2**	**3**	**4**	**5**
SIT-SMOS [cm]	Q_1	0.00	0.04	0.08	0.43	1.05	0.9	0.02	0.08	0.16	0.67	1.17	1.00
	M	0.03	0.07	0.15	0.76	1.22	1.18	0.03	0.16	0.26	1.07	1.24	1.26
	Q_3	0.04	0.13	0.25	1.20	1.26	1.26	0.05	0.35	0.41	1.21	1.28	1.30
SIT-CS2SM. [cm]	Q_1	0.06	0.11	0.12	0.50	0.96	1.42	0.06	0.19	0.21	0.81	1.71	2.28
	M	0.07	0.28	0.21	0.68	1.21	1.84	0.08	0.42	0.35	1.21	2.02	2.78
	Q_3	0.12	0.78	0.33	0.88	1.38	2.56	0.48	0.92	0.52	1.64	2.31	3.32
SIC [%]	Q_1	14	75	93	99	98	96	15	85	97	99	99	99
	M	40	88	98	99	99	99	39	97	99	99	99	99
	Q_3	65	94	99	100	99	99	66	99	100	100	99	99

Table 6.4: Summary of the segmentation result and class interpretation indicating the class-specific periods of occurrence, time of maximum extend (Max), assigned SoD, associated SIC and SIT range according to values of the products SIT-SMOS (Classes 0–2) and SIT-CS2SMOS (Classes 3–5) as well as the identified drift of the corresponding SIT Median (MED) values along the freeze up.

Class	**0**	**1**	**2**	**3**	**4**	**5**
Period of occurrance	year-round	mid-Mar – mid-Oct	mid-Sep – end Aug	Oct – end Mar	Nov – end Mar	Aug – mid-Jul
Max	end Jul	end Aug	mid-Jul	mid-Mar	mid-Mar	Oct
SoD (freeze-up)	grey ice, nilas	FYI (Greenland)	thin FYI	medium FYI	thick FYI, MYI	MYI
SoD (melt)	SIC (ponded ice)	Wet cond. (Stage 3)	Wet cond. (Stage 2)	-	-	Wet cond. (Stage 1)
SIC [%]	< 70	> 50	70–95	95–100	~ 100	~ 100
SIT [cm] (Nov/2016)	< 10	< 20	10–40	40–90	90–140	> 140
SIT [cm] (Mar/2017)	< 10	< 40	10–70	70–170	170–230	> 230
MED Drift in [cm/mth]	0.04	1.06	1.47	9.33	13.92	16.52

6.5 Discussion

The implemented Bayesian segmentation algorithm serves as a probabilistic framework to integrate the information contained in multi-source data sets. It is capable of recognizing patterns by considering both the statistical characteristics and spatial interactions in an

unsupervised manner, and classes are formed based on the similarities and differences of the input features. Insights about spatial and temporal sea ice variability can be obtained from the 'hidden link' between multiple complementary observations, which is represented by a HMRF model, whereas the statistical characteristics are considered by the mean values and covariances of the GMM. The optimal latent field of class patterns in physical space and clusters in features space are obtained using an iterative process based on MCMC. Unlike in other Machine Learning algorithms, the method has the advantage to provide metrics including the statistical model parameters (means and covariances), the spatial heterogeneity coefficient, and the class membership probabilities. They can be evaluated for subsequent class analysis to compute performance metrics such as correlation coefficient, distance- and density-based separability indices, as well as information entropy for model uncertainty quantification.

Prior to segmentation, the algorithm requires the selection of an adequate number of representative classes to which each data point is assigned iteratively and unsupervised. They can be determined in a purely stochastic and automated way based on different information criteria such as BIC and AIC. These criteria provide the optimal number of classes based on the statistical nature of the data, but have the disadvantage of not taking into account possible correlations between neighboring observations. Another way to estimate the number of classes is the analysis of the global separability of the resulting classes after an initial segmentation step. This method takes into account both the statistical characteristics and the spatial correlations of satellite images, and it can provide more accurate estimations in case of, for instance, strong discontinuities in physical space. Class selection can also be made subjectively based on prior knowledge of the sensitivity range between the satellite data and specific parameters in the context of the observed environment. The classes can be related to a set of expected discrete categories, such as stages of development or specific ranges of SIT and SIC. This method favors a more straightforward classification of the resulting class patterns by evaluating the accuracy and mismatch with a distribution target parameters. Whether the appropriate choice of the number of classes is made in a purely statistical way based on information criteria, if it requires additional information about the spatial distribution of the data points, or it is made subjectively, depends both on prior knowledge about the dynamics and complexity of the observed environment and on the application.

The application of the Bayesian segmentation algorithm to high-resolution SAR images aimed to enhance the reliability of sea ice classification using a two-step approach with previous incidence-angle normalization. It includes spatial correlations beyond purely statistical feature space representation – similar to the approach to automatically estimate SIC based on K-means clustering and Markov Random Fields [Deng and Clausi, 2005]. An Expectation-Maximization step was used to assess whether the amount of water in an observed water is significant to form a separable class. The subsequently applied Bayesian

segmentation step is to find the class corresponding to the image fraction of surface water. More accurate results are obtained for periods of high SIC, where current algorithms are known to underestimate SIC. The ability to detect different types of ice is highly dependent on the location and time of year, and is ambiguous due to the dependence of surface signatures on wind speed and direction. Discriminating sea ice from surface water is more accurate during freeze-up, but especially difficult in the advanced melt season when sea ice properties change and melt ponds become more numerous [Casey et al., 2016]. Thus, the development of an automated technique using SAR data-based surface signatures remains challenging.

T_B values show larger differences among observations at increased incidence angles. In addition, the emissivity depends on the optical path length through the ice, and observations at different incidence angles contain complementary information on the composition of the ice – especially for thin ice. PR calculated from T_B at horizontal and vertical polarization reduces the effects of the physical surface temperature and surface roughness. In a second application, the algorithm was used to segment multi-incidence angle PR maps from SMOS observations in the Arctic along the freeze-up period from September to December 2016. The estimation of a constant number of temporally stable and separable classes revealed periods, when T_B observations can be similarly related to sea ice properties. The resulting latent field indicates classes corresponding to newly formed thin sea ice, a transition zone of intermediate thickness, and thick ice, where the SMOS sensor is saturated. The spatial patterns can be used to extract the heterogeneity of the underlying sea ice properties. Information entropy can be computed to point out both uncertain zones between segmented classes and anomalies which can form sub-classes. As an example, melt ponds on sea ice during summer show distinct surface characteristics, which may result in a further discriminable class only during that particular period. Since class mean values represent the most significant observations at every segmentation step, their temporal evolution can be used to define dynamic tie points. These tie points can be analyzed to investigate how sensitive input features respond to changes in sea ice properties.

Some remarks can be made about the significance of the latent field results in terms of reproducibility and the possibility of comparing and interpreting them with common sea ice products. If the identified classes are robust and stable over time, they have a physical meaning, and they can be reproduced in an automated manner using the same set of satellite data. However, class formation depends largely on the spatial resolution, the temporal sampling, the absolute data length, and on the processing level and interpolation scheme used to produce the input features for segmentation. Different products rely on alternative methods for classifying sea ice and use different data sources and retrieval methods, which may be process-based or data-driven, and automated or manual. In addition to the information contained in the considered data sets, the selection of categories for sea ice developmental stages in common products such as those defined in

sea ice charts have been also influenced based on the importance for specific applications such as navigation, mineral exploration and climate modelling. Important processes and features of sea ice occur on characteristic temporal and spatial scales that are often below the resolution of satellite observations. Only partial information is available about sea ice types and their underlying composition for efficiently validating the class results. In case of sea ice, where in-situ data are not sufficiently available, the results of validating one satellite product with a second product are therefore often a matter of interpretation, as the observations included in both products may reflect different sea ice phenomena.

The sample-based MCMC method used to update the modelling parameters and *a posteriori* distribution has the disadvantage of becoming computationally expensive due to the linear algebra operations in a high-dimensional space. Unlike expectation maximization (EM), which is faster to solve, but may be caught in the proximate local optimum, MCMC is robust and more flexible to get rid of the local optimum and find the global optimum. It requires several iterations and computation time to converge to the Gaussian target distribution, and to eventually reach the stable mix chain. MCMC sampling works well with moderately large 2D data sets, but the convergence can be very slow for 3D segmentation. The computational cost scales linearly with the segmented period and temporal sampling, and Markov fields may be intractable for data sets with high-resolution and high temporal sampling. In future applications, larger data sets including a higher number of input features, and more classes will be used to train the model. Also, the jump length of the model parameter in the MCMC method is based purely heuristic, and a more sophisticated choice can still improve the efficiency of the method. Therefore, future research could examine the implementation of adaptive methods which find the global minimum faster, especially in case of high-dimensional target functions. The 3D Markov chain model could be modified so that the temporal dimension is separated from the spatial direction [Ulvmoen and Omre, 2010]. The temporal dimension could be sampled by a direct solver, while the MCMC sampler iterates over the lateral 2D dimensions, resulting in faster convergence compared to full 3D MCMC sampling. Further algorithms for more efficient parameter estimation may include Hamiltonian Monte Carlo (HMC) or adaptive MCMC. The most general inversion methods are often computationally intractable when applied to large data, and there is a need to better understand the implications of simplification [Linde et al., 2015].

The Bayesian framework has the advantage of being capable of combining different data sources to provide complementary information. However, the input features may also potentially contain redundant, erroneous, or unnecessary information about the sea ice parameters to be estimated. These redundant observations carry the risk that the segmented hidden field is potentially biased in the features entered. The included observations can be pre-assessed to pinpoint or to reduce its dimensionality, and to evaluate the possibility that the latent field is biased towards a specific sub-set of input features. In addition, gridded data is often used in applications because it facilitates the integration

of data between sensors, which is also the case with the AMSR2 T_B product, where multi-frequency observations with different resolutions are projected onto a common grid, which can lead to a reduction of the data integrity for the low resolution channels. In particular when data from different sensors are combined, the use of the original swath data is more accurate. However, downscaling algorithms and interpolation schemes are necessary to obtain maps with full coverage and regular temporal sampling, but can introduce model biases that can cause misclassification. Using products at lower processing levels or raw radiances can reduce biases potentially introduced through too strong assumptions in the observational operators like in emission models or RTMs.

7 | Sea Ice Thickness Retrieval

This chapter focuses on a predictive regression NN framework approach to infer SIT based on the first FMPL-2 T_B acquisitions provided by the FSSCat mission [Herbert et al., 2021b]. To do so, two separate NNs were implemented to generate Arctic and Antarctic SIT maps by combining FMPL-2 T_B data with ancillary maps of SIC from the European Organisation for the Exploitation of Meteorological Satellites (EUMETSAT), and skin temperature provided by the ECMWF. The first model is devoted to model thin SIT up to 0.6 m while using the thin sea ice product SIT-SMOS as ground truth. The second network is designed to model full-range SIT. Input data are further complemented by CryoSat-2 (CS2) Fb estimates to extend the previous model, using a merged product SIT-CS2SMOS as ground truth. The selection of input features, the implementation of the two NNs, and the inference of SIT are described in Section 7.1.

Both of the SIT models are trained during the period from 15 October to 4 December 2020, and allowed to generate weekly composite maps of Arctic thin and full-range SIT. The Arctic data set that was used to train the full-range model was compared to the same set of observations collected over Antarctic sea ice in terms of its variable ranges and densities. Because the Arctic training data encompasses most parts of the Antarctic data set, the prediction of Antarctic sea ice based on the Arctic model was considered to be reasonable in statistical terms. Both thin and the full-range models trained in the Arctic were applied to Antarctic data to estimate maps of Antarctic SIT.

The SIT products is stored in Network Common Data Form (NetCDF) and publicly available at `https://catalogue.nextgeoss.eu/`. In addition to the SIT products, based on a NN approach using data from both sensors on the FSSCat FMPL-2 payload – the GNSS-R instrument and the T_B L-band radiometer, maps of the SIC and SIE over both poles, and global SM over land were also created (Section 7.2).

7.1 Inference of Sea Ice Thickness using FSSCat Data

The major part of sea ice in the Northern Ocean occurs at 65 °N northwards, whereas, in the Southern Ocean, excluding the Antarctic continent, it roughly extends between 60 °S and 70 °S, with fluctuating sea ice margins. Because ^{3}Cat-5/A is a polar orbit satellite, its passes become denser towards the poles and produce more frequent overlaps. T_B maps

can be acquired with sufficient coverage (> 80 % after filtering usable tracks) in less than five days and two complete consecutive maps can be obtained within three weeks. This allows for the production of weekly Arctic and monthly Antarctic SIT composite maps of the ice-covered areas, respectively. It is noteworthy that the revisit time could be further decreased if the satellite was able to operate with a larger duty cycle, or in the case more ^{3}Cat-5/A-like CubeSats were added to the existing constellation. After the commissioning phase, data are available from 1 October to 4 December 2020. The observed period falls into the beginning of the Arctic freeze up, after sea ice having reached its annual minimum extent on 15 September 2020. Hereby, sea ice mainly consists of the remaining MYI with an increasing amount of thin FYI. In contrast to the Arctic, the Southern Ocean melts and re-freezes almost completely on a yearly basis and it consists mainly of first-year ice. Sea ice around Antarctica had passed its maximum extent on September 2020, and it is declining during the observation period [Comiso et al., 2020].

7.1.1 Ancillary Data

Ancillary data are included to enable the network to capture the information on the sea ice conditions at higher resolution. This enables the model to better address local SIT variability, which is supposed to be contained in the relationship between the input features. The availability of maps with sufficient temporal resolution with polar coverage and from both hemispheres was one requirement. Figure 7.1 visualizes maps of T_B and ancillary data as an example on 11 November 2020.

Sea Ice Concentration

FMPL-2 T_B observations at the ocean-ice boundaries can be ambiguous, because their values partially consist of OW and sea ice. This often leads to an underestimation of thin ice, especially at low-concentrated areas around sea ice margins. The Ocean and Sea Ice Satellite Application Facility (OSI-SAF) OSI-401-b product by EUMETSAT provides SIC maps using a dynamic tie-point algorithm applied to T_B data from the Special Sensor Microwave Imager/Sounder (SSMIS) at 19 GHz and 37 GHz vertical, and at 37 GHz horizontal polarization [Comiso et al., 1997]. The SIC maps are available on a daily basis at a 10 km Polar Stereographic grid projection true at 70 °N/S for both hemispheres, respectively, and images can be downloaded from `http://osisaf.met.no/p/ice/`, (accessed on 07 February 2021). These maps were regridded to a 12.5 km Equal-Area Scalable Earth (EASE)-Grid 2 to build a sea ice coverage mask. Only input data with a SIC > 15 % were considered for training the network.

Surface Temperature

At microwave frequencies below 117 GHz, Planck's law of electromagnetic radiation can be simplified using the Rayleigh–Jeans approximation, resulting in T_B being the product

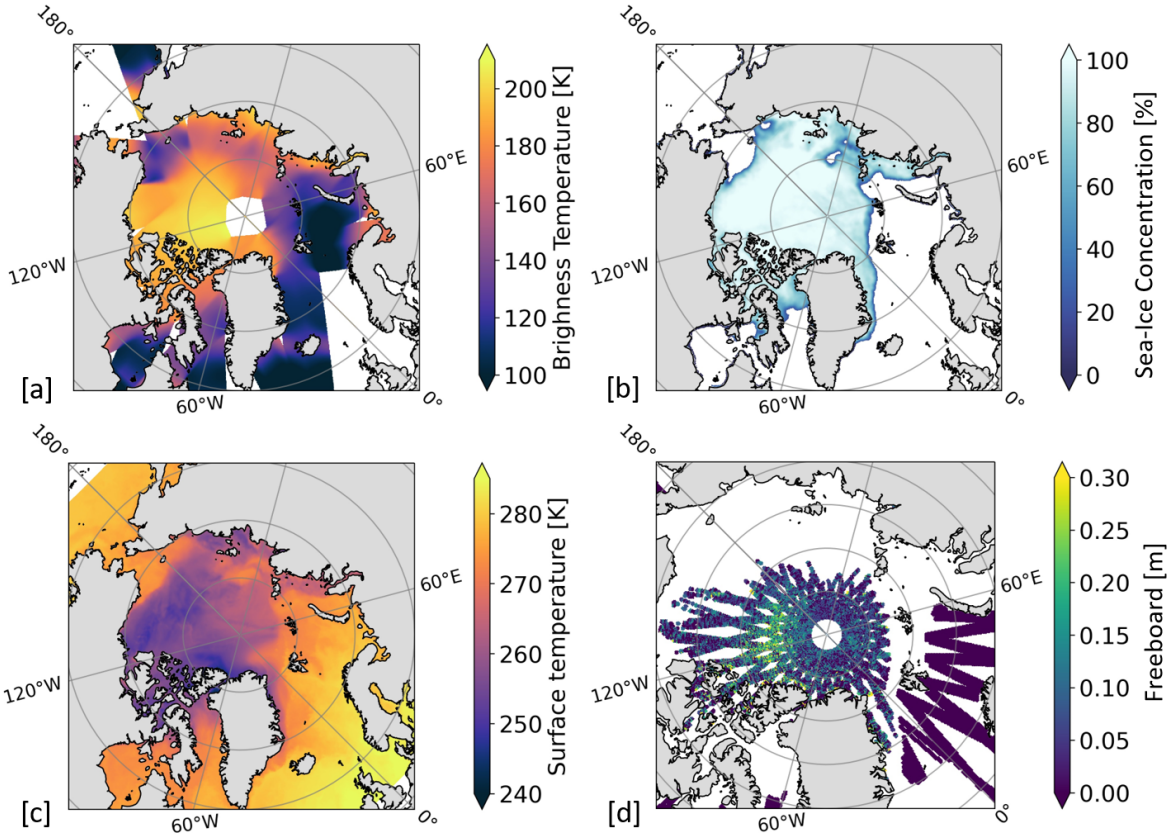

Figure 7.1: Maps of the input features for 11 November 2020, comprising (**a**) FMPL-2 T_B, (**b**) OSI-SAF OSI-401-b SIC, (**c**) ECMWF Skin temperature, and (**d**) CS2 sea ice Fb (weekly composite).

of the physical temperature (T_{Ph}) and the ice emissivity with an error of <1 % [Ulaby et al., 1986]. Hereby, the emissivity contains the actual information about the sea ice composition, including SIT, of the radiating layer. Figure 7.2 shows the relationship between T_B and SIT as a function of T_{Ph} and sea ice types that are based on a RTM considering two nadir-pointing observations at frequencies corresponding to L-band and P-band (500 MHz), respectively. The model assumes a horizontally-layered column of sea ice above water (without snow on top) using empirically determined values for sea ice properties, such as salinity and surface roughness [Menashi et al., 1993]. While the L-band signal already saturates around 0.6 m, the model reveals that observations at P-band contain information on SIT beyond 1.5 m and, in principle, they can be used to extend the sensitivity range of current retrieval algorithms. T_{Ph} can strongly vary among the pole areas, and it has a gradient along the ice profile, which influences the penetration depth of the emitted signal at L-band. Additional physical properties, such as density and ice type, can further depend on the distribution of temperature, which makes a direct correction of T_{Ph} based on T_B complicated. The skin temperature (T_S) product provided by the ECMWF represents the temperature value of the uppermost surface layer that satisfies the surface energy balance equation [Zeng and Beljaars, 2005].

Daily T_S maps were considered to be relevant input features for model training. They were linearly interpolated to a 12.5 km EASE-Grid 2.0 for Northern and Southern hemispheres.

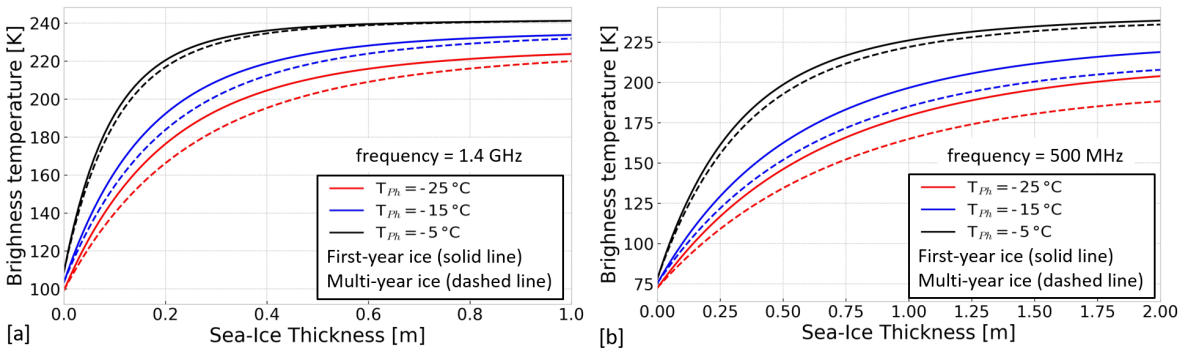

Figure 7.2: Relationship between T_B and SIT as a function of T_{Ph} of sea ice and sea ice types. Estimations are obtained using a RTM based on empirically determined values for salinity, density, and surface roughness. The curves represent circular-polarized emissions obtained with a nadir-pointing antenna at two frequencies, (**a**) at L-band (1.4 GHz, similar to T_B observations of the FMPL-2 radiometer) and (**b**) at P-band (500 MHz).

Sea Ice Freeboard

The CS2 mission, which was launched by ESA in 2010, carries the SAR Interferometric Radar Altimeter (SIRAL) operating at Ku-band (∼13.6 GHz) to detect and monitor topographical fluctuations and trends over land and sea ice [Laxon et al., 2013, Wingham et al., 2006]. A combination of elevation data with ancillary data, including sea ice type and snow depth and density, enables the estimation of sea ice Fb, i.e. the height of sea ice above sea level [Warren et al., 1999]. CS2 altimetry data have shown to be sensitive to SIT above 1 m, with increasing uncertainty for thinner ice [Laxon et al., 2013]. Because Fb data contain information on the sea ice variability, predominantly thicker ice, it was considered to be a relevant input parameter to complement the L-band observations. Time series of the CS2 L2 SIRAL Geophysical Data Record-2 full-orbit segments were projected onto a 12.5 km EASE-Grid 2.0 to generate daily Fb maps. The data are available for both hemispheres and they can be downloaded from `https://science-pds.cryosat.esa.int/` (accessed on 07 February 2021) [No, 2009].

Sea Ice Thickness

Two separate SIT products are selected as ground truth data in the NN, covering the respective ranges of thin sea ice up to 0.6 m, and full-range SIT. Hereby, daily SMOS L3 SIT maps (SIT-SMOS) are used for thin SIT retrieval [Tian-Kunze et al., 2014], and weekly composites of the merged SMOS and CS2 L4 SIT maps (SIT-CS2SMOS) were used to yield full-range SIT [Ricker et al., 2017]. Both of the maps are obtained from SMOS L-band T_B measurements on the basis of a thermodynamic and a RTM considering

the variations of ice-physical properties [Kaleschke et al., 2012]. In the latter product, daily SMOS-derived SIT is combined in an optimal interpolation scheme with the weekly CS2 SIT. The SIT-CS2SMOS product contains information on surface height and sea ice Fb included in the different modes of the SIRAL L1b data. Both of the data sets are available from 2010 onwards at Arctic scale from mid-October to mid-April on a 25 km EASE-Grid 2.0 and they are provided by the Alfred Wegener Institute (AWI) for Polar and Marine Research. The data can be downloaded from `https://smos-diss.eo.esa.int/socat/L3_SIT_Open`, (accessed on 07 February 2021) and `https://smos-diss.eo.esa.int/socat/L4_SIT_Open`, (accessed on 07 February 2021).

7.1.2 Implementation of the Regression Neural Network

The goal of this study is to estimate Arctic and Antarctic SIT from the selected set of input features. Targeting continuous values of SIT based on the relationship between the input features represents a regression task. Linear regression models typically adjust a number of model parameters to a set of training data in an iterative process by minimizing a cost function, which eventually converges to an optimal fit. The gradient descent () method is a common technique to find the optimum solution. It computes the local gradient with respect to the model parameters and a cost function, following the direction of descending gradient until reaching convergence [Chong and Zak, 2004]. In a first attempt, a simple regression model without hidden layers was selected, but the model did neither converge nor generalize well on the test set. This implied that the input features are not linearly separable, but rather non-linearly related.

NNs can manage complex regression tasks and they are more adequate than traditional approaches when dealing with non-linear relationships between the variables. In its basic structure, a NN consists of an input layer, an output layer, and interposed hidden layers, with each layer consisting of a number of neurons [LeCun et al., 2015]. The observations for training are assigned to the input layer with the number of neurons being the number of input features. The output layer of a regression task has a single neuron that represents the retrieved continuous target parameter. At least one hidden layer between the input and output layer makes the model different from a simple regression framework by enabling the network to learn the relationships that are contained in the data set. In this work, the networks were built as sequentially dense layers, i.e., each neuron of the previous layer is fully connected to all neurons of the following layer. The specific model set-up was adjusted during the training and Figure 7.3 illustrates the final network architecture for the thin and full-range model. Similar to the coefficients in a linear regression, each connection (lines) between neurons represents the weight of the output of the neuron in the previous layer. The output value Y of each neuron is determined by forward propagating the weighted sum of the inputs coming from the neurons i of the previous layer with the

weights ω and an additive bias b

$$Y = f\Big(\sum_i (\omega_i * input_i) + b\Big) \quad \text{with} \quad f(x) = max(0, x). \tag{7.1}$$

The activation function f of each hidden layer introduces the non-linearity between the input features and the target variable, without which the regression network would be entirely linear. ReLU (ReLU), representing the activation function defined above, is a commonly used function in regression tasks, and it has the advantage of being computationally efficient and it does not saturate for positive values [Géron, 2019]. The weights and biases of the neurons are updated according to the final error of the cost function via back-propagation. The number of hidden layers and neurons per layer can be increased to capture more feature interactions, depending on the complexity of the problem.

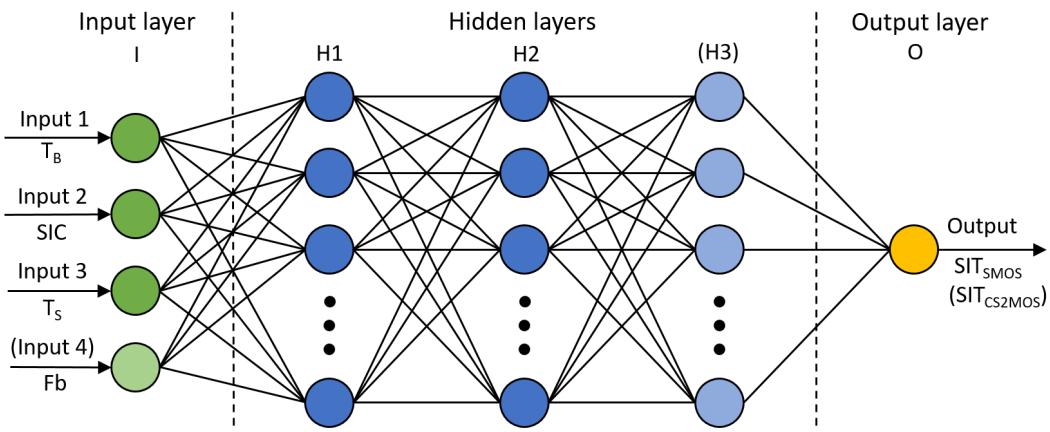

Figure 7.3: Principle architecture of the implemented NN consisting of a multiple-input normalization layer adapted to the number of input features, i.e., T_B, SIC, T_S, and Fb (in case of the full-range model), a number of non-linear hidden layers with a number of neurons per layer, and a linear single-output layer yielding continuous values of SIT. The final network architecture contains 2 or 3 hidden layers with 64 neurons per layer regarding the thin or full-range model, respectively.

The specific model set-up was adjusted during the training. Adaptive Moment (Adam) estimation was selected as an optimizer [Kingma and Ba, 2014]. Model parameters (ω, b) were randomly initialized and a small learning rate of 0.001 was chosen to obtain smooth convergence. The entire feature set was split into a training set (80%) and a test set (20%). The training set was further split into a reduced training set (80%) and validation set (20%). The performance of the different models was quantified using the Mean Absolute Error (MAE) as a cost function, being defined as the average sum of absolute differences between ground truth and predicted SIT. The MAE value indicates the training and validation loss at each epoch of the training. The best performing model with the lowest MAE on the validation set was trained on the entire training set, and the resulting model was evaluated with the remaining test set.

Although preliminary results of an unconstrained network revealed low MAE for the

known training data, the validation and training loss were not converging in the same way and the network resulted in different performances on training and validation set. Therefore, several constraints on the model hyperparameters were introduced to prevent the model from overfitting and overgeneralization. Regularization is used to prevent the model from overfitting by constraining the model complexity by keeping many model parameters close to zero (L2-regularization) or zero (L1-regularization) [Kuhn et al., 2013]. Hereby, the terms L1 and L2 refer to the norm, i.e., the L1-norm being the sum of the absolute values and the L2-norm being the square root of the squared distances. Weak L1 and L2 regularization was applied to all of the hidden layers in the regression network and the penalty terms were added to the cost function. Secondly, an Early Stopping technique prevents the model from overfitting by interrupting the training at the respective epoch, at which the validation loss reaches a minimum or stops to improve, i.e., no progress is obtained within a predefined number of epochs (patience interval). To train the model more efficiently, a relatively high number of neurons per layer (64) was selected in combination with Early Stopping regularization [Jaderberg et al., 2017, Smith, 2018]. A sufficient amount of training data ($\sim$350,000 samples for thin ice and 60,000 samples for the full-range SIT) allowed to set the batch size up to 1024 to restrain the amplitude of fluctuations of the validation loss and to reduce the total training time.

The two predictive NNs were first trained in the Arctic. Subsequently, the network to estimate thin SIT was applied to the Arctic sea, and the network to estimate full-range SIT was applied to both Arctic and Antarctic seas. Prior to the training, the input features were processed to be treatable by the NN. Because the NN was trained using GD method, it was required to scale and normalize the input features. This included normalization after filtering outliers to keep the variables within the reasonable ranges of values. Figures 7.4 and 7.5 show the KDE charts of input features after defining their ranges of values, which were eventually used to train the thin and full-range SIT model, respectively.

An ocean-land mask was applied to all maps to exclude land areas. Additionally, an ocean-ice mask was applied to preserve data points over areas with a SIC $> 15\,\%$, being the minimum value for which the OSI-401-b SIC product is defined. T_B increases monotonically as a function of SIT and the interval of suitable values is defined between 100 K and 210 K, which is in agreement with the expected dynamic range of T_B when considering a SIT up to 0.6 m in Figure 7.2a (also under cold conditions). Only a small amount of larger values was filtered ($< 0.1\,\%$ after applying the ocean-land and ocean-ice masks), which could be attributed to areas of possible land-sea contamination. For thin SIT prediction, a cutoff thickness ($SIT_{max} = 0.6$ m) was defined as the limit beyond which the sensitivity of T_B to SIT is assumed to be negligible. Regarding sea ice Fb, a threshold of 0.4 m is used as the upper limit for training the full-range model. As aforementioned, selective scaling and normalization of the input features were considered in the input layer of the network, according to the individual distribution of the input features. Table 7.1

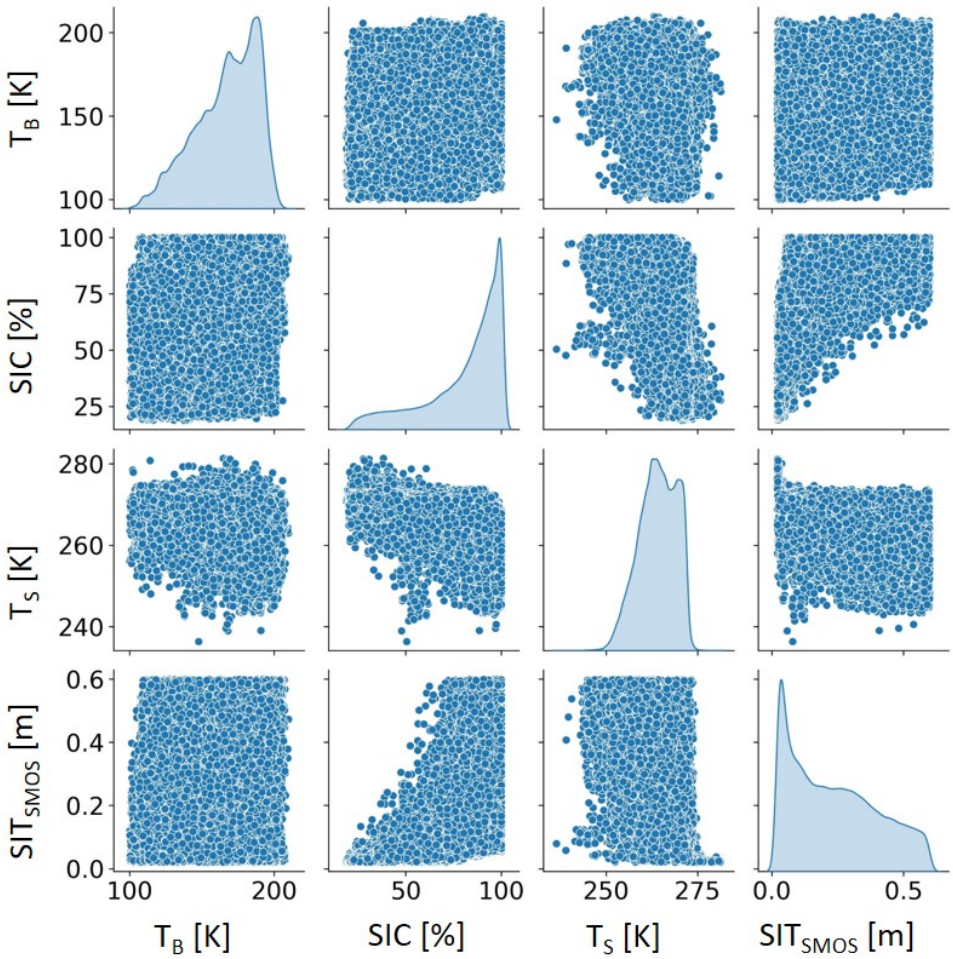

Figure 7.4: KDE charts of the NN training sets used to train the thin sea ice model including the marginal probability density functions of the filtered data sets. The thin model is based on T_B, SIC, T_S and ground truth thin SIT derived from SMOS data (SIT-SMOS).

provides the summary statistics representing the final distribution and dispersion of the input features. After processing the data, a total of 348,009 and 63,330 instances were suitable for training the thin and full-range SIT models, respectively. Ground truth SIT-SMOS and SIT-CS2SMOS are only available from mid-October onwards and Fb data have a delayed delivery time of about one month. Therefore, the thin SIT model was trained with data from 15 October to 4 December, and the full-range SIT model was trained from 15 October to 21 November 2020, respectively. The thin and the full-range SIT models were both trained based on Arctic T_B and ancillary data, and the model with the best fit was stored.

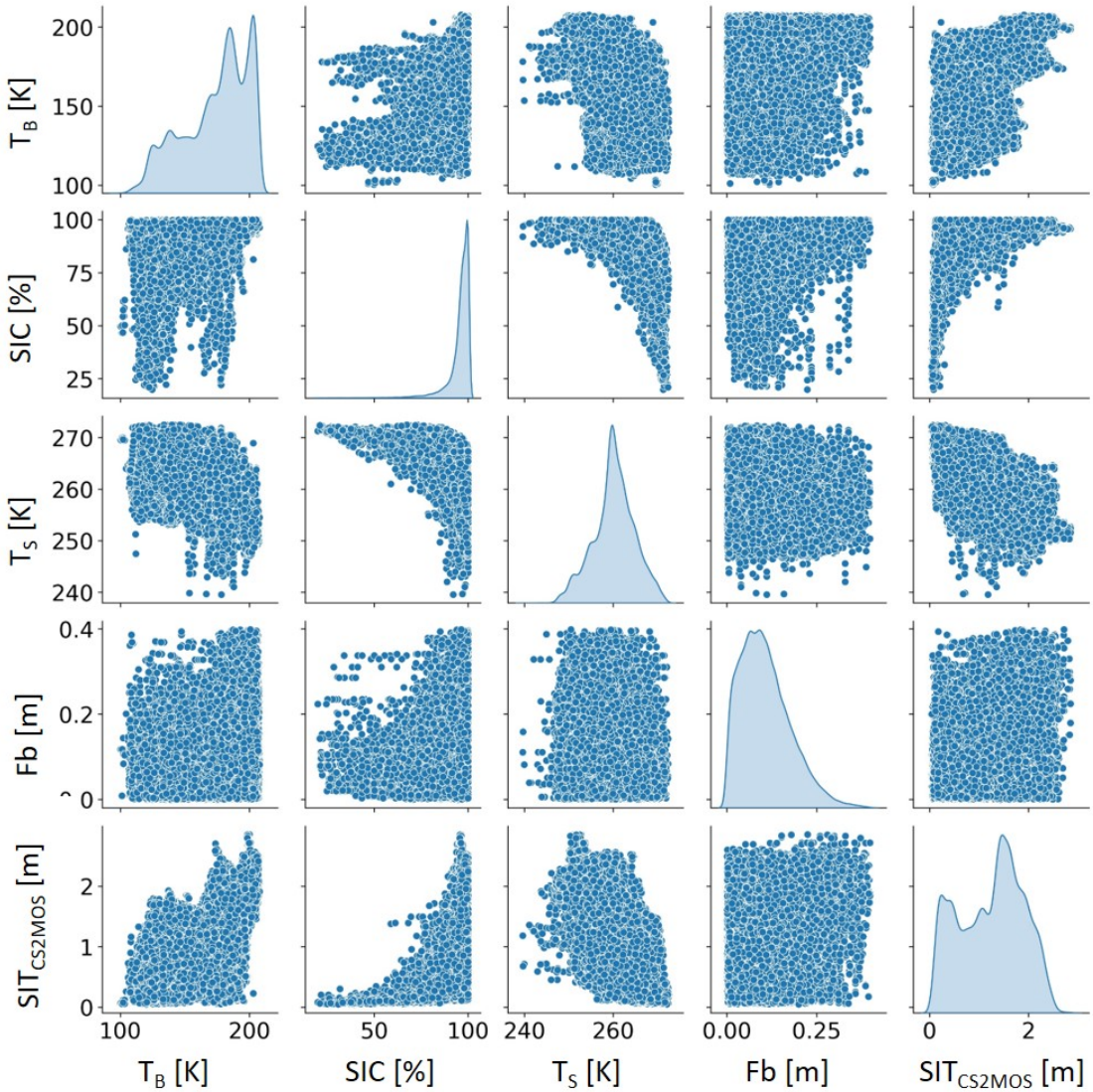

Figure 7.5: KDE charts of the NN training sets used to train the full-range model including the marginal probability density functions of the filtered data sets. The full-range SIT model is based on T_B, SIC, T_S, Fb, and ground truth SIT derived from CS2 and SMOS (SIT-CS2SMOS).

Table 7.1: Summary statistics of the NN training set used to predict thin ice (top) and full-range thickness (bottom). The description includes the Mean, Standard Deviation (StDev), Minimum, and Maximum values of the observations.

Model	Input Feature	Mean	StDev	Min	Max
Thin ice	T_B [K]	166.8	21.3	100.0	209.7
	SIC [%]	80.4	20.1	18.8	100.0
	T_S [K]	264.1	5.1	236.4	281.4
	SIT-SMOS [m]	0.239	0.165	0.020	0.600
Full-range	T_B [K]	173.8	24.7	100.4	207.8
	SIC [%]	95.3	7.5	19.9	100.0
	T_S [K]	260.2	4.6	239.6	272.5
	Fb [m]	0.108	0.070	0.000	0.399
	SIT-CS2SMOS [m]	1.248	0.639	0.045	2.853

Unlike in simple regression or process-based models, the results of a NN cannot be extrapolated, since its input features are non-linearly related. NNs are based on the underlying statistics of the observations and a trained model can only be applied to new data in case the corresponding range of values is covered by that of the original training set. Thus, a reliable model prediction requires the variable space of the available training data to include the predicted data as an already learned subset. This can be assessed by comparing the training and prediction data sets regarding its variable ranges and the density of values. In case the values of the new data set are located within the multi-dimensional convex hull of the original training data set, the model output can be considered to be reliable. The convex hulls around the points clouds of all combinations of input features are presented in a 2D sub-feature space in Figure 7.6, for the Arctic data (blue markers and black solid line) and for the Antarctic data (orange markers and red dashed line).

Both of the data sets are of the same quality and processed identically. The total number of valid observations for Arctic ice is higher because both the Fb and the T_B observations are less dense at higher latitudes, which reduces the amount of data for Antarctic sea ice. Regarding the distributions of T_B, Fb and SIC, the ranges and densities of the observations in the Antarctic, are entirely covered within the hull of observations in the Arctic. Therefore, the full-range model, which was trained with Arctic data, is considered to be reliable for an application to the Antarctic data. It is important to mention that a small amount of T_S values in the Antarctic data set is close to the sea ice melting point ($>270\,\mathrm{K}$). This is because the Antarctic summer had already started and the temperatures are high enough, so that sea ice located at lower latitudes begins to melt. The corresponding subset is not located within the convex hull of Arctic training data, which limits the reliability of the model predictions for these particular values.

7.1.3 Inference of Arctic and Antarctic Sea Ice Thickness

This section presents the results of the thin and full-range NN models. Section 7.1.3 describes the training procedure and indicates the model architectures of the best model fits. In Section 7.1.3, the corresponding models are applied to predict maps of Arctic thin SIT, and Arctic and Antarctic full-range SIT.

Training of the NN Models

During the training, various model architectures were adjusted and evaluated to minimize the generalization error (MAE) in order to obtain the model that fits the training data best. The hyperparameters were tuned to find a trade-off between training efficiency and convergence of the validation and training losses. The objective was to maintain the resemblance between the learning curves throughout the training to prevent overfitting and overgeneralization. Each model was trained with a maximum number of 1000 epochs,

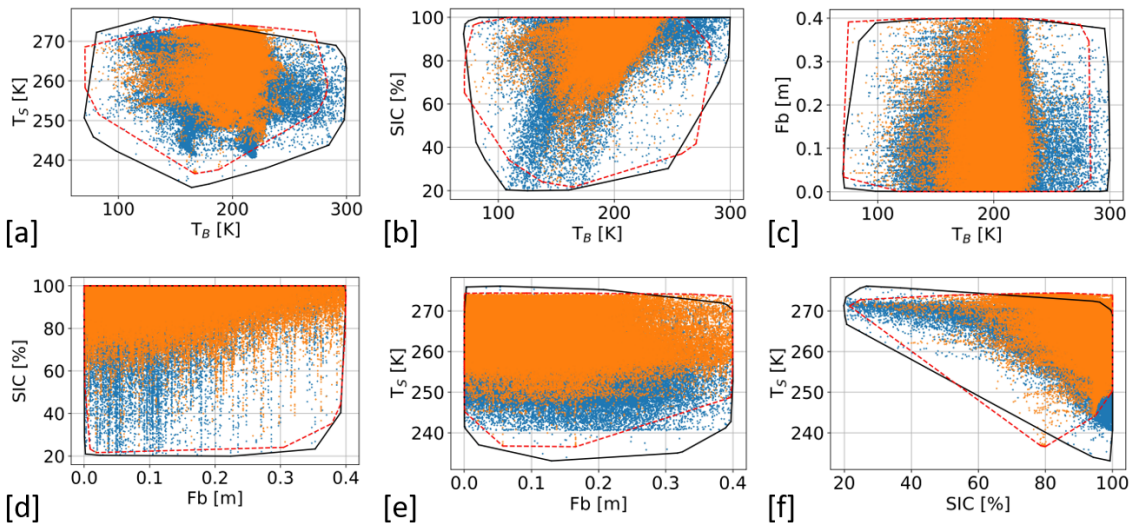

Figure 7.6: Convex hulls around the point clouds in 2D sub-feature space of Arctic data (black solid line around blue markers), and Antarctic data (red dashed line around yellow markers) (Feature pairs: (**a**) T_B–T_S, (**b**) T_B–SIC, (**c**) T_B–Fb, (**d**) Fb–SIC, (**e**) Fb–T_S, and (**f**) SIC–T_S). The application of the full-range model to Antarctic data is considered to be reliable, since most of its values are located within the convex hull and at denser areas of Arctic training data.

and both the training and validation losses were evaluated after each epoch, with a constant learning rate of 0.001. This rate turned out to be large enough to obtain a fast improvement of the learning curve at the beginning of the training (short burn-in phase) and small enough to lead to smooth convergence without bouncing around the optimum towards the end. In both NN (thin SIT and full-range SIT), the batch size, the number of hidden layers, and the patience interval of Early Stopping regularization were tuned, where the number of neurons per layer was kept constant to 64. An increase of the batch size up to a value of 1024 did not significantly influence the converging trend, but it considerably decreased the amplitude of the fluctuations in the validation loss and speeded up the training time. A higher number of hidden layers usually allows a network a fast build-up of sufficient complexity. In this case, more hidden layers (>3) led to a notable reduction of the training loss, whereas the validation loss was only slightly improving. This implied that, although the obtained model complexity apparently represented the reduced training set, it did not generalize well on the validation set. The validation loss fluctuated, but it showed a decreasing trend until it stagnated, when the model started to overfit the training data. Early Stopping with a patience interval eventually prevented the model from this overfitting. The fit was stopped after the validation loss did not show improvement anymore during the corresponding patience interval and the best fit was called-back and saved.

Table 7.2 provides a summary of the final architecture and the optimal training hyperparameters of the NNs and the SIT-range-specific MAE obtained from the prediction for the thin and full-range SIT models. The learning curves for the thin and full-range

model are presented in Figures 7.7a and 7.9a, respectively. Regarding both of the models, training and validation loss converged well, and no overfitting of the training data could be observed. Validation and training curves of the thin SIT model both match well throughout the training, whereas a small mismatch remained between those of the full-range SIT model towards the end of the training. The evaluation of the test set resulted in a final MAE of 0.065 m for the thin and 0.237 m for the full-range model, respectively.

Table 7.2: Summary of training (top) and prediction (bottom) characteristics corresponding to the thin and full-range SIT models. The training characteristics comprise the model architecture and the adjusted hyperparameters for the optimal fit, including the total trained instances, the number of hidden layers and neurons per layer, batch size, patience interval for Early Stopping, and the number of trained epochs. Regarding the predictions, the obtained MAE values are indicated for specific SIT ranges.

Trained model	**Instances**	**Layers**	**Neurons**	**Batch Size**	**Patience**	**Epochs**
Thin ice	348,009	2	64	1024	30 epochs	198
Full-range	63,330	3	64	1024	40 epochs	353
Prediction	**Thin Ice Model**		**Full-Range Model**			
SIT range [m]	0–0.6		0–0.5	0.5–1.5	1.5–2.5	0–2.5
MAE [m]	0.065		0.160	0.275	0.149	0.237

Prediction of Arctic and Antarctic SIT

The performance of the optimal fits was evaluated after applying the NN models to the unknown Arctic test set. The prediction error, the distribution of the MAE with SIT, and the relation between predicted and ground truth SIT are displayed in the Figure 7.7b–d for thin SIT. This model performs well with the error being widely unbiased up to a SIT of 0.4 m, but it underestimates the values for higher SIT. Predicted values deviate more from ground truth values with increasing SIT, until reaching a maximum error of around 9.5 cm at a SIT of approximately 30 cm. For predictions larger than 0.5 m, the MAE again shows lower values. This could be explained, because the model generally contains a small bias towards higher values and ground truth values beyond 0.6 m were filtered beforehand.

In Figure 7.8, two estimated weekly composite maps that are based on the thin SIT model are compared to the corresponding SIT-SMOS maps in the periods from 15–21 October and from 12–18 November 2020. In mid-October, sea ice mainly consisted of the remaining thick multi-year ice and regions of newly-formed thin ice were observed around the Beaufort Sea. In this period, only a small amount of under- and overestimated values are present. Positive deviations can be attributed to most-recently formed thin ice. Until mid-November, freeze-up had already advanced in the Arctic ocean, and thin sea ice below 0.6 m became more abundant. The increasing amount of newly-formed thin ice in the East Siberian Sea and the Laptev Sea, which is visible in the SIT-SMOS product, is in agreement with the values that were obtained from the NN model. In this period, the

number of underestimated values increases as sea ice gets thicker. The deviations between the ground truth and the predicted values reveal that underestimated values are located around the 0.6 m threshold, where the model range is limited. They can be related to areas in the Beaufort Sea and the Greenland Sea, where sea ice started to thicken beyond the sensitivity range of T_B observations.

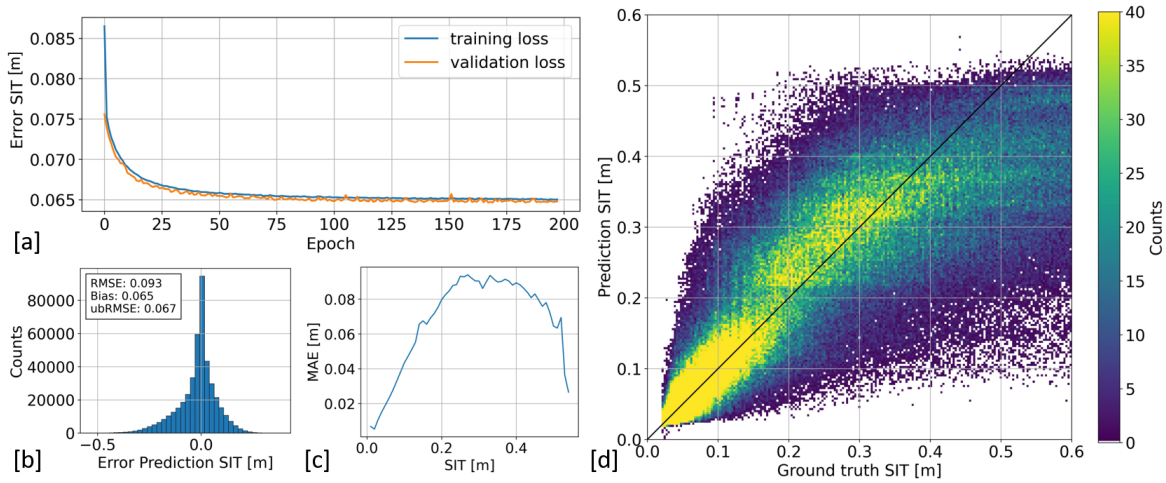

Figure 7.7: Evaluation of training and prediction of the thin SIT model. (**a**) Validation and training error determined after each epoch; early stopping occurred at 198 iterations and the model resulted in a MAE of 0.065 m; (**b**) prediction error after application of the model to the entire Arctic data set; (**c**) distribution of the MAE with SIT; and, (**d**) relation between predicted and ground truth SIT-SMOS.

Figures 7.9b–d show the evaluation of the full-range SIT model. The model performs well for thin (<0.5 m) and for thicker ice (>1.5 m), in which a substantial amount of values is given. These include the individual sub-ranges, where T_B and altimetry observations are known to be more sensitive to SIT, and where uncertainties of the SIT-SMOS and the SIT-CS2SMOS products are expected to be lower. Most part of the elevated value of the MAE (0.237 m) is made up by the high deviations of for SIT between 0.5 m and 1.5 m ($\sim$0.25–0.30 m, with a MAE of 0.275 m in Table 7.2). This may occur due to the fact that, after summer melt and at the beginning of the freeze-up period, mainly thick multi-year ice remained together with thin newly-formed ice. Instead, only a few values of sea ice in the intermediate thickness range can be provided for model training during the observed period. Therefore, the intermediate range may be underrepresented in the resulting predictions. In addition, the ground truth values are based on T_B and altimetry observations using an optimal interpolation scheme. This may introduce some artifacts at intermediate SIT ranges, resulting in distortions in the training that cannot be adequately conceptualized by the NN model.

In Figure 7.10, the predicted weekly composite based on the full-range SIT model is compared to the corresponding SIT-CS2SMOS map in the period from 22–28 October 2020. The over- and underestimations may be due to the large footprint of the antenna,

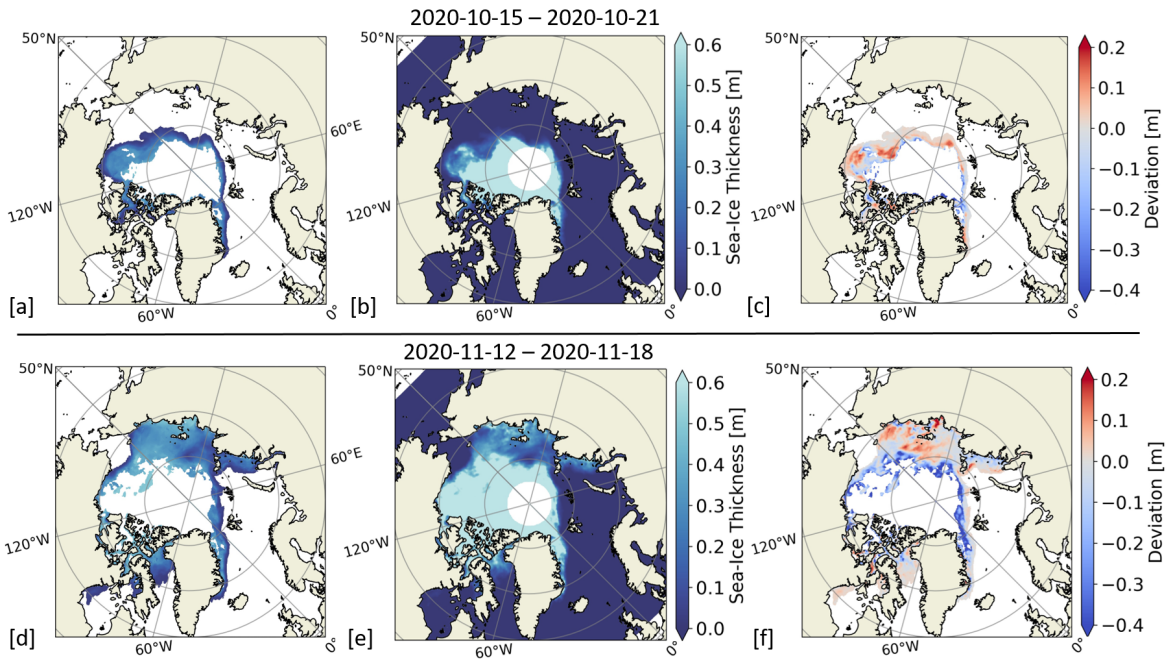

Figure 7.8: Weekly maps of predicted thin SIT ((**a**) and (**d**)), the corresponding ground truth SIT-SMOS ((**b**) and (**e**)), and deviations with respect to SIT-SMOS ((**c**) and (**f**)), over the Arctic sea from 15–21 October and from 12–18 November 2020, respectively. Areas with SIT-SMOS > 0.6 m were filtered in the predictions.

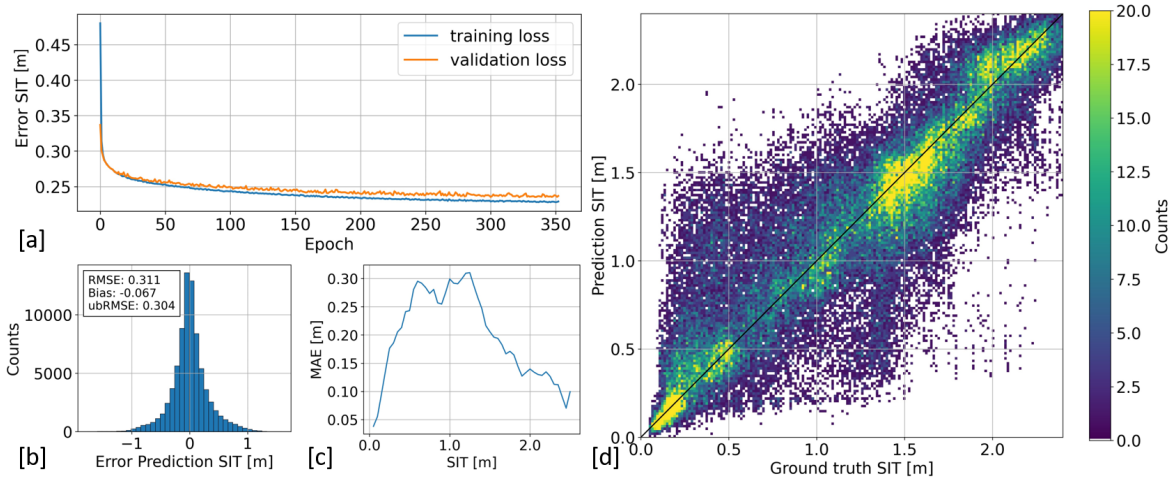

Figure 7.9: Evaluation of training and prediction of the full-range SIT model. (**a**) Validation and training error determined after each epoch converge close to each other; early stopping occurred around 353 iterations and the model resulted in a MAE of 0.237 m; (**b**) prediction error after application of the model to the entire Arctic data set; (**c**) distribution of the MAE with SIT; (**d**) relation between predicted and ground truth SIT-CS2SMOS; Good generalization is obtained for thin ice (SIT < 0.5 m) and thicker ice (SIT > 1.5 m).

which smoothes out the observations, reducing the small-scale variability. Underestimations (indicated in blue) can be attributed to areas of more heterogeneous multi-year ice. Most of the overestimated values (indicated in red) are located in the Beaufort Sea and in areas with high contrasts between newly-formed thin ice and thicker ice. Hereby, pre-

dicted values are within the intermediate SIT range, in which the model performance is also less accurate. Highly overestimated values are located to the north of the Baffin Bay around North-Western Greenland. This anomaly may also be due to land-sea contamination or to most recently formed ice, which is not yet captured in the predicted weekly composite.

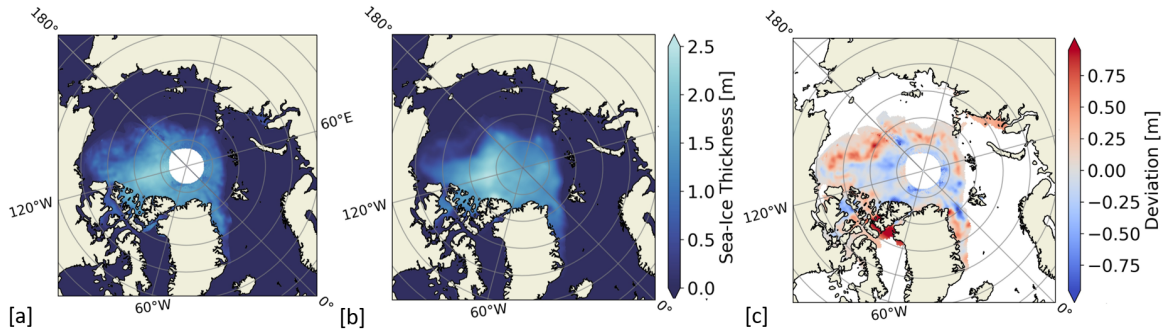

Figure 7.10: Comparison between the weekly composites of Arctic full-range SIT maps (**a**) and the corresponding ground truth SIT-CS2SMOS product (**b**), including their deviations (**c**), from 22–28 October 2020.

Figure 7.11 shows the predicted SIT map over the Antarctic sea from 15 October to 14 November 2020 (monthly composite), obtained after applying the full-range SIT model to Antarctic data. The massive ice shelves (e.g., Ronne and Ross) located in the Ross and Weddell sea were excluded from the predictions. It is important to note that a disseminated product of SIT at the Antarctic scale was at the time of the study not available for comparison. Therefore, the model cannot be validated in the same way as for the Arctic. SIT has an important impact on the melting trend of sea ice and it can be a good proxy of the upcoming SIE distribution. Antarctic SIE is already decreasing after having passed its annual sea ice maximum around mid-September. Thus, the spatial patterns of the distribution of SIT can be compared to those of future SIE, assuming that areas consisting of mainly thin ice are supposed to melt first. Because Antarctic sea ice melts and refreezes almost completely during a course of a year, it is mainly composed by thinner first-year ice. This is in agreement with the model predictions, which result in an average SIT of 0.67 m for the Antarctic, in comparison with 1.25 m obtained for the Arctic. Additionally, the maximum estimated SIT of 2 m in the Antarctic is lower than in the Arctic, where values up to 2.5 m were predicted.

7.2 FSSCat Sea Ice Products

Following the successful launch of the FSSCat mission on-board Vega flight VV16 on 3 September 2020, and the approximately one-month commissioning of the FMPL-2 instrument and its validation using recordings from 1–13 October 2020, observations between 15 October and 4 December 2020, were selected to provide products of SIT and SIC over sea

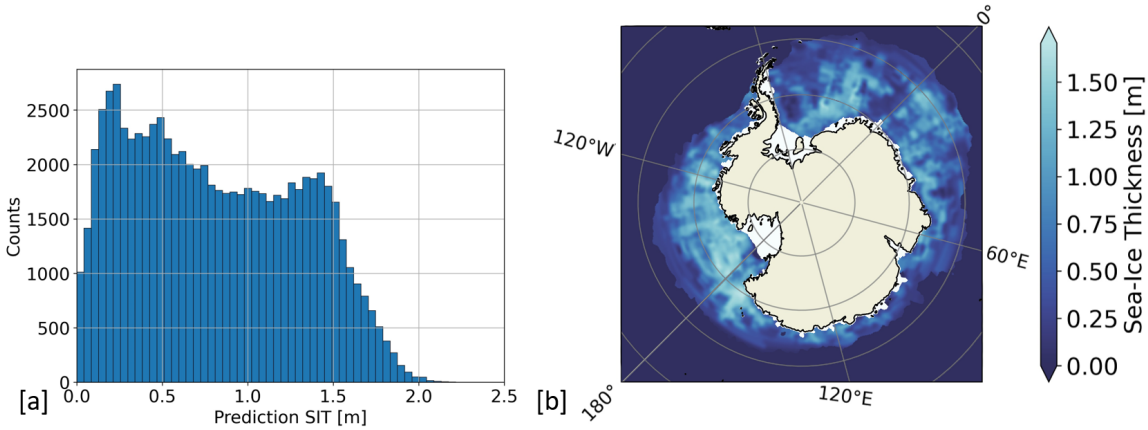

Figure 7.11: Application of the Arctic full-range SIT model to Antarctic data. (**a**) Distribution of the predicted SIT values; (**b**) Monthly composite of Antarctic full-range SIT from 15 October to 14 November 2020.

ice, sea surface salinity and wind speed over ocean, and soil moisture over land [Herbert et al., 2021b, Llaveria et al., 2021, Munoz-Martin et al., 2021b, Munoz-Martin and Camps, 2021]. All geophysical quantities were determined globally, i.e. sea ice parameters for both Arctic and Antarctic, by combining FMPL-2 observations with different auxiliary data based on various NN approaches.

Prediction of Arctic and Antarctic SIC and SIE

In addition to the thin and full-range SIT prediction models explained in the section above, maps of SIC and SIE were obtained using data from both sensors of the FMPL-2 payload – the recorded points by the GNSS-R instrument and T_B data of the L-band radiometer. As auxiliary information, land cover maps from MODIS were used to mask out land masses to account for potentially contaminated land-sea areas due to the large footprint of the FMPL-2 antenna. Similar to the approaches for SIT retrieval, skin temperature data was added to include dependencies on the physical temperature. Two NNs were set up and trained independently for each of the SIC and SIE retrievals. EUMETSAT OSI-SAF Global Sea Ice Concentration product OSI-401-b was used as ground truth for network training. The two SIC models are neural regression networks that produce a continuous output with values between 0 and 100 %, while the two SIE models consist of a binary classification output to discriminate OW and sea ice, respectively. In the first network in each case, only the T_B data – including standard deviation and gradient – and the two auxiliary data sets were used as input to train the networks. In the second models, GNSS-R data – reflected signal elevation angle, reflectivity and standard deviation, and signal-to-noise ratio – were added to the respective inputs of the first networks to achieve a conditional improvement in retrieval accuracy wherever specular reflection points were available. In the first network configurations using T_B data, the absolute error for the SIC retrievals is less than 5 % for both poles, and the classification accuracy for the SIE

estimates are 98.2 % for the Arctic and 96.1 % for the Antarctic. Supplementing the networks with high-resolution GNSS-R data resulted in a lower absolute error for the SIC retrievals of less than 3 % for both poles and a classification accuracy for the SIE estimates of 98.9 % for the Arctic and 99.0 % for the Antarctic, respectively [Llaveria et al., 2021]. An example of Arctic and Antarctic SIC estimate is given in Figure 7.12.

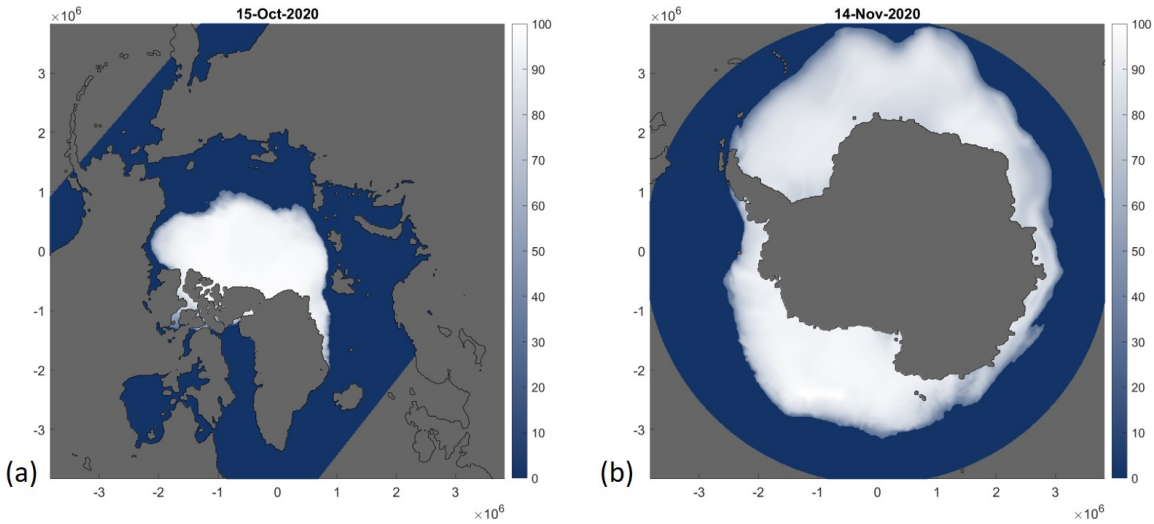

Figure 7.12: Maps of predicted SIC (**a**) for the Arctic on October 15, 2020 and (**b**) for the Antarctic between November 13-15, 2020

Disseminated Sea Ice Products

Images of FSSCat/FMPL-2 T_B and GNSS-R and derived geophysical parameters are publicly available and can be downloaded at `https://catalogue.nextgeoss.eu/`. Sea ice parameters are provided at different processing levels and estimations are projected onto a 12.5 km EASE-Grid 2.0. and are stored in NetCDF. As for SIT maps, L2, L3, and L4 processing level products are produced separately and are available for the Arctic and Antarctic. The range of products comprise the daily estimated tracks of L2 thin SIT, the weekly composites (running mean) of L3 thin SIT, and the weekly composite (running mean) of L4 full-range SIT. Examples of maps of the Arctic and Antarctic L3 products are provided in Figures 7.13 and 7.14, and maps of the Arctic and Antarctic L4 products are provided in Figures 7.15 and 7.16, respectively.

7.3 Discussion

Based on the first results of the FMPL-2 T_B observations of the FSSCat mission, two separate SIT models based on regression NN were implemented. The thin SIT model performed well for sea ice up to ~ 0.5 m. Above 0.5 m – where T_B is less sensitive to SIT – the values are notably underestimated, and the network is not capable of inferring SIT at higher range from the input feature interactions [Naoki et al., 2008]. The retrieval

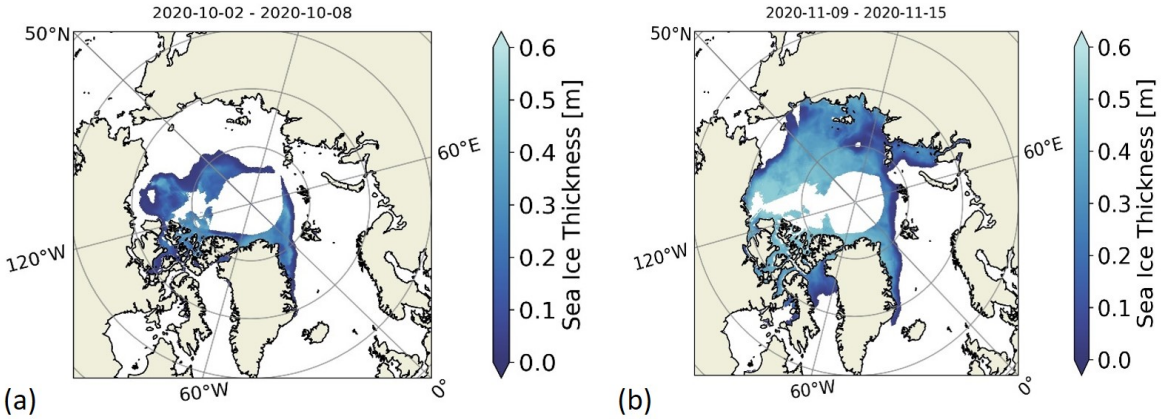

Figure 7.13: Maps of predicted Arctic L3 weekly thin SIT (**a**) from 2–8 October and (**b**) from 9–15 November 2020, respectively.

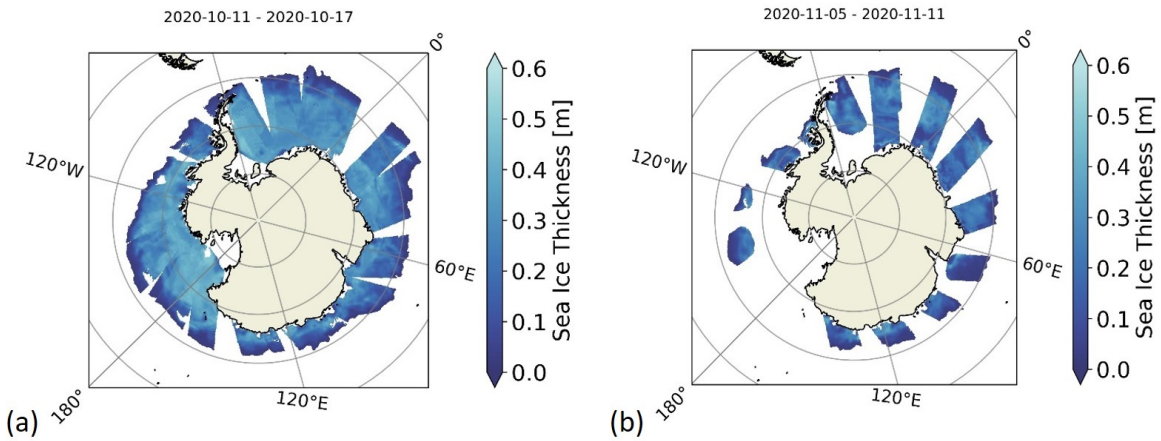

Figure 7.14: Maps of predicted Antarctic L3 weekly thin SIT (**a**) from 11–17 October and (**b**) from 5–11 November 2020, respectively.

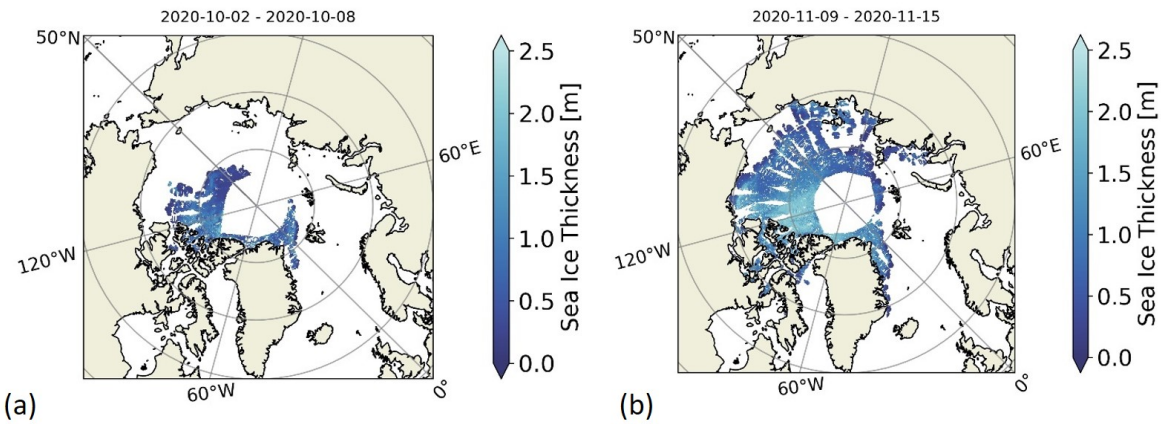

Figure 7.15: Maps of predicted Arctic L4 weekly full-range SIT (**a**) from 2–8 October and (**b**) from 9–15 November 2020, respectively.

algorithm of the corresponding SIT-SMOS product used as ground truth depends on the distribution of the physical temperature of sea ice and performs better for cold conditions

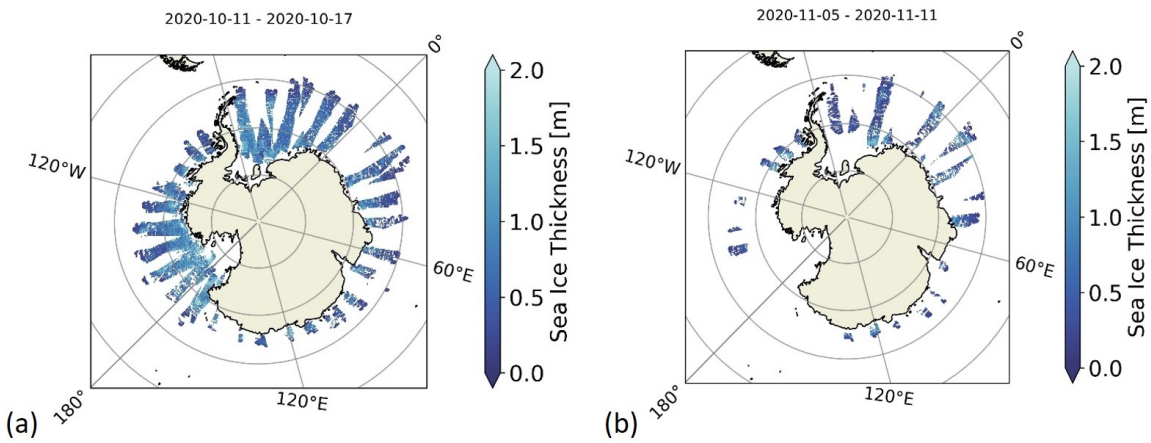

Figure 7.16: Maps of predicted Antarctic L4 weekly full-range SIT (**a**) from 11–17 October and (**b**) from 5–11 November 2020, respectively.

[Tian-Kunze et al., 2014]. This may contribute to the observed deviations between the model prediction and ground truth data for higher SIT. In order to extend the sensitivity range of the thin model, the input features are complemented with sea ice Fb observations from the CS2 mission to yield full-range SIT, using the SIT-CS2SMOS product as ground truth data. The full-range model performs well for values above 1.5 m and for thin SIT. However, between 0.5 m and 1.5 m, a gap of higher errors of magnitudes around 0.25 m to 0.3 m remains. The uncertainty of the merged SIT-CS2SMOS product is a combination of those of the original SIT maps that are derived from SMOS (SIT-SMOS) and CS2 (SIT-CS2) [Ricker et al., 2017]. The observed errors of the model predictions in the intermediate SIT range between 0.5 m and 1.5 m are in agreement with those of the SIT-SMOS and SIT-CS2 products, revealing high relative uncertainties between 25 % and 75 % in the same SIT range. Thus, the higher uncertainty of the SIT-CS2SMOS product at the mostly interpolated intermediate SIT range may affect the learning process during model training, and it limits the prediction accuracy of the network at that particular range.

Instead of using the interpolated SIT-CS2SMOS product as a single target variable in the output layer of the network, more consistent predictions may be obtained by using SIT-SMOS and SIT-CS2 data as two separate variables. The two predicted outputs could be interpolated a posteriori according to their individual error distributions. A conceivable solution to generally overcome the challenge of the remaining sensitivity gap – which is not covered by the altimetry measurements and the radiometry observations at L-band – will be to introduce another feature to the training set. For example, radiometry observations at P-band ($\sim$ 500 MHz), as indicated in Figure 7.2b in Section 7.1.1, can complement the lack of sensitivity in the intermediate range. It can provide the necessary information content to the network to overcome the limitations of both the saturation of T_B for higher SIT and the predominantly high uncertainties of sea ice Fb corresponding to small SIT values.

Although ancillary data at higher resolution are added to reveal information of sea

ice at smaller scale, the large radiometer footprint ($\sim 350 \times 500\,\mathrm{km}^2$ smoothes out the observations and limits the detectable small-scale features of the SIT. Large-scale averaging overall reduces the standard deviation and the dynamic range of the T_B observations. Predictions of the full-range model are currently underestimated at areas of predominately thicker and more heterogeneous multi-year ice, where T_B observations at L-band are already saturated. Overestimated values are mostly located at the transitions between first-year and multi-year ice, and where high contrasts in SIT due to local variability are given. Therefore, the accuracy of SIT estimations while considering smaller scales is limited by the local heterogeneity of sea ice. The actual resolution of the FMPL-2 observations also depends on the orientation between the flight direction relative to the contrasts in surface structures of sea ice. Thus, it would be feasible to deploy a network of FMPL-2 like sensors in a constellation of CubeSats to shorten the revisit time.

The T_B discontinuities between land and sea ice close to coastal areas can lead to oscillations in the image reconstruction process (Gibbs phenomenon). T_B observations over land are sensitive to the soil moisture content, and values at L-band for circular-polarized near-nadir observations can range between around 175–275 K [De Roo et al., 2004]. This often results in higher T_B and an overestimation of SIT in land-sea contaminated areas. The accompanied artifacts can be corrected using a Gibbs algorithm similar to that which is used to derive T_B maps from SMOS data, but has not yet been implemented in the FMPL-2 T_B retrievals [Oliva et al., 2020].

Regarding the range and density of values of Arctic training data, and Antarctic prediction data, the application of the full-range model to predict Antarctic SIT was considered to be reliable during the study period. Because the Arctic and Antarctic regions represent different environments, accurate models require greater understanding on the temporal variability, sensitivity, and uncertainty contributions of the selected input features with respect to SIT estimations. So far, there is no validated product of Antarctic-wide SIT available using a process-based approach, mainly because these models require information on the physical properties, including snow cover. The signatures of radiometry measurements at L-band are sensitive to the intrinsic ice-physical properties, which change over the course of a year, and the conversion of satellite altimeter observations of Fb to SIT requires accurate knowledge of snow cover. Snow depth has been successfully estimated using approaches that are based on both emission models and NNs [Maaß et al., 2013, Liu et al., 2019]. The uncertainty of SIT retrievals is largely determined by the uncertainty of current snow products, and the development of statistics-based models based on a appropriate set of features is promising, but it still remains challenging.

Because the seasons of freeze up and melting in the Northern Hemisphere are the opposite of those in the Southern Hemisphere and sea ice is located towards lower latitudes in the Antarctic, it largely consists of first-year ice throughout the year, which is generally shallower than in the Arctic. This is in agreement with the predictions of the full-range model, which result in an average SIT of 1.25 m for the Arctic and 0.67 m for the Antarctic,

respectively. In the beginning of the Arctic freeze up, sea ice mainly consists of newly-formed thin ice and thick multi-year ice, agreeing with the range of thicker ice between 2 m and 2.5 m, which was only predicted over the Arctic. Unlike in the Arctic, parts of Antarctic sea ice surface temperatures reach the melting point during the observed period, which limits the reliability of the full-range model predictions for these particular values. In case the period of available training data was longer than the observed two months, the model training set should be periodically updated with new data, once any of the input features of the Antarctic prediction data set reaches the limits of the training set.

Part III

Conclusions and Future Research

8 Conclusions

This dissertation has addressed novel data-driven approaches to synergize Earth Observation data to improve the retrieval of subsurface SM, and sea ice parameters.

In the first part, the relationship between satellite-based SM and RZSM observations were investigated on the basis of DTW – a TSA technique capable of quantifying the time lag between non-linearly shifted and distorted time series based on their common prominent features. The DTW technique was used to estimate the response time between the surface-sensitive, high-resolution SMOS L4 product, provided by the BEC, and in-situ profile SM. Topsoil and RZSM observations at 5, 25 and 50 cm from four representative stations within the semi-arid REMEDHUS SM network were selected regarding their land use and soil properties. DTW was applied to the normalized trend series of SMOS L4 and to in-situ observations from 2016 to 2018, and the time lag evolution was obtained accordingly. DTW parameters were customized to the particular input time series to obtain a robust and meaningful time lag. Positive and negative slopes, which correspond to the rate of accumulation and reduction of time lag, respectively, were controlled to consider the natural behaviour of dry periods and heavy rains. In the case of the anormal year 2017, intermittent heavy rains with drier conditions in summer resulted erroneously in an unreasonable accumulation of the time lag, when time series in fact showed clear alignment. To account for this phenomenon, a method based on the curvature of the cumulative sum of precipitation was implemented to determine the onsets of pronounced precipitation events. When alignment of the time series was forced at heavy precipitation events and the time lag was reset to zero, the time lag continued to evolve naturally.

The response time shows strong seasonal variations and differences among different soil properties and land uses. The capability of the method to include the relevant SM-related factors was investigated to understand its impact on the resulting time lag. Climate conditions are mainly variable on large spatial scales and are therefore considered to be captured similarly in both the areal satellite and the point-scale observations. The comparison of long-term precipitation recordings and PET estimations over REMEDHUS allowed the classification of SM seasons, which is specific for a semi-arid region – i.e. recharge, utilization and deficit. Similar climatic conditions and a distinction of the prevailing processes among these three seasons support the interpretation of the time lag. In contrast, the presence of crops and the influence of processes such as root-water uptake

during the main growing season are relevant at the smaller field scale, making SM also locally variable. MODIS NDVI time series at 1 km revealed the phenological cycle of the predominant land use of the study area, which mainly consists of rainfed cereals. During the main growing season, the spatial heterogeneity of land cover was analyzed from Sentinel-2 NDVI images at 10 m resolution to estimate the level of spatial representativity of the SMOS L4 pixel with the corresponding in-situ stations. The spatial scale of cultivated fields is typically much smaller than the 1 km pixel, and heterogeneity led to non-negligible differences among observations at in-situ stations in the area integrated by the satellite product.

The following conclusions can be drawn regarding the evolution of time lag at the particular stations. Finer-textured soils result in higher time lag. The deficit season clearly shows the highest time lag. When abundant rains prevent long-term dry out during recharge and utilization seasons, essentially less time lag is accumulated. In most cases, time lag increases with increasing depth. This is given for the two most representative stations `M5` and `E10`. An inverse behaviour could be observed at station `J12`, where strong root-water uptake was present during the main growing season. Hereby, RZSM was consumed rapidly, whereas soil at shallow depths dried out more slowly, which resulted in less accumulation of time lag.

The exponential filter is an independent TSA method which is often used to validate the results of novel RZSM retrieval algorithms. The method was applied to SMOS L4 time series to determine the SWI while optimising the characteristic time length in days up to which profile SM is influenced by previous satellite observations. For each station and depth level, the time length was optimized on the basis of different validation metrics for the respective SM seasons. The representative SM-season-specific optimal time lengths largely resemble the seasonally averaged response time results using DTW – which were particularly high during the deficit season. By considering the time length to be characteristic for each SM season – rather than being a constant for each station and depth only – led to a better performance of the exponential filter. Besides the analysis of the seasonal differences in SM dynamics, the relationship between SM time series and other surrogate parameters – such as land use information – that clearly influence the SM regime, require further investigation to enhance the retrieval of profile SM.

The second part of the thesis is focused on the segmentation of sea ice using a Bayesian Unsupervised learning framework to combine multi-source satellite observations, and the retrieval of SIT using data of the FSSCat mission on the basis of an NN approach.

In a first application, the 2D Bayesian approach was used to segment high-resolution Sentinel-1 SAR images to discriminate water from sea ice, with the aim of estimating the fraction of closed surface water including melt ponds and leads, and the associated SIC. A common challenge in current sea ice classification algorithms using SAR imagery is the dependence of the backscatter coefficient on small variations in surface roughness as well as its non-linear angular dependence, which shows differences between different

sea ice types and calm waters compared to rough, wind-induced waves over the ocean. Images at incidence angles lower than 30 ° were discarded and a single slope correction was applied to account for angular variation along the period when sea ice was present. Unambiguous categorization through the observed SAR surface signatures is only possible when sufficient contrast is given, which limits the accuracy of any segmentation method. Bayesian inference was preceded by an EM step to estimate whether the amount of data points in the observed area representing water is significantly high to form a separate class in the segmentation.

The method was applied to an area in the northern Barents Sea which allowed the estimation of high-resolution SIC during a full annual cycle from the Arctic freeze-up in September to the ice-free period in August. The obtained patterns of the segmented images were compared with optical data from Sentinel-2 at the dates, when the extracted SIC largely differed from the reference SIC. These differences may have originated from the presence of melt ponds. Since the optical images are affected by cloud coverage, the collection of sufficient ground-truth images is challenging, but can be further considered for evaluating the classes. Due to the probabilistic approach, the model uncertainty of the detected surface water class can be determined from the class probability distribution for each pixel. The method may be a major step towards the automatic segmentation of SAR images to produce high-resolution SIC maps, and to overcome the known limitations of SIC retrievals based on low-resolution microwave radiometry observations only.

In a second application, the approach was applied to multi-incidence angle SMOS T_B observations over the Arctic in the period of late summer melt and early freeze-up in 2016. Classes are formed based on the the link between the sea ice properties and the differences and similarities of the PR at high incidence angles. The number of relevant classes was determined a priori from the PR distribution, and it was verified a posteriori using GSI. Model uncertainty was determined using information entropy which allowed to distinguish well-determined regions from uncertain ones. High global separability was achieved considering two classes during late summer melt and three classes during freeze up, respectively. A comparison with existing maps of thin sea ice (SIT-SMOS product) indicated that classes can be attributed to SIT ranges. During late summer melt, two classes could be attributed to remaining thick ice, and a transition zone, showing differences in the correlations of the input features. With the beginning of the formation of new thin ice during freeze up, an additional class could be discriminated based on the occurrence of higher PR values. However, the decrease in relative abundance of newly formed ice to the total sea ice during freeze up resulted thin sea ice to be less significant and led to higher overlap between classes. The underlying sea ice properties and the corresponding variation in PR have to be better understood to draw conclusions of the obtained classes, considering an entire annual cycle of Arctic sea ice formation and melting.

The 2D-segmentation performed individually at each time step showed limited tempo-

ral stability of the classes. Along the freeze-up, the number of significant classes changes and classes have consistently different physical meaning, because not all ice types are equally well represented during the development of sea ice, showing non-negligible shifts in the resulting class mean values. The segmentation requires reasonable manual selection of the number of classes, which makes its formation unreliable under changing ice conditions, and automatic segmentation – which is necessary for operational monitoring – is constrained. So far, the algorithm was applied to observations comprising the late summer melt, and the beginning of the freeze up and classes were mainly analyzed during the formation of sea ice. Sea ice undergoes an annual cycle of freezing and melting periods and classes emerge and disappear seasonally according to the changing surface conditions.

The 2D spatial algorithm was extended to three dimensions to include temporal interaction to be able to capture the full spatio-temporal context of sea ice. The algorithm was successfully verified to be able to reconstruct the underlying structure of a synthetic four-featured 3D data set, generated with Gaussian emission functions. The basic idea is that all data points are connected in space and time, based on a Markov field, and the information of each voxel gradually iterates through the entire model space. Voxel-based segmentation has the advantage over pixel-based implementation that the total number of significant classes with respect to the selected set of input features needs to be determined only once. Classes are supposed to recur on an annual basis, and 3D segmentation can be performed without manual guidance at each time step.

3D segmentation was applied to SMOS and AMSR2 T_B data to investigate the joint effect of multi-frequency observations, similar to those of the future CIMR mission. A total number of six classes along an entire annual cycle seemed a suitable choice with respect to the evolution of spatial patterns in physical space. The corresponding location of the mean values of the clusters in the marginal features space between 18 and 36 GHz is often used in common algorithms to infer SIC. The segmented classes were ranked in ascending order regarding the mean values of SMOS low-frequency feature. Feature-specific mean values of each class can be related to the frequency-depending radiometric properties – such as scattering phenomena – to reveal the underlying sea ice state, and the linear dependence between the features is characterized by the covariance matrix. Variability of class membership clearly indicates both the beginning of the freezing period and the start of the melting season. In summer, sea ice conditions change due to stronger irradiation and higher air temperatures, and observations lose sensitivity to sea ice composition, such that these classes could be associated with different stages of wet conditions. Segmentation of data in courser time intervals over the period from 2012 to 2019 resulted in temporally stable annually recurring classes.

The spatial consistency of the segmentation result was evaluated by comparing the class patterns with maps of SoD of operational ice charts, and current SIC and SIT products. Class shapes can be identified with those of the most common SoD, including nilas, thin FYI and old ice in early winter, and thick FYI and old ice as sea ice formation pro-

gresses. Concerning SIC, Class 0 represents newly formed sea ice with low concentration at the sea ice edge, Class 1 can be primarily associated with ponded ice with reduced SIC due to the presence of melt ponds during advanced melting in late summer, and the remaining classes contain fully ice-covered areas. Within the freeze-up period classes can be clearly attributed to SIT ranges. Classes 0-2 resemble thin SIT ranges, where low-frequent observations have sufficient penetration depth. Classes 3-5 can be related to the full-range SIT-CS2SMOS product and show a clear positive trend along the freeze-up. This could be explained because as sea ice ages, its surface conditions change. Thus, sea ice age can be used as a proxy to indirectly estimate SIT ranges beyond the sensitivity range of microwave radiometry observations.

The use of nanosatellite data for Earth observation applications to determine geophysical parameters can be a cost-effective alternative or valuable complement to large satellite missions. A novel approach was developed to retrieve SIT maps over polar areas based on predictive regression NNs using the first results of the FMPL-2 L-band microwave radiometry observations of the FSSCat mission. Unlike process-based or simple regression models, data-driven approaches enable to adequately address the complex nature of sea ice. Information regarding non-linearly related sea ice parameters are contained in the link between a selected number of variables. These relationships were considered in the hidden layers of the NN model.

Two independent models have been implemented and trained with Arctic data to yield maps of Arctic thin SIT and full-range SIT. The model input features comprise the FMPL-2 T_B observations and ancillary data, including SIC and skin temperature maps. A thin SIT model was implemented using the SIT-SMOS product as ground truth data and targets SIT values up to 0.6 m, being limited by the sensitivity of L-band T_B observations. Adding complementary information of CS2 sea ice Fb data to the existing input features allowed us to extend the sensitivity range to values that are larger than those covered by the thin SIT model. This enabled implementing a second model yielding full-range SIT, which was evaluated using maps of the merged SIT-CS2SMOS product as ground truth data.

Both models were trained on Arctic data during early Arctic freeze up from 15 October to 4 December 2020. Hyperparameters were adjusted to prevent the models from data overfitting to obtain the optimal fit through the minimization of the MAE cost function. The thin ice model shows good performance with an overall MAE of 0.065 m, and it generalizes well up to a SIT of 0.5 m, while underestimating for higher SIT values. The best fit of the full-range model results in a MAE of 0.237 m, and the predictions match well for thin ice and SIT above 1.5 m. Hereby, the main error contribution originates from predicted values in the intermediate SIT range. Major losses may be attributed to either an existing sensitivity gap of the sensors or to the limited availability of sufficient values for training during the observed period. The predictive models allowed for producing weekly composite maps of thin and full-range SIT at the Arctic scale. The full-range model that

was obtained from Arctic data was also applied to Antarctic data to produce monthly composites of Antarctic SIT. It is important to note that a disseminated product of full-range SIT maps at Antarctic scale was not available for comparison during the observed period.

9 Future Work

The link between surface-sensitive and profile SM measurements has been investigated using DTW to quantify the time lag based on the similarity between SMOS L4 data and in-situ time series. Both time series respond to heavy precipitation events and the time lag shows seasonal variability with larger values in the SM deficit season. Assuming that the response time between subsurface and surface sensitive SM is a constant – as it is common using the exponential filter technique – can significantly reduce the accuracy of RZSM retrievals for certain seasons due to potential oversmoothing. The precipitation and PET patterns allowed to define SM seasons, i.e. periods of recharge, utilization and deficit, which reflect the variability of the typical SM regime of the investigated semi-arid region. Future work could include applying the approach to other SM networks in other climates where the coupling between surface and RZSM is different, and SM seasons can be defined accordingly. In humid climates, after continuous rain, another surplus season may occur after continuous recharge when the field capacity – which limits the SM storage – is reached. Once the relationship between the SM regime and the response time for different climates is better understood, the RZSM can be estimated assuming individual characteristic time lengths for each SM season.

In addition to the importance of different climatic conditions and soil types for the soil-water balance, other factors such as the heterogeneity of land use and the representativity of the network station within the satellite pixel can also have a critical impact on the reliability of the technique. A harmonic analysis of successive land cover observations derived from the satellite-based NDVI (indicating the plant's health) can be performed to describe the temporal variation of land use, i.e. typical land use, and higher harmonic terms, obtained from the frequency of specific land covers in the observed time series.

The large spatial sampling of satellite-based SM products is an ongoing challenge since satellite sensor designs are a trade-off between sensitivity and spatial resolution. Downscaling approaches such as the SMOS L4 algorithm will continue to rely on approximations using auxiliary information like NDVI and land surface temperature to capture the small-scale variation. The analysis of subsurface SM together with the atmospheric state variables temperature and humidity in coupled land-atmosphere data assimilation approach may lead to mutual enhancement of the analysis to provide SM at higher resolution more accurately [Reichle et al., 2008, De Lannoy et al., 2019].

The warping path as being the evolution of the time lag, could be introduced into a neural network framework together with atmospheric parameters to investigate the contribution of each variable to the RZSM. The total warping path can be used as a global measure which represents the overall dissimilarity between the time series. It can be used to categorize the relationship between observations at different locations to estimate the characteristic coupling between surface and RZSM. It can also serve as a proxy for the penetration depth of the signal into the ground by assessing the sensitivity of the satellite-based time series to finely sampled multi-depth sensors.
TSA techniques have the advantage – unlike process-based models that solve for the flow and transport equations – that they do not depend on many variables, which is a useful simplification when there is not enough information to fully understand all the processes. Since time series are the only source of information on which TSA techniques rely, it is important to understand the influence of temporal sampling and total data length on the estimations. The temporal evolution of the response time can be investigated at different timescales to better assess which processes are captured in the time lag between surface and subsurface SM.

Observations of polar-orbiting satellites, which acquire data in the low-microwave spectrum, have resolutions $\sim$10–50 km and do not resolve the small-scale heterogeneous state of sea ice. The large satellite pixels comprise a distribution of SIT, but only provide a single value if the spatial interaction are not considered. The implemented probabilistic inference model using HMRF takes into account the interactions in space and time between neighboring voxels. The multivariate Gaussian distributions of classes comprise mixed sea ice states. Each pixel has a non-zero probability to belong to each of the segmented classes, which are previously validated and assigned to a specific sea ice state, i.e. encompassing a certain SIT range. If the relationship between each class and sea ice parameters, such as the SIT ranges, is known, the SIT distribution at each voxel can be estimated based on the respective class membership probability. Each pixel then contains the information about the typically occurring classes in a given spatial and temporal surrounding. In theory – this enables the algorithm to capture the sub-pixel distribution of SIT.

Changes in SIT can then be predicted by evaluating the transitions between classes in the probability distribution – which typically occur at a certain geographic location and time of the year, or due to specific external atmospheric forcing and irradiation – over a longer period (e.g. several years). The transition between classes (which can be referred to sea ice states) can be investigated to better understand the local and seasonal behavior of sea ice growth and melting. Automated segmentation of the polar regions requires reliable and physically meaningful classes representing the same sea ice properties with multi-year consistency to determine SIT and SIC of similar quality as in current operational products produced by experienced sea ice analysts – also on the local and seasonal level. So far,

the positive trend along the freeze-up period between SIT-CS2SMOS and Classes 4–6 has been verified at Arctic scale. Beyond the sensitivity range of microwave radiometry observations to thin ice, sea ice age can be used as a reliable proxy for SIT estimation if the relationship between classes and the sea ice state is fully understood on the seasonal and local scale.

The estimated classes can be evaluated using a RTM such as the Snow Microwave Radiative Transfer (SMRT) thermal emission and backscatter model [Picard et al., 2018]. Different sets of segmented input features yield hidden field patterns which represent different sea ice properties. For each resulting class the expected electromagnetic signal can be simulated in a forward modelling approach to estimate the corresponding sea ice properties as model parameters. The model parameters can be adjusted accordingly for single or mixed ice types to approximate the radiations which resemble the class mean values for all the respective input features best. The relationship of satellite observations at multiple frequencies can be assessed to obtain an appropriate set of input features that enhances the sensitivity to sea ice parameters, such as SIT. Also, in case a set of observations is included in a retrieval, it is important to know which of the observed properties dominates the formation of a particular class. It can be further evaluated which observation can be added or removed as an input feature to improve the total information content by reducing redundancy in order to optimally resolve the remaining ambiguities.

However, the data are never completely sufficient to unambiguously characterize all the relevant sea ice properties of interest. For many applications, the information content from the data provided by current satellite missions is limited. The number of model parameters to fully characterize the state of sea ice exceeds the space-based capability to provide all necessary observations, and the inference problem remains ill-posed. Therefore, retrieval algorithms continue to rely to some extent on auxiliary data, simplifications, and empirical relationships to constrain the model parameters.

Future missions such as CIMR, the Copernicus Polar Ice and Snow Topography Altimeter (CRISTAL), and the Radar Observing System for Europe – L-band (ROSE-L), are planning the deployment of new sensors with higher spatial and temporal resolutions, and increased coverage to fill existing capacity gaps to eventually reduce the model uncertainty. In particular, the simultaneous collection of multi-sensor data (as in CIMR) would greatly reduce representativity errors that occur when combining non-collocated observations. As a general tool to evaluate the synergistic effect of combining spatial and temporal multi-source data sets, the algorithm has a wide range of applications and is particularly useful to assess in advance how the data produced by these new satellite missions can be efficiently blended together.

The sea ice edge is the most variable zone where sea ice forms newly and the fastest changes and the largest variation in sea ice parameters occur. For example, the significance of the definition of SIC depends on the observed scale, and for smaller grid cells

– apart from the sea ice edge – only values of 0 and 1 are obtained. Therefore, SIC can be considered a continuous variable around the marginal ice zone. Apart from the wet conditions during summer melt, which are generally difficult to determine based on microwave radiometry observations, the large areas of closed ice are only gradually changing and mostly stable in the short term. The proposed unsupervised machine learning algorithm segments sea ice into a number of most significant classes, and the resulting patterns are formed according to the most frequently occurring values. Since all data points are required to be assigned to one of the classes, some classes are more robust and separable, where others are less cohesive and contain a broader range of values. In terms of sea ice, the least significant class in which the highest uncertainty may comprise the most interesting areas for specific applications where values change the fastest and over the shortest distances like in deformations and the opening of leads. In the application of the algorithm to multi-incidence SMOS data, the thin ice class encompasses observations where input features are the least correlated, but may contain the most valuable information about the underlying sea ice properties. In the detection of deformations or rarely occurring surface signatures based on SAR images, the misclassified pixels may be the target. Future work could focus more on the sea ice margin in an informative segmentation to give more weight to this most relevant areas and to better resolve the distributions. This spatial target areas could be pinpointed, for example, by evaluating when sea ice-related atmospheric conditions change beyond a certain threshold, or by using a hierarchical algorithm and performing local segmentation for the uncertain areas.

NNs have the advantage to be adaptive to new data sets and models are able to capture variable sea ice conditions and changing relationships of the input variables when considering longer learning periods. Future tasks may comprise the application of the methodology to additional data to better identify limitations and to evaluate model performance on regional scale. The inferred products demonstrated the success of the FSSCat mission and the potential of applying FMPL-2 T_B to estimate SIT over polar areas using data from a single CubeSat. Using a constellation of ^{3}Cat-5/A-like CubeSats may effectively increase the satellite revisit and the spatial resolution of T_B maps, with the potential to improve overall model accuracy. These constellations would provide a feasible moderate-cost alternative to complement large satellite missions. They may substitute them during gaps of non-existent data in order to guarantee the continuous monitoring of polar sea ice at both hemispheres.

Part IV

Back of the Thesis

Appendices

A Application of DTW to Relate Gaussian Distributions

In Chapter 4, DTW technique is applied to compare SM time series from satellite observations and multi-depth in-situ measurements. In this example, the technique is demonstrated by means of synthetic data which represent the diffusion of a random variable. The time series to be related are represented by two snapshots of Gaussian distributions. This example could represent how an initial concentration of a substance (e.g. caused by a spillage or leak), is spreading over time due to diffusion and advection processes.

The intermediate steps to obtain the optimal warping path between the two time series are visualized in Figure A.1. In Figure A.1a, the initial and final distributions are given. The initial concentration is represented by a sharper distribution `gauss1`, with the mean at time step 40. The time-lagged final distribution `gauss2` has the mean at time step 100. The Euclidean distance matrix D_E is pairwise computed from the differences in magnitude at every sample (Figure A.1b). The largest distances between the two series are given at the row and column entries along the corresponding maxima of the distributions. Hereby, element (40,100) shows a local distance minimum represented by a clear bottleneck. The accumulated cost matrix C_{acc} is computed from the distance matrix and reveals a clear low-cost valley, along which the optimal warping path p^{opt} evolves (Figure A.1c). The saddle point of the warping path coincides with the aforementioned local minimum with a forced alignment at the elements (0,0) and (200,200). Throughout the entire period, the concentration in distribution `gauss1` accelerates faster and hence is always ahead of distribution `gauss2`. The allocation plot between the two time series is given in Figure A.1d. One sample of `gauss1` is always allocated to multiple samples of `gauss2`, which eventually leads to an accumulated time lag of the warping path.

Both distributions converge monotonically towards zero concentration and, since `gauss1` is faster-accelerating than `gauss2` within the entire period, the time lag is accumulating until the boundary condition forces alignment at (200,200). Unless the change of concentration in the synthetically created input series is already negligible for `gauss1` at long times, the warping path gets trapped at very high time lags. In nature, these non-detectable low values can be in the order of the noise level where the concentration is already of irrelevant magnitude. Customization of the DTW technique, described in the

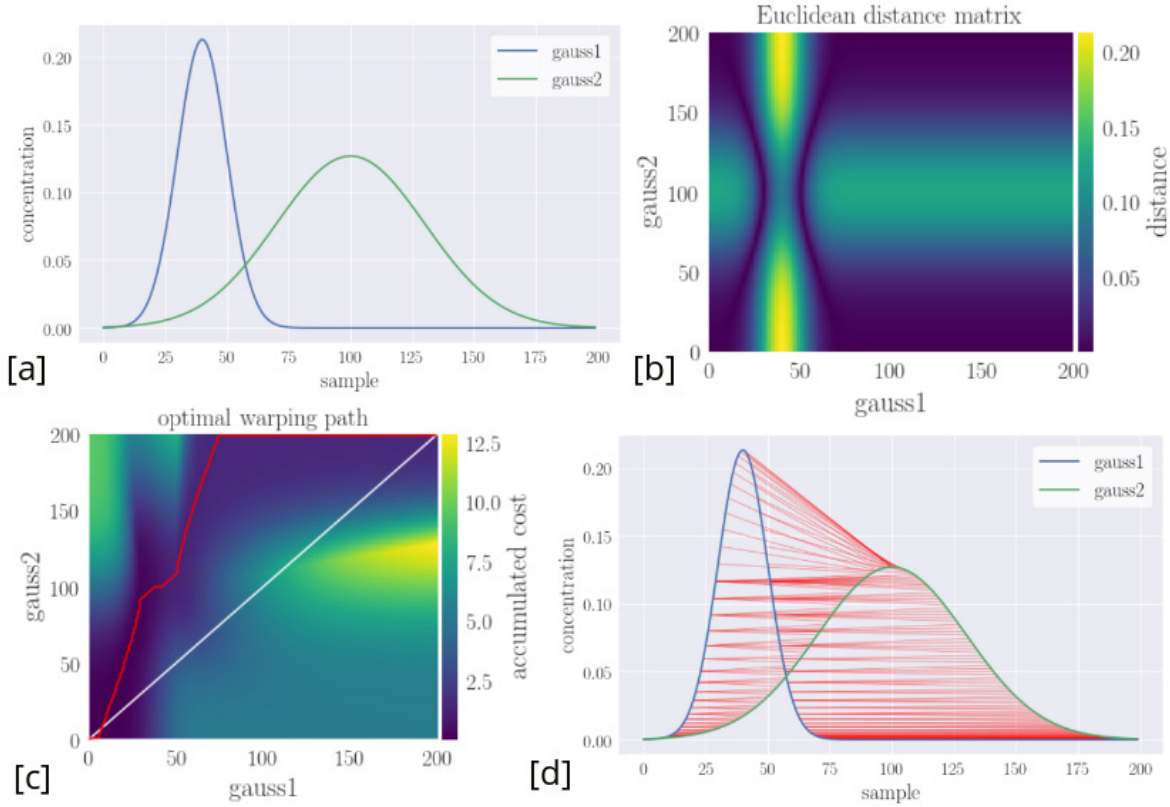

Figure A.1: DTW technique explained on the basis of a synthetic example: **[a]** input time series including the initial concentration (blue) and temporally evolved concentration (green); **[b]** Euclidean distance matrix; **[c]** accumulated cost matrix and the optimal warping path with forced alignment boundary conditions at the beginning and the end of the sequences. The diagonal of the cost matrix is indicated by a white line and represents the alignment of the time series along the entire period; **[d]** corresponding point allocations.

next Section 3.2.2, can avoid unreasonable time lag evolution, when tailored for specific application. Hereby, an adequate step-size can control the speed of the warping path and a maximum allowed time lag prevents the warping path to become trapped at high time lags.

B Implementation of the Bayesian Segmentation Algorithm

Algorithm 1: Parallel Gibbs sampler

Input : k-Colored MRF, $\mathbf{y}$, $\Phi^{(t)} = (\boldsymbol{\mu}^{(t)}, \boldsymbol{\Sigma}^{(t)}, \beta^{(t)})$, $\mathbf{x}^{(t)}$

1 **for** *the k colors* κ_i : $i \in \{1,2,...,k\}$ **do**

2 **parafor** *all voxels in the i-th color* $j \in V_{\kappa_i}$

3 calculate the local *a posteriori* distribution $p(X_j \mid y_j, \mathbf{x}_{\partial_j}{}^{(t)}, \mu_{x_j}{}^{(t)}, \Sigma_{x_j}{}^{(t)}, \beta^{(t)})$;

4 draw candidate $x_j{}^* \sim p(X_j \mid y_j, \mathbf{x}_{\partial_j}{}^{(t)}, \mu_{x_j}{}^{(t)}, \Sigma_{x_j}{}^{(t)}, \beta^{(t)})$;

5 calculate the local energy $U'(x_j{}^*, \mathbf{x}_{\partial_j}{}^{(t)}), U'(x_j^{(t)}, \mathbf{x}_{\partial_j}{}^{(t)})$;

6 accept $x_j^{(t+1)} = x_j{}^*$ with probability $\min\{1, \exp[U'(x_j^{(t)}, \mathbf{x}_{\partial_j}{}^{(t)}) - U'(x_j{}^*, \mathbf{x}_{\partial_j}{}^{(t)})]\}$;

7 **end parafor**

8 **end for**

Return $\mathbf{x}^{(t+1)}$

Figure B.1: Scheme of the parallel Gibbs sampler [Wang et al., 2017].

Algorithm 2: Bayesian parameter estimation using M-H algorithm

Input : $\mathbf{y}$, $\Phi^{(t)} = (\boldsymbol{\mu}^{(t)}, \boldsymbol{\Sigma}^{(t)}, \beta^{(t)})$, $\mathbf{x}^{(t+1)}$

1 **for** *the label* $l \in \{1,2,...,n\}$ **do**

2 update $\mu_l^{(t)}$ to $\mu_l^{(t+1)}$ conditional on $\tilde{\mu} = \{\mu_1^{(t+1)},...,\mu_{l-1}^{(t+1)},\mu_{l+1}^{(t)},...,\mu_n^{(t)}\}, \mathbf{y}, \mathbf{x}^{(t+1)}, \boldsymbol{\Sigma}^{(t)}, \beta^{(t)}$;

3 **end for**

4 **for** *the label* $l \in \{1,2,...,n\}$ **do**

5 update $\Sigma_l^{(t)}$ to $\Sigma_l^{(t+1)}$ conditional on $\tilde{\Sigma} = \{\Sigma_1^{(t+1)},...,\Sigma_{l-1}^{(t+1)},\Sigma_{l+1}^{(t)},...,\Sigma_n^{(t)}\}$, $\mathbf{y}, \mathbf{x}^{(t+1)}, \boldsymbol{\mu}^{(t+1)}, \beta^{(t)}$;

6 **end for**

7 update $\beta^{(t)}$ to $\beta^{(t+1)}$ conditional on $\mathbf{y}, \mathbf{x}^{(t+1)}, \boldsymbol{\mu}^{(t+1)}, \boldsymbol{\Sigma}^{(t+1)}$

Return $\Phi^{(t+1)} = (\boldsymbol{\mu}^{(t+1)}, \boldsymbol{\Sigma}^{(t+1)}, \beta^{(t+1)})$

Figure B.2: Scheme of the parameter estimation using a Metropolis-Hastings algorithm [Wang et al., 2017].

C | Preliminary Comparison between SAR images and Airborne EM

Several airborne field campaigns were conducted in the Arctic and Antarctic to estimate SIT using EMI measurements such as ESA's SMOSIce [Haas et al., 2009,Kaleschke et al., 2016] or laser altimetry observations such as NASA's Operation IceBridge [Kurtz et al., 2013] that has be used for validation. Here, the Bayesian segmentation approach is applied to assess the relationship between Sentinel-1 SAR images and the tracks of airborne EMI observations. In this first attempt, aim was to segment the 1D tracks into a number of classes and to estimate how the backscatter coefficient and the SIT are related in each case for preliminary classification. In the 1D approach, the heterogeneous model parameter β is a scalar which takes into account the spatial interactions between the two neighboring points of a central observation along the track.

The input data for segmentation consist of the EMI-derived SIT data acquired from 9–11 November 2017 in the Wester Ross Sea (`https://doi.pangaea.de/10.1594/PANGAEA.925092` and the Sentinel-1 L1 GRD EW HH images at 15 m resolution (`https://www.sentinel-hub.com/`. The airborne EMI measurements have a footprint of approx. 45 m, with a sampling of 6 m and a total survey length of approx. 800 km, and the derived SIT is provided with an accuracy of 0.1 m. Figure C.1 illustrates the SIT survey tracks and the corresponding SAR image with the backscattering coefficient created at the same time interval as the field campaign. Since the backscattering coefficient shows strong angular variations (19–47 °), a subset is selected for segmentation in which the incidence angle variation of less then 2 ° (corresponding to the section in Figure C.1b). The grid centres of the SAR images are projected onto the airborne EMI samples using nearest neighbor interpolation to obtain regularly sampled 1D γ_0 data at the same locations as the SIT data points).

Segmentation was applied for 300 iterations to the set of two 1D vectors of SIT and γ_0 for a significant number of 5 classes predefined using BIC score. The diagnostics of the segmentation are given in Figure Figure C.2, comprising the evolution of the heterogeneity coefficient and the class-specific correlation obtained in the iterative sampling process. The segmented latent field is initially heterogeneous and evolves into more homogeneous patterns for more iterations when considering the spatial interactions between neighboring

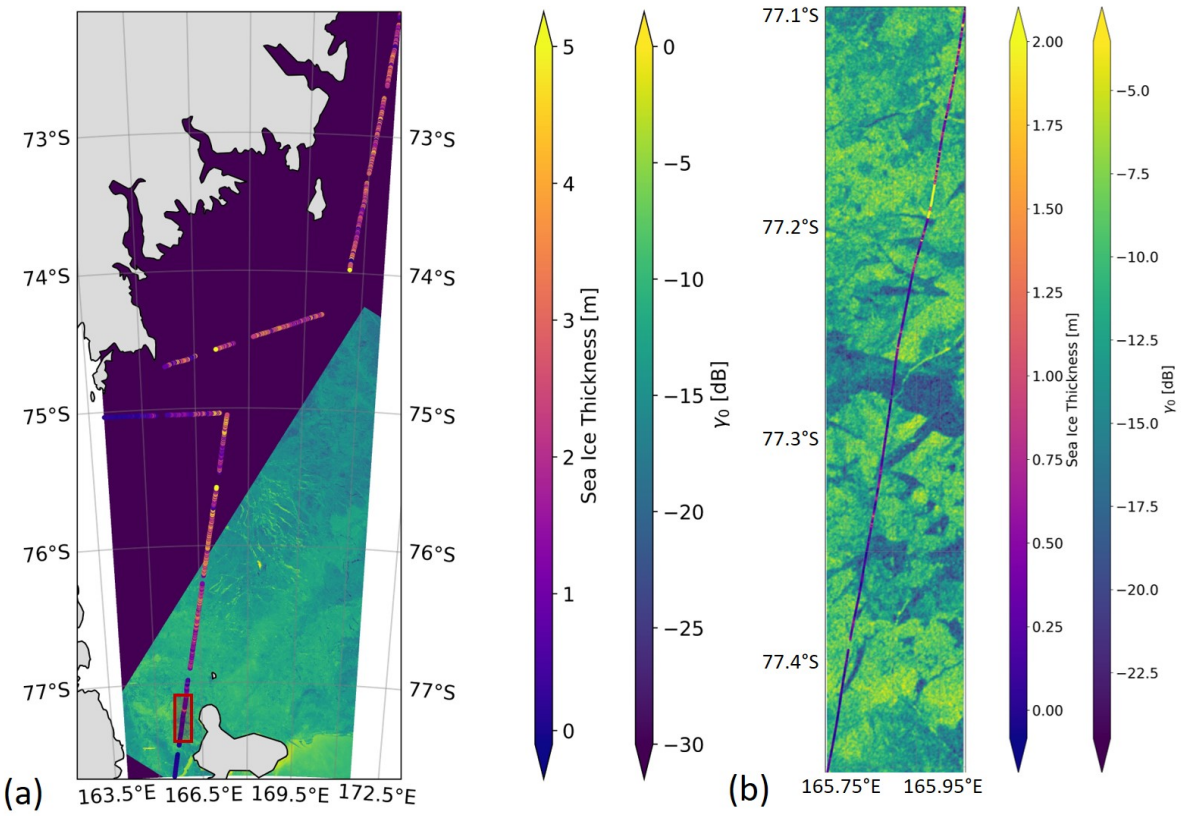

Figure C.1: Tracks of EMI-derived SIT and Sentinel-1 SAR image recorded at the same days over the Western Ross Sea. (**a**) entire 3 airborne tracks acquired from 9–11 November 2017 with a total track length of approx. 800 km; (**b**) smaller section of the SIT track and the corresponding γ_0 background.

points. The resulting latent field in physical space is presented in Figure C.4.

The 5 classes can be classified according to the structures of the underlying SAR image, and the location of the clusters in feature space (Figure C.3). For example, in the upper section of the track the magnified circular feature (Figure C.4a top) as part of class 4 reveals a thick multi-year ice floe. Class 1 in the section (Figure C.4a bottom) can be attributed to a very thin ice layer and smooth surface conditions. A possible interpretation between the classes with regard to the state of sea ice is given in Table C.1. The consistency of this preliminary classification is limited due to the fact that the exact time of the EMI acquisitions show a temporal mismatch with the collected SAR images, which is non-negligible considering high sea ice drift velocities. To match the two techniques more precisely, one can select a region where all relevant ice types can be observed, but where the sea ice is less dynamic - such as in ice plugs, where sea ice can remain largely static over multiple years.

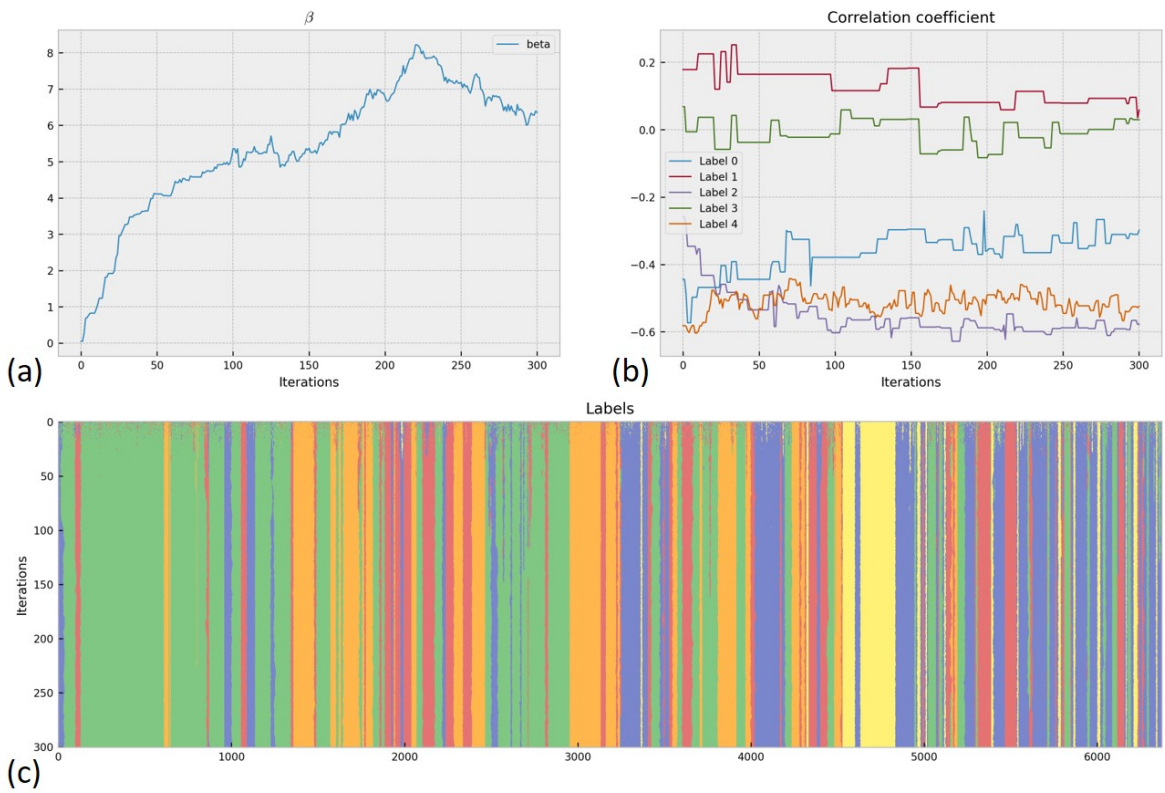

Figure C.2: Segmentation diagnostics of the iterative sampling process using SIT and γ_0. (**a**) heterogeneity coefficient β; (**b**) Correlation between the SIT and γ_0 for each class; (**c**) segmented latent field patterns along the 6500 samples for each iteration step.

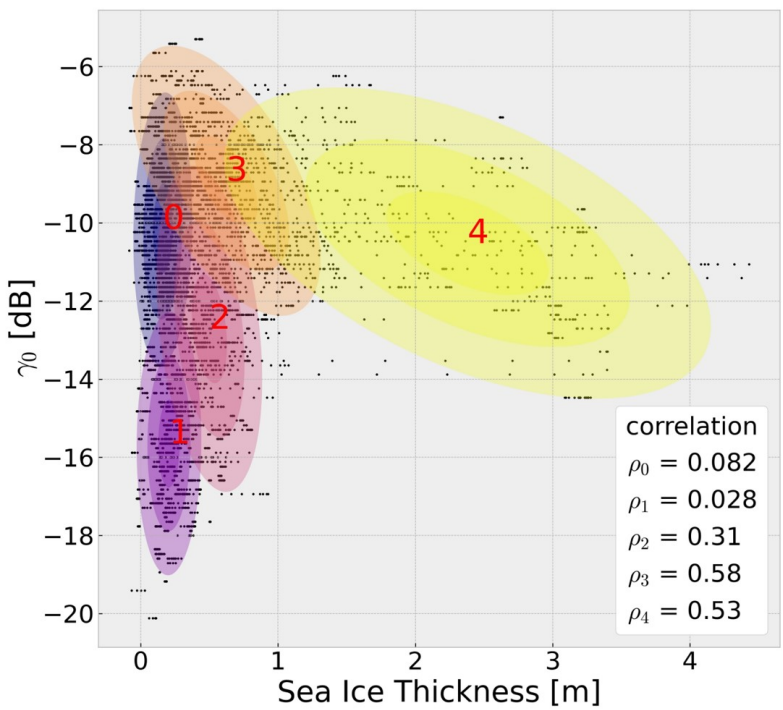

Figure C.3: Clustering results of the 1D segmentation in feature space and the correlation between SIT and γ_0.

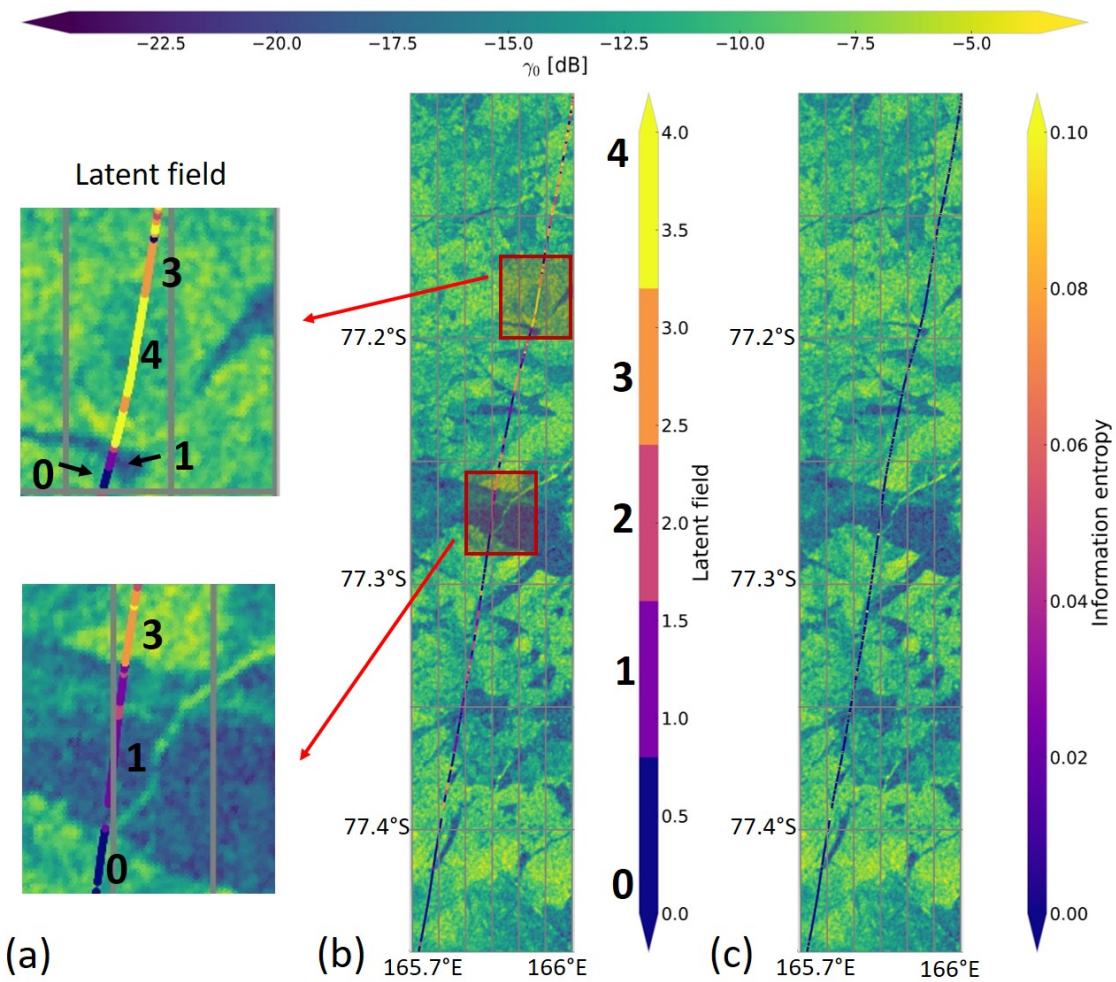

Figure C.4: Results of the 1D segmentation in physical space. (**a**) Magnified features comprising a rough and thick MYI floe (top) and smooth and thin ice (bottom); (**b**) segmented patterns of 5 classes; **c**) model uncertainty using entropy obtained from the class probability.

Table C.1: Statistical and spatial class interpretation based on the attributed intervals of SIT and γ_0 values and their correlation.

Class	Correlation	SIT	Backscatter	Interpretation
0	Low < 0.3	Thin < 0.5 m	High $>$ -14 dB	Thin young ice, rough surface
1	Low < 0.3	Thin < 0.5 m	Low $<$ -12 dB	Water or very thin ice, smooth surface
2	Moderate $0.3 < \sigma < 0.5$	Medium < 1 m	Medium -17 dB $< \gamma_0 <$ -8 dB	FYI, heterogeneous SIT, thermodynamic ice growth
3	Strong > 0.5	Medium > 1.5 m	High $>$ -12 dB	FYI, deformation- induced ice growth
4	Strong > 0.5	Thick > 1 m	High $>$ -14 dB	Rough and deformed thick MYI

D | Distribution of SIT

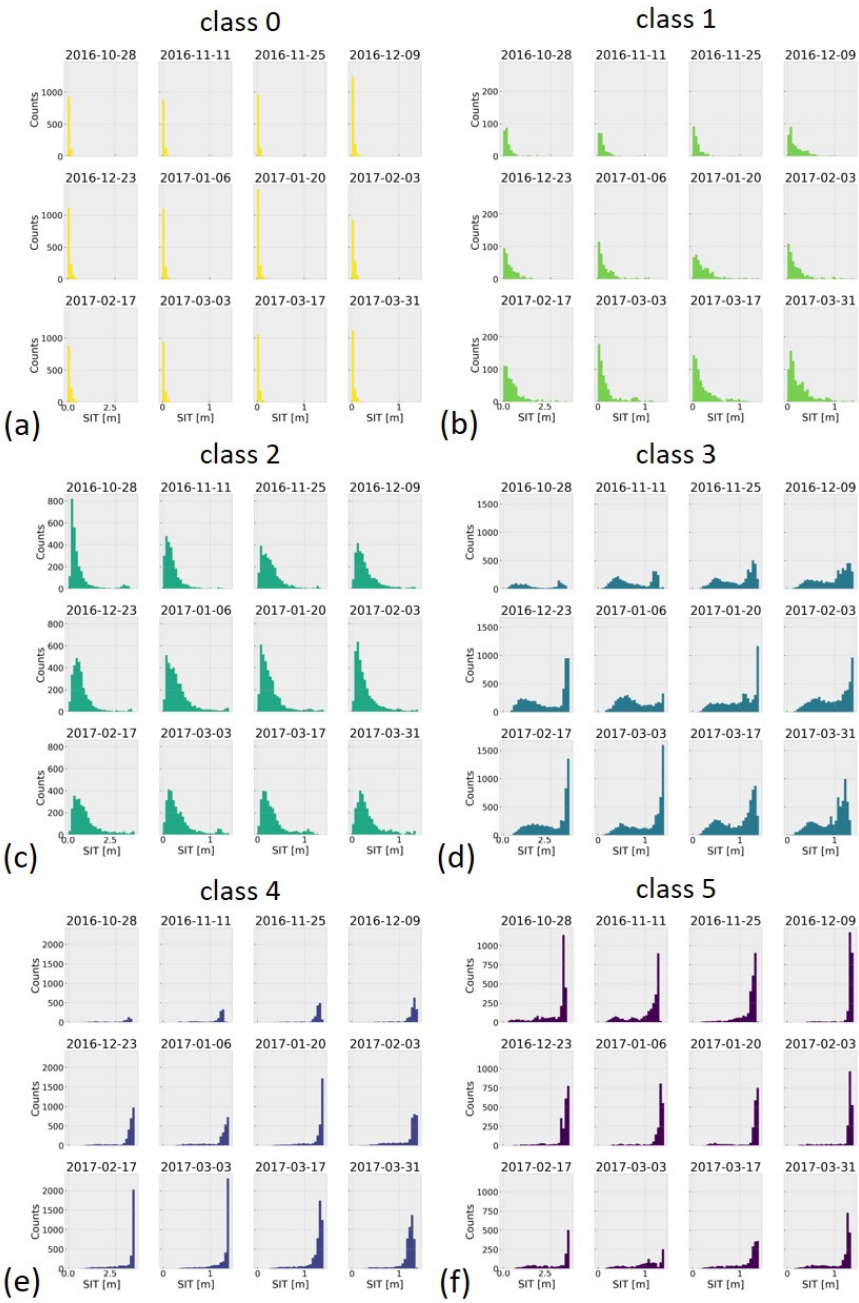

Figure D.1: Evolution of the SIT distribution for each class with respect to the thin SIT-SMOS product along the freeze-up period from October 15, 2016 to April 15, 2017.

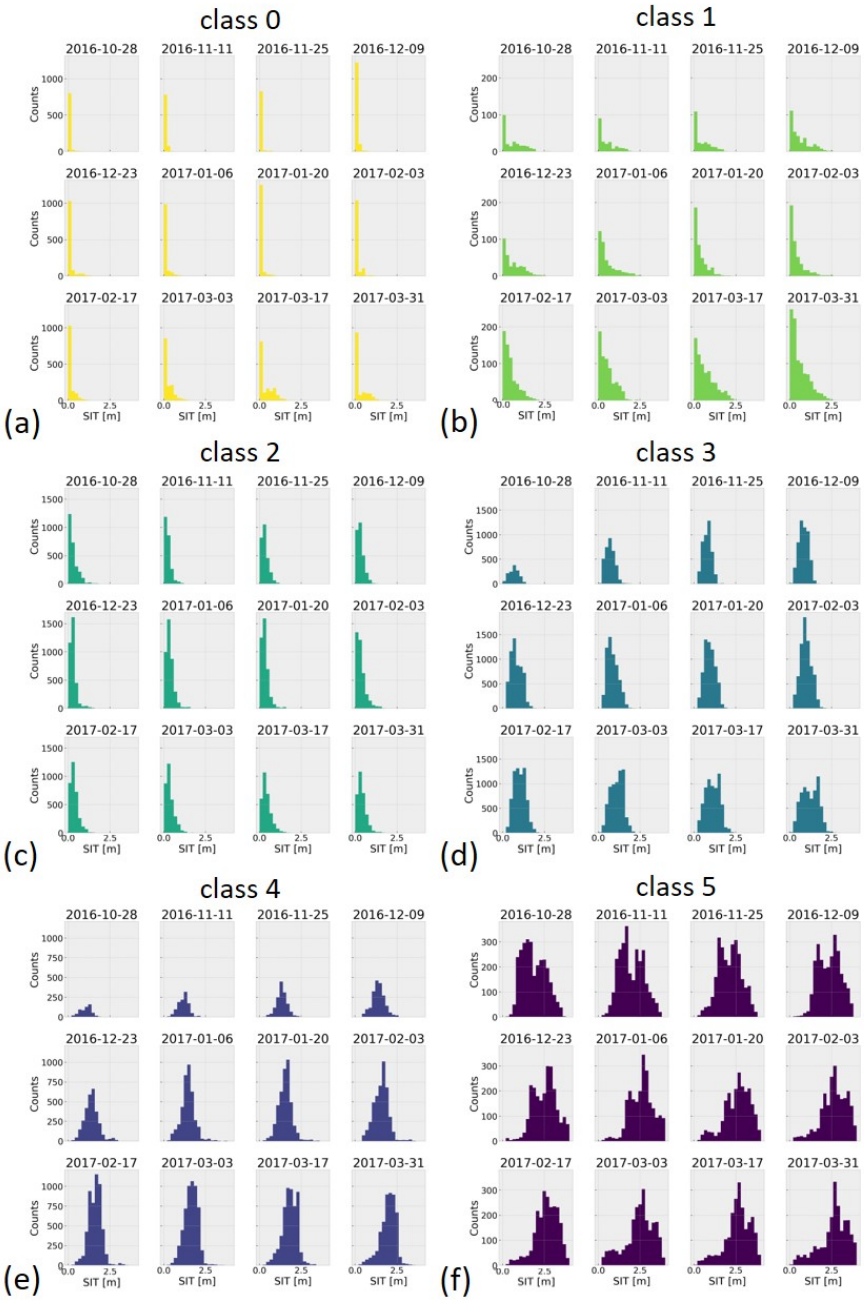

Figure D.2: Evolution of the SIT distribution with respect to the full-range merged SIT-CS2SMOS product along the freeze-up period from October 15, 2016 to April 15, 2017.

Publications and Conference Contributions

First-author Journal Publications

Herbert, C.; Pablos, M.; Vall-llossera, M.; Camps, A.; and Martínez-Fernández, J. *Analyzing spatio-temporal factors to estimate the response time between SMOS and in-situ soil moisture at different depths*, Remote Sensing (2020).

Herbert, C.; Camps, A.; Wellmann, F.; Vall-Llossera, M. *Bayesian unsupervised machine learning approach to segment Arctic sea ice using SMOS data*, Geophysical Research Letters (2021).

Herbert, C.; Munoz-Martin, J.F.; LLaveria, D.; Pablos, M.; Camps, A. *Sea ice thickness estimation based on regression neural networks using L-band microwave radiometry data from the FSSCat mission*, Remote Sensing (2021).

Other Journal Publications

Munoz-Martin, J.F.; LLaveria, D.; Herbert, C.; Pablos, M.; Park, H.; Camps, A. *Soil moisture estimation synergy using GNSS-R and L-band microwave radiometry data from FSSCat/FMPL-2*, Remote Sensing (2021).

LLaveria, D.; Munoz-Martin, J.F.; Herbert, C.; Pablos, M.; Park, H.; Camps, A. *Sea ice concentration and sea ice extent mapping with L-band microwave radiometry and GNSS-R data from the FFSCat Mission using neural networks*, Remote Sensing (2021).

Selected Talks and Conference Publications

ESA Living Planet Symposium (05/2022):
Organizer of the polar scientific session 'Sea Ice Remote Sensing', *Spatial and Temporal Segmentation to Synergize CIMR-equivalent SMOS and AMSR2 Observations for Sea Ice Parameter Retrieval* (oral presentation).

ESA Earth Observation Phi-Week (10/2021):
Invited keynote speaker: *First results of sea ice thickness retrieval using data of the FSS-Cat CubeSat Mission* (oral presentation).

International Geoscience and Remote Sensing Symposium (IGARSS) (07/2021):
Chair of the session 'Sea Ice', *'Probabilistic inference method to discriminate closed water from sea ice using Sentinel-1 SAR signatures* (oral presentation).

European Geosciences Union (EGU) General Assembly (04/2021):
Sea ice thickness retrieval based on predictive regression neural networks using L-band microwave radiometry data from the FSSCat mission (oral presentation).

Microwave Radiometry and Remote Sensing of the Environment (MicroRAD) (11/2020):
Estimating Arctic sea ice distribution from SMOS multi-incidence angle brightness temperatures using unsupervised learning algorithms (oral presentation).

European Geosciences Union (EGU) General Assembly (05/2020):
Dynamic time warping analysis of the evolution of SMOS surface and in-situ soil moisture time series (poster presentation).

American Geophysical Union (AGU) Fall Meeting (12/2019):
The inference of Arctic sea ice thickness from SMOS multi-incidence angle brightness temperature using unsupervised learning algorithms (poster presentation).

European Geosciences Union General Assembly (04/2019):
Extracting heterogeneity of subsoil from geophysical measurements using unsupervised learning algorithms (oral presentation).

Bibliography

[WMO, 2014] (2014). Sea-ice nomenclature: snapshot of the wmo sea ice nomenclature. *JCOMM Technical Report*, 1–3(259):121pp.

[ita, 2020] (2020). Agrarian technological institute of castilla and león (itacyl): Maps of soil types. `http://suelos.itacyl.es/`. Accessed: 2020-08-01.

[Ainsworth, 1988] Ainsworth, W. (1988). Speech recognition by machine peter peregrinus. *IEE, London*.

[Akaike, 1974] Akaike, H. (1974). A new look at the statistical model identification. *IEEE transactions on automatic control*, 19(6):716–723.

[Al-Yaari et al., 2014] Al-Yaari, A., Wigneron, J.-P., Ducharne, A., Kerr, Y., De Rosnay, P., De Jeu, R., Govind, A., Al Bitar, A., Albergel, C., Munoz-Sabater, J., et al. (2014). Global-scale evaluation of two satellite-based passive microwave soil moisture datasets (smos and amsr-e) with respect to land data assimilation system estimates. *Remote Sensing of Environment*, 149:181–195.

[Albergel et al., 2008] Albergel, C., Rüdiger, C., Pellarin, T., Calvet, J.-C., Fritz, N., Froissard, F., Suquia, D., Petitpa, A., Piguet, B., and Martin, E. (2008). From near-surface to root-zone soil moisture using an exponential filter: an assessment of the method based on in-situ observations and model simulations. *Hydrology and Earth System Sciences*, 12(6):1323–1337.

[Allen et al., 1998] Allen, R. G., Pereira, L. S., Raes, D., Smith, M., et al. (1998). Crop evapotranspiration-guidelines for computing crop water requirements-fao irrigation and drainage paper 56. *Fao, Rome*, 300(9):D05109.

[Atchley and Maxwell, 2011] Atchley, A. L. and Maxwell, R. M. (2011). Influences of subsurface heterogeneity and vegetation cover on soil moisture, surface temperature and evapotranspiration at hillslope scales. *Hydrogeology Journal*, 19(2):289–305.

[Baldwin et al., 2019] Baldwin, D., Manfreda, S., Lin, H., and Smithwick, E. A. (2019). Estimating root zone soil moisture across the eastern united states with passive microwave satellite data and a simple hydrologic model. *Remote Sensing*, 11(17):2013.

[Balenzano et al., 2010] Balenzano, A., Mattia, F., Satalino, G., and Davidson, M. W. (2010). Dense temporal series of c-and l-band sar data for soil moisture retrieval over agricultural crops. *IEEE Journal of Selected Topics in Applied Earth Observations and Remote Sensing*, 4(2):439–450.

[Balsamo et al., 2015] Balsamo, G., Albergel, C., Beljaars, A., Boussetta, S., Brun, E., Cloke, H., Dee, D., Dutra, E., Muñoz-Sabater, J., Pappenberger, F., et al. (2015). Era-interim/land: a global land surface reanalysis data set. *Hydrology and Earth System Sciences*, 19(1):389–407.

[Basara and Crawford, 2002] Basara, J. B. and Crawford, K. C. (2002). Linear relationships between root-zone soil moisture and atmospheric processes in the planetary boundary layer. *Journal of Geophysical Research: Atmospheres*, 107(D15):ACL–10.

[Batool et al., 2019] Batool, A., Cheng, Z.-G., Akram, N. A., Lv, G.-C., Xiong, J.-L., Zhu, Y., Ashraf, M., and Xiong, Y.-C. (2019). Partial and full root-zone drought stresses account for differentiate root-sourced signal and yield formation in primitive wheat. *Plant methods*, 15(1):1–14.

[Belchansky et al., 2008] Belchansky, G., Douglas, D. C., and Platonov, N. G. (2008). Fluctuating arctic sea ice thickness changes estimated by an in situ learned and empirically forced neural network model. *Journal of Climate*, 21(4):716–729.

[Belgiu and Csillik, 2018] Belgiu, M. and Csillik, O. (2018). Sentinel-2 cropland mapping using pixel-based and object-based time-weighted dynamic time warping analysis. *Remote sensing of environment*, 204:509–523.

[Bell et al., 2001] Bell, T. H., Barrow, B. J., and Miller, J. T. (2001). Subsurface discrimination using electromagnetic induction sensors. *IEEE transactions on geoscience and remote sensing*, 39(6):1286–1293.

[Benesty et al., 2009] Benesty, J., Chen, J., Huang, Y., and Cohen, I. (2009). Pearson correlation coefficient. In *Noise reduction in speech processing*, pages 1–4. Springer.

[Bentley, 1975] Bentley, J. L. (1975). Multidimensional binary search trees used for associative searching. *Communications of the ACM*, 18(9):509–517.

[Berndt and Clifford, 1994] Berndt, D. J. and Clifford, J. (1994). Using dynamic time warping to find patterns in time series. In *KDD workshop*, volume 10, pages 359–370. Seattle, WA.

[Bojinski et al., 2014] Bojinski, S., Verstraete, M., Peterson, T. C., Richter, C., Simmons, A., and Zemp, M. (2014). The concept of essential climate variables in support of climate research, applications, and policy. *Bulletin of the American Meteorological Society*, 95(9):1431–1443.

[Braakmann-Folgmann and Donlon, 2019] Braakmann-Folgmann, A. and Donlon, C. (2019). Estimating snow depth on arctic sea ice using satellite microwave radiometry and a neural network. *The Cryosphere*, 13(9):2421–2438.

[Brocca et al., 2011] Brocca, L., Hasenauer, S., Lacava, T., Melone, F., Moramarco, T., Wagner, W., Dorigo, W., Matgen, P., Martínez-Fernández, J., Llorens, P., et al. (2011). Soil moisture estimation through ascat and amsr-e sensors: An intercomparison and validation study across europe. *Remote Sensing of Environment*, 115(12):3390–3408.

[C3S, 2017] C3S (2017). ERA5: Fifth generation of ECMWF atmospheric reanalyses of the global climate. `https://cds.climate.copernicus.eu/cdsapp#!/home`. Accessed: 2020-01-10.

[Callegary et al., 2007] Callegary, J. B., Ferré, T. P., and Groom, R. (2007). Vertical spatial sensitivity and exploration depth of low-induction-number electromagnetic-induction instruments. *Vadose Zone Journal*, 6(1):158–167.

[Camps, 2019] Camps, A. (2019). Nanosatellites and applications to commercial and scientific missions. In *Satellites and Innovative Technology*. IntechOpen.

[Carranza et al., 2021] Carranza, C., Nolet, C., Pezij, M., and van der Ploeg, M. (2021). Root zone soil moisture estimation with random forest. *Journal of hydrology*, 593:125840.

[Casey et al., 2016] Casey, J. A., Howell, S. E., Tivy, A., and Haas, C. (2016). Separability of sea ice types from wide swath c-and l-band synthetic aperture radar imagery acquired during the melt season. *Remote sensing of environment*, 174:314–328.

[Cavalieri et al., 1984] Cavalieri, D. J., Gloersen, P., and Campbell, W. J. (1984). Determination of sea ice parameters with the nimbus 7 smmr. *Journal of Geophysical Research: Atmospheres*, 89(D4):5355–5369.

[Cavalieri et al., 1997] Cavalieri, D. J., Parkinson, C. L., Gloersen, P., and Zwally, H. J. (1997). Arctic and antarctic sea ice concentrations from multichannel passive-microwave satellite data sets: October 1978-september 1995 user's guide.

[Ceballos et al., 2005] Ceballos, A., Scipal, K., Wagner, W., and Martínez-Fernández, J. (2005). Validation of ers scatterometer-derived soil moisture data in the central part of the duero basin, spain. *Hydrological Processes: An International Journal*, 19(8):1549–1566.

[Celeux et al., 2003] Celeux, G., Forbes, F., and Peyrard, N. (2003). Em procedures using mean field-like approximations for markov model-based image segmentation. *Pattern recognition*, 36(1):131–144.

[Chan et al., 2016] Chan, S. K., Bindlish, R., O'Neill, P. E., Njoku, E., Jackson, T., Colliander, A., Chen, F., Burgin, M., Dunbar, S., Piepmeier, J., et al. (2016). Assessment of the smap passive soil moisture product. *IEEE Transactions on Geoscience and Remote Sensing*, 54(8):4994–5007.

[Chi and Kim, 2017] Chi, J. and Kim, H.-c. (2017). Prediction of arctic sea ice concentration using a fully data driven deep neural network. *Remote Sensing*, 9(12):1305.

[Chong and Zak, 2004] Chong, E. K. and Zak, S. H. (2004). *An introduction to optimization*. John Wiley & Sons.

[Claeskens et al., 2008] Claeskens, G., Hjort, N. L., et al. (2008). Model selection and model averaging. *Cambridge Books*.

[Colliander et al., 2020] Colliander, A., Jackson, T. J., Berg, A., Bosch, D., Caldwell, T., Chan, S., Cosh, M. H., Collins, C. H., Martínez-Fernández, J., McNairn, H., et al. (2020). Effect of rainfall events on smap radiometer-based soil moisture accuracy using core validation sites. *Journal of Hydrometeorology*, 21(2):255–264.

[Colliander et al., 2017] Colliander, A., Jackson, T. J., Bindlish, R., Chan, S., Das, N., Kim, S., Cosh, M., Dunbar, R., Dang, L., Pashaian, L., et al. (2017). Validation of smap surface soil moisture products with core validation sites. *Remote Sensing of Environment*, 191:215–231.

[Comiso, 1995] Comiso, J. C. (1995). *SSM/I sea ice concentrations using the bootstrap algorithm*, volume 1380. National Aeronautics and Space Administration, Goddard Space Flight Center.

[Comiso, 2012] Comiso, J. C. (2012). Large decadal decline of the arctic multiyear ice cover. *Journal of climate*, 25(4):1176–1193.

[Comiso et al., 1997] Comiso, J. C., Cavalieri, D. J., Parkinson, C. L., and Gloersen, P. (1997). Passive microwave algorithms for sea ice concentration: A comparison of two techniques. *Remote sensing of Environment*, 60(3):357–384.

[Comiso and Nishio, 2008] Comiso, J. C. and Nishio, F. (2008). Trends in the sea ice cover using enhanced and compatible amsr-e, ssm/i, and smmr data. *Journal of Geophysical Research: Oceans*, 113(C2).

[Comiso et al., 2020] Comiso, J. C., Parkinson, C. L., Markus, T., Cavalieri, D. J., and Gersten, R. (2020). Current state of sea ice cover. `https://earth.gsfc.nasa.gov/cryo/data/current-state-sea-ice-cover`. Accessed: 2020-12-30.

[Corbella et al., 2005] Corbella, I., Torres, F., Camps, A., Colliander, A., Martín-Neira, M., Ribó, S., Rautiainen, K., Duffo, N., and Vall-llossera, M. (2005). Miras end-to-end

calibration: Application to smos l1 processor. *IEEE Transactions on Geoscience and Remote Sensing*, 43(5):1126–1134.

[Cristea et al., 2020] Cristea, A., van Houtte, J., and Doulgeris, A. P. (2020). Integrating incidence angle dependencies into the clustering-based segmentation of sar images. *IEEE Journal of Selected Topics in Applied Earth Observations and Remote Sensing*, 13:2925–2939.

[Crow et al., 2012] Crow, W. T., Berg, A. A., Cosh, M. H., Loew, A., Mohanty, B. P., Panciera, R., de Rosnay, P., Ryu, D., and Walker, J. P. (2012). Upscaling sparse ground-based soil moisture observations for the validation of coarse-resolution satellite soil moisture products. *Reviews of Geophysics*, 50(2).

[Csillik et al., 2019] Csillik, O., Belgiu, M., Asner, G. P., and Kelly, M. (2019). Object-based time-constrained dynamic time warping classification of crops using sentinel-2. *Remote sensing*, 11(10):1257.

[Cvijanovic et al., 2017] Cvijanovic, I., Santer, B. D., Bonfils, C., Lucas, D. D., Chiang, J. C., and Zimmerman, S. (2017). Future loss of arctic sea-ice cover could drive a substantial decrease in california's rainfall. *Nature communications*, 8(1):1–10.

[Daganzo-Eusebio et al., 2013] Daganzo-Eusebio, E., Oliva, R., Kerr, Y. H., Nieto, S., Richaume, P., and Mecklenburg, S. M. (2013). Smos radiometer in the 1400–1427-mhz passive band: Impact of the rfi environment and approach to its mitigation and cancellation. *IEEE Transactions on Geoscience and Remote Sensing*, 51(10):4999–5007.

[De Lannoy et al., 2007a] De Lannoy, G. J., Houser, P. R., Verhoest, N. E., Pauwels, V. R., and Gish, T. J. (2007a). Upscaling of point soil moisture measurements to field averages at the ope3 test site. *Journal of Hydrology*, 343(1-2):1–11.

[De Lannoy et al., 2007b] De Lannoy, G. J., Pauwels, V. R., Houser, P. R., Gish, T., and Verhoest, N. E. (2007b). Representativeness of point soil moisture observations, upscaling and assimilation. *IAHS PUBLICATION*, 313:249.

[De Lannoy et al., 2019] De Lannoy, G. J., Rosnay, P., and Reichle, R. H. (2019). Soil moisture data assimilation. Technical report, Springer Nature.

[De Roo et al., 2004] De Roo, R. D., England, A. W., and Munn, J. (2004). Circular polarization for l-band radiometric soil moisture retrieval. In *2004 IEEE Aerospace Conference Proceedings (IEEE Cat. No. 04TH8720)*, volume 2, pages 1015–1023. IEEE.

[Dempster et al., 1977] Dempster, A. P., Laird, N. M., and Rubin, D. B. (1977). Maximum likelihood from incomplete data via the em algorithm. *Journal of the Royal Statistical Society: Series B (Methodological)*, 39(1):1–22.

[Deng and Clausi, 2005] Deng, H. and Clausi, D. A. (2005). Unsupervised segmentation of synthetic aperture radar sea ice imagery using a novel markov random field model. *IEEE Transactions on Geoscience and Remote Sensing*, 43(3):528–538.

[Donlon et al., 2019] Donlon, C. et al. (2019). Copernicus imaging microwave radiometer (cimr) mission requirements document, version 2.0. *available from the European Space Agency, ESTEC, Noordwijk, The Netherlands*, 164.

[Dorigo et al., 2015] Dorigo, W., Gruber, A., De Jeu, R., Wagner, W., Stacke, T., Loew, A., Albergel, C., Brocca, L., Chung, D., Parinussa, R., et al. (2015). Evaluation of the esa cci soil moisture product using ground-based observations. *Remote Sensing of Environment*, 162:380–395.

[Dorigo et al., 2021] Dorigo, W., Himmelbauer, I., Aberer, D., Schremmer, L., Petrakovic, I., Zappa, L., Preimesberger, W., Xaver, A., Annor, F., Ardö, J., et al. (2021). The international soil moisture network: serving earth system science for over a decade. *Hydrology and earth system sciences*, 25(11):5749–5804.

[Dorigo et al., 2011] Dorigo, W., Wagner, W., Hohensinn, R., Hahn, S., Paulik, C., Xaver, A., Gruber, A., Drusch, M., Mecklenburg, S., Oevelen, P. v., et al. (2011). The international soil moisture network: a data hosting facility for global in situ soil moisture measurements. *Hydrology and Earth System Sciences*, 15(5):1675–1698.

[Dorigo et al., 2013] Dorigo, W., Xaver, A., Vreugdenhil, M., Gruber, A., Hegyiova, A., Sanchis-Dufau, A., Zamojski, D., Cordes, C., Wagner, W., and Drusch, M. (2013). Global automated quality control of in situ soil moisture data from the international soil moisture network. *Vadose Zone Journal*, 12(3).

[Drusch et al., 2009] Drusch, M., Scipal, K., De Rosnay, P., Balsamo, G., Andersson, E., Bougeault, P., and Viterbo, P. (2009). Towards a kalman filter based soil moisture analysis system for the operational ecmwf integrated forecast system. *Geophysical Research Letters*, 36(10).

[Dubes and Jain, 1988] Dubes, R. C. and Jain, A. K. (1988). Algorithms for clustering data.

[Eicken et al., 2002] Eicken, H., Krouse, H., Kadko, D., and Perovich, D. (2002). Tracer studies of pathways and rates of meltwater transport through arctic summer sea ice. *Journal of Geophysical Research: Oceans*, 107(C10):SHE–22.

[Entekhabi et al., 2010a] Entekhabi, D., Njoku, E. G., O'Neill, P. E., Kellogg, K. H., Crow, W. T., Edelstein, W. N., Entin, J. K., Goodman, S. D., Jackson, T. J., Johnson, J., et al. (2010a). The soil moisture active passive (smap) mission. *Proceedings of the IEEE*, 98(5):704–716.

[Entekhabi et al., 2010b] Entekhabi, D., Reichle, R. H., Koster, R. D., and Crow, W. T. (2010b). Performance metrics for soil moisture retrievals and application requirements. *Journal of Hydrometeorology*, 11(3):832–840.

[Entin et al., 2000] Entin, J. K., Robock, A., Vinnikov, K. Y., Hollinger, S. E., Liu, S., and Namkhai, A. (2000). Temporal and spatial scales of observed soil moisture variations in the extratropics. *Journal of Geophysical Research: Atmospheres*, 105(D9):11865–11877.

[Escorihuela et al., 2010] Escorihuela, M.-J., Chanzy, A., Wigneron, J.-P., and Kerr, Y. (2010). Effective soil moisture sampling depth of l-band radiometry: A case study. *Remote Sensing of Environment*, 114(5):995–1001.

[Evett, 2003] Evett, S. R. (2003). Soil water measurement by time domain reflectometry. *Encyclopedia of water science*, pages 894–898.

[Falkenmark, 2013] Falkenmark, M. (2013). Growing water scarcity in agriculture: future challenge to global water security. *Philosophical Transactions of the Royal Society A: Mathematical, Physical and Engineering Sciences*, 371(2002):20120410.

[Fan et al., 2016] Fan, J., McConkey, B., Wang, H., and Janzen, H. (2016). Root distribution by depth for temperate agricultural crops. *Field Crops Research*, 189:68–74.

[Font et al., 2009] Font, J., Camps, A., Borges, A., Martín-Neira, M., Boutin, J., Reul, N., Kerr, Y. H., Hahne, A., and Mecklenburg, S. (2009). Smos: The challenging sea surface salinity measurement from space. *Proceedings of the IEEE*, 98(5):649–665.

[Ford et al., 2014] Ford, T., Harris, E., and Quiring, S. (2014). Estimating root zone soil moisture using near-surface observations from smos. *1foldr Import 2019-10-08 Batch 11*.

[Gabarró et al., 2016] Gabarró, C., Pla Resina, J., Turiel, A., Portabella, M., Martínez, J., Olmedo, E., and González, V. (2016). Arctic sea ice concentration estimation with smos data.

[Gamerman and Lopes, 2006] Gamerman, D. and Lopes, H. F. (2006). *Markov chain Monte Carlo: stochastic simulation for Bayesian inference*. Chapman and Hall/CRC.

[Gao et al., 2013] Gao, X., Wu, P., Zhao, X., Zhou, X., Zhang, B., Shi, Y., and Wang, J. (2013). Estimating soil moisture in gullies from adjacent upland measurements through different observation operators. *Journal of hydrology*, 486:420–429.

[Gao et al., 2019] Gao, X., Zhao, X., Brocca, L., Pan, D., and Wu, P. (2019). Testing of observation operators designed to estimate profile soil moisture from surface measurements. *Hydrological Processes*, 33(4):575–584.

[Garré et al., 2011] Garré, S., Javaux, M., Vanderborght, J., Pagès, L., and Vereecken, H. (2011). Three-dimensional electrical resistivity tomography to monitor root zone water dynamics. *Vadose Zone Journal*, 10(1):412–424.

[Geman and Geman, 1984] Geman, S. and Geman, D. (1984). Stochastic relaxation, gibbs distributions, and the bayesian restoration of images. *IEEE Transactions on pattern analysis and machine intelligence*, (6):721–741.

[Géron, 2019] Géron, A. (2019). *Hands-on machine learning with Scikit-Learn, Keras, and TensorFlow: Concepts, tools, and techniques to build intelligent systems*. O'Reilly Media.

[Giesgen, 2018] Giesgen, T. (2018). Coupling unsupervised segmentation in wells with automatic implicit modeling in a bayesian framework.

[Gonçalves et al., 2017] Gonçalves, Í. G., Kumaira, S., and Guadagnin, F. (2017). A machine learning approach to the potential-field method for implicit modeling of geological structures. *Computers & Geosciences*, 103:173–182.

[González-Zamora et al., 2015] González-Zamora, Á., Sanchez, N., Gumuzzio, A., Piles, M., Olmedo, E., and Martínez-Fernández, J. (2015). Validation of smos l2 and l3 soil moisture products over the duero basin at different spatial scales. *The International Archives of Photogrammetry, Remote Sensing and Spatial Information Sciences*, 40(7):1183.

[González-Zamora et al., 2016] González-Zamora, Á., Sánchez, N., Martínez-Fernández, J., and Wagner, W. (2016). Root-zone plant available water estimation using the smos-derived soil water index. *Advances in Water Resources*, 96:339–353.

[Goodchild et al., 1994] Goodchild, M., Chih-Chang, L., and Leung, Y. (1994). Visualizing fuzzy maps. *Visualization in geographical information systems*, pages 158–167.

[Greene, 2001] Greene, J. (2001). Feature subset selection using thornton's separability index and its applicability to a number of sparse proximity-based classifiers. In *Proceedings of Annual Symposium of the Pattern Recognition Association of South Africa*.

[Grinsted et al., 2004] Grinsted, A., Moore, J. C., and Jevrejeva, S. (2004). Application of the cross wavelet transform and wavelet coherence to geophysical time series.

[Guddat et al., 2015] Guddat, C., Deger, J., Marschall, K., Zorn, W., and Götz, R. (2015). Guidelines for efficient and environmentally sustainable production of winter wheat. *Thuringian Regional Institute for Agriculture*, 8.

[Guerreiro et al., 2017] Guerreiro, K., Fleury, S., Zakharova, E., Kouraev, A., Rémy, F., and Maisongrande, P. (2017). Comparison of cryosat-2 and envisat radar freeboard

over arctic sea ice: toward an improved envisat freeboard retrieval. *The Cryosphere*, 11(5):2059.

[Gupta et al., 2019] Gupta, M., Gabarro, C., Turiel, A., Portabella, M., and Martinez, J. (2019). On the retrieval of sea-ice thickness using smos polarization differences. *Journal of Glaciology*, 65(251):481–493.

[Haas et al., 2009] Haas, C., Lobach, J., Hendricks, S., Rabenstein, L., and Pfaffling, A. (2009). Helicopter-borne measurements of sea ice thickness, using a small and lightweight, digital em system. *Journal of Applied Geophysics*, 67(3):234–241.

[Hänsch et al., 2020] Hänsch, R., Amao Oliva, J. A., Horn, R., Jäger, M., and Scheiber, R. (2020). Unsupervised clustering of c-band polsar data over sea ice.

[He et al., 2017] He, L., Qin, Q., Panciera, R., Tanase, M., Walker, J. P., and Hong, Y. (2017). An extension of the alpha approximation method for soil moisture estimation using time-series sar data over bare soil surfaces. *IEEE Geoscience and Remote Sensing Letters*, 14(8):1328–1332.

[Herbert et al., 2021a] Herbert, C., Camps, A., Wellmann, F., and Vall-llossera, M. (2021a). Bayesian unsupervised machine learning approach to segment arctic sea ice using smos data. *Geophysical Research Letters*, 48(6):e2020GL091285.

[Herbert et al., 2021b] Herbert, C., Munoz-Martin, J. F., Llaveria, D., Pablos, M., and Camps, A. (2021b). Sea ice thickness estimation based on regression neural networks using l-band microwave radiometry data from the fsscat mission. *Remote Sensing*, 13(7):1366.

[Herbert et al., 2020] Herbert, C., Pablos, M., Vall-llossera, M., Camps, A., and Martínez-Fernández, J. (2020). Analyzing spatio-temporal factors to estimate the response time between smos and in-situ soil moisture at different depths. *Remote Sensing*, 12(16):2614.

[Hinneburg et al., 2000] Hinneburg, A., Aggarwal, C. C., and Keim, D. A. (2000). What is the nearest neighbor in high dimensional spaces? In *26th Internat. Conference on Very Large Databases*, pages 506–515.

[Hollmann et al., 2013] Hollmann, R., Merchant, C. J., Saunders, R., Downy, C., Buchwitz, M., Cazenave, A., Chuvieco, E., Defourny, P., de Leeuw, G., Forsberg, R., et al. (2013). The esa climate change initiative: Satellite data records for essential climate variables. *Bulletin of the American Meteorological Society*, 94(10):1541–1552.

[Houle et al., 2010] Houle, M. E., Kriegel, H.-P., Kröger, P., Schubert, E., and Zimek, A. (2010). Can shared-neighbor distances defeat the curse of dimensionality? In

International Conference on Scientific and Statistical Database Management, pages 482–500. Springer.

[Huang et al., 2008] Huang, C., Li, X., Lu, L., and Gu, J. (2008). Experiments of one-dimensional soil moisture assimilation system based on ensemble kalman filter. *Remote sensing of environment*, 112(3):888–900.

[Huisman et al., 2002] Huisman, J., Snepvangers, J., Bouten, W., and Heuvelink, G. (2002). Mapping spatial variation in surface soil water content: comparison of ground-penetrating radar and time domain reflectometry. *Journal of hydrology*, 269(3-4):194–207.

[Huisman et al., 2003] Huisman, J. A., Hubbard, S. S., Redman, J. D., and Annan, A. P. (2003). Measuring soil water content with ground penetrating radar: A review. *Vadose zone journal*, 2(4):476–491.

[Huntemann et al., 2014] Huntemann, M., Heygster, G., Kaleschke, L., Krumpen, T., Mäkynen, M., and Drusch, M. (2014). Empirical sea ice thickness retrieval during the freeze up period from smos high incident angle observations. *The Cryosphere*, 8(2):439–451.

[Jackson, 2002] Jackson, T. J. (2002). Remote sensing of soil moisture: implications for groundwater recharge. *Hydrogeology journal*, 10(1):40–51.

[Jaderberg et al., 2017] Jaderberg, M., Dalibard, V., Osindero, S., Czarnecki, W. M., Donahue, J., Razavi, A., Vinyals, O., Green, T., Dunning, I., Simonyan, K., et al. (2017). Population based training of neural networks. *arXiv preprint arXiv:1711.09846*.

[Jain, 2010] Jain, A. K. (2010). Data clustering: 50 years beyond k-means. *Pattern recognition letters*, 31(8):651–666.

[Jiménez-Martínez et al., 2009] Jiménez-Martínez, J., Skaggs, T., Van Genuchten, M. T., and Candela, L. (2009). A root zone modelling approach to estimating groundwater recharge from irrigated areas. *Journal of Hydrology*, 367(1-2):138–149.

[Jol, 2008] Jol, H. M. (2008). *Ground penetrating radar theory and applications*. elsevier.

[Kaleschke et al., 2016] Kaleschke, L., Tian-Kunze, X., Maaß, N., Beitsch, A., Wernecke, A., Miernecki, M., Müller, G., Fock, B. H., Gierisch, A. M., Schlünzen, K. H., et al. (2016). Smos sea ice product: Operational application and validation in the barents sea marginal ice zone. *Remote sensing of environment*, 180:264–273.

[Kaleschke et al., 2012] Kaleschke, L., Tian-Kunze, X., Maaß, N., Mäkynen, M., and Drusch, M. (2012). Sea ice thickness retrieval from smos brightness temperatures during the arctic freeze-up period. *Geophysical Research Letters*, 39(5).

[Kaleschke et al., 2015] Kaleschke, L., Tian-Kunze, X., Maaß, N., Ricker, R., Hendricks, S., and Drusch, M. (2015). Improved retrieval of sea ice thickness from smos and cryosat-2. In *2015 IEEE International Geoscience and Remote Sensing Symposium (IGARSS)*, pages 5232–5235. IEEE.

[Kang et al., 2009] Kang, Y., Khan, S., and Ma, X. (2009). Climate change impacts on crop yield, crop water productivity and food security–a review. *Progress in natural Science*, 19(12):1665–1674.

[Kerr, 2007] Kerr, Y. H. (2007). Soil moisture from space: Where are we? *Hydrogeology journal*, 15(1):117–120.

[Kerr et al., 2016] Kerr, Y. H., Al-Yaari, A., Rodriguez-Fernandez, N., Parrens, M., Molero, B., Leroux, D., Bircher, S., Mahmoodi, A., Mialon, A., Richaume, P., et al. (2016). Overview of smos performance in terms of global soil moisture monitoring after six years in operation. *Remote Sensing of Environment*, 180:40–63.

[Kerr et al., 2012] Kerr, Y. H., Waldteufel, P., Richaume, P., Wigneron, J. P., Ferrazzoli, P., Mahmoodi, A., Al Bitar, A., Cabot, F., Gruhier, C., Juglea, S. E., et al. (2012). The smos soil moisture retrieval algorithm. *IEEE transactions on geoscience and remote sensing*, 50(5):1384–1403.

[Kerr et al., 2010] Kerr, Y. H., Waldteufel, P., Wigneron, J.-P., Delwart, S., Cabot, F., Boutin, J., Escorihuela, M.-J., Font, J., Reul, N., Gruhier, C., et al. (2010). The smos mission: New tool for monitoring key elements ofthe global water cycle. *Proceedings of the IEEE*, 98(5):666–687.

[Kerr et al., 2001] Kerr, Y. H., Waldteufel, P., Wigneron, J.-P., Martinuzzi, J., Font, J., and Berger, M. (2001). Soil moisture retrieval from space: The soil moisture and ocean salinity (smos) mission. *IEEE transactions on Geoscience and remote sensing*, 39(8):1729–1735.

[Kilic et al., 2018] Kilic, L., Prigent, C., Aires, F., Boutin, J., Heygster, G., Tonboe, R. T., Roquet, H., Jimenez, C., and Donlon, C. (2018). Expected performances of the copernicus imaging microwave radiometer (cimr) for an all-weather and high spatial resolution estimation of ocean and sea ice parameters. *Journal of Geophysical Research: Oceans*, 123(10):7564–7580.

[Kingma and Ba, 2014] Kingma, D. P. and Ba, J. (2014). Adam: A method for stochastic optimization. *arXiv preprint arXiv:1412.6980*.

[Köhler et al., 2010] Köhler, A., Ohrnberger, M., and Scherbaum, F. (2010). Unsupervised pattern recognition in continuous seismic wavefield records using self-organizing maps. *Geophysical Journal International*, 182(3):1619–1630.

[Koller and Friedman, 2009] Koller, D. and Friedman, N. (2009). *Probabilistic graphical models: principles and techniques*. MIT press.

[Komarov and Buehner, 2019] Komarov, A. S. and Buehner, M. (2019). Detection of first-year and multi-year sea ice from dual-polarization sar images under cold conditions. *IEEE Transactions on Geoscience and Remote Sensing*, 57(11):9109–9123.

[Kornelsen and Coulibaly, 2014] Kornelsen, K. C. and Coulibaly, P. (2014). Root-zone soil moisture estimation using data-driven methods. *Water Resources Research*, 50(4):2946–2962.

[Kramer, 2014] Kramer, H. (2014). Flock 1 Imaging Constellation built by Planet Labs Inc. `https://earth.esa.int/web/eoportal/satellite-missions/f/flock-1`. Accessed: 2021-01-21.

[Kuffour et al., 2020] Kuffour, B. N., Engdahl, N. B., Woodward, C. S., Condon, L. E., Kollet, S., and Maxwell, R. M. (2020). Simulating coupled surface–subsurface flows with parflow v3. 5.0: capabilities, applications, and ongoing development of an open-source, massively parallel, integrated hydrologic model. *Geoscientific Model Development*, 13(3):1373–1397.

[Kuhn et al., 2013] Kuhn, M., Johnson, K., et al. (2013). *Applied predictive modeling*, volume 26. Springer.

[Kulu, 2020] Kulu, E. (2020). World's largest database of nanosatellites, over 2700 nanosats and cubesats (2014-2020). `https://www.nanosats.eu/`. Accessed: 2020-12-30.

[Kurtz et al., 2013] Kurtz, N., Farrell, S., Studinger, M., Galin, N., Harbeck, J., Lindsay, R., Onana, V., Panzer, B., and Sonntag, J. (2013). Sea ice thickness, freeboard, and snow depth products from operation icebridge airborne data. *The Cryosphere*, 7(4):1035–1056.

[Kurtz and Harbeck, 2017] Kurtz, N. and Harbeck, J. (2017). Cryosat-2 level 4 sea ice elevation, freeboard, and thickness, version 1, boulder, colorado usa. *NASA National Snow and Ice Data Center Distributed Active Archive Center*.

[Laguna et al., 1994] Laguna, P., Jané, R., and Caminal, P. (1994). Automatic detection of wave boundaries in multilead ecg signals: Validation with the cse database. *Computers and biomedical research*, 27(1):45–60.

[Lavergne et al., 2019] Lavergne, T., Sørensen, A. M., Kern, S., Tonboe, R., Notz, D., Aaboe, S., Bell, L., Dybkjær, G., Eastwood, S., Gabarro, C., et al. (2019). Version 2 of the eumetsat osi saf and esa cci sea-ice concentration climate data records. *The Cryosphere*, 13(1):49–78.

[Laxon et al., 2013] Laxon, S. W., Giles, K. A., Ridout, A. L., Wingham, D. J., Willatt, R., Cullen, R., Kwok, R., Schweiger, A., Zhang, J., Haas, C., et al. (2013). Cryosat-2 estimates of arctic sea ice thickness and volume. *Geophysical Research Letters*, 40(4):732–737.

[LeCun et al., 2015] LeCun, Y., Bengio, Y., and Hinton, G. (2015). Deep learning. *nature*, 521(7553):436–444.

[Lee et al., 2019] Lee, C. S., Sohn, E., Park, J. D., and Jang, J.-D. (2019). Estimation of soil moisture using deep learning based on satellite data: a case study of south korea. *GIScience & Remote Sensing*, 56(1):43–67.

[Lee et al., 2016] Lee, S., Im, J., Kim, J., Kim, M., Shin, M., Kim, H.-c., and Quackenbush, L. J. (2016). Arctic sea ice thickness estimation from cryosat-2 satellite data using machine learning-based lead detection. *Remote Sensing*, 8(9):698.

[Li et al., 2017] Li, H., Perrie, W., Li, Q., and Hou, Y. (2017). Estimation of melt pond fractions on first year sea ice using compact polarization sar. *Journal of Geophysical Research: Oceans*, 122(10):8145–8166.

[Lin and Yang, 2012] Lin, H. and Yang, L. (2012). A hybrid neural network model for sea ice thickness forecasting. In *2012 8th International Conference on Natural Computation*, pages 358–361. IEEE.

[Lind et al., 2018] Lind, S., Ingvaldsen, R. B., and Furevik, T. (2018). Arctic warming hotspot in the northern barents sea linked to declining sea-ice import. *Nature climate change*, 8(7):634–639.

[Linde et al., 2015] Linde, N., Renard, P., Mukerji, T., and Caers, J. (2015). Geological realism in hydrogeological and geophysical inverse modeling: A review. *Advances in Water Resources*, 86:86–101.

[Liu et al., 2019] Liu, J., Zhang, Y., Cheng, X., and Hu, Y. (2019). Retrieval of snow depth over arctic sea ice using a deep neural network. *Remote Sensing*, 11(23):2864.

[Liu, 2003] Liu, Y. (2003). Spatial patterns of soil moisture connected to monthly-seasonal precipitation variability in a monsoon region. *Journal of Geophysical Research: Atmospheres*, 108(D22).

[Llaveria et al., 2021] Llaveria, D., Munoz-Martin, J. F., Herbert, C., Pablos, M., Park, H., and Camps, A. (2021). Sea ice concentration and sea ice extent mapping with l-band microwave radiometry and gnss-r data from the ffscat mission using neural networks. *Remote Sensing*, 13(6):1139.

[Lohse et al., 2020] Lohse, J., Doulgeris, A. P., and Dierking, W. (2020). Mapping sea-ice types from sentinel-1 considering the surface-type dependent effect of incidence angle. *Annals of Glaciology*, pages 1–11.

[Lunt et al., 2005] Lunt, I., Hubbard, S., and Rubin, Y. (2005). Soil moisture content estimation using ground-penetrating radar reflection data. *Journal of hydrology*, 307(1-4):254–269.

[Maaß et al., 2013] Maaß, N., Kaleschke, L., Tian-Kunze, X., and Drusch, M. (2013). Snow thickness retrieval over thick arctic sea ice using smos satellite data. *The Cryosphere*, 7(6):1971–1989.

[Maeda et al., 2015] Maeda, T., Taniguchi, Y., and Imaoka, K. (2015). Gcom-w1 amsr2 level 1r product: Dataset of brightness temperature modified using the antenna pattern matching technique. *IEEE Transactions on Geoscience and Remote Sensing*, 54(2):770–782.

[Mahalanobis, 1936] Mahalanobis, P. C. (1936). On the generalized distance in statistics. National Institute of Science of India.

[Mahmud et al., 2018] Mahmud, M. S., Geldsetzer, T., Howell, S. E., Yackel, J. J., Nandan, V., and Scharien, R. K. (2018). Incidence angle dependence of hh-polarized c-and l-band wintertime backscatter over arctic sea ice. *IEEE Transactions on Geoscience and Remote Sensing*, 56(11):6686–6698.

[Mäkynen and Karvonen, 2017] Mäkynen, M. and Karvonen, J. (2017). Incidence angle dependence of first-year sea ice backscattering coefficient in sentinel-1 sar imagery over the kara sea. *IEEE Transactions on Geoscience and Remote Sensing*, 55(11):6170–6181.

[Manfreda et al., 2014] Manfreda, S., Brocca, L., Moramarco, T., Melone, F., and Sheffield, J. (2014). A physically based approach for the estimation of root-zone soil moisture from surface measurements. *Hydrology and Earth System Sciences*, 18(3):1199–1212.

[Mann et al., 2017] Mann, M. E., Rahmstorf, S., Kornhuber, K., Steinman, B. A., Miller, S. K., and Coumou, D. (2017). Influence of anthropogenic climate change on planetary wave resonance and extreme weather events. *Scientific reports*, 7(1):1–12.

[Markus and Cavalieri, 2000] Markus, T. and Cavalieri, D. J. (2000). An enhancement of the nasa team sea ice algorithm. *IEEE Transactions on Geoscience and Remote Sensing*, 38(3):1387–1398.

[Markus and Cavalieri, 2009] Markus, T. and Cavalieri, D. J. (2009). The amsr-e nt2 sea ice concentration algorithm: Its basis and implementation. *Journal of The Remote Sensing Society of Japan*, 29(1):216–225.

[Markus et al., 2018] Markus, T., Comiso, J., and Meier, W. (2018). Amsr-e/amsr2 unified level-3 daily 25 km brightness temperatures and sea ice concentration polar grids, version 1. [weekly brightness temperatures at vertical polarization from july 2012 to december 2019]. `https://nsidc.org/data/au_si25/versions/1`. Accessed: 2021-10-01.

[Martín-Neira et al., 2016] Martín-Neira, M., Oliva, R., Corbella, I., Torres, F., Duffo, N., Durán, I., Kainulainen, J., Closa, J., Zurita, A., Cabot, F., et al. (2016). Smos instrument performance and calibration after six years in orbit. *Remote sensing of environment*, 180:19–39.

[Martínez-Fernández and Ceballos, 2003] Martínez-Fernández, J. and Ceballos, A. (2003). Temporal stability of soil moisture in a large-field experiment in spain. *Soil Science Society of America Journal*, 67(6):1647–1656.

[Martínez-Fernández et al., 2015] Martínez-Fernández, J., González-Zamora, A., Sánchez, N., and Gumuzzio, A. (2015). A soil water based index as a suitable agricultural drought indicator. *Journal of Hydrology*, 522:265–273.

[Masialeti et al., 2010] Masialeti, I., Egbert, S., and Wardlow, B. D. (2010). A comparative analysis of phenological curves for major crops in kansas. *GIScience & Remote Sensing*, 47(2):241–259.

[Maus et al., 2016] Maus, V., Câmara, G., Cartaxo, R., Sanchez, A., Ramos, F. M., and de Queiroz, G. R. (2016). A time-weighted dynamic time warping method for land-use and land-cover mapping. *IEEE Journal of Selected Topics in Applied Earth Observations and Remote Sensing*, 9(8):3729–3739.

[McNeill, 1980] McNeill, J. D. (1980). Electromagnetic terrain conductivity measurement at low induction numbers.

[Menashi et al., 1993] Menashi, J. D., St. Germain, K. M., Swift, C. T., Comiso, J. C., and Lohanick, A. W. (1993). Low-frequency passive-microwave observations of sea ice in the weddell sea. *Journal of Geophysical Research: Oceans*, 98(C12):22569–22577.

[Miyan, 2015] Miyan, M. A. (2015). Droughts in asian least developed countries: vulnerability and sustainability. *Weather and Climate Extremes*, 7:8–23.

[Mohanty et al., 2017] Mohanty, B. P., Cosh, M. H., Lakshmi, V., and Montzka, C. (2017). Soil moisture remote sensing: State-of-the-science. *Vadose Zone Journal*, 16(1):1–9.

[Monerris et al., 2006] Monerris, A., Vall-llossera, M., Camps, A., Sabia, R., Villarino, R., Cardona, M., Alvarez, E., and Sosa, S. (2006). Soil moisture retrieval using l-band

radiometry: Dependence on soil type and moisture profiles. In *2006 IEEE MicroRad*, pages 171–175. IEEE.

[Mthembu and Marwala, 2008] Mthembu, L. and Marwala, T. (2008). A note on the separability index. *arXiv preprint arXiv:0812.1107*.

[Müller, 2007] Müller, M. (2007). *Information retrieval for music and motion*, volume 2. Springer.

[Munoz-Martin and Camps, 2021] Munoz-Martin, J. F. and Camps, A. (2021). Sea surface salinity and wind speed retrievals using gnss-r and l-band microwave radiometry data from fmpl-2 onboard the fsscat mission. *Remote Sensing*, 13(16):3224.

[Munoz-Martin et al., 2020] Munoz-Martin, J. F., Capon, L. F., Ruiz-de Azua, J. A., and Camps, A. (2020). The flexible microwave payload-2: A sdr-based gnss-reflectometer and l-band radiometer for cubesats. *IEEE Journal of Selected Topics in Applied Earth Observations and Remote Sensing*, 13:1298–1311.

[Munoz-Martin et al., 2021a] Munoz-Martin, J. F., Fernandez, L., Perez, A., Ruiz-de Azua, J. A., Park, H., Camps, A., Domínguez, B. C., and Pastena, M. (2021a). In-orbit validation of the fmpl-2 instrument—the gnss-r and l-band microwave radiometer payload of the fsscat mission. *Remote Sensing*, 13(1):121.

[Munoz-Martin et al., 2021b] Munoz-Martin, J. F., Llaveria, D., Herbert, C., Pablos, M., Park, H., and Camps, A. (2021b). Soil moisture estimation synergy using gnss-r and l-band microwave radiometry data from fsscat/fmpl-2. *Remote Sensing*, 13(5):994.

[Nagler et al., 2015] Nagler, T., Rott, H., Hetzenecker, M., Wuite, J., and Potin, P. (2015). The sentinel-1 mission: New opportunities for ice sheet observations. *Remote Sensing*, 7(7):9371–9389.

[Naoki et al., 2008] Naoki, K., Ukita, J., Nishio, F., Nakayama, M., Comiso, J. C., and Gasiewski, A. (2008). Thin sea ice thickness as inferred from passive microwave and in situ observations. *Journal of Geophysical Research: Oceans*, 113(C2).

[No, 2009] No, D. (2009). Cryosat ground segment.

[NSIDC, 2020] NSIDC (2020). Arctic sea ice at minimum extent for 2020 (September 2020). `https://nsidc.org/news/newsroom/arctic-sea-ice-minimum-extent-2020`. Accessed: 2021-01-13.

[Ochsner et al., 2013] Ochsner, T. E., Cosh, M. H., Cuenca, R. H., Dorigo, W. A., Draper, C. S., Hagimoto, Y., Kerr, Y. H., Larson, K. M., Njoku, E. G., Small, E. E., et al. (2013). State of the art in large-scale soil moisture monitoring. *Soil Science Society of America Journal*, 77(6):1888–1919.

[Ogden et al., 2017] Ogden, F. L., Allen, M. B., Lai, W., Zhu, J., Seo, M., Douglas, C. C., and Talbot, C. A. (2017). The soil moisture velocity equation. *Journal of Advances in Modeling Earth Systems*, 9(2):1473–1487.

[Oliva et al., 2016] Oliva, R., Daganzo, E., Richaume, P., Kerr, Y., Cabot, F., Soldo, Y., Anterrieu, E., Reul, N., Gutierrez, A., Barbosa, J., et al. (2016). Status of radio frequency interference (rfi) in the 1400–1427 mhz passive band based on six years of smos mission. *Remote sensing of environment*, 180:64–75.

[Oliva et al., 2020] Oliva, R., Martín-Neira, M., Corbella, I., Closa, J., Zurita, A., Cabot, F., Khazaal, A., Richaume, P., Kainulainen, J., Barbosa, J., et al. (2020). Smos third mission reprocessing after 10 years in orbit. *Remote Sensing*, 12(10):1645.

[Omran et al., 2007] Omran, M. G., Engelbrecht, A. P., and Salman, A. (2007). An overview of clustering methods. *Intelligent Data Analysis*, 11(6):583–605.

[Or et al., 2005] Or, D., Tuller, M., and Wraith, J. M. (2005). Soil water potential. *Encyclopedia of soils in the environment*, 3:270–277.

[Owe et al., 2008] Owe, M., de Jeu, R., and Holmes, T. (2008). Multisensor historical climatology of satellite-derived global land surface moisture. *Journal of Geophysical Research: Earth Surface*, 113(F1).

[Owe and Van de Griend, 1998] Owe, M. and Van de Griend, A. A. (1998). Comparison of soil moisture penetration depths for several bare soils at two microwave frequencies and implications for remote sensing. *Water resources research*, 34(9):2319–2327.

[Pablos et al., 2018] Pablos, M., González-Zamora, Á., Sánchez, N., and Martínez-Fernández, J. (2018). Assessment of root zone soil moisture estimations from smap, smos and modis observations. *Remote Sensing*, 10(7):981.

[Pablos et al., 2016] Pablos, M., Martínez-Fernández, J., Piles, M., Sánchez, N., Vall-llossera, M., and Camps, A. (2016). Multi-temporal evaluation of soil moisture and land surface temperature dynamics using in situ and satellite observations. *Remote Sensing*, 8(7):587.

[Pablos et al., 2017] Pablos, M., Martínez-Fernández, J., Sánchez, N., and González-Zamora, Á. (2017). Temporal and spatial comparison of agricultural drought indices from moderate resolution satellite soil moisture data over northwest spain. *Remote Sensing*, 9(11):1168.

[Pablos et al., 2019] Pablos, M., Piles, M., and González-Haro, C. (2019). Bec smos land products description. `http://bec.icm.csic.es/doc/BEC-SMOS-0003-PD-Land.pdf`. Accessed: 2019-09-15.

[Palmisano et al., 2020] Palmisano, D., Mattia, F., Balenzano, A., Satalino, G., Pierdicca, N., and Guarnieri, A. V. M. (2020). Sentinel-1 sensitivity to soil moisture at high incidence angle and the impact on retrieval over seasonal crops. *IEEE Transactions on Geoscience and Remote Sensing*, 59(9):7308–7321.

[Paloscia et al., 2013] Paloscia, S., Pettinato, S., Santi, E., Notarnicola, C., Pasolli, L., and Reppucci, A. (2013). Soil moisture mapping using sentinel-1 images: Algorithm and preliminary validation. *Remote Sensing of Environment*, 134:234–248.

[Parkinson et al., 1999] Parkinson, C. L., Cavalieri, D. J., Gloersen, P., Zwally, H. J., and Comiso, J. C. (1999). Arctic sea ice extents, areas, and trends, 1978–1996. *Journal of Geophysical Research: Oceans*, 104(C9):20837–20856.

[Paţilea et al., 2019] Paţilea, C., Heygster, G., Huntemann, M., and Spreen, G. (2019). Combined smap–smos thin sea ice thickness retrieval. *The Cryosphere*, 13(2):675–691.

[Pellarin et al., 2003] Pellarin, T., Wigneron, J.-P., Calvet, J.-C., Berger, M., Douville, H., Ferrazzoli, P., Kerr, Y. H., Lopez-Baeza, E., Pulliainen, J., Simmonds, L. P., et al. (2003). Two-year global simulation of l-band brightness temperatures over land. *IEEE Transactions on Geoscience and Remote Sensing*, 41(9):2135–2139.

[Petropoulos et al., 2015] Petropoulos, G. P., Ireland, G., and Barrett, B. (2015). Surface soil moisture retrievals from remote sensing: Current status, products & future trends. *Physics and Chemistry of the Earth, Parts A/B/C*, 83:36–56.

[Picard et al., 2018] Picard, G., Sandells, M., and Löwe, H. (2018). Smrt: An active–passive microwave radiative transfer model for snow with multiple microstructure and scattering formulations (v1. 0). *Geoscientific Model Development*, 11(7):2763–2788.

[Pietola and Alakukku, 2005] Pietola, L. and Alakukku, L. (2005). Root growth dynamics and biomass input by nordic annual field crops. *Agriculture, ecosystems & environment*, 108(2):135–144.

[Piles et al., 2014] Piles, M., Sánchez, N., Vall-llossera, M., Camps, A., Martínez-Fernández, J., Martínez, J., and González-Gambau, V. (2014). A downscaling approach for smos land observations: Evaluation of high-resolution soil moisture maps over the iberian peninsula. *IEEE Journal of Selected Topics in Applied Earth Observations and Remote Sensing*, 7(9):3845–3857.

[Poljansek et al., 2017] Poljansek, K., Marín Ferrer, M., De Groeve, T., and Clark, I. (2017). *Science for disaster risk management 2017: knowing better and losing less*. ETH Zurich.

[Portal et al., 2020] Portal, G., Jagdhuber, T., Vall-llossera, M., Camps, A., Pablos, M., Entekhabi, D., and Piles, M. (2020). Assessment of multi-scale smos and smap soil moisture products across the iberian peninsula. *Remote Sensing*, 12(3):570.

[Portal et al., 2018] Portal, G., Vall-Llossera, M., Piles, M., Camps, A., Chaparro, D., Pablos, M., and Rossato, L. (2018). A spatially consistent downscaling approach for smos using an adaptive moving window. *IEEE Journal of Selected Topics in Applied Earth Observations and Remote Sensing*, 11(6):1883–1894.

[Qi et al., 2018] Qi, P., Zhang, G., Xu, Y. J., Wang, L., Ding, C., and Cheng, C. (2018). Assessing the influence of precipitation on shallow groundwater table response using a combination of singular value decomposition and cross-wavelet approaches. *Water*, 10(5):598.

[Rakthanmanon et al., 2012] Rakthanmanon, T., Campana, B., Mueen, A., Batista, G., Westover, B., Zhu, Q., Zakaria, J., and Keogh, E. (2012). Searching and mining trillions of time series subsequences under dynamic time warping. In *Proceedings of the 18th ACM SIGKDD international conference on Knowledge discovery and data mining*, pages 262–270.

[Reichle et al., 2008] Reichle, R. H., Crow, W. T., and Keppenne, C. L. (2008). An adaptive ensemble kalman filter for soil moisture data assimilation. *Water resources research*, 44(3).

[Reichle and Koster, 2004] Reichle, R. H. and Koster, R. D. (2004). Bias reduction in short records of satellite soil moisture. *Geophysical Research Letters*, 31(19).

[Reynolds, 1970] Reynolds, S. (1970). The gravimetric method of soil moisture determination part ia study of equipment, and methodological problems. *Journal of Hydrology*, 11(3):258–273.

[Ricker et al., 2014] Ricker, R., Hendricks, S., Helm, V., Skourup, H., and Davidson, M. (2014). Sensitivity of cryosat-2 arctic sea-ice freeboard and thickness on radar-waveform interpretation. *The Cryosphere*, 8(4):1607–1622.

[Ricker et al., 2017] Ricker, R., Hendricks, S., Kaleschke, L., Tian-Kunze, X., King, J., and Haas, C. (2017). A weekly arctic sea-ice thickness data record from merged cryosat-2 and smos satellite data. *Cryosphere*, 11(4):1607–1623.

[Rignot and Van Zyl, 1993] Rignot, E. J. and Van Zyl, J. J. (1993). Change detection techniques for ers-1 sar data. *IEEE Transactions on Geoscience and Remote sensing*, 31(4):896–906.

[Rodriguez-Fernandez et al., 2019] Rodriguez-Fernandez, N., Al Bitar, A., Colliander, A., and Zhao, T. (2019). Soil moisture remote sensing across scales. *Remote Sensing*, 11:190.

[Rondinelli et al., 2015] Rondinelli, W. J., Hornbuckle, B. K., Patton, J. C., Cosh, M. H., Walker, V. A., Carr, B. D., and Logsdon, S. D. (2015). Different rates of soil drying after rainfall are observed by the smos satellite and the south fork in situ soil moisture network. *Journal of Hydrometeorology*, 16(2):889–903.

[Rosenbaum et al., 2012] Rosenbaum, U., Bogena, H. R., Herbst, M., Huisman, J., Peterson, T., Weuthen, A., Western, A., and Vereecken, H. (2012). Seasonal and event dynamics of spatial soil moisture patterns at the small catchment scale. *Water Resources Research*, 48(10).

[Sabater et al., 2007] Sabater, J. M., Jarlan, L., Calvet, J.-C., Bouyssel, F., and De Rosnay, P. (2007). From near-surface to root-zone soil moisture using different assimilation techniques. *Journal of Hydrometeorology*, 8(2):194–206.

[Sakoe and Chiba, 1978] Sakoe, H. and Chiba, S. (1978). Dynamic programming algorithm optimization for spoken word recognition. *IEEE transactions on acoustics, speech, and signal processing*, 26(1):43–49.

[Salvador and Chan, 2007] Salvador, S. and Chan, P. (2007). Toward accurate dynamic time warping in linear time and space. *Intelligent Data Analysis*, 11(5):561–580.

[Samouëlian et al., 2005] Samouëlian, A., Cousin, I., Tabbagh, A., Bruand, A., and Richard, G. (2005). Electrical resistivity survey in soil science: a review. *Soil and Tillage research*, 83(2):173–193.

[Sanchez et al., 2012] Sanchez, N., Martínez-Fernández, J., Scaini, A., and Perez-Gutierrez, C. (2012). Validation of the smos l2 soil moisture data in the remedhus network (spain). *IEEE Transactions on Geoscience and Remote Sensing*, 50(5):1602–1611.

[Scarlat et al., 2020] Scarlat, R. C., Spreen, G., Heygster, G., Huntemann, M., Paţilea, C., Pedersen, L. T., and Saldo, R. (2020). Sea ice and atmospheric parameter retrieval from satellite microwave radiometers: Synergy of amsr2 and smos compared with the cimr candidate mission. *Journal of Geophysical Research: Oceans*, 125(3):e2019JC015749.

[Schwarz et al., 1978] Schwarz, G. et al. (1978). Estimating the dimension of a model. *The annals of statistics*, 6(2):461–464.

[Shannon, 1948] Shannon, C. E. (1948). A mathematical theory of communication. *The Bell system technical journal*, 27(3):379–423.

[Shellito et al., 2016] Shellito, P. J., Small, E. E., Colliander, A., Bindlish, R., Cosh, M. H., Berg, A. A., Bosch, D. D., Caldwell, T. G., Goodrich, D. C., McNairn, H., et al. (2016). Smap soil moisture drying more rapid than observed in situ following rainfall events. *Geophysical research letters*, 43(15):8068–8075.

[Shen et al., 2017] Shen, X.-y., Zhang, J., Meng, J.-m., and Ke, C.-q. (2017). Sea ice type classification based on random forest machine learning with cryosat-2 altimeter data. In *2017 International Workshop on Remote Sensing with Intelligent Processing (RSIP)*, pages 1–5. IEEE.

[Sherlock and McDonnell, 2003] Sherlock, M. D. and McDonnell, J. J. (2003). A new tool for hillslope hydrologists: spatially distributed groundwater level and soilwater content measured using electromagnetic induction. *Hydrological Processes*, 17(10):1965–1977.

[Shi et al., 2006] Shi, J., Jiang, L., Zhang, L., Chen, K.-S., Wigneron, J.-P., Chanzy, A., and Jackson, T. J. (2006). Physically based estimation of bare-surface soil moisture with the passive radiometers. *IEEE transactions on geoscience and remote sensing*, 44(11):3145–3153.

[Sinergise, 2020] Sinergise, L. (2020). Modified copernicus sentinel data 2020/sentinel hub. `https://sentinel-hub.com`. Accessed: 2020-08-01.

[Skøien et al., 2003] Skøien, J. O., Blöschl, G., and Western, A. W. (2003). Characteristic space scales and timescales in hydrology. *Water Resources Research*, 39(10).

[Smith, 2018] Smith, L. N. (2018). A disciplined approach to neural network hyper-parameters: Part 1–learning rate, batch size, momentum, and weight decay. *arXiv preprint arXiv:1803.09820*.

[SpaceNews, 2020] SpaceNews (2020). Spire adding cross links to cubesat constellation (September 2020). `https://spacenews.com/spire-adding-cross-links-to-cubesat-constellation/`. Accessed: 2021-01-21.

[Spinoni et al., 2018] Spinoni, J., Vogt, J. V., Naumann, G., Barbosa, P., and Dosio, A. (2018). Will drought events become more frequent and severe in europe? *International Journal of Climatology*, 38(4):1718–1736.

[Srivastava et al., 2014] Srivastava, P. K., O'Neill, P., Cosh, M., Kurum, M., Lang, R., and Joseph, A. (2014). Evaluation of dielectric mixing models for passive microwave soil moisture retrieval using data from comrad ground-based smap simulator. *IEEE Journal of Selected Topics in Applied Earth Observations and Remote Sensing*, 8(9):4345–4354.

[Steffen, 1992] Steffen, K. (1992). Considerations for microwave remote sensing of thin sea ice. *Microwave Remote Sensing of Sea Ice*, page 291.

[SU et al., 2014] SU, S. L., Singh, D., and Baghini, M. S. (2014). A critical review of soil moisture measurement. *Measurement*, 54:92–105.

[Tanaka et al., 2016] Tanaka, Y., Tateyama, K., Kameda, T., and Hutchings, J. K. (2016). Estimation of melt pond fraction over high-concentration arctic sea ice using amsr-e passive microwave data. *Journal of Geophysical Research: Oceans*, 121(9):7056–7072.

[Tang et al., 2014] Tang, Q., Zhang, X., and Francis, J. A. (2014). Extreme summer weather in northern mid-latitudes linked to a vanishing cryosphere. *Nature Climate Change*, 4(1):45–50.

[Tedesco et al., 2004] Tedesco, M., Pulliainen, J., Takala, M., Hallikainen, M., and Pampaloni, P. (2004). Artificial neural network-based techniques for the retrieval of swe and snow depth from ssm/i data. *Remote sensing of Environment*, 90(1):76–85.

[Thorndike et al., 1975] Thorndike, A. S., Rothrock, D. A., Maykut, G. A., and Colony, R. (1975). The thickness distribution of sea ice. *Journal of Geophysical Research*, 80(33):4501–4513.

[Thornton, 1998] Thornton, C. (1998). Separability is a learner's best friend. In *4th Neural Computation and Psychology Workshop, London, 9–11 April 1997*, pages 40–46. Springer.

[Tian-Kunze et al., 2014] Tian-Kunze, X., Kaleschke, L., Maaß, N., Mäkynen, M., Serra, N., Drusch, M., and Krumpen, T. (2014). Smos-derived thin sea ice thickness: algorithm baseline, product specifications and initial verification. *The Cryosphere*, 8:997–1018.

[Tilling et al., 2018] Tilling, R. L., Ridout, A., and Shepherd, A. (2018). Estimating arctic sea ice thickness and volume using cryosat-2 radar altimeter data. *Advances in Space Research*, 62(6):1203–1225.

[Tobin et al., 2017] Tobin, K. J., Torres, R., Crow, W. T., and Bennett, M. E. (2017). Multi-decadal analysis of root-zone soil moisture applying the exponential filter across conus. *Hydrology and Earth System Sciences*, 21(9):4403–4417.

[Toppaladoddi and Wettlaufer, 2015] Toppaladoddi, S. and Wettlaufer, J. S. (2015). Theory of the sea ice thickness distribution. *Physical review letters*, 115(14):148501.

[Ulaby et al., 1986] Ulaby, F. T., Moore, R., and Fung, A. (1986). Microwave remote sensing: Active and passive. volume 3-from theory to applications.

[Ulvmoen and Omre, 2010] Ulvmoen, M. and Omre, H. (2010). Improved resolution in bayesian lithology/fluid inversion from prestack seismic data and well observations: Part 1—methodology. *Geophysics*, 75(2):R21–R35.

[Van Vuuren et al., 2011] Van Vuuren, D. P., Edmonds, J., Kainuma, M., Riahi, K., Thomson, A., Hibbard, K., Hurtt, G. C., Kram, T., Krey, V., Lamarque, J.-F., et al. (2011). The representative concentration pathways: an overview. *Climatic change*, 109(1):5–31.

[Vereecken et al., 2014] Vereecken, H., Huisman, J., Pachepsky, Y., Montzka, C., Van Der Kruk, J., Bogena, H., Weihermüller, L., Herbst, M., Martinez, G., and Vanderborght, J. (2014). On the spatio-temporal dynamics of soil moisture at the field scale. *Journal of Hydrology*, 516:76–96.

[Wagner et al., 2013] Wagner, W., Hahn, S., Kidd, R., Melzer, T., Bartalis, Z., Hasenauer, S., Figa, J., De Rosnay, P., Jann, A., Schneider, S., et al. (2013). The ascat soil moisture product: A review of its. *Meteorologische Zeitschrift*, 22(1):1–29.

[Wagner et al., 1999] Wagner, W., Lemoine, G., and Rott, H. (1999). A method for estimating soil moisture from ers scatterometer and soil data. *Remote sensing of environment*, 70(2):191–207.

[Wagner et al., 2007] Wagner, W., Naeimi, V., Scipal, K., de Jeu, R., and Martínez-Fernández, J. (2007). Soil moisture from operational meteorological satellites. *Hydrogeology Journal*, 15(1):121–131.

[Walker et al., 2004] Walker, J. P., Willgoose, G. R., and Kalma, J. D. (2004). In situ measurement of soil moisture: a comparison of techniques. *Journal of Hydrology*, 293(1-4):85–99.

[Wang et al., 2019] Wang, H., Wellmann, F., Zhang, T., Schaaf, A., Kanig, R. M., Verweij, E., von Hebel, C., and van der Kruk, J. (2019). Pattern extraction of topsoil and subsoil heterogeneity and soil-crop interaction using unsupervised bayesian machine learning: An application to satellite-derived ndvi time series and electromagnetic induction measurements. *Journal of Geophysical Research: Biogeosciences*, 124(6):1524–1544.

[Wang et al., 2017] Wang, H., Wellmann, J. F., Li, Z., Wang, X., and Liang, R. Y. (2017). A segmentation approach for stochastic geological modeling using hidden markov random fields. *Mathematical Geosciences*, 49(2):145–177.

[Wang et al., 2015] Wang, J., Ge, Y., Heuvelink, G., and Zhou, C. (2015). Upscaling in situ soil moisture observations to pixel averages with spatio-temporal geostatistics. *Remote Sensing*, 7(9):11372–11388.

[Wang and Qu, 2009] Wang, L. and Qu, J. J. (2009). Satellite remote sensing applications for surface soil moisture monitoring: A review. *Frontiers of Earth Science in China*, 3(2):237–247.

[Wang et al., 2013] Wang, X., Mueen, A., Ding, H., Trajcevski, G., Scheuermann, P., and Keogh, E. (2013). Experimental comparison of representation methods and distance measures for time series data. *Data Mining and Knowledge Discovery*, 26(2):275–309.

[Warren et al., 1999] Warren, S. G., Rigor, I. G., Untersteiner, N., Radionov, V. F., Bryazgin, N. N., Aleksandrov, Y. I., and Colony, R. (1999). Snow depth on arctic sea ice. *Journal of Climate*, 12(6):1814–1829.

[Welch et al., 1995] Welch, G., Bishop, G., et al. (1995). An introduction to the kalman filter.

[Wellmann and Regenauer-Lieb, 2012] Wellmann, J. F. and Regenauer-Lieb, K. (2012). Uncertainties have a meaning: Information entropy as a quality measure for 3-d geological models. *Tectonophysics*, 526:207–216.

[Wigneron et al., 2017] Wigneron, J.-P., Jackson, T., O'neill, P., De Lannoy, G., de Rosnay, P., Walker, J., Ferrazzoli, P., Mironov, V., Bircher, S., Grant, J., et al. (2017). Modelling the passive microwave signature from land surfaces: A review of recent results and application to the l-band smos & smap soil moisture retrieval algorithms. *Remote Sensing of Environment*, 192:238–262.

[Wingham et al., 2006] Wingham, D., Francis, C., Baker, S., Bouzinac, C., Brockley, D., Cullen, R., de Chateau-Thierry, P., Laxon, S., Mallow, U., Mavrocordatos, C., et al. (2006). Cryosat: A mission to determine the fluctuations in earth's land and marine ice fields. *Advances in Space Research*, 37(4):841–871.

[Wu et al., 2002] Wu, W., Geller, M. A., and Dickinson, R. E. (2002). The response of soil moisture to long-term variability of precipitation. *Journal of Hydrometeorology*, 3(5):604–613.

[Ye et al., 2020] Ye, N., Walker, J. P., Yeo, I.-Y., Jackson, T. J., Kerr, Y., Kim, E., McGrath, A., Popstefanija, I., Goodberlet, M., and Hills, J. (2020). Toward p-band passive microwave sensing of soil moisture. *IEEE Geoscience and Remote Sensing Letters*, 18(3):504–508.

[Zakhvatkina et al., 2019] Zakhvatkina, N., Smirnov, V., and Bychkova, I. (2019). Satellite sar data-based sea ice classification: An overview. *Geosciences*, 9(4):152.

[Zege et al., 2015] Zege, E., Malinka, A., Katsev, I., Prikhach, A., Heygster, G., Istomina, L., Birnbaum, G., and Schwarz, P. (2015). Algorithm to retrieve the melt pond fraction and the spectral albedo of arctic summer ice from satellite optical data. *Remote Sensing of Environment*, 163:153–164.

[Zeng and Beljaars, 2005] Zeng, X. and Beljaars, A. (2005). A prognostic scheme of sea surface skin temperature for modeling and data assimilation. *Geophysical Research Letters*, 32(14).

[Zhang et al., 2020] Zhang, R., Sun, C., Zhu, J., Zhang, R., and Li, W. (2020). Increased european heat waves in recent decades in response to shrinking arctic sea ice and eurasian snow cover. *NPJ Climate and Atmospheric Science*, 3(1):1–9.

[Zhuang et al., 2020] Zhuang, R., Zeng, Y., Manfreda, S., and Su, Z. (2020). Quantifying long-term land surface and root zone soil moisture over tibetan plateau. *Remote sensing*, 12(3):509.

[Zifan et al., 2006] Zifan, A., Saberi, S., Moradi, M. H., and Towhidkhah, F. (2006). Automated ecg segmentation using piecewise derivative dynamic time warping. *International Journal of Biological and Medical Sciences*, 1(3).